SISSA
Scuola
Internazionale
Superiore di
Studi Avanzati

Physics Area - PhD course in
Statistical Physics

Entanglement in many-body systems

Candidate:
Federico Rottoli

Advisor:
Prof. Pasquale Calabrese

Academic Year 2023-24

Alla mia bimba, alla mia famiglia,
e alla mia gatta, che di certo
non si sarebbe mai fatta mettere in scatola.

Into this wild Abyss,
The womb of Nature, and perhaps her grave,
Of neither sea, nor shore, nor air, nor fire,
But all these in their pregnant causes mixed
Confusedly, and which thus must ever fight,
Unless th' Almighty Maker them ordain
His dark materials to create more worlds
— John Milton, *Paradise Lost*, Book II, 910–916

List of publications

[1] FR, C. Rylands, and P. Calabrese, *Entanglement Hamiltonians and the quasiparticle picture*, arXiv:2407.01730.

[2] FR, M. Fossati, and P. Calabrese, *Entanglement Hamiltonian in the non-Hermitian SSH model*, J. Stat. Mech. (2024) 063102.

[3] FR, F. Ares, P. Calabrese, and D. X. Horváth, *Entanglement entropy along a massless renormalisation flow: the tricritical to critical Ising crossover*, JHEP **02** (2024) 053.

[4] FR, S. Murciano, and P. Calabrese, *Finite temperature negativity Hamiltonians of the massless Dirac fermion*, JHEP **06** (2023) 139.

[5] FR, S. Murciano, E. Tonni, and P. Calabrese, *Entanglement and negativity Hamiltonians for the massless Dirac field on the half line*, J. Stat. Mech. (2023) 013103.

[6] L. Capizzi, S. Scopa, FR, and P. Calabrese, *Domain wall melting across a defect*, EPL **141** (2023) 31002.

[7] FR, S. Scopa, and P. Calabrese, *Entanglement Hamiltonian during a domain wall melting in the free Fermi chain*, J. Stat. Mech. (2022) 063103.

Contents

Chapter 1

Introduction

> *EINSTEIN ATTACKS QUANTUM THEORY;*
> *Scientist and Two Colleagues Find It Is Not*
> *'Complete' Even Though 'Correct.'*
> — *The New York Times,* May 4, 1935

To the present day knowledge, quantum mechanics provides the most fundamental understanding of nature. The discovery of quantum mechanics in the first half of the XX century was accompanied by a debate regarding one of its most peculiar properties, *entanglement* [1, 2]. The clearest example of this phenomenon is the spin singlet state

$$|\psi\rangle = \frac{|{\uparrow_A}\rangle \otimes |{\downarrow_B}\rangle - |{\downarrow_A}\rangle \otimes |{\uparrow_B}\rangle}{\sqrt{2}}\,, \tag{1.1}$$

where we have denoted with A the first spin and with B the second one. If by measuring spin A we observe it in, e.g., the up direction, the collapse of the wave function immediately tells us that spin B must be in the down direction. At first glance this appears intuitive; because of angular momentum conservation, gaining knowledge on one spin would immediately give us information also on the other one. The non-classical nature of entanglement becomes instead apparent when considering non-commuting observables.

In 1964, Bell demonstrated that in a probabilistic model, if we require that every observable has independent existence before the measurement and that the theory does not admit non-local effects, the correlations between the observables must satisfy certain inequalities, known as *Bell's inequalities* [3–5]. Models for which the previous assumptions hold are known as local hidden variable models. A useful formulation of Bell's inequalities is the Clauser-Horne-Shimony-Holt (CHSH) one [5]

$$|E(A_1, B_1) + E(A_1, B_2) + E(A_2, B_1) - E(A_2, B_2)| \leqslant 2\,, \tag{1.2}$$

where we have divided our system in two subsystems and A_i, B_j are observables in respectively the first and second subsystem. In Eq. (1.2), $E(A_i, B_j)$ denotes the correlation between the two observables. In quantum mechanics, the left hand side of Eq. (1.2) is computed as the expectation value of Bell's operator

$$\hat{\mathscr{B}} = \hat{A}_1 \otimes \hat{B}_1 + \hat{A}_1 \otimes \hat{B}_2 + \hat{A}_2 \otimes \hat{B}_1 - \hat{A}_2 \otimes \hat{B}_2 \,, \tag{1.3}$$

where $\hat{A}_i$ and $\hat{B}_j$ are the Hermitian operators corresponding to the observables A_i and B_j in Eq. (1.2). The remarkable property of entangled states is that the expectation value of Eq. (1.3) for non-commuting observables can violate Eq. (1.2). To give an example, in a system with two spins $1/2$, we consider as observables $\hat{A}_1 = \sigma^z$, $\hat{A}_2 = \sigma^x$ acting on the first spin and $\hat{B}_1 = (\sigma^z + \sigma^x)/\sqrt{2}$, $\hat{B}_2 = (\sigma^z - \sigma^x)/\sqrt{2}$ acting on the second one, where σ^x and σ^z are the Pauli matrices. With this choice, the expectation value of Bell's operator (1.3) on the singlet state (1.1) is

$$\left| \langle \hat{\mathscr{B}} \rangle \right| = 2\sqrt{2} \,, \tag{1.4}$$

exceeding the maximum value predicted by Eq. (1.2).

The CHSH inequality (1.2) offered a method to experimentally distinguish quantum mechanics from local hidden variables models. Quantum mechanics passed this test with flying colours when Friedmann and Clauser observed experimentally violations of the CHSH inequality in the polarisation of entangled photons [6], later replicated by Aspect [7]. For their discovery, Clauser and Aspect were jointly awarded the 2022 Nobel prize in physics. To date, violations of Bell's inequalities and the existence of quantum entanglement have been verified across a wide range of energies and length scales, with the very recent measurement of entanglement in top quark pair production at LHC [8].

Since the work of Bell, the quantification of entanglement has attracted interest not only across several different branches of physics but also in other fields such as computer science. In quantum information and quantum complexity theory [9], encoding information in entangled states allows to perform task which are otherwise classically intractable, such as quantum error correction and quantum algorithms which achieve a speedup over their classical counterparts [10]. The different scaling of entanglement in gapped and gapless phases (which we will review in the following) makes it useful to distinguish phases of matter in statistical mechanics [11–13] and in condensed matter physics [14]. Finally, in high energy physics, entanglement has been related to the Bekenstein-Hawking entropy of black holes [15] and, in the context of AdS/CFT holography, the Ryu-Takayanagi formula provides a geometric way of computing entanglement in large-N conformal field theories (CFTs) [16, 17].

The present thesis will focus on a tiny portion of the vast applicability of quantum entanglement, concentrating of the physics of low-dimensional many-body quantum systems. To this avail, we will apply several different techniques ranging from lattice computations to low-energy effective quantum field theories (QFTs) and hydrodynamics. Before presenting our work, in the rest of this Introduction we will review the main quantifications of entanglement which will appear in the rest of the thesis.

1.1 The entanglement entropy and the area law

When studying bipartitions of pure states, the most studied quantification of entanglement are the entanglement entropies. Let us consider a bipartition of space in two regions A and B. We assume that the Hilbert space factorises as a tensor product of spaces of states in the two regions $\mathcal{H} = \mathcal{H}_A \otimes \mathcal{H}_B$. A pure state $|\psi\rangle \in \mathcal{H}$ is said to be *separable* if it can be written as a tensor product of pure states in the two subsystems

$$|\psi\rangle = |\psi_A\rangle \otimes |\psi_B\rangle \,, \qquad |\psi_A\rangle \in \mathcal{H}_A \text{ and } |\psi_B\rangle \in \mathcal{H}_B \,. \tag{1.5}$$

Conversely, a pure state is entangled if it is not separable. This is the case for, e.g., the singlet state (1.1) that we have previously discussed. Tracing out the degrees of freedom in, i.e., the Hilbert space $\mathcal{H}_B$, we obtain the reduced density matrix (RDM)

$$\rho_A = \mathrm{Tr}_B\, \rho \,, \tag{1.6}$$

where $\rho = |\psi\rangle \langle\psi|$ is the density matrix of the whole state. If the total state ρ is entangled, the RDM ρ_A is a mixed state, reflecting loss of knowledge on the subsystem B. Defining now the von Neumann S_A and the n-Rényi entanglement entropies $S_A^{(n)}$ ($n \geqslant 2$) as the entropies of the RDM [18]

$$S_A^{(n)} \equiv \frac{1}{1-n} \log \mathrm{Tr}\, \rho_A^n \,, \qquad S_A \equiv -\,\mathrm{Tr}\left[\rho_A \log \rho_A\right] = \lim_{n\to 1} S_A^{(n)} \,, \tag{1.7}$$

these are non-vanishing if and only if the pure state $|\psi\rangle$ is entangled. Importantly, the von Neumann entropy can be obtained as the *replica limit* $n \to 1$ of the n-Rényi entropies.

Let us remark that, while the assumption that the Hilbert space $\mathcal{H}$ factorises is valid for lattice models, it fails in quantum field theories. The consequence of this lack of factorisation is that in QFTs the reduced density matrix (1.6) is a not well-defined operator and the entanglement entropy presents ultraviolet (UV) divergences even for the vacuum state, requiring a regularisation to obtain finite results. In the majority of the systems that we will treat in this thesis, the QFTs under study are assumed to emerge as low-energy effective descriptions of microscopic lattice models, which provide a natural non-universal UV cut-off. More in general, one needs to assume that the two subsystems A and B are not adjacent but are separated by a small regularising length ϵ. In terms of this cut-off ϵ, in gapped models in $d+1$ dimensions, the von Neumann entanglement entropy of the vacuum state generically scales as [19]

$$S_A \approx \frac{|\partial A|}{\epsilon^{d-1}} + \dots \,, \tag{1.8}$$

i.e., the leading term is proportional to the area of the boundary ∂A between the two regions A and B, rather than to the volume of A like the thermal entropy. For this reason, the behaviour in Eq. (1.8) is called *area law*.

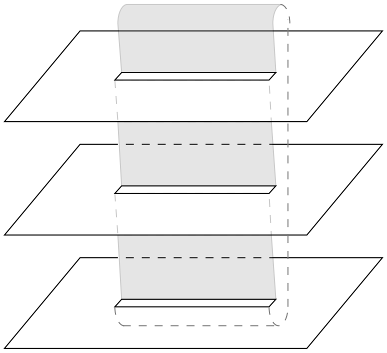

Figure 1.1: Replicated manifold for $n = 3$ replicas. In a path integral representation, the n-Rényi entanglement entropies can be computed from the partition function Z_n of the QFT on the depicted manifold through Eq. (1.10).

An important observation is that, because the leading term of Eq. (1.8) is proportional to the cut-off ϵ^{1-d}, the coefficient of the leading divergence is non-universal. To find universal properties of the QFT we need to look to logarithmic corrections to Eq. (1.8), which appear generically in gapless models. The most important example is provided by the entanglement entropies of conformal field theories (CFT) in $1+1$-dimensions. In these models, the logarithmic contribution is actually leading with respect to the area term, which reduces to a non-universal constant κ_n, leading to a violation of the area law in $1+1$-dimensional CFTs. The classic result of Refs. [20–22] then states that, for an interval of length ℓ in the ground state of a CFT, the coefficient of the logarithmic term $\log \ell$ is indeed universal and it is proportional to the central charge c of the CFT

$$S_A^{(n)} = \frac{c}{6}\left(1 + \frac{1}{n}\right) \log \frac{\ell}{\epsilon} + \kappa_n. \tag{1.9}$$

The computation of Eq. (1.9) and of several other result for the entanglement entropies of QFTs have been made possible by employing the *replica trick*. From Eq. (1.7), we see that the n-Rényi entropies are given by the trace of the product of n reduced density matrices ρ_A. Moving to a path integral representation, the matrix elements of the RDM are given by path integrals on a space-time with a cut in the position of the subsystem A. Multiplying together multiple RDM is equivalent to cyclically glue together the space-times along the cut, as depicted in Fig. 1.1. It was argued then that the product appearing in the Rényi entropies (1.7) is given by the ratio of the partition function on the replicated manifold in Fig. 1.1 Z_n and on the original one Z_1 [22]

$$\operatorname{Tr} \rho_A^n = \frac{Z_n}{Z_1^n}\,. \tag{1.10}$$

The von Neumann entropy is then recovered as the replica limit $n \to 1$ of the Rényi entropies. In the literature, the explicit computation of Eq. (1.10) has been carried over using several different approaches, like the use of *twist fields* (both in CFTs and in integrable models) and the *annulus method*, which are reviewed in more detail in Chapters 5 and 6, respectively.

Despite the usefulness of the entropies (1.7), they do not characterise completely the bipartite entanglement. To provide a more complete understanding, we need to consider the entanglement Hamiltonian, which we review in the next section.

1.2 The entanglement Hamiltonian

Let us again consider a spatial bipartition $A \cup B$ and let ρ_A be the RDM defined in Eq. (1.6). Since the reduced density matrix ρ_A is Hermitian and positive-definite, it can be written as the logarithm of an Hermitian matrix, the entanglement (or modular) Hamiltonian (EH) K_A [19, 23–25]

$$\rho_A = \frac{1}{Z_A} e^{-2\pi K_A}, \qquad Z_A = \mathrm{Tr}\, e^{-2\pi K_A}\,. \tag{1.11}$$

The entanglement Hamiltonian (1.11) contains the full information on the reduced density matrix and, as a consequence, it provides the most complete characterisation of the quantum correlation. On the other hand, in the general case the EH is significantly more difficult to compute than the entropies (1.7) and few results are known analytically. In the case of QFTs, the most fundamental of these results comes from a theorem in algebraic QFT, the Bisognano-Wichmann theorem [26, 27] (see also [19, 23–25]).

Let us consider a relativistic QFT in a $d+1$-dimensional space-time and let our subsystem be the half-space $A = \{x \in \mathbb{R}^{d+1} | x^1 > 0, x^0 = 0\}$. The Bisognano-Wichmann theorem states that the entanglement Hamiltonian of the ground state is the generator of Lorentz boosts which preserve the Rindler wedge [26, 27]

$$K_A = \int_{x^1>0} \mathrm{d}^d x\, x^1\, T_{00}(x)\,, \tag{1.12}$$

where T_{00} is the energy density in the QFT. This result is remarkable for several reasons. Notice first that the theorem (1.12) is extremely general, holding for every unitary Lorentz invariant quantum field theory. Another surprising property is that Eq. (1.12) has a local structure, being given by the integral of a local operator. Finally, the Bisognano-Wichmann theorem is interesting also from the point of view of high-energy physics, providing a mathematical proof of the Unruh effect [28–30].

For generic interacting gapped QFTs, the Bisognano-Wichmann theorem in Eq. (1.12) is the only known analytic result. On the other hand, for conformal field theories (CFTs), the extended space-time symmetry allows one to recover the entanglement Hamiltonian in more general geometries. In particular, the Hislop-Longo theorem [23, 31] (see also [31–34]) provides the EH in a ball-shaped region in any $d+1$-dimensional CFT. Restricting ourselves to the $1+1$-dimensional models that we will be interested in, the Hislop-Longo EH for an interval $A = [0, \ell]$ takes the form [31–34]

$$K_A = \int_0^\ell \mathrm{d}x \, \frac{x\,(\ell - x)}{\ell} \, T_{00}(x) \,. \tag{1.13}$$

In fact, the infinite conformal symmetry in $1+1$-dimensional CFTs makes it possible to recover the entanglement Hamiltonian in many more cases, such as a single interval at finite temperature or finite size and even in inhomogeneous and out-of-equilibrium protocols, by mapping the configuration of interest in the one in which the Bisognano-Wichmann theorem (1.12) applies. As was observed in Ref. [34,35], this mapping is possible in any case in which, after removing two small regularising circles at the boundary of the subsystem A, the space-time geometry is topologically equivalent to the one of an annulus, i.e., the same topology of the Bisognano-Wichmann theorem. Whenever this holds, the entanglement Hamiltonian inherits the local structure of the theorem (1.12), as we can see, e.g., from the EH of an interval in Eq. (1.13). Conversely, when the topology is different, like in the case of multiple intervals, or for excited states or in presence of zero modes, the EH will generically not be local and its structure will be highly model dependent. We will see examples of this failure in Chapters 2 and 3. We remark that the locality of the entanglement Hamiltonian, is not only interesting for theoretical reasons but it can be used to efficiently reconstruct the ground state in quantum simulators using a variational approach [36–40].

Even when the previously outlined strategy cannot be applied, several results have been obtained for non-interacting systems, both on the lattice and in QFTs. In these models, the reduced density matrix is Gaussian, i.e., it is quadratic in the fields or lattice operators, with potentially non-local couplings between them. To make an explicit example, in free fermionic lattice models, the Gaussian RDM can be written as

$$\rho_A = \frac{1}{Z_A} \exp\left\{ -\sum_{i,j} c_i^\dagger h_{ij} c_j \right\} , \tag{1.14}$$

where $c_i^\dagger, c_j$ are fermionic creation and annihilation operators, which satisfy the canonical anti-commutation relations, and h_{ij} is the kernel, i.e., the single particle EH. In a Gaussian state like the one in Eq. (1.14), Wick's theorem relates the two-point correlation function restricted to the subsystem $C_A = \langle c_i^\dagger c_j \rangle_{i,j\in A}$ to the single particle EH h via Peschel's formula [41,42]

$$C_A = \frac{1}{1+e^h} . \tag{1.15}$$

Eq. (1.15) applies both to lattice models and (with the appropriate changes) to QFTs. Using Eq. (1.15), the entanglement entropies can be expressed in terms of the eigenvalues σ_j of the correlation matrix C_A as

$$S_A^{(n)} = \frac{1}{1-n} \sum_j \log\left[\sigma_j^n + (1-\sigma_j)^n\right] , \qquad S_A = \sum_j \left[-\sigma_j \log \sigma_j - (1-\sigma_j) \log(1-\sigma_j)\right] . \tag{1.16}$$

In the rest of the thesis, Eqs. (1.15) and (1.16) will be our main numerical tools to obtain the entanglement Hamiltonian and entropies in lattice models.

Leaving now the realm of non-interacting systems, several analytical results have been obtained in $1+1$-dimensional integrable lattice models [41–56]. In these systems, the EH of the ground state in the half-space $x > 0$ is intimately related to Baxter's corner transfer matrix (CTM) $\widehat{A}$ [57–59]. Considering, for example, isotropic square lattices, the effect of the CTM is to add a full angular segment to a piece of lattice, mapping a horizontal row to a vertical one and vice versa. Using this property it is possible to show that the lattice reduced density matrix in the half-line can be expressed as the product of four CTMs [22, 41, 60]

$$\rho_A = \frac{\widehat{A}^4}{\mathrm{Tr}\,\widehat{A}^4}, \tag{1.17}$$

where $Z = \mathrm{Tr}\,\widehat{A}^4$ is the partition function. Recalling the definition (1.11) of the EH, Eq. (1.17) implies that it is proportional to the logarithm of fourth power of the CTM [41]

$$K_A = -\log \widehat{A}^4. \tag{1.18}$$

This correspondence between EHs and CTMs has made it possible to obtain the EHs in several integrable models. It has been observed that in certain integrable models, the logarithm of the CTM and the EH can be written in terms of the density of the lattice Hamiltonian h_j with a linearly increasing local temperature

$$K_A \propto \sum_{j=0}^{\infty} j\, h_j\,, \tag{1.19}$$

with a non-trivial proportionality constant. This behaviour has been identified in various spin systems such as the Ising model [41, 44, 45], the XXZ [46, 47, 57], the XYZ chains [48–50], the anisotropic XX chain [52], and in bosonic models such as the harmonic chain [42, 51, 52]. Comparing Eq. (1.19) with the Bisognano-Wichmann theorem in Eq. (1.12), it is evident that the two EHs share the same structure. In fact, the connection between the two results runs deeper than a superficial similarity. Tetel'man [48] and Itoyama and Thacker [49, 61–63] independently showed that in these integrable models the logarithm of the CTM is the generator of a continuous group of lattice Lorentz transformations, akin to the role played by the generator of Lorentz boosts in the Bisognano-Wichmann theorem.

Finally, we mention that the spectrum of the entanglement Hamiltonian (the *entanglement spectrum*) has been proven useful to characterise topological states of matter [64–66], being much more efficient than the entanglement entropies [67, 68]. In Ref. [64] it was recognised that in topological phases the low lying part of the entanglement spectrum agrees with the energy level of a CFT living on the entangling surface. This phenomenon is again a consequence of the application of the Bisognano-Wichmann theorem in Eq. (1.12) to the topological QFT that describes the bulk of the topological phase [66].

1.3 Entanglement in mixed states

The characterisations of entanglement that we have described up until now are efficient for bipartition of pure states. When considering mixed states or tripartite entanglement, however, the entropies (1.7) and the entanglement Hamiltonian (1.11) lose their meaning as characterisation of entanglement since the entropies are always non-zero for a mixed state, even if it is separable.

Let us first extend the definition of separable state (1.5) to mixed states

$$\rho = \sum_k p_k \, \rho_A^{(k)} \otimes \rho_B^{(k)} , \tag{1.20}$$

where $\sum_k p_k = 1$ and $\rho_A^{(k)} \in \mathcal{H}_A, \rho_B^{(k)} \in \mathcal{H}_B$ are pure states. Again, a state is said to be entangled if and only if it is not separable. Several measures of mixed states entanglement have been introduced in the years, however, most of them are computationally expensive even for few qubits. In fact, it was demonstrated that the problem of deciding if a mixed density matrix is separable is computationally intractable, differently from the pure case [69–71]. This implies that any computationally efficient condition for separability can only be sufficient but not necessary.

A very well studied, computationally efficient sufficient (but not necessary) condition for separability is given by the Peres-Horodecki or positive partial transpose (PPT) criterion, based on the *partial transpose* operation [72, 73]. Let $|e_A^{(i)}\rangle$ and $|e_B^{(j)}\rangle$ be bases of the Hilbert spaces $\mathcal{H}_A$ and $\mathcal{H}_B$, respectively. In these bases, the density matrix can be written as

$$\rho = \sum_{i,j,k,l} \langle e_A^{(i)}, e_B^{(j)} | \, \rho \, | e_A^{(k)}, e_B^{(l)} \rangle \, | e_A^{(i)}, e_B^{(j)} \rangle \, \langle e_A^{(k)}, e_B^{(l)} | \; . \tag{1.21}$$

The partial transpose operation is defined by transposing the matrix elements of the density matrix only in, e.g., the subsystem A

$$\rho^{T_A} = \sum_{i,j,k,l} \langle e_A^{(k)}, e_B^{(j)} | \, \rho \, | e_A^{(i)}, e_B^{(l)} \rangle \, | e_A^{(i)}, e_B^{(j)} \rangle \, \langle e_A^{(k)}, e_B^{(l)} | \; . \tag{1.22}$$

where we have exchanged the indices i, k in the matrix element with respect to Eq. (1.21). According to the Peres-Horodecki criterion, if the density matrix ρ is separable, its partial transpose ρ^{T_A} remain positive semi-definite. Conversely, if the partial transpose in Eq. (1.22) has negative eigenvalues, the density matrix ρ is entangled.

In light of the Peres-Horodecki criterion, the *logarithmic negativity* [74–76]

$$\mathcal{E} \equiv \log \mathrm{Tr} \left| \rho^{T_A} \right| , \tag{1.23}$$

was introduced as measures of entanglement in mixed states. Indeed, using the fact that the trace of ρ^{T_A} remains equal to one, it is possible to see that Eq. (1.23) quantifies how negative are the eigenvalues λ_i of the partial transpose

$$\mathcal{E} = \log\left[1 + 2\sum_{\lambda_i<0} |\lambda_i|\right]. \tag{1.24}$$

In particular, from Eq. (1.24), we see that $\mathcal{E}$ is always greater than or equal to zero, vanishing only if ρ^{T_A} is positive semi-definite. Another important property of the logarithmic negativity $\mathcal{E}$ in Eq. (1.23) is that when the state is pure, $\mathcal{E}$ reduces to the $1/2$-Rényi entanglement entropy $S_A^{(1/2)}$ for the subsystem A.

Similarly the entanglement entropy, also the negativity (1.23) can be computed via a replica trick by introducing the Rényi negativity

$$\mathcal{E}^{(n)} = \log \mathrm{Tr}\left[\left(\rho^{T_A}\right)^n\right]. \tag{1.25}$$

The negativity is then obtained by continuing analytically to $n = 1$ the Rényi negativity with even n

$$\mathcal{E} = \lim_{n\to 1} \mathcal{E}^{(n \text{ even})}. \tag{1.26}$$

While we have introduced the logarithmic negativity in the context of bipartite entanglement in mixed states, it proves useful also for tripartitions of pure ones. To characterise tripartite entanglement, we first consider a bipartition $A \cup B$ and we compute the reduced density matrix ρ_A in A by tracing out the degrees of freedom in $\mathcal{H}_B$, as we did in Eq. (1.6). We then consider a further bipartition $A = A_1 \cup A_2$ and we compute the logarithmic negativity of ρ_A by performing the partial transposition of ρ_A in, e.g., A_1. In the case of QFTs, tripartite Rényi negativities can be obtained through a path integral construction similar to the one described in Sec. 1.2 for the entanglement entropies [77–80]. It was found that the effect of multiplying two transposed matrices is to glue the path integral in the opposite direction, which leads to the surface depicted in Fig. 1.2 [77–80].

As was the case for the entropies, the logarithmic negativity offers only limited information on mixed state entanglement. Very recently, based on the definition (1.11) of the entanglement Hamiltonian, Ref. [81] introduced the *negativity Hamiltonian* (NH)

$$\rho_A^{T_1} \equiv \frac{1}{Z_A} e^{-2\pi\mathcal{N}_A}, \qquad Z_A = \mathrm{Tr}\, e^{-2\pi\mathcal{N}_A}, \tag{1.27}$$

as an operatorial characterisation of entanglement in mixed states. In Ref. [81], the authors introduced a procedure to compute the negativity Hamiltonian from the knowledge of the entanglement one in the same geometry and they used it to obtain the NH of two intervals in the ground state of the Dirac fermion. We will review in detail this procedure in Sec. 2.3. We remark that, differently from the EH, the negativity Hamiltonian in the ground state is always computed for more than one interval, due to the required tripartition. As a consequence, even in CFTs, the relevant geometry can never be mapped in the one in which

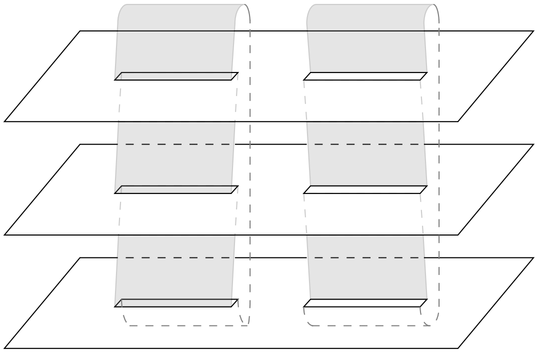

Figure 1.2: Replicated manifold for two intervals with $n = 3$ replicas, where the left interval has been transposed. The effect of the transposition is to glue the left interval in the opposite direction with respect to the right one (compare also with Fig. 1.1). In the path integral representation, the n-Rényi negativities (1.25) can be computed in terms of the partition function on this manifold.

the Bisognano-Wichmann theorem (1.12) applies, and the NH is always model dependent and non-local (albeit mildly). In the thesis we will present several novel results for this quantity, alongside a proper demonstration of the procedure of Ref. [81] for its computation.

1.4 Symmetry resolution of the entanglement entropy

A final topic that will be present in this thesis is the interplay of entanglement and global symmetries. Since the seminal work of Ref. [82], this field has attracted a significant interest and has lead to many results. To present the main ideas, we will focus on an $U(1)$ global symmetry. Let the local charge Q be the generator of this global transformation. Dividing our system as $A \cup B$, the charge can be decomposed as the sum of the charges in the subsystem A and in its complement $Q = Q_A + Q_B$. If a state ρ is invariant under the action of Q, by tracing over the Hilbert space $\mathcal{H}_B$ we find that also the RDM ρ_A is invariant

$$[\rho, Q] = 0 \qquad \Longrightarrow \qquad [\rho_A, Q_A] = 0\,. \tag{1.28}$$

If Eq. (1.28) holds, then by Schur's lemma ρ_A takes a block diagonal form, as the direct sum over the representations of the group, i.e., over the charge sectors

$$\rho_A = \bigoplus_q [\Pi_q \rho_A \Pi_q] = \bigoplus_q p_{A,q}\, \rho_{A,q}\,. \tag{1.29}$$

where Π_q denotes the projector on the charge sector with charge q. In Eq. (1.29), we have introduced $\rho_{A,q}$ which is the normalised RDM in the sector q and p_q which is the classical probability of finding a charge q in the subsystem A, which satisfy $\mathrm{Tr}\, \rho_{A,q} = 1$ and $p_q \geqslant 0$, $\sum_q p_q = 1$.

Given a state written as (1.29), the *symmetry resolved entanglement entropies* were introduced as the entanglement entropies in each charge sector [82]

$$S^{(n)}_{A,q} = \frac{1}{1-n} \log \mathrm{Tr}\left[\rho^n_{A,q}\right], \qquad S_{A,q} = \lim_{n\to 1} S^{(n)}_{A,q} = -\,\mathrm{Tr}\left[\rho_{A,q} \log \rho_{A,q}\right], \tag{1.30}$$

where, as was the case for the entanglement entropies in Eq. (1.7), the von Neumann symmetry resolved entropy $S_{A,q}$ can be obtained as the replica limit $n \to 1$ of the Rényi ones $S^{(n)}_{A,q}$. A remarkable property of the von Neumann entropy, is that the full entanglement entropy S_A can be written as the sum of two terms

$$S_A = \sum_q p_q\, S_{A,q} - \sum_q p_q \log p_q = S_c + S_n\,. \tag{1.31}$$

The first term is called *configurational* entropy and is the average over all charges sector of the symmetry resolved von Neumann entropies (1.30). The second one, instead, is the *number* entropy and is the contribution due to the fluctuation of the charge in the subsystem A. Interestingly, it was found that the entanglement entropy is identically distributed in the charge sector, i.e., the symmetry resolved entropies $S_{A,q}$ are independent of the charge q [83]. This property goes under the name of entanglement equipartition [83].

The direct computation of Eq. (1.30) is particularly difficult due to the presence of the projectors Π_q. A less direct but easier route is to compute the charged moments [82]

$$Z_n(\alpha) = \mathrm{Tr}\left[\rho_A\, e^{\mathrm{i}\alpha Q_A}\right], \tag{1.32}$$

whose Fourier transform yields the symmetry resolved n-Rényi entropy

$$\mathcal{Z}_n(q) = \int_{-\pi}^{\pi} \frac{\mathrm{d}\alpha}{2\pi} e^{-\mathrm{i}\alpha q} = \mathrm{Tr}\left[\Pi_q \rho^n_A\right], \qquad S^{(n)}_{A,q} = \frac{1}{1-n} \log\left[\frac{\mathcal{Z}_n(q)}{\mathcal{Z}_1(q)^n}\right]. \tag{1.33}$$

Eqs. (1.32) and (1.33) are especially efficient in the case of CFTs. Recall that in QFTs, through Eq. (1.10) the entanglement entropies can be obtained from the partition function on the replicated manifold depicted in Fig. 1.1. Following Ref. [82], we thread a flux α in the replica manifold. When a particle move from one replica to another and comes back to the initial one, it acquires an Aharonov-Bohm phase $e^{\mathrm{i}\alpha q}$, where q is the charge in the subsystem A. We therefore see that the charged moments (1.32) can be computed from the partition function on the replica manifold with the introduction of an appropriate flux. In Chapter 5, we will discuss how this partition function can be computed in practice as the correlation function of composite twist fields.

1.5 Organisation of the thesis

The present thesis is organised in three main parts, each focusing on a different aspect of entanglement in many body quantum systems. Part I, comprised of three chapters, will be devoted to the study of entanglement and negativity Hamiltonians in fermionic systems at equilibrium. As we mentioned in Secs. 1.2 and 1.3, these operators offers the most comprehensive characterisation of entanglement in pure and mixed states, respectively. In Chapter 2 we will study the free massless Dirac field theory in the presence of a boundary. We obtain the analytical expression for the EH and NH of multiple intervals in the ground state, generalising several previous results. In the following Chapter 3, we continue the study of the Dirac fermion CFT, turning our attention to mixed states; we compute the NH at finite temperature, both in a bipartite and tripartite configuration.

Most of the previously known results on the entanglement Hamiltonian have been obtained in unitary theories. Chapter 4 concludes Part I by instead focusing on an example of non-Hermitian fermionic lattice theory, the non-Hermitian Su-Schrieffer-Heeger model. We conduct a numerical analysis of the ground state EH in this model, both in a gapped phase and at a critical point described by the bc-ghost CFT. We propose a conjecture for the EH in this non-unitary CFT, which remarkably contains an additional term with respect to Eq. (1.13) for unitary theories.

Part II, consisting of Chapter 5, will focus on the entanglement properties of integrable QFTs, with particular emphasis on the behaviour of entanglement along a renormalisation group flow. We study the massless renormalisation group which interpolates between the tricritical and the critical Ising CFTs, using the form factor formalism (see Chapter 5 for details). We obtain the form factors of standard and composite twist fields in two different ways, by directly solving the bootstrap equations in the massless flow and as a limit of the form factors in the sinh-Gordon theory, showing that they give the same result. We then use these form factors to compute the entanglement entropy along the flow.

Finally, in Part III, containing three chapters, we will concentrate on out-of-equilibrium problems. In Chapters 6 and 7 we consider a prototypical example of out-of-equilibrium protocol, the melting of a domain wall state. In this protocol, the initial state is prepared at at time $t = 0$ to be completely full on the right of the origin and completely empty on the left, and is subsequently evolved with a free fermion hopping Hamiltonian. This problem has attracted a lot of interest in the past and many results are known, including in particular the entanglement entropies which are known to grow logarithmically in time. In Chapter 6 we make a step further by computing the entanglement Hamiltonian, which remarkably presents the same local structure inherited from the Bisognano-Wichmann theorem. Later, in Chapter 7 we consider a modification of this setup, in which a conformal defect is placed in the position of the domain wall. We compute the entanglement entropies during the evolution, observing that even the smallest defect has a dramatic effect on entanglement, modifying its growth from logarithmic to linear in time.

We conclude Part III and this thesis with Chapter 8, in which we study global quenches in non-interacting fermionic models. Using the quasiparticle picture of entanglement evolution, we show that the reduced density matrix after a generic quench can be approximated as the tensor product of a pure and an entangling part, the latter of which describes the low-lying entanglement spectrum, and we obtain an explicit expression for the EH describing the entangling part.

Part I

Entanglement and Negativity Hamiltonians

Chapter 2

Entanglement and negativity Hamiltonians for the massless Dirac field on the half-line

As we have discussed in the Introduction, the entanglement Hamiltonian defined in Eq. (1.11) constitutes the most complete characterisation of bipartite entanglement in pure states. For tripartite entanglement or mixed states, the negativity Hamiltonian in Eq. (1.27) provides an analogous quantification [81]. These operators will be the main subject of this first part of the thesis, especially in configurations that go beyond the local structure of the Bisognano-Wichmann theorem (1.12) and its corollaries. In particular, in this Chapter, based on Ref. [84], we obtain the analytic expression for the entanglement Hamiltonian of a subsystem composed of an arbitrary number of intervals, in the ground state of the massless Dirac fermion in the presence of a boundary. This EH will then be the starting point for the derivation of the negativity Hamiltonian in the presence of a boundary, using the methodology put forward in [81], that we review in Sec. 2.3.

Systems with physical boundaries are interesting for several reasons: experimental solid-state systems typically have open boundary conditions (OBC); in trapped cold atoms, the vanishing of the density outside the trap induces OBC in the inhomogeneous gas that can be treated through field theories in curved space [85]; in some non-equilibrium protocols like a quantum quench, the initial state can be seen as a boundary state in imaginary time formalism [86].

For the theory under study, several results were known in the previous literature. Ref. [87] (see also [88]) obtained the ground state EH for an arbitrary interval in the absence of any boundary. As we will show in the following, an intriguing feature of this EH is the presence of non-local contributions coupling points in different intervals. Later, Ref. [89] considered the problem in the presence of a boundary, obtaining the EH for a single interval separated from the boundary. The results of this Chapter generalise and extend both these works.

2.1 Dirac fermions in the presence of a boundary

Before treating the problem of the computation of the entanglement Hamiltonian, we wish to briefly review the main properties of the theory under consideration, the massless Dirac fermion in $1+1$-dimensional half-Minkowski space-time, with a boundary condition that guarantees energy conservation [90–92]. In particular, we show that this boundary condition can be implemented by two distinct phases [89,93–96], which correspond to models characterised by different conservation laws, preserving either charge or helicity but not both of them at the same time. As a consequence, this induces a coupling between the left- and right-moving chiral components of the Dirac field.

The complex Dirac fermion is given by the doublet

$$\Psi(x,t) = \begin{pmatrix} \psi_R(x-t) \\ \psi_L(x+t) \end{pmatrix}, \tag{2.1}$$

where the two components are respectively the right- and the left-moving chiral fermions. A property that we will use later is the fact that each of these components can be written in terms of two real Majorana fermions μ^1 and μ^2 as

$$\begin{cases} \psi(x,t) = \mu^1(x,t) + \mathrm{i}\mu^2(x,t), \\ \psi^\dagger(x,t) = \mu^1(x,t) - \mathrm{i}\mu^2(x,t). \end{cases} \tag{2.2}$$

Writing the gamma matrices as

$$\gamma^0 = \begin{pmatrix} 0 & 1 \\ 1 & 0 \end{pmatrix}, \qquad \gamma^1 = \begin{pmatrix} 0 & -1 \\ 1 & 0 \end{pmatrix}, \tag{2.3}$$

the dynamics of the model is described by the Lagrangian density

$$\begin{aligned} \mathcal{L}(x,t) &= \mathrm{i}\,\Psi^\dagger(x,t)\,\gamma^0\gamma^\mu\,\partial_\mu\Psi(x,t) \\ &= \mathrm{i}\,\psi_R^\dagger(x-t)\,(\partial_t+\partial_x)\,\psi_R(x-t) + \mathrm{i}\,\psi_L^\dagger(x+t)\,(\partial_t-\partial_x)\,\psi_L(x+t)\,, \end{aligned} \tag{2.4}$$

in which, as expected for a CFT, the two chiral components are decoupled. From the Lagrangian (2.4), we can find the two-point correlation function of the Dirac fermion. For the two chiral fermions, the equal time two-point correlation functions are

$$\begin{cases} \langle \psi_R^\dagger(x-t)\psi_R(y-t)\rangle = C(x-y)\,, \\ \langle \psi_L^\dagger(x+t)\psi_L(y+t)\rangle = C(-x+y)\,, \end{cases} \tag{2.5}$$

where

$$C(x-y) \equiv \frac{1}{2\pi\mathrm{i}}\frac{1}{(x-y)-\mathrm{i}\epsilon} = \frac{1}{2}\delta(x-y) - \frac{\mathrm{i}}{2\pi}\mathcal{P}\frac{1}{x-y}\,, \tag{2.6}$$

and $\mathcal{P}$ denotes the Cauchy principal value. We remark that, for the massless Dirac field on the line, the two chiralities are decoupled because the two-point correlators involving the components with different chirality vanish.

The Lagrangian (2.4) is invariant under two global $U(1)$ transformations: the vector phase transformation

$$\begin{pmatrix}\psi_R(x-t)\\ \psi_L(x+t)\end{pmatrix} \longrightarrow e^{\mathrm{i}\theta_v}\begin{pmatrix}\psi_R(x-t)\\ \psi_L(x+t)\end{pmatrix}, \tag{2.7}$$

which multiplies both chiralities by the same phase, and the axial phase transformation

$$\begin{pmatrix}\psi_R(x-t)\\ \psi_L(x+t)\end{pmatrix} \longrightarrow \begin{pmatrix}e^{-\mathrm{i}\theta_a}\,\psi_R(x-t)\\ e^{\mathrm{i}\theta_a}\,\psi_L(x+t)\end{pmatrix}, \tag{2.8}$$

which multiplies them by conjugate phases.

When a CFT is defined on the half-line $x \geqslant 0$, it is natural to impose boundary conditions that ensure global energy conservation [90–92]. For the massless Dirac field, such requirement leads to two possible boundary conditions that mix the components with different chirality and break either the vector or the axial symmetry [89,93]. Each boundary condition defines a specific model (or phase). We distinguish the two phases according to which bulk symmetry is preserved by the boundary condition.

Vector phase: Denoting the massless Dirac field on the half-line $x \geqslant 0$ as

$$\Lambda(x,t) = \begin{pmatrix}\lambda_R(x-t)\\ \lambda_L(x+t)\end{pmatrix}, \tag{2.9}$$

where λ_R and λ_L are the two chiral components, the vector phase is defined by the following family of boundary condition at $x = 0$ [89, 93]

$$\lambda_R(t) = e^{\mathrm{i}\alpha_v}\lambda_L(t), \qquad \alpha_v \in [0, 2\pi)\,. \tag{2.10}$$

In this phase, because of the boundary condition, the vector symmetry (2.7) is preserved, while the axial one (2.8) is broken. The occurrence of a coupling at the boundary between the components of the massless Dirac field leads to non vanishing correlators between fields having different chirality. The equal time correlation matrix in the vector phase reads [89]

$$\begin{aligned}\langle\Lambda(x,t)\Lambda^\dagger(y,t)\rangle &= \begin{pmatrix}\langle\lambda_R(x-t)\lambda_R^\dagger(y-t)\rangle & \langle\lambda_R(x-t)\lambda_L^\dagger(y+t)\rangle\\ \langle\lambda_L(x+t)\lambda_R^\dagger(y-t)\rangle & \langle\lambda_L(x+t)\lambda_L^\dagger(y+t)\rangle\end{pmatrix}\\ &= \begin{pmatrix}C(x-y) & e^{\mathrm{i}\alpha_v}C(x+y)\\ e^{-\mathrm{i}\alpha_v}C(-x-y) & C(-x+y)\end{pmatrix} \equiv \mathscr{C}(x,y;\alpha_v),\end{aligned} \tag{2.11}$$

in terms of (2.6) and of the phase α_v characterising the boundary condition (2.10).

Axial phase: In this case it is convenient to denote the massless Dirac field on the half-line $x \geqslant 0$ as follows

$$X(x,t) = \begin{pmatrix} \chi_R^\dagger(x-t) \\ \chi_L(x+t) \end{pmatrix}, \tag{2.12}$$

where χ_R and χ_L are the two chiral components. The global energy conservation condition is solved also by the following boundary condition at $x = 0$ [89, 93]

$$\chi_R(t) = e^{-\mathrm{i}\alpha_a} \chi_L^\dagger(t), \qquad \alpha_a \in [0, 2\pi) . \tag{2.13}$$

This boundary condition preserves the axial symmetry (2.8) and breaks the vector one (2.7).

In terms of the doublet $X(x,t)$, the correlation matrix turns out to be identical to (2.11) for the vector phase [89]

$$\langle X(x,t) X^\dagger(y,t) \rangle = \begin{pmatrix} \langle \chi_R^\dagger(x-t)\chi_R(y-t)\rangle & \langle \chi_R^\dagger(x-t)\chi_L^\dagger(y+t)\rangle \\ \langle \chi_L(x+t)\chi_R(y-t)\rangle & \langle \chi_L(x+t)\chi_L^\dagger(y+t)\rangle \end{pmatrix} = \mathscr{C}(x,y;\alpha_a) , \tag{2.14}$$

in terms of the phase α_a which parameterises the family of boundary conditions (2.13).

Since the correlation matrices (2.11) and (2.14) are the same in the vector and in the axial phase, one can treat them in a unified way by introducing the doublet

$$\Psi(x,t) = \begin{pmatrix} \psi_R(x-t) \\ \psi_L(x+t) \end{pmatrix} = \begin{cases} \Lambda(x,t), & \text{vector phase} \\ X(x,t), & \text{axial phase} , \end{cases} \tag{2.15}$$

which will be used throughout this Chapter.

2.2 Entanglement Hamiltonian for the union of disjoint intervals

In this section we will present the derivation of one of the main results of this Chapter, the entanglement Hamiltonian for a multi-interval subsystem in the presence of a boundary. To this avail, we will employ the techniques used in Ref. [87, 88] for the EH in the absence of boundaries. This computation is based on the application of Peschel's formula (1.15) (reviewed in Sec. 1.2 in the Introduction) to the two-point correlation functions in Eqs. (2.5) and (2.6). In the following, we first review the computation of Refs. [87, 88] and, following Refs. [89, 96], we then extend it to the case in the presence of a boundary.

2.2.1 Entanglement Hamiltonian on the line

Recall from the Introduction that the entanglement Hamiltonian in the ground state of a CFT can be obtained from the Bisognano-Wichmann theorem (1.12) whenever the configuration has the topology of an annulus [34]. This is however not the case when the subsystem

$A = [a_1, b_1] \cup [a_2, b_2] \cup \ldots \cup [a_n, b_n]$ is the union of n disjoint intervals. Indeed, as we will see, in this case the entanglement Hamiltonian has additional non-local terms beyond the local Bisognano-Wichmann-like one [87,88,97,98].

While the Bisognano-Wichmann theorem cannot be applied to the system under study, as discussed in the Introduction, for fermionic Gaussian states Wick's theorem relates the entanglement Hamiltonian to the correlation matrix C_A restricted to the subsystem A via Peschel's formula (1.15). Since this construction only depends on Wick's theorem, it applies both to lattice models and to continuous QFTs. To apply Eq. (1.15) to the massless Dirac QFT, we write the quadratic EH as

$$K_A = \frac{1}{2\pi} \int_A \mathrm{d}x \, \Psi^\dagger(x) H_A(x, y) \Psi(y), \tag{2.16}$$

where Ψ is the Dirac fermion doublet in Eq. (2.1) and $H_A(x, y)$ is the kernel of the EH, i.e., the single-particle entanglement Hamiltonian. Eq. (1.15) then relates the kernel $H_A(x, y)$ to the two-point correlation function $C_A(x, y) = \langle \Psi^\dagger(x)\Psi(y)\rangle\big|_{x,y\in A}$ reported in Eqs. (2.5) and (2.6). In particular, Eq. (1.15) implies that C_A and the kernel H_A share the same eigenfunctions, and that the eigenvalues e_s of the latter are related to the eigenvalues σ_s of the former through

$$e_s = \log\left(\frac{1 - \sigma_s}{\sigma_s}\right). \tag{2.17}$$

Therefore, as done in Ref. [87,88], by finding the eigenfunctions and the eigenvalues of C_A it is possible to apply this relation to obtain an analytical expression for the entanglement Hamiltonian.

For the sake of simplicity, we describe the procedure for the right-moving chiral fermions $\psi_R(x-t)$, but similar steps apply to the left-moving ones as well. Let $A = [a_1, b_1] \cup \ldots \cup [a_n, b_n]$ be composed of n intervals. The correlation function for $\psi_R(x - t)$ on the line is $C_A(x - y)$, given by Eq. (2.6). Exploiting the results found in Ref. [99], the spectral problem for the correlator of a chiral component of the Dirac fermions has been solved [87, 88]: the eigenvalues take values in $[0, 1]$ and they can be written as

$$\sigma_s = \frac{1}{2}\big[1 + \tanh(\pi s)\big], \qquad s \in \mathbb{R}. \tag{2.18}$$

Each eigenvalue σ_s has an n-fold degeneracy and the corresponding eigenfunctions take the form [87, 88]

$$\phi_p^s(x) = k_p(x) e^{-\mathrm{i}sz(x)}, \tag{2.19}$$

where the function $z(x)$ at the exponent is

$$z(x) = \log\left[-\prod_{i=1}^{n} \frac{(x - a_i)}{(x - b_i)}\right], \tag{2.20}$$

a_i and b_i are the endpoints of the intervals and

$$k_p(x) = \frac{(-1)^{n+1}}{N_p} \frac{1}{(x-a_p)} \sqrt{-\prod_{i=1}^{n} \frac{(x-a_i)}{(x-b_i)}}\,, \qquad N_p = \sqrt{2\pi} \sqrt{\frac{\prod_{i\neq p}(a_i-a_p)}{\prod_{i=1}^{n}(b_i-a_p)}}\,. \tag{2.21}$$

These eigenfunctions form a complete orthonormal basis [87,88]. From Eqs. (1.15) and (2.18), one finds that the eigenvalues of the entanglement Hamiltonian kernel H_A (for right-moving chiral fermions) are

$$e_s = -2\pi s. \tag{2.22}$$

Then, the kernel can be written in spectral representation as follows [87, 88]

$$H_A(x,y) = \sum_{p=1}^{n} \int_{-\infty}^{+\infty} \mathrm{d}s\, \phi_p^s(x) \big(-2\pi s\big) \phi_p^{s*}(y) = -k(x,y) \int_{-\infty}^{+\infty} \mathrm{d}s\, s\, e^{-\mathrm{i}s[z(x)-z(y)]}, \tag{2.23}$$

where we have introduced

$$k(x,y) \equiv 2\pi \sum_{p=1}^{n} k_p(x) k_p(y). \tag{2.24}$$

The integral over the eigenvalue s is proportional to the derivative of a delta function

$$\int_{-\infty}^{+\infty} \mathrm{d}s\, s\, e^{-\mathrm{i}s[z(x)-z(y)]} = 2\pi\mathrm{i}\, \frac{1}{2} \left[\frac{\partial_x}{z'(x)} - \frac{\partial_y}{z'(y)} \right] \delta(z(x)-z(y))\,, \tag{2.25}$$

which imposes that the kernel only couples *conjugate points* x and y where the function z in Eq. (2.20) takes the same value, i.e. satisfying

$$z(y) = z(x). \tag{2.26}$$

This equation has the trivial solution $y = x$ and $n-1$ non-trivial ones $y = \tilde{x}_p$ with $1 \leqslant p \leqslant n-1$. Using the properties of the delta function in (2.25), the kernel is

$$\begin{aligned} H_A(x,y) =& \; -2\pi k(x,y) \left[\frac{\mathrm{i}}{2} \frac{(\partial_x - \partial_y)\, \delta(x-y)}{z'(x) z'(y)} - \frac{\mathrm{i}}{2} \sum_{p=1}^{n-1} \left(\frac{\partial_y \delta(y-\tilde{x}_p)}{z'(\tilde{x}_p) z'(y)} - \frac{\partial_x \delta(x-\tilde{y}_p)}{z'(x) z'(\tilde{y}_p)} \right) \right] \\ =& \; H_A^{\mathrm{loc}}(x,y) + H_A^{\mathrm{bl}}(x,y). \end{aligned} \tag{2.27}$$

We see that the trivial solution give rise to a local Bisognano-Wichmann-like (see Eq. (1.12)) term $H_A^{\mathrm{loc}}(x,y)$, while the non-trivial ones are responsible for $n-1$ terms $H_A^{\mathrm{bl}}(x,y)$ which couple each points with their conjugates $\tilde{x}_p$ [87, 88, 97]. These terms are called *bi-local* and are responsible for a very mild non-locality in the entanglement Hamiltonian. In order to find the explicit expression of the EH, it is convenient to use the properties of the $k_p(x)$ functions, which lead to [88, 89]

$$k(x,x) = 2\pi \sum_{p=1}^{n} k_p(x) k_p(x) = z'(x), \quad k(x,\tilde{x}_p) = 0, \quad \partial_y k(x,y)\big|_{y=\tilde{x}_p} = \frac{z'(x)}{x-\tilde{x}_p}. \tag{2.28}$$

Plugging $H_A^{\rm loc}(x,y)$ into (2.16) and integrating by parts, the local term yields [87, 88]

$$\begin{aligned} K_A^{\rm loc} &= -\int_A \mathrm{d}x \int_A \mathrm{d}y \, \frac{k(x,y)}{z'(x)z'(y)} \big[\, (\partial_x - \partial_y)\, \delta(x-y) \big] \, \frac{\mathrm{i}}{2} :\psi_R^\dagger(x)\psi_R(y): \\ &= \int_A \mathrm{d}x \int_A \mathrm{d}y \, \frac{k(x,y)}{z'(x)z'(y)} \delta(x-y) \, \frac{\mathrm{i}}{2} :\!\Big(\partial_x \psi_R^\dagger(x)\psi_R(y) - \psi_R^\dagger(x)\partial_y\psi_R(y)\Big)\!: \\ &= \int_A \mathrm{d}x \, \frac{T_R(x,t=0)}{z'(x)} \; \equiv \int_A \mathrm{d}x \, \beta_{\rm loc}(x) \, T_R(x,t=0), \end{aligned} \tag{2.29}$$

where we used $\partial_x k(x,y)\big|_{y=x} = \partial_y k(x,y)\big|_{y=x}$ and $:\cdots:$ indicates that the corresponding operators are normal ordered. We recognise that the local term is the integral over A of the chiral stress-energy tensor [100, 101]

$$T_R(x,t) = \frac{\mathrm{i}}{2} :\!\Big[\partial_x \psi_R^\dagger(x-t)\psi_R(x-t) - \psi_R^\dagger(x-t)\partial_x\psi_R(x-t)\Big]\!:, \tag{2.30}$$

weighted by the *entanglement temperature*

$$\beta_{\rm loc}(x) \equiv \frac{1}{z'(x)}\,, \tag{2.31}$$

which is the inverse of the derivative of the function $z(x)$ in Eq. (2.20) [88, 89]. When A consists of one single interval, this local term agrees with the general CFT result [34]

$$z(x) = \log\left[\frac{b-x}{x-a}\right]. \tag{2.32}$$

This function is the uniformising transformation which maps the worldsheet into the annulus configuration (see discussion in the Introduction) and $\beta_{\rm loc}(x) = 1/z'(x)$ is the predicted value for the entanglement temperature in Eq. (1.13).

The bi-local term takes instead the form [87, 88]

$$\begin{aligned} K_A^{\rm bl} &= -\int_A \mathrm{d}x \int_A \mathrm{d}y \, \big(-k(x,y)\big) \sum_{p=1}^{n-1} \left[\frac{\partial_y \delta(y-\tilde{x}_p)}{z'(\tilde{x}_p)z'(y)} - \frac{\partial_x \delta(x-\tilde{y}_p)}{z'(x)z'(\tilde{y}_p)}\right] \frac{\mathrm{i}}{2} :\psi_R^\dagger(x)\psi_R(y): \\ = &-\sum_{p=1}^{n-1} \int_A \mathrm{d}x \int_A \mathrm{d}y \frac{\partial_y k(x,y)}{z'(\tilde{x}_p)z'(y)} \, \delta(y-\tilde{x}_p) \, \frac{\mathrm{i}}{2} :\!\Big(\psi_R^\dagger(x)\psi_R(y) - \psi_R^\dagger(y)\psi_R(x)\Big)\!: \\ = &\sum_{p=1}^{n-1} \int_A \mathrm{d}x \, \frac{1}{x-\tilde{x}_p} \, \frac{1}{z'(\tilde{x}_p)} \, T_R^{\rm bl}(x,\tilde{x}_p,t=0) \; = \sum_{p=1}^{n-1} \int_A \mathrm{d}x \, \frac{\beta_{\rm loc}(\tilde{x}_p)}{x-\tilde{x}_p} \, T_R^{\rm bl}(x,\tilde{x}_p,t=0), \end{aligned} \tag{2.33}$$

where we have introduced the following *bi-local operator* [87, 88]

$$T_R^{\mathrm{bl}}(x,y,t) \;=\; \frac{\mathrm{i}}{2} :\Big[\psi_R^\dagger(x-t)\psi_R(y-t) - \psi_R^\dagger(y-t)\psi_R(x-t)\Big]: , \tag{2.34}$$

that must be evaluated at the non-trivial solutions $y=\tilde{x}_p$, and the weight function in the integrand is

$$\beta_{\mathrm{bl}}(x) \equiv \frac{\beta_{\mathrm{loc}}(\tilde{x}_p)}{x-\tilde{x}_p} . \tag{2.35}$$

In order to extend this argument to the left-moving fermions, recall that the two-point correlation function (2.6) is equal to $C_A(-x+y)$. As a consequence, we can see that for left-moving fermions the eigenvectors of the two-point correlation matrix are again given by Eqs. (2.19) to (2.21), while its eigenvalues are $\frac{1}{2}\left[1-\tanh(\pi s)\right]$. Using Eqs. (1.15) and (2.17), we find that the entanglement spectrum for left-movers is $+2\pi s$, that is, the opposite of that of right-movers. Therefore, the previous calculations are analogous up to an additional minus sign. Summing up the contributions of the two chiral fermions, the entanglement Hamiltonian of a free massless Dirac fermion is [87, 88]

$$K_A = \int_A \mathrm{d}x\, \beta_{\mathrm{loc}}(x)\, T_{00}(x) + \sum_{p=1}^{n-1} \int_A \mathrm{d}x\, \frac{\beta_{\mathrm{loc}}(\tilde{x}_p)}{x-\tilde{x}_p}\, T_{\mathrm{diag}}^{\mathrm{bl}}(x,\tilde{x}_p,t=0), \tag{2.36}$$

where T_{00} is the energy density

$$\begin{aligned} T_{00}(x,t) = \frac{\mathrm{i}}{2} :\Big[&\Big(\partial_x\psi_R^\dagger(x-t)\psi_R(x-t) - \psi_R^\dagger(x-t)\partial_x\psi_R(x-t)\Big) \\ &- \Big(\partial_x\psi_L^\dagger(x+t)\psi_L(x+t) - \psi_L^\dagger(x+t)\partial_x\psi_L(x+t)\Big)\Big]: , \end{aligned} \tag{2.37}$$

and the bi-local operator for both chiralities takes the form [87, 88]

$$\begin{aligned} T_{\mathrm{diag}}^{\mathrm{bl}}(x,y,t) = \frac{\mathrm{i}}{2} :\Big[&\Big(\psi_R^\dagger(x-t)\psi_R(y-t) - \psi_R^\dagger(y-t)\psi_R(x-t)\Big) \\ &- \Big(\psi_L^\dagger(x+t)\psi_L(y+t) - \psi_L^\dagger(y+t)\psi_L(x+t)\Big)\Big]: . \end{aligned} \tag{2.38}$$

It is worthwhile to compare the entanglement Hamiltonian for multiple intervals in Eq. (2.36) with the one for a single interval that we presented in Eq. (1.13) in the Introduction. The single interval geometry has an annulus topology and the entanglement Hamiltonian (1.13) is obtained from the Bisognano-Wichmann one (1.12) [34]. As a consequence, Eq. (1.13) has a local structure. On the other hand, as we previously mentioned, for multiple intervals the argument is invalid and the EH in Eq. (2.36) presents the bi-local terms.

Before concluding, we point out an interesting feature of the entanglement Hamiltonian (2.36): the local term can be obtained as the limit of the bi-local one when $y \to x$.

In order to see this, let us observe that the first order term of the Taylor expansion of the bi-local operator (2.38) around $y = x$ is proportional to the energy density

$$T^{\mathrm{bl}}_{\mathrm{diag}}(x, y, t) \approx -(y - x)\, T_{00}(x, t)\,. \tag{2.39}$$

Using this expansion, we immediately find that the limit of the bi-local term in which the conjugate point approaches x reduces to the local contribution as

$$\lim_{y \to x} \int_A \mathrm{d}x\, \frac{\beta_{\mathrm{loc}}(y)}{x - y}\, T^{\mathrm{bl}}_{\mathrm{diag}}(x, y, t = 0) = \int_A \mathrm{d}x\, \beta_{\mathrm{loc}}(x)\, T_{00}(x, t = 0)\,. \tag{2.40}$$

Beside providing a check for the consistency of Eq. (2.36), this result suggests that the local term can be interpreted as the analogous of the bi-local one relative to the trivial solution $y = x$ of Eq. (2.26).

2.2.2 Entanglement Hamiltonians on the half-line

We now study the entanglement Hamiltonian of n disjoint intervals $A = [a_1, b_1] \cup \ldots \cup [a_n, b_n]$ on the half-line $x \geqslant 0$ with $a_1 > 0$ for the massless Dirac field in the phases discussed in section 2.1, which are characterised by the boundary conditions (2.10) and (2.13) and whose correlation matrices $\mathscr{C}_A(x, y; \alpha)$ are (2.11) and (2.14) respectively. This extends the analysis performed in Ref. [89] for $n = 1$.

In order to find the entanglement Hamiltonian we first need to solve the spectral problem associated to the restricted correlation matrix $\mathscr{C}_A(x, y; \alpha)$

$$\int_A dy\, \mathscr{C}_A(x, y; \alpha)\, \Phi^s_p(y) = \sigma_s\, \Phi^s_p(x). \tag{2.41}$$

For this purpose, following [89], let us consider the symmetric auxiliary configuration on the line $A_{\mathrm{sym}} \equiv [-b_n, -a_n] \cup \ldots \cup [-b_1, -a_1] \cup [a_1, b_1] \cup \ldots \cup [a_n, b_n] \subset \mathbb{R}$, obtained by reflecting the subsystem A with respect to the position of the boundary at $x = 0$ (see Fig. 2.1), and the corresponding eigenfunctions $\phi^{s\,(\mathrm{sym})}_p(x) = k^{\mathrm{sym}}_p(x) e^{-\mathrm{i} s z_{\mathrm{sym}}(x)}$ of the correlator $C_{A_{\mathrm{sym}}}$ restricted to A_{sym}. The number of disjoint intervals in the symmetric auxiliary geometry A_{sym} depends on the fact if the first interval is adjacent to the boundary or not. In the former case, as depicted in Fig. 2.2, there is one interval which crosses the boundary and A_{sym} is composed of $2n - 1$ disjoint intervals. For $a_1 > 0$, shown in Fig. 2.1, instead, A_{sym} contains $2n$ intervals since none of them crosses the boundary. For simplicity, in the following we will call $\widetilde{n} + 1$ the number of intervals contained in the symmetric auxiliary geometry, i.e., $\widetilde{n} = 2n - 1$ for $a_1 > 0$ and $\widetilde{n} = 2n - 2$ for $a_1 = 0$.

A straightforward extension of the observation made in Ref. [89] leads us to write the eigenfunctions of the spectral problem (2.41) as follows

$$\Phi^s_p(x) = \begin{pmatrix} e^{\mathrm{i}\alpha}\, \phi^{s\,(\mathrm{sym})}_p(x) \\ \phi^{s\,(\mathrm{sym})}_p(-x) \end{pmatrix}, \qquad 1 \leq p \leq \widetilde{n} + 1\,, \tag{2.42}$$

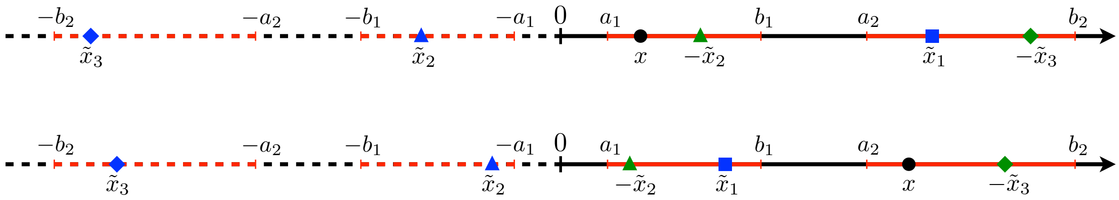

Figure 2.1: Symmetric auxiliary configuration A_{sym} on the line for the case of two intervals $A = [a_1, b_1] \cup [a_2, b_2]$ on the half-line $x \geqslant 0$ not adjacent to the boundary at $x = 0$. The conjugate points and their reflections are indicated for either $x \in [a_1, b_1]$ (top) or $x \in [a_2, b_2]$ (bottom). The blue symbols denote the points conjugate to x in A_{sym} and the green ones the corresponding reflected points that occur in the entanglement Hamiltonian of A.

whose corresponding eigenvalues are $\sigma_s = \frac{1}{2}[1 + \tanh(\pi s)]$, with $s \in \mathbb{R}$. This solution of the spectral problem on the half-line allows us to write the entanglement Hamiltonian kernel in Eq. (2.16) through its spectral representation as follows

$$\begin{aligned} H_A(x,y) &= \sum_{p=1}^{\widetilde{n}+1} \int_{-\infty}^{+\infty} \mathrm{d}s\, \Phi_p^s(x)\big(-2\pi s\big)\Phi_p^{s\dagger}(y) \\ &= \sum_{p=1}^{\widetilde{n}+1} \int_{-\infty}^{+\infty} \mathrm{d}s\, \big(-2\pi s\big) \begin{pmatrix} \phi_p^s(x)\phi_p^{s*}(y) & e^{\mathrm{i}\alpha}\phi_p^s(x)\phi_p^{s*}(-y) \\ e^{-\mathrm{i}\alpha}\phi_p^s(-x)\phi_p^{s*}(y) & \phi_p^s(-x)\phi_p^{s*}(-y) \end{pmatrix} \\ &= \begin{pmatrix} -k^{\text{sym}}(x,y)W_{\text{sym}}(x,y) & -e^{\mathrm{i}\alpha}k^{\text{sym}}(x,-y)W_{\text{sym}}(x,-y) \\ -\,e^{-\mathrm{i}\alpha}k^{\text{sym}}(x,-y)W_{\text{sym}}(-x,y) & -k^{\text{sym}}(x,y)W_{\text{sym}}(-x,-y) \end{pmatrix}, \end{aligned} \tag{2.43}$$

where $x, y \in A$, we used that $k^{\text{sym}}(x,-y) = k^{\text{sym}}(-x,y)$ for A_{sym} and, for $x, y \in A$, we have introduced

$$W_{\text{sym}}(x,y) \equiv \int_{-\infty}^{+\infty} \mathrm{d}s\, s\, e^{-\mathrm{i}s[z_{\text{sym}}(x)-z_{\text{sym}}(y)]} = \pi\mathrm{i}\left[\frac{\partial_x}{z'_{\text{sym}}(x)} - \frac{\partial_y}{z'_{\text{sym}}(y)}\right]\delta(z_{\text{sym}}(x) - z_{\text{sym}}(y)). \tag{2.44}$$

Unlike the case without boundaries, now the entanglement Hamiltonian is non-diagonal in the chiral fermions, as already found in Ref. [89] for $n = 1$, where the bi-local term was provided entirely by the out-of-diagonal term in the kernel. Instead, for $n > 1$ we will show that both the diagonal and out-of-diagonal elements contribute to the bi-local part of the entanglement Hamiltonian.

Diagonal terms: The diagonal elements of H_A are analogous to the kernel in the problem without boundary since they are localised along the solutions of the equation $z_{\text{sym}}(y) = z_{\text{sym}}(x)$. For a subsystem A with n intervals, beside the trivial solution $y = x$, the equation

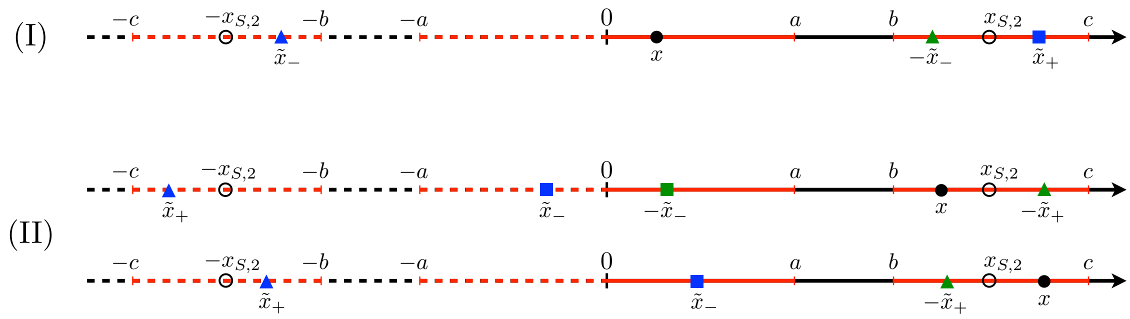

Figure 2.2: Symmetric auxiliary configuration A_{sym} on the line for the case of two intervals $A = [0,a] \cup [b,c]$ on the half-line $x \geqslant 0$. For a given x, two conjugate points occur in the entanglement Hamiltonian, which are indicated following the notation established in Figure 2.1. The two possible cases (I) $x \in [0,a]$ and (II) $x \in [b,c]$ are represented. In (II), it is distinguished whether $x \in [b, x_{S,2})$ (top) or $x \in (x_{S,2}, c]$ (bottom). The self-conjugate point $x_{S,2}$ is defined in (2.59).

(2.26) has $\widetilde{n}$ non-trivial ones $y = \tilde{x}_p$, i.e., either $2n-2$ or $2n-1$ depending if the first interval is adjacent to the boundary or not. However, differently from the case without boundary, now the only acceptable solutions are those that belong to the original subsystem A; hence we only need to keep $x, y > 0$. While this condition is always verified for the trivial solution, for the non-trivial ones we must restrict ourselves to $\tilde{x}_p > 0$ only. For $n = 2$, in Fig. 2.1 and Fig. 2.2 we show qualitatively the configurations of these points when either $a_1 > 0$ or $a_1 = 0$ respectively. In the latter case (I) and (II) correspond respectively to $x \in A_1$ and $x \in A_2$.

Thus, the diagonal part of the kernel can be written as

$$\begin{aligned} H_A^{\text{diag}}(x,y) = &- 2\pi k^{\text{sym}}(x,y) \begin{pmatrix} 1 & 0 \\ 0 & -1 \end{pmatrix} \frac{\mathrm{i}}{2} \left\{ \frac{(\partial_x - \partial_y)\, \delta(x-y)}{z'_{\text{sym}}(x) z'_{\text{sym}}(y)} \right. \\ &\left. - \sum_{p=1}^{\widetilde{n}} \left[\frac{\partial_y \delta(y - \tilde{x}_p)}{z'_{\text{sym}}(\tilde{x}_p) z'_{\text{sym}}(y)} - \frac{\partial_x \delta(x - \tilde{y}_p)}{z'_{\text{sym}}(x) z'_{\text{sym}}(\tilde{y}_p)} \right] \right\} \\ = &\, H_A^{\text{loc}}(x,y) + H_A^{\text{bl, diag}}(x,y)\,, \end{aligned} \tag{2.45}$$

where we have separated the local part from the bi-local one.

The final step of the calculation is to substitute the kernel (2.45) in the expression of the entanglement Hamiltonian (2.16) and integrate by parts, keeping in mind that now the kernel is a 2 × 2 matrix. For the local component we find

$$\begin{aligned}
K_A^{\mathrm{loc}} &= \frac{1}{2\pi}\int_A \mathrm{d}x \int_A \mathrm{d}y \; :\!\Big(\psi_R^\dagger(x), \psi_L^\dagger(x)\Big) H_A^{\mathrm{loc}}(x,y) \begin{pmatrix}\psi_R(y)\\ \psi_L(y)\end{pmatrix}\!: \\
&= \int_A \mathrm{d}x \int_A \mathrm{d}y \; \frac{k(x,y)}{z'_{\mathrm{sym}}(x) z'_{\mathrm{sym}}(y)} \; \delta(x-y) \times \\
&\qquad \times \frac{\mathrm{i}}{2} :\!\Big[\Big(\partial_x\psi_R^\dagger(x)\psi_R(y) - \psi_R^\dagger(x)\partial_y\psi_R(y)\Big) - \Big(\partial_x\psi_L^\dagger(x)\psi_L(y) - \psi_L^\dagger(x)\partial_y\psi_L(y)\Big)\Big]\!: \\
&= \int_A \mathrm{d}x \, \frac{T_{00}(x,t=0)}{z'_{\mathrm{sym}}(x)} = \int_A \mathrm{d}x \, \beta_{\mathrm{loc}}^{\mathrm{sym}}(x)\, T_{00}(x,t=0)\,,
\end{aligned} \tag{2.46}$$

where we recognise the same form of the local term occurring in the case without boundaries in Eq. (2.29). However, now the entanglement temperature corresponds to the one for the auxiliary configuration A_{sym}

$$\beta_{\mathrm{loc}}^{\mathrm{sym}}(x) = \frac{1}{z'_{\mathrm{sym}}(x)}\,. \tag{2.47}$$

Similarly, by plugging (2.45) in (2.16), for the diagonal bi-local component we find

$$\begin{aligned}
K_A^{\mathrm{bl,\,diag}} &= \frac{1}{2\pi}\int_A \mathrm{d}x \int_A \mathrm{d}y \; :\!\Big(\psi_R^\dagger(x), \psi_L^\dagger(x)\Big) H_A^{\mathrm{bl,\,diag}}(x,y) \begin{pmatrix}\psi_R(y)\\ \psi_L(y)\end{pmatrix}\!: \\
&= -\sum_{p=1}^{\widetilde{n}} \int_A \mathrm{d}x \int_A \mathrm{d}y \; \frac{\partial_y k^{\mathrm{sym}}(x,y)}{z'_{\mathrm{sym}}(\tilde{x}_p) z'_{\mathrm{sym}}(y)} \; \delta(y-\tilde{x}_p) \times \\
&\qquad \times \frac{\mathrm{i}}{2} :\!\Big[\Big(\psi_R^\dagger(x)\psi_R(y) - \psi_R^\dagger(y)\psi_R(x)\Big) - \Big(\psi_L^\dagger(x)\psi_L(y) - \psi_L^\dagger(y)\psi_L(x)\Big)\Big]\!: \\
&= \sum_{p=1}^{\widetilde{n}} \int_A \mathrm{d}x \left(\frac{1}{x-\tilde{x}_p}\;\frac{1}{z'_{\mathrm{sym}}(\tilde{x}_p)}\right) \Theta(\tilde{x}_p)\, T_{\mathrm{diag}}^{\mathrm{bl}}(x,\tilde{x}_p,t=0) \\
&= \sum_{p=1}^{\widetilde{n}} \int_A \mathrm{d}x \, \frac{\beta_{\mathrm{loc}}^{\mathrm{sym}}(\tilde{x}_p)}{x-\tilde{x}_p}\, \Theta(\tilde{x}_p)\, T_{\mathrm{diag}}^{\mathrm{bl}}(x,\tilde{x}_p,t=0),
\end{aligned} \tag{2.48}$$

where we recognise the same bi-local operator (2.38) which occurs in the bi-local term of the case without boundary and does not mix different chiralities. Notice that the integration of the Dirac delta on the finite domain $A > 0$ gives rise to the Heaviside theta function $\Theta(\tilde{x}_p)$, which guarantees that the only solutions that contribute to the final result are $\tilde{x}_p > 0$, i.e., those belonging to the physical subsystem. This term does not depend on the boundary condition; hence it is the same in both phases. The main difference of the term (2.48) with respect to the case without boundary is the presence of the theta function $\Theta(\tilde{x}_p)$, which imposes that the conjugate points belong to A.

Out-of-diagonal terms: The out-of-diagonal terms in Eq. (2.43) provide the coupling between the two different chiralities, as already observed for the single interval $A = [a_1, b_1]$ in [89]. These components are proportional to the distribution $W_{\text{sym}}(x, -y)$. Thus, we need to solve the equation $z_{\text{sym}}(y) = z_{\text{sym}}(-x)$ constrained by $x, y > 0$. Knowing the solutions to the problem $z_{\text{sym}}(y) = z_{\text{sym}}(x)$, we immediately find that these equation is satisfied by $y = -x$ and $y = -\tilde{x}_p$. Because of the condition $x, y > 0$, the solution $y = -x$ is never acceptable, so we will only have contributions from the others. We can therefore write the off-diagonal components of the kernel as

$$
\begin{aligned}
H_A^{\text{bl, mix}}(x,y) = &- 2\pi k^{\text{sym}}(x,-y) \begin{pmatrix} 0 & e^{\mathrm{i}\alpha} \\ -e^{-\mathrm{i}\alpha} & 0 \end{pmatrix} \\
&\times \frac{\mathrm{i}}{2} \sum_{p=1}^{\tilde{n}} \left[\frac{\partial_y \delta(y + \tilde{x}_p)}{z'_{\text{sym}}(\tilde{x}_p) z'_{\text{sym}}(y)} + \frac{\partial_x \delta(x + \tilde{y}_p)}{z'_{\text{sym}}(x) z'_{\text{sym}}(\tilde{y}_p)} \right], \qquad x, y \in A\,.
\end{aligned}
\tag{2.49}
$$

Plugging Eq. (2.49) into the expression for the entanglement Hamiltonian (2.16), we finally get

$$
\begin{aligned}
K_A^{\text{bl, mix}} &= \frac{1}{2\pi} \int_A \mathrm{d}x \int_A \mathrm{d}y \; :\!\left(\psi_R^\dagger(x), \psi_L^\dagger(x)\right) H_A^{\text{bl, mix}}(x,y) \begin{pmatrix} \psi_R(y) \\ \psi_L(y) \end{pmatrix}\!: \\
&= \sum_{p=1}^{\tilde{n}} \int_A \mathrm{d}x \int_A \mathrm{d}y \, \frac{\partial_y k^{\text{sym}}(-x,y)}{z'_{\text{sym}}(\tilde{x}_p) z'_{\text{sym}}(y)} \delta(y + \tilde{x}_p) \\
&\quad \times \frac{\mathrm{i}}{2} :\!\left[e^{\mathrm{i}\alpha} \left(\psi_R^\dagger(x)\psi_L(y) + \psi_R^\dagger(y)\psi_L(x) \right) - e^{-\mathrm{i}\alpha} \left(\psi_L^\dagger(x)\psi_R(y) + \psi_L^\dagger(y)\psi_R(x) \right) \right]\!: \\
&= \sum_{p=1}^{\tilde{n}} \int_A \mathrm{d}x \, \frac{1}{x - \tilde{x}_p} \, \frac{1}{z'_{\text{sym}}(\tilde{x}_p)} \, \Theta(-\tilde{x}_p) \, T_{\text{mix}}^{\text{bl}}(x, -\tilde{x}_p, t = 0; \alpha) \\
&= \sum_{p=1}^{\tilde{n}} \int_A \mathrm{d}x \, \frac{\beta_{\text{loc}}(\tilde{x}_p)}{x - \tilde{x}_p} \, \Theta(-\tilde{x}_p) \, T_{\text{mix}}^{\text{bl}}(x, -\tilde{x}_p, t = 0; \alpha)\,,
\end{aligned}
\tag{2.50}
$$

where we used the property that for a symmetrical geometry A_{sym} the function $z_{\text{sym}}(x)$ is odd (and thus its derivative is even $z'_{\text{sym}}(-x) = z'_{\text{sym}}(x)$) and now the integration over A gives rise to $\Theta(-\tilde{x}_p)$, implying that $\tilde{x}_p$ belong the reflection of A on the other side of the boundary. In this term, we find the same bi-local operator that appeared in Ref. [89]

$$
\begin{aligned}
T_{\text{mix}}^{\text{bl}}(x,y,t;\alpha) = \frac{\mathrm{i}}{2} :\!\Big[& e^{\mathrm{i}\alpha} \left(\psi_R^\dagger(x-t)\psi_L(y+t) + \psi_R^\dagger(y-t)\psi_L(x+t) \right) + \\
& - e^{-\mathrm{i}\alpha} \left(\psi_L^\dagger(x+t)\psi_R(y-t) + \psi_L^\dagger(y+t)\psi_R(x-t) \right) \Big]\!:\,.
\end{aligned}
\tag{2.51}
$$

This operator is non-diagonal in the chiral fermions and is dependent on the boundary condition. In particular, as showed in Ref. [89], the explicit form of Eq. (2.51) changes between the two phases. Using Eq. (2.15), in the vector phase the operator is equal to

$$\begin{aligned} T^{\text{bl}}_{\text{mix, vec}}(x,y,t;\alpha_v) = \frac{\mathrm{i}}{2} :\Big[& e^{\mathrm{i}\alpha_v} \Big(\lambda^\dagger_R(x-t)\lambda_L(y+t) + \lambda^\dagger_R(y-t)\lambda_L(x+t)\Big) \\ & - e^{-\mathrm{i}\alpha_v} \Big(\lambda^\dagger_L(x+t)\lambda_R(y-t) + \lambda^\dagger_L(y+t)\lambda_R(x-t)\Big)\Big]: , \end{aligned} \tag{2.52}$$

while in the axial phase

$$\begin{aligned} T^{\text{bl}}_{\text{mix, ax}}(x,y,t;\alpha_a) = \frac{\mathrm{i}}{2} :\Big[& e^{\mathrm{i}\alpha_a} \Big(\chi_R(x-t)\chi_L(y+t) + \chi_R(y-t)\chi_L(x+t)\Big) \\ & - e^{-\mathrm{i}\alpha_a} \Big(\chi^\dagger_L(x+t)\chi^\dagger_R(y-t) + \chi^\dagger_L(y+t)\chi^\dagger_R(x-t)\Big)\Big]: . \end{aligned} \tag{2.53}$$

Notice that in the axial phase the non-diagonal bi-local operator violates the conservation of electric charge. This is a consequence of the explicit breaking of the vector symmetry. Another important difference with respect to the diagonal bi-local term (2.48) is that $\tilde{x}_p < 0$, i.e. it must belong to the reflection of the physical subsystem with respect to the boundary.

Putting together the terms discussed above, as first major result of this Chapter, we find the entanglement Hamiltonian of a multi-interval geometry on the half-line

$$\begin{aligned} K_A = & K_A^{\text{loc}} + K_A^{\text{bl, diag}} + K_A^{\text{bl, mix}} = \int_A \mathrm{d}x\, \beta^{\text{sym}}_{\text{loc}}(x)\, T_{00}(x,t=0) \\ & + \sum_{p=1}^{\widetilde{n}} \int_A \mathrm{d}x\, \frac{\beta^{\text{sym}}_{\text{loc}}(\tilde{x}_p)}{x-\tilde{x}_p} \Big[\Theta(\tilde{x}_p)\, T^{\text{bl}}_{\text{diag}}(x,\tilde{x}_p,t=0) + \Theta(-\tilde{x}_p)\, T^{\text{bl}}_{\text{mix}}(x,-\tilde{x}_p,t=0;\alpha)\Big], \end{aligned} \tag{2.54}$$

written in terms of the operators (2.37) and (2.38), which do not mix the fields with different chiralities, and either (2.52) or (2.53) for the vector and axial phase respectively. We remind the reader that $\widetilde{n}$ is equal to $2n-1$ when $a_1 > 0$ and to $2n-2$ when $a_1 = 0$.

Let us compare Eq. (2.54) with the entanglement Hamiltonian in the absence of boundaries in Eq. (2.36) in the special case of $A = A_{\text{sym}}$. Beside the obvious difference between the integration domains, the weight functions and the entire local terms are the same. The main difference is due to the bi-local operator; indeed, in Eq. (2.54) different bi-local operators occur in the terms corresponding to different p's, depending on the sign of $\tilde{x}_p$. In particular, when $\tilde{x}_p > 0$ the corresponding bi-local operator is (2.38), which does not mix different chiralities, while the bi-local operator associated to $\tilde{x}_p < 0$ is (2.51) (that becomes either (2.52) or (2.53), depending on the phase), which couples fields with different chirality and explicitly depends on the boundary condition parameter.

The bi-local operator $T^{\text{bl}}_{\text{mix}}$ is evaluated in $-\tilde{x}$; hence $x \in [a_j, b_j]$ for some j, we have that $\tilde{x} \in [-b_j, -a_j]$ and therefore $-\tilde{x}$ belongs to the physical subsystem A. In Fig. 2.1 and Fig. 2.2 the two intervals case is considered (with the first interval either separated or adjacent to the boundary respectively): the same type of marker denotes both the conjugate points belonging to the symmetric auxiliary geometry (blue symbols) and their reflections with respect to the boundary that belong to A (green symbols). As discussed in Ref. [89], the consequence is that in the j-th interval there is one point $x_{S,j}$ that is conjugated to its own reflection, i.e. $\tilde{x}_{S,j} = -x_{S,j}$; hence we refer to them as *self-conjugate points.* If $a_1 > 0$, in Fig. 2.1 these points correspond to x (the black dot) that coincides with the conjugate point in the same interval. Since $z_{\mathrm{sym}}(x) = z_{\mathrm{sym}}(y)$ for conjugate points, the self-conjugate points satisfy $z_{\mathrm{sym}}(x_{S,j}) = z_{\mathrm{sym}}(-x_{S,j})$. Being $z_{\mathrm{sym}}(x)$ an odd function of $x \in A_{\mathrm{sym}}$, we conclude that $z_{\mathrm{sym}}(x_{S,j}) = -z_{\mathrm{sym}}(x_{S,j})$, which implies that the self-conjugate points are *all and only* the zeroes of $z_{\mathrm{sym}}(x)$ on the positive real semi-axis. Moreover, for a generic point y conjugate to $x_{S,j}$ we have that $z_{\mathrm{sym}}(y) = z_{\mathrm{sym}}(x_{S,j}) = 0$, i.e. y is also a self-conjugate point. In Fig. 2.1, when the black dot coincides with a green marker in one interval, also the two remaining conjugate points coincide in the other interval. Hence, all the self-conjugate points are conjugate among themselves. If A is made by n intervals, $z_{\mathrm{sym}}(x) = 0$ admits n solutions with $x \geqslant 0$, corresponding to the self-conjugate points. Since $z_{\mathrm{sym}}(x)$ is a continuous monotonic function in each interval $[a_j, b_j]$, $j = 1, \dots, n$, which tends to $-\infty$ as $x \to a_j$ and to $+\infty$ as $x \to b_j$, each interval contains one and only one self-conjugate point.

Another interesting feature of our main result in Eq. (2.54) occurs when the first interval is adjacent to the boundary, i.e. for $a_1 = 0$, as depicted in Fig. 2.2. In this case, the boundary at $x = 0$ trivially satisfies $z_{\mathrm{sym}}(x = 0) = 0$, meaning that it is also a self-conjugate point, albeit a degenerate one. Since all self-conjugate points are conjugate among themselves, the other $n - 1$ self-conjugate points are conjugated to the boundary and $x_{S,j} \in [a_j, b_j]$, with $j = 2, \dots, n$. A cross-over in the bi-local operator occurs at these points. Indeed, when $x \in [a_j, b_j]$, for $x \in [a_j, x_{S,j}]$ we have $\tilde{x}_p < 0$ and therefore the bi-local operator is non-diagonal; while for $x \in [x_{S,j}, b_j]$ we have $\tilde{x}_p > 0$ and the corresponding operator is diagonal (see also Fig. 2.2). Despite this change of operator, the entanglement Hamiltonian (2.54) is continuous at $x_{S,j}$; indeed, from the boundary conditions (2.10) and (2.13), both in the vector and in the axial phase, at $x_{S,j}$ one can show that

$$T^{\mathrm{bl}}_{\mathrm{mix}}(x_{S,j}, 0, t; \alpha) = T^{\mathrm{bl}}_{\mathrm{diag}}(x_{S,j}, 0, t), \tag{2.55}$$

for the non-diagonal operator (2.51) and the diagonal one (2.38). We stress that this cross-over occurs only when the first interval is adjacent to the boundary because the origin does not belong to A_{sym} when $a_1 > 0$. Thus, for $n \geqslant 2$ an important qualitative difference is observed between the cases where $a_1 > 0$ and the ones where $a_1 = 0$.

In the next section we discuss the entanglement Hamiltonian of two disjoint intervals on the half-line when $a_1 = 0$. This is the simplest example where the cross-over in the bi-local term described above is explicitly realised.

2.2.3 Entanglement Hamiltonian for two intervals with one adjacent to the boundary

Consider the subsystem $A = [0,a] \cup [b,c]$ on the half-line, made by two disjoint intervals where the first one is adjacent to the boundary. The corresponding auxiliary symmetric configuration is $A_{\text{sym}} = [-c,-b] \cup [-a,a] \cup [b,c]$, which is made by three disjoint intervals on the line and includes the origin. The function $z_{\text{sym}}(x)$ associated to A_{sym} reads

$$z_{\text{sym}}(x) \,=\, \log\left[\frac{(x+c)(x+a)(x-b)}{(x+b)(x-a)(c-x)}\right], \tag{2.56}$$

and it provides the following entanglement temperature

$$\beta_{\text{loc}}^{\text{sym}}(x) = \frac{1}{z'_{\text{sym}}(x)} = \left[\frac{2a}{x^2-a^2} - \frac{2b}{x^2-b^2} - \frac{2c}{c^2-x^2}\right]^{-1}. \tag{2.57}$$

The conjugate points are the solutions of $z_{\text{sym}}(y) = z_{\text{sym}}(x)$, which is a third order algebraic equation in this case. One solution is the trivial $y = x$, while the other two read (see Fig. 2.2)

$$y = \tilde{x}_{\pm}(x) \equiv \frac{\left(x_{S,2}^2 - x_\infty^2\right)x \pm \sqrt{\left(x_{S,2}^2 - x_\infty^2\right)^2 x^2 + 4x_\infty^2(x_\infty^2 - x^2)(x_{S,2}^2 - x^2)}}{2(x_\infty^2 - x^2)}, \tag{2.58}$$

where we have introduced the two points

$$x_{S,2} = \sqrt{ab+bc-ca}\,, \qquad x_\infty = \sqrt{\frac{abc}{a-b+c}}\,, \qquad a < x_\infty < b < x_{S,2} < c\,. \tag{2.59}$$

The point $x_{S,2}$ corresponds to the self-conjugate point described in the previous subsection. Indeed, one can show that $\tilde{x}_+(x_{S,2}) = -x_{S,2}$. Moreover, we have that $\tilde{x}_-(x_{S,2}) = 0$. This tells us that at $x_{S,2}$ the bi-local operator calculated in $\tilde{x}_-$ changes its nature from mixed to diagonal, in agreement with the general discussion made in the previous subsection. The points x_∞ and $-x_\infty$ are instead the only poles of respectively $\tilde{x}_+$ and $\tilde{x}_-$; because neither belong to the subsystem A, we conclude that as expected Eq. (2.58) is analytical in A.

Under (2.58), the other points of the subsystem A are mapped as in Fig. 2.3

$$\begin{cases} \tilde{x}_+([0,a]) = [x_{S,2}, c] \\ \tilde{x}_+([b,c]) = [-c,-b]\,, \end{cases} \qquad \begin{cases} \tilde{x}_-([0,a]) = [-x_{S,2}, -b] \\ \tilde{x}_-([b,x_{S,2}]) = [-a, 0] \\ \tilde{x}_-([x_{S,2}, c]) = [0, a]\,. \end{cases} \tag{2.60}$$

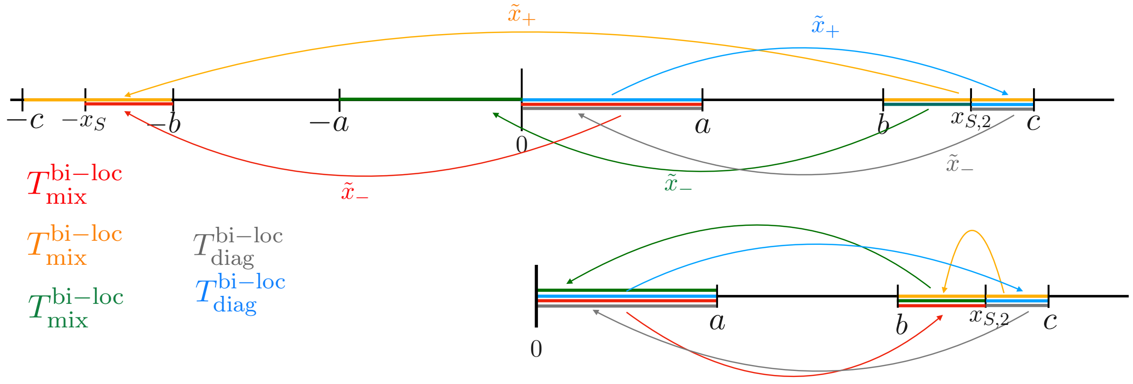

Figure 2.3: Pictorial representation of the mappings $\tilde{x}_+$ and $\tilde{x}_-$ of two intervals with the first adjacent to the boundary, according to (2.60). In the top panel, we report how the intervals $[0, a]$, $[b, x_{S,2}]$ and $[x_{S,2}, c]$ are mapped under conjugation in the auxiliary symmetric geometry A_{sym} (see (2.59) for the self-conjugate point $x_{S,2}$); in the bottom panel, the $x < 0$ points are reflected with respect to the boundary. In A_{sym}, the operators coupling points on the same side of the boundary are diagonal in the chiral fermions, while the others are mixed.

Taking into account the constraints due to the theta functions, the expression (2.54) specialised to this bipartition of the half-line becomes

$$\begin{aligned} K_A = & \int_A \mathrm{d}x \, \beta^{\text{sym}}_{\text{loc}}(x) \, T_{00}(x) + \int_0^a \mathrm{d}x \, \frac{\beta^{\text{sym}}_{\text{loc}}(\tilde{x}_+)}{x - \tilde{x}_+} \, T^{\text{bl}}_{\text{diag}}(x, \tilde{x}_+, 0) \\ & + \int_b^c \mathrm{d}x \, \frac{\beta^{\text{sym}}_{\text{loc}}(\tilde{x}_+)}{x - \tilde{x}_+} \, T^{\text{bl}}_{\text{mix}}(x, -\tilde{x}_+, 0; \alpha) + \int_{x_{S,2}}^c \mathrm{d}x \, \frac{\beta^{\text{sym}}_{\text{loc}}(\tilde{x}_-)}{x - \tilde{x}_-} \, T^{\text{bl}}_{\text{diag}}(x, \tilde{x}_-, 0) \\ & + \left(\int_0^a + \int_b^{x_{S,2}} \right) \mathrm{d}x \, \frac{\beta^{\text{sym}}_{\text{loc}}(\tilde{x}_-)}{x - \tilde{x}_-} \, T^{\text{bl}}_{\text{mix}}(x, -\tilde{x}_-, 0; \alpha) . \end{aligned} \tag{2.61}$$

In the remaining part of this section, we study some relevant limits of this expression that provide the known results of Refs. [87–89].

Limit $a \to 0$: When the length of the first interval vanishes, we expect to recover the result of Ref. [89] for the half-line bipartite by an interval. For $x \in [b, c]$, the conjugate point $\tilde{x}_+$ has a finite limit and it reduces to the expression one would obtain for two symmetric intervals $[-c, -b] \cup [b, c]$

$$\tilde{x}_+ \longrightarrow \tilde{x} \equiv -\frac{bc}{x} , \tag{2.62}$$

while the other conjugate point tends to zero with a linear correction in a, $\tilde{x}_- \sim \mathcal{O}(a)$. The self-conjugate point $x_{S,2}$ assumes the value of the one-interval case computed in Ref. [89]

$$x_{S,2} \longrightarrow \sqrt{bc} \, . \tag{2.63}$$

Notice that this point remains self-conjugate in the limit, i.e. $\tilde{x}(\sqrt{bc}) = -\sqrt{bc}$.

As for the entanglement temperature in this limit the expression found in Ref. [89] is obtained

$$\beta_{\mathrm{loc}}^{\mathrm{sym}}(x) \longrightarrow \frac{(x^2-b^2)(c^2-x^2)}{2(c-b)(bc+x^2)}\,. \tag{2.64}$$

By employing also the limits of the conjugate points, we find that the weight function of the bi-local term calculated in $\tilde{x}_+$ reproduces the analogous weight in the result of Ref. [89]

$$\frac{\beta_{\mathrm{loc}}^{\mathrm{sym}}(\tilde{x}_+)}{x-\tilde{x}_+} \longrightarrow \frac{bc(x^2-b^2)(c^2-x^2)}{2(c-b)x(bc+x^2)^2}. \tag{2.65}$$

Instead, by employing the explicit expression of $\tilde{x}_-$ in terms of the entangling points, one finds that the corresponding weight function vanishes as $\beta_{\mathrm{loc}}^{\mathrm{sym}}(\tilde{x}_-) \sim \mathcal{O}(a)$.

Thus, after the limits only the bi-local term mixing the chiralities (evaluated in $-\tilde{x}_+$) remains. This finally reproduces the result obtained in [89]

$$K_A \longrightarrow \int_b^c \mathrm{d}x\, \beta_{\mathrm{loc}}^{\mathrm{sym}}(x)\, T_{00}(x) + \int_b^c \mathrm{d}x\, \frac{\beta_{\mathrm{loc}}^{\mathrm{sym}}(\tilde{x})}{x-\tilde{x}}\, T_{\mathrm{mix}}^{\mathrm{bl}}(x,-\tilde{x},0;\alpha). \tag{2.66}$$

Limit $c \to b$: Let $\ell_2 \equiv c-b$ be the length of the second interval. In the limit $\ell_2 \to 0$ in which this interval vanishes, we expect to recover the result for a single interval $[0,a]$ adjacent to the boundary; in this case the entanglement Hamiltonian is purely local and the entanglement temperature is the parabolic law (1.13) for the entanglement Hamiltonian of a single interval in a CFT. For $x \in [0,a]$, in this limit both conjugate points tend to a constant $\tilde{x}_\pm \sim \pm b + \mathcal{O}(\ell_2)$ and the subleading correction is linear. The self-conjugate point tends to b as well, as expected from the fact that the interval it belongs to vanishes.

The limit of the entanglement temperature reproduces the parabolic law (1.13)

$$\beta_{\mathrm{loc}}^{\mathrm{sym}} \longrightarrow \frac{a^2-x^2}{2a}, \tag{2.67}$$

while both weight functions occurring in the bi-local terms vanish as $\beta_{\mathrm{loc}}^{\mathrm{sym}}(\tilde{x}_\pm) \sim \mathcal{O}(\ell_2)$. Thus, the only term remaining after the limit is the local one and the entanglement Hamiltonian reduces to the known parabolic result (1.13) for one interval adjacent to the boundary.

Limit $b \to a$: Let $d \equiv b-a$ be the distance between the two intervals. In the limit $d \to 0$, they become adjacent to each other and the parabolic law (1.13) for a single interval $[0,c]$ adjacent to the boundary is expected again. However, while in the limit $c \to b$ only the local term of the first interval contributed to the limit, now the parabolic law will be reproduced by gluing together the entanglement temperatures of the two intervals $[0,a] \cup [a+d,c]$ when $d \to 0$. Indeed, for $x \in [0,c]$ the entanglement temperature will reduce to

$$\beta_{\mathrm{loc}}^{\mathrm{sym}}(x) \sim \frac{c^2-x^2}{2c} + \mathcal{O}(d). \tag{2.68}$$

We stress that for d small but finite, $\beta_{\text{loc}}^{\text{sym}}$ vanishes at the extrema a and $a+d$. Only when $d=0$ exactly these zeros disappear, giving the expected limit.

Both conjugate points tend to a constant up to a linear correction $\tilde{x}_\pm \sim \pm a + \mathcal{O}(d)$ and the weight functions of the non-local terms instead vanish linearly in d: $\beta_{\text{loc}}^{\text{sym}}(\tilde{x}_\pm) \sim \mathcal{O}(d)$. Thus, for this geometry we only find a local term, whose weight function is the half-parabola in Eqs. (1.13) and (2.68), as one could expect for one interval at the beginning of a semi-infinite line.

Limit $b \to \infty$, with finite ℓ_2: It is worth considering the limit of large separation between the two intervals, while their lengths are kept fixed. The entanglement temperature reduces to the parabolic law (1.13) in the corresponding interval

$$\beta_{\text{loc}}^{\text{sym}} \longrightarrow \begin{cases} \dfrac{a^2-x^2}{2a}, & x \in [0,a] \\[2ex] \dfrac{(x-b)(c-x)}{(c-b)}, & x \in [b,c]\,. \end{cases} \tag{2.69}$$

As for the weight function in the bi-local terms of Eq. (2.61), while both the numerators $\beta_{\text{loc}}^{\text{sym}}(\tilde{x}_+)$ and $\beta_{\text{loc}}^{\text{sym}}(\tilde{x}_-)$ remain finite, the denominators diverge as $x - \tilde{x}_\pm \sim \mathcal{O}(b)$. Thus, all the bi-local terms vanish in this limit and we obtain the sum of two local entanglement Hamiltonians, one for the single interval $[0,a]$ adjacent to the boundary and one for the single isolated interval $[b,c]$ on the full line, i.e.

$$K_A \longrightarrow \int_0^a \mathrm{d}x\, \beta_{\text{loc}}^{\text{sym}}(x)\, T_{00}(x) + \int_b^c \mathrm{d}x\, \beta_{\text{loc}}^{\text{sym}}(x)\, T_{00}(x)\,. \tag{2.70}$$

This result agrees with the intuition that the second interval is not affected by the presence of the boundary in this limit when it is very far from it.

Limit $\ell_2 \to \infty$, with finite b: We find it interesting to consider the limiting regime where $\ell_2 \to \infty$ while b is kept fixed. This limit has been explored also in Ref. [89] in the special case of $a=0$. The entanglement temperature reduces to

$$\beta_{\text{loc}}^{\text{sym}}(x) \longrightarrow \frac{(x^2-a^2)(x^2-b^2)}{2(b-a)(ab+x^2)} \geqslant 0, \qquad x \in A, \tag{2.71}$$

where now the right hand side is the opposite of the entanglement temperature (2.64) in the entanglement Hamiltonian of a single interval $[a,b]$ on the half-line [89].

As for the weight functions of the bi-local terms in (2.61), for the one corresponding to $\tilde{x}_+$ we find

$$\frac{\beta_{\text{loc}}^{\text{sym}}(\tilde{x}_+)}{x-\tilde{x}_+} \longrightarrow \frac{(b^2-x^2)(x^2-a^2)}{2(b-a)x(ab-x^2)}, \tag{2.72}$$

which is not vanishing. However, since $\tilde{x}_+ \sim \mathcal{O}(\ell_2)$, i.e. it is divergent, the bi-local operators calculated in this point do not contribute because the fermionic fields $\psi_i(\tilde{x}_+)$ with $i = L, R$ vanish as $\tilde{x}_+ \to \infty$, as already observed in Ref. [89] for a similar case. On the other hand, for the mapping $\tilde{x}_-$ we find

$$\tilde{x}_- \longrightarrow \tilde{x} = -\frac{ab}{x}\,, \tag{2.73}$$

and the corresponding weight function reproduces the opposite of the bi-local weight (2.65) obtained for one interval $[a, b]$ on the half-line [89]

$$\frac{\beta^{\text{sym}}_{\text{loc}}(\tilde{x}_-)}{x - \tilde{x}_-} \longrightarrow \frac{ab(x^2 - a^2)(x^2 - b^2)}{2(b - a)x(ab + x^2)^2}\,. \tag{2.74}$$

Thus, the entanglement Hamiltonian (2.61) in this limit simplifies to

$$K_A \longrightarrow \int_A \mathrm{d}x\, \beta^{\text{sym}}_{\text{loc}}(x)\, T_{00}(x) + \int_A \mathrm{d}x\, \frac{\beta^{\text{sym}}_{\text{loc}}(\tilde{x})}{x - \tilde{x}}\, T^{\text{bl}}_{\text{mix}}(x, -\tilde{x}, 0; \alpha), \tag{2.75}$$

with entanglement temperature and bi-local weight function given by Eqs. (2.71) and (2.74), respectively.

We remark that the entanglement Hamiltonian (2.75) is similar to the one of the single interval $[a, b]$ on the half-line [89] (see also (2.66)), with the crucial difference that now the integration domain is the complement $A = [0, a] \cup [b, \infty)$ on the half-line. Combining (2.75) with the entanglement Hamiltonian found in Ref. [89], one obtains the full modular Hamiltonian $K_A \otimes \mathrm{Id}_B - \mathrm{Id}_A \otimes K_B$ (here Id_X denotes the identity on the subsystem X) for the bipartition of the half-line $x \geqslant 0$ given by $[a, b]$ with $a > 0$.

2.2.4 Entanglement entropy

Let us consider a bipartition of the real line (i.e. without boundaries) with a multi-component subsystem $A_{\text{sym}} = [-b_n, -a_n], \dots, [-b_1, a_1] \cup [a_1, b_1], \dots [a_n, b_n]$, with $a_1 > 0$, composed of $2n$ intervals placed in a symmetric position with respect to the origin 0, as shown in Fig. 2.1. For the massless Dirac fermion, the Rényi entropies are [102–107]

$$\begin{aligned} S^{(m)}_{A_{\text{sym}}} = \frac{m+1}{6m} \Bigg(& 2\sum_{i,j}^{n} \log|a_i - b_j| - 2\sum_{i<j}^{n} \Big[\log|a_i - a_j| + \log|b_i - b_j| \Big] - 2n \log\epsilon \\ & + \sum_{i,j}^{n} \Big[\log|b_i + b_j| + \log|a_i + a_j| \Big] - \sum_{i\leqslant j}^{n} \Big[\log|a_i + b_j| + \log|b_i + a_j| \Big] \Bigg) \\ = \frac{m+1}{6m} & \sum_{j=1}^{n} \left[z_{\text{sym}}(b_j - \epsilon) - z_{\text{sym}}(a_j + \epsilon) \right], \end{aligned} \tag{2.76}$$

where $\epsilon > 0$ is an ultraviolet infinitesimal cut-off. The fact that the sum in the last line only runs from 1 to n, despite the presence of $2n$ intervals, is a consequence of the symmetric geometry we are considering. This result can be obtained by writing the moments of the reduced density matrix as the correlation functions of the branch-point twist fields [22] (see the review in Sec. 5.2 of Chapter 5) or from the knowledge of the eigenvalues and eigenvectors of the entanglement Hamiltonian [87]. Following the latter approach, let us compute the Rényi entropies when the subsystem A is made by n disjoint intervals on the half-line. When $n = 1$, the solution of the spectral problem for the entanglement Hamiltonian has been already used in Ref. [89] to write the Rényi entropies, finding that they are half of the value of (2.76) for the auxiliary symmetric geometry $A_{\text{sym}} = [-b, -a] \cup [a, b]$ on the real line. In this section, we extend this analysis to $A = \cup_{i=1}^{n} [a_i, b_i]$ on the half-line for $n \geqslant 1$.

The Rényi entanglement entropies of order $m \geqslant 2$ in terms of the correlation matrix restricted to A are given by [108–111]

$$S_A^{(m)} = \frac{1}{1-m} \operatorname{Tr}\left[g_m(C_A)\right], \qquad \text{with} \quad g_m(\sigma) = \log[\sigma^m + (1-\sigma)^m]. \tag{2.77}$$

By employing the expression (2.42) of the eigenvectors $\Phi_p^s(x)$ of the correlation matrix, of the eigenvalues (2.18) and introducing $A_\epsilon \equiv \cup_{i=1}^{n}[a_i + \epsilon, b_i - \epsilon] \subset A$, one finds

$$S_A^{(m)} = \frac{1}{1-m} \sum_{p=1}^{2n} \int_{-\infty}^{+\infty} \mathrm{d}s \int_{A_\epsilon} \mathrm{d}x \, g_m(\sigma_s) \operatorname{Tr}\left[\Phi_p^s(x) \Phi_p^{s*}(x)\right]. \tag{2.78}$$

From the properties of the eigenfunctions reported in (2.28), we obtain

$$\sum_{p=1}^{2n} \operatorname{Tr}\left[\Phi_p^s(x) \Phi_p^{s*}(x)\right] = 2 \sum_{p=1}^{2n} k_p(x) k_p(x) = \frac{z'(x)}{\pi}, \tag{2.79}$$

which is independent of the parameters α and s. This leads to the factorisation of the two-fold integral in Eq. (2.78). Plugging (2.79) into the integral (2.78) and exploiting $\int_{-\infty}^{+\infty} ds \, g_m(\sigma_s) = \frac{\pi(1-m^2)}{12m}$, we finally find

$$S_A^{(m)} = \frac{m+1}{12m} \sum_{j=1}^{n} \left[z_{\text{sym}}(b_j - \epsilon) - z_{\text{sym}}(a_j + \epsilon)\right], \tag{2.80}$$

which is half of the value for the duplicated geometry without a boundary in Eq. (2.76). This is consistent with what one would expect from the calculation of the correlation of twist fields in the presence of a boundary. We conclude this section by remarking that in Eq. (2.79) the dependence on the boundary scattering phase α cancels out. Thus, as already observed in Ref. [89], while the entanglement Hamiltonian depends explicitly on the boundary condition parameter α through the non-diagonal operator $T_{\text{mix}}^{\text{bl}}$, which takes the different forms (2.52) and (2.53) in the vector and axial phases respectively, the entanglement entropy is independent of the boundary condition. This is a typical scenario in which the entanglement Hamiltonian does contain more information with respect to the Rényi entropies.

2.3 Negativity Hamiltonian

We now pass to the study of tripartite entanglement in the previously considered configurations. As discussed the Introduction, while the entanglement Hamiltonian and entropies are good characterisation of bipartite entanglement, they are not sufficient when dealing with a tripartite system $A \cup B$, with $A = A_1 \cup A_2$. In this scenario, the negativity Hamiltonian $\mathcal{N}_A$, defined in Eq. (1.27) in terms of the partial transpose $\rho_A^{T_1}$ (1.22), offers an operatorial characterisation of tripartite entanglement [81]. The definition for such operation reported in Eq. (1.22) is appropriate for bosonic systems, but it turns out to be ill-suited for fermions: while the partial transposition of Gaussian bosonic states is still a Gaussian state, due to the anti-commutation relation this is not the case for a fermionic one [112, 113], and this makes the computation difficult even for Gaussian states [114–116]. In light of this, Refs. [117–121] introduced a more appropriate definition for fermionic systems, which subsequently found widespread application (see e.g. [122–128]). This definition is motivated by the observation that in a bosonic system, the partial transposition is equivalent to a partial time-reversal or a mirror reflection in phase space [73]. To see that this is indeed the case, consider a bosonic coherent state $|\alpha\rangle = e^{\alpha a^\dagger}|0\rangle$. On this state, the time-reversal transformation acts simply as the conjugation $|\alpha\rangle \to |\alpha^*\rangle$ [73], therefore the relative density matrix goes into its own transpose

$$|\alpha^*\rangle\langle\alpha| \longrightarrow |\alpha\rangle\langle\alpha^*| = (|\alpha^*\rangle\langle\alpha|)^T . \tag{2.81}$$

For fermionic systems, instead, the two transformations are not equivalent anymore. Under time-reversal, a fermionic coherent state $|\xi\rangle = e^{-\xi c^\dagger}|0\rangle, \langle\bar{\xi}| = \langle 0| e^{-c\bar{\xi}}$ transforms as [117]

$$|\xi\rangle\langle\bar{\xi}| \longrightarrow |\mathrm{i}\bar{\xi}\rangle\langle\mathrm{i}\xi| , \tag{2.82}$$

which is different from the transposed density matrix because of the imaginary factor i. The proposal of Refs. [117–121] is then to define the partially time-reversed reduced density matrix $\rho_A^{R_1}$, obtained by acting with Eq. (2.82) only in A_1 (in the following, we will use the apex R to distinguish it from the bosonic partial transpose denoted as T). This operation provides the fermionic logarithmic negativity $\mathcal{E}$ as

$$\mathcal{E} \equiv \log \mathrm{Tr}\left|\rho_A^{R_1}\right| = \log \mathrm{Tr}\sqrt{\rho_A^{R_1\dagger}\rho_A^{R_1}} . \tag{2.83}$$

A drawback of the partially-time reversed RDM is that $\rho_A^{R_1}$ is not Hermitian and its spectrum is in general not real [120]. Because of this, $\mathcal{E}$ in Eq. (2.83) does not have the meaning of quantifying the negativeness of the spectrum of $\rho_A^{R_1}$, in contrast with the bosonic one (1.23). To amend this, Ref. [120] introduced the *twisted* partially time-reversed RDM

$$\rho_A^{\widetilde{R}_1} = \rho_A^{R_1}(-1)^{F_{A_1}}, \tag{2.84}$$

where $F_{A_1} = \sum_{j\in A_1} n_j$ is the number of fermions in the transposed subsystem A_1. This new operator is Hermitian and the logarithmic negativity takes the form [120]

$$\mathcal{E} = \log \operatorname{Tr} \left| \rho_A^{\widetilde{R}_1} \right|, \tag{2.85}$$

recovering its meaning as measure of the negativeness of the eigenvalues of $\rho_A^{\widetilde{R}_1}$. In this sense, the twisted fermionic partial transpose has a more transparent interpretation of the fermionic negativity and allows for the measure of mixed-state entanglement also from its moments, in full analogy with the bosonic partial transpose [129,130]. Before continuing, we remark that in [117], the fermionic partial transpose has also been written in the occupation-number and in the Majorana fermion bases. These definitions are equivalent to the time-reversal operation (2.82) up to a unitary transformation: while this does not give any problems in the evaluation of the spectrum of $\rho_A^{R_1}$, we should be careful if we are interested in the effect of partial transposition on the operators.

Following the definition of the bosonic negativity Hamiltonian (1.27), Ref. [81] also introduced the fermionic negativity Hamiltonian $\mathcal{N}_A$ as the logarithm of the (appropriately normalised) partially time-reversed reduced density matrix $\rho_A^{R_1}$

$$\rho_A^{R_1} \equiv \frac{e^{-2\pi\mathcal{N}_A}}{Z_A}. \tag{2.86}$$

In order to compute this operator, in Ref. [81] it was introduced a physically motivated procedure to construct the negativity Hamiltonian (2.86) from the knowledge of the entanglement Hamiltonian. Later in Ref. [131] (on which Chapter 3 is based), the resolvent method of Ref. [87] was applied to rigorously justify the construction of this operator. We will present this application of the resolvent method in Sec. 3.A. Similarly to Eq. (2.86), the twisted negativity Hamiltonian is defined starting from Eq. (2.84) as [81]

$$\rho_A^{\widetilde{R}_1} \equiv \frac{e^{-\widetilde{\mathcal{N}}_A}}{Z_A}. \tag{2.87}$$

While in this Chapter we focus only on the NH in Eq. (2.86), we will come back to the twisted one $\widetilde{\mathcal{N}}_A$ in Sec. 3.3 of the next one.

Since we will use it in the rest of this section, we now review the procedure to compute $\mathcal{N}_A$ introduced in Ref. [81] (and we refer to Sec. 3.A for more details). Let us consider the multi-component subsystem $A = [a_1, b_1] \cup \ldots \cup [a_n, b_n]$ studied earlier in Sec. 2.2.1 and, to fix the ideas, let us reverse only one interval $A_1 = [a_j, b_j]$; this case can be straightforwardly generalised to multiple reversed intervals. In this geometry, the entanglement Hamiltonian K_A is given by Eqs. (2.20) and (2.36) [87, 88]. Under the path-integral construction of Refs. [77, 78, 80], the partial transpose has the net effect of applying a spatial reversal in the transposed interval [81]. This can be understood in terms of CPT symmetry: because of this symmetry, the time-reversal operation of Eqs. (2.81) and (2.82) is equivalent to a parity transformation followed by a charge conjugation. The parity transformation is implemented by exchanging the extrema a_j, b_j of the reversed interval in the expression of the entanglement Hamiltonian [81]. Under this procedure, the function (2.20) becomes

$$z^R(x) = \log\left[-\frac{x-b_j}{x-a_j}\prod_{i\neq j}\frac{x-a_i}{x-b_i}\right]. \tag{2.88}$$

As a consequence, the entanglement temperature becomes $\beta^R_{\text{loc}}(x) = 1/z^R(x)'$, which we will call *negativity temperature*, and the conjugate points $\tilde{x}^R_p$ appearing in the bi-local term will be the solutions of the equation $z^R(y) = z^R(x)$. Moreover, the partial time-reversal affects the Dirac spinor $\psi = \begin{pmatrix}\psi_R \\ \psi_L\end{pmatrix}$. In Ref. [81], the negativity Hamiltonian was written in the Majorana (real) fermion basis, μ, where the fermionic partial transpose is implemented as $\mu(x) \to \mathrm{i}\mu(x)$ for $x \in [a_k, b_k]$. Rewriting the Dirac spinor ψ in terms of two Majorana spinors as done in Eq. (2.2), we find out that the effect of the partial transposition is simply $\psi(x) \to \mathrm{i}\psi(x)$, $\psi^\dagger(x) \to \mathrm{i}\psi^\dagger(x)$ for $x \in [a_k, b_k]$. This transformation can be also obtained directly using the resolvent method as shown in Sec. 3.A. Let us stress that this transformation does not correspond to perform a time-reversal operation on the complex fermions, despite our starting point for the definition of the partial transposition in the coherent state basis.

Putting all together, the negativity Hamiltonian for n disjoint intervals on the plane reversing a single interval $A_1 = [a_j, b_j]$ takes the form [81, 131]

$$\begin{aligned}\mathcal{N}_A &= \mathcal{N}^{\text{loc}}_A + \mathcal{N}^{\text{bl}}_A \\ &= \int_A \mathrm{d}x\, \beta^R_{\text{loc}}(x)\, T_{00}(x) + \sum_{p=1}^{n-1}\int_A \mathrm{d}x\, \frac{\beta^R_{\text{loc}}(\tilde{x}^R_p)}{x-\tilde{x}^R_p}\, \mathrm{i}^{\Theta_1(x)}(-\mathrm{i})^{\Theta_1(\tilde{x}^R_p)}\, T^{\text{bl}}_{\text{diag}}(x, \tilde{x}^R_p, 0)\,,\end{aligned} \tag{2.89}$$

where we have introduced the function

$$\Theta_1(x) = \begin{cases} 1, & x \in A_1, \\ 0, & x \notin A_1, \end{cases} \tag{2.90}$$

which is equal to 1 if x is in the reversed interval and 0 otherwise. Notice that the expression has an additional minus sign when the conjugate point is in reversed interval, which can be obtained from the explicit computation of Sec. 3.A. Comparing Eq. (2.89) with the entanglement Hamiltonian (2.36), we see that the main difference is the presence of the imaginary units in the bi-local terms [81]. This has the effect that whenever either x or a conjugate point $\tilde{x}_p$ is contained in the reversed interval, the corresponding bi-local term is anti-Hermitian [81]. For later convenience, we specialise the negativity Hamiltonian (2.89) to the case of two intervals $A = [a_1, b_1] \cup [a_2, b_2]$ transposing the second one, first obtained in Ref. [81]

$$\mathcal{N}_A = \int_A \mathrm{d}x\, \beta^R_{\mathrm{loc}}(x)\, T_{00}(x) - \mathrm{i} \left(\int_{a_1}^{b_1} - \int_{a_2}^{b_2} \right) \mathrm{d}x\, \frac{\beta^R_{\mathrm{loc}}(\tilde{x}^R)}{x - \tilde{x}^R}\, T^{\mathrm{bl}}_{\mathrm{diag}}(x, \tilde{x}^R, 0), \tag{2.91}$$

where the negativity temperature is

$$\beta^R_{\mathrm{loc}}(x) = \left[\frac{1}{x - a_1} + \frac{1}{b_1 - x} + \frac{1}{x - b_2} + \frac{1}{a_2 - x} \right]^{-1}, \tag{2.92}$$

and the conjugated point is

$$\tilde{x}^R = \frac{(b_1 a_2 - a_1 b_2)x + (b_1 + a_2) a_1 b_2 - (a_1 + b_2) b_1 a_2}{(b_1 - a_1 + a_2 - b_2)x + a_1 b_2 - b_1 a_2}. \tag{2.93}$$

As we mentioned, the bi-local term is anti-Hermitian due to the imaginary factor coming from the partial time reversal.

It is immediate to extend the procedure of Ref. [81] to the case in the presence of a boundary, which is of interest in this Chapter. In our case, we have to transpose both the interval $[a_j, b_j]$ and its reflection $[-b_j, -a_j]$ in the symmetric auxiliary geometry. This can again be implemented by simply exchanging the extremes a_j and b_j everywhere in the expression of the entanglement Hamiltonian with a boundary (2.54). We also need to introduce an appropriate imaginary factor for each fermion belonging to the reversed interval. In the following section, we show explicitly how to obtain the negativity Hamiltonian in the case of two intervals when one of them is adjacent to the boundary.

2.3.1 Negativity Hamiltonian for two intervals with one adjacent to the boundary

Let us consider the subsystem $A = [0, a] \cup [b, c]$ on the half-line studied in Sec. 2.2.3. By transposing the second interval $[b, c]$, the function $z^R_{\mathrm{sym}}(x)$ for the symmetric auxiliary geometry is obtained by exchanging b and c in the expression of $z_{\mathrm{sym}}(x)$, finding

$$z^R_{\mathrm{sym}}(x) = \log \left[\frac{(x + b)(x + a)(c - x)}{(x + c)(x - a)(x - b)} \right]. \tag{2.94}$$

Hence, the negativity temperature reads

$$\beta^{R\,\mathrm{sym}}_{\mathrm{loc}}(x) = \frac{1}{{z^R_{\mathrm{sym}}}'(x)} = \left[\frac{2a}{x^2 - a^2} + \frac{2b}{x^2 - b^2} + \frac{2c}{c^2 - x^2} \right]^{-1}. \tag{2.95}$$

The conjugate points are obtained as the solutions of the equation $z^R_{\text{sym}}(y) = z^R_{\text{sym}}(x)$. Also for the negativity Hamiltonian we find a self-conjugate point $x^R_{S,2} \in [b,c]$, whose explicit expression is $x^R_{S,2} = \sqrt{ca + bc - ab}$. Similarly to what happened for the entanglement Hamiltonian, under the mapping $\tilde{x}^R_+$ the self-conjugate point $x^R_{S,2}$ is conjugated to the boundary. This leads to a similar cross-over from the diagonal to the mixed operator in the bi-local term of the negativity Hamiltonian. The various intervals are mapped under conjugation as

$$\begin{cases} \tilde{x}^R_+([0,a]) = [b, x^R_{S,2}]\,, \\ \tilde{x}^R_+\Big([b, x^R_{S,2}]\Big) = [0,a]\,, \\ \tilde{x}^R_+\Big([x^R_{S,2}, c]\Big) = [-a, 0]\,, \end{cases} \qquad \begin{cases} \tilde{x}^R_-([0,a]) = [-x^R_{S,2}, -c]\,, \\ \tilde{x}^R_-([b,c]) = [-c,-b]\,. \end{cases} \tag{2.96}$$

Thus, in the bi-local operator, the terms corresponding to $\tilde{x}^R_+([0,a] \cup [b, x^R_{S,2}])$ contain fermions with the same chirality, while the other ones provide terms that couple fermions with different chiralities, which also depend explicitly on the boundary condition.

Moreover, under the partial transpose, the fermions receive an imaginary factor $\psi \to \mathrm{i}\psi$ when they are evaluated in the transposed interval $[b,c]$. As a consequence, the bi-local operator that couples a point in $[0,a]$ with one in $[b,c]$ receives only one imaginary factor and is anti-Hermitian.

Taking care of the sign of the conjugate points, the negativity Hamiltonian can be written more explicitly as follows

$$\begin{aligned} \mathcal{N}_A = &\int_A \mathrm{d}x\, \beta^{R\text{ sym}}_{\text{loc}}(x)\, T_{00}(x,0) - \mathrm{i}\left(\int_0^a - \int_b^{x^R_{S,2}}\right) \mathrm{d}x\, \frac{\beta^{R\text{ sym}}_{\text{loc}}(\tilde{x}^R_+)}{x - \tilde{x}^R_+}\, T^{\text{bl}}_{\text{diag}}(x, \tilde{x}^R_+, 0) \\ &+ \mathrm{i}\int_{x^R_{S,2}}^c \mathrm{d}x\, \frac{\beta^{R\text{ sym}}_{\text{loc}}(\tilde{x}^R_+)}{x - \tilde{x}^R_+}\, T^{\text{bl}}_{\text{mix}}(x, -\tilde{x}^R_+, 0; \alpha) \\ &+ \left(-\mathrm{i}\int_0^a + \int_b^c\right) \mathrm{d}x\, \frac{\beta^{R\text{ sym}}_{\text{loc}}(\tilde{x}^R_-)}{x - \tilde{x}^R_-}\, T^{\text{bl}}_{\text{mix}}(x, -\tilde{x}^R_-, 0; \alpha). \end{aligned} \tag{2.97}$$

We point out that the bi-local mixed term $T^{\text{bl}}_{\text{mix}}(x, -\tilde{x}^R_-, 0; \alpha)$ contains $\psi(x)$ and $\psi(-\tilde{x}^R_-)$ when integrated over $[b,c]$, and they both take an imaginary unit factor under partial transposition because $x, -\tilde{x}^R_- \in [b,c]$. As a consequence, this operator is Hermitian, differently from the same operator $T^{\text{bl}}_{\text{mix}}(x, -\tilde{x}^R_-, 0; \alpha)$ integrated over $[0,a]$.

2.4 Numerical lattice computations

In this section, we study the entanglement Hamiltonian in a critical lattice model, the tight binding chain, in order to check the validity of our predictions from CFT. As we discussed in the Introduction and in Sec. 2.2, for free fermionic models the entanglement Hamiltonian can be directly obtained from the correlation matrix according to Eq. (1.15), both on the lattice and in the continuum. The comparison between the lattice entanglement Hamiltonian and the QFT prediction turns out however to be a non-trivial problem, as lengthily discussed in Refs. [25,52,53,55,132–137]. The main obstacle is the fact that, even for a single interval, while the CFT EH (1.13) is local, the lattice one presents hoppings between fermions at all distances [132–134]. These higher-distance couplings are not negligible and, indeed, it was shown in Ref. [133,134] that a proper continuum limit of the lattice EH requires taking into account also these terms. In the following, before presenting the results of the exact numerical computation, we will review the continuum limit procedure of Ref. [133,134], showing how the higher hoppings have to be included.

2.4.1 Correlation matrix techniques

The model we consider is the tight-binding chain, with Hamiltonian

$$H = -\frac{1}{2}\sum_j \left[c_j^\dagger c_{j+1} + c_{j+1}^\dagger c_j\right], \tag{2.98}$$

where the fermionic creation and annihilation operators $c_i, c_i^\dagger$ satisfy the canonical anticommutation relations

$$\{c_i, c_j^\dagger\} = \delta_{ij}, \qquad \{c_i, c_j\} = \{c_i^\dagger, c_j^\dagger\} = 0\,. \tag{2.99}$$

On the real line, the two-point correlation matrix is

$$(C_A)_{i,j} = \frac{\sin(k_F(i-j))}{\pi(i-j)}\,, \tag{2.100}$$

where k_F is the Fermi momentum. In the half-chain, whose sites are labelled by $i \in \mathbb{N}$, we choose to impose open boundary conditions (OBC) on the first site (also known as Neumann boundary conditions). The corresponding two-point correlation matrix has the following generic element [110,138]

$$(C_A)_{i,j} = \frac{\sin(k_F(i-j))}{\pi(i-j)} - \frac{\sin(k_F(i+j))}{\pi(i+j)}\,. \tag{2.101}$$

In our numerical computations we focus on the half-filled case, where $k_F = \frac{\pi}{2s}$, being s the lattice spacing, that is set to $s = 1$ in the numerical analysis.

In order to get the kernel H_A in Eq. (2.16), we use the discretised version of Eq. (1.15). In this free fermionic model, the reduced density matrix can be written as in Eq. (1.14) [110,111],

$$\rho_A = \frac{1}{Z_A}e^{-2\pi K_A} = \frac{1}{Z_A}\exp\Big\{-\sum_{i,j} c_i^\dagger h_{i,j} c_j\Big\}. \tag{2.102}$$

If σ_k are the eigenvalues of the matrix C_A and $\phi_k(j)$ its eigenvectors, from Eq. (1.15) the finite-dimensional spectral representation of h reads

$$h = V E V^{\dagger}, \tag{2.103}$$

where the columns of V are the eigenvectors ϕ_k, while the matrix E is diagonal and its elements are the eigenvalues e_k, related to the σ_k as in Eq. (2.17). Because of particle-hole symmetry, at half-filling both the correlation matrix of the infinite chain in Eq. (2.100) and of the half-chain with OBC in Eq. (2.101) have a checkerboard structure such that only matrix elements with $i-j$ odd are non-zero. This feature is inherited by h [134] and such checkerboard structure greatly simplifies the continuum limit procedure, as we discuss later.

We find it worth remarking that, in this numerical inspection, it is crucially important that the numerical values of σ_k remain distinct from 0 and 1; hence the numerical analysis must be performed with high precision. We have used the python library `mpmath` [139], keeping up to 300 digits for the lengths that we have considered.

The previous scheme can be adapted to the calculation of the negativity Hamiltonian [81]. In order to review this procedure, for simplicity we consider the subsystem $A = [a_1, b_1] \cup [a_2, b_2]$ made by the union of two disjoint blocks in the infinite chain. The covariance matrix is defined as follows

$$\Gamma_A \,=\, \mathrm{Id}_A - 2\, C_A \,=\, \begin{pmatrix} \Gamma_{11} & \Gamma_{12} \\ \Gamma_{21} & \Gamma_{22} \end{pmatrix}, \tag{2.104}$$

where Γ_{11} and Γ_{22} are the covariance matrices restricted to the blocks $[a_1, b_1]$ and $[a_2, b_2]$, respectively, while Γ_{12} and Γ_{21} contain the cross correlations between them. The partial time reversal of $[a_2, b_2]$ maps Γ_A into a matrix whose generic element is the corresponding element of Γ_A multiplied by an imaginary unit for each index belonging to $[a_2, b_2]$. The result is

$$\Gamma_A^{R_2} = \begin{pmatrix} \Gamma_A^{(1,1)} & \mathrm{i}\,\Gamma_A^{(1,2)} \\ \mathrm{i}\,\Gamma_A^{(2,1)} & -\Gamma_A^{(2,2)} \end{pmatrix}, \qquad \left(\Gamma_A^{R_2}\right)^{\dagger} = \begin{pmatrix} \Gamma_A^{(1,1)} & -\mathrm{i}\,\Gamma_A^{(1,2)} \\ -\mathrm{i}\,\Gamma_A^{(2,1)} & -\Gamma_A^{(2,2)} \end{pmatrix}. \tag{2.105}$$

The operator $\rho_A^{R_2}$ obtained from ρ_A after a partial time transposition of the block $[a_2, b_2]$ reads

$$\rho_A^{R_2} = \frac{1}{Z_A} e^{-2\pi N_A} = \frac{1}{Z_A} \exp\Big\{ -\sum_{i,j} c_i^{\dagger} \eta_{i,j} c_j \Big\}, \tag{2.106}$$

where N_A is the lattice negativity Hamiltonian, whose kernel η can be written in terms of the matrix $\Gamma_A^{R_2}$ in (2.105) as follows

$$\eta = \log\left[\frac{\mathrm{Id}_A + \Gamma_A^{R_2}}{\mathrm{Id}_A - \Gamma_A^{R_2}} \right] = \log\Big(\big[C_A^{R_2} \big]^{-1} - \mathrm{Id}_A \Big). \tag{2.107}$$

This matrix can again be obtained numerically by first solving the eigenvalue problem for $C_A^{R_2}$ and then employing its spectral representation. However, the difference with respect to Eq. (2.103) is that $C_A^{R_2}$ and, consequently, η are non-Hermitian. This implies that the matrix of the eigenvectors is non-unitary and Eq. (2.103) needs to be modified as $\eta = VEV^{-1}$. Finally, we consider the twisted partial-time reversal $\rho_A^{\widetilde{R}_2}$ (2.87). This operator is Gaussian, too, and its kernel $\widetilde{\eta}$ is related to the reversed covariance matrix (2.105) as

$$\widetilde{\eta} = \log\left[\frac{\mathrm{Id}_A + \Gamma_A^{R_2}}{\mathrm{Id}_A - \Gamma_A^{R_2}}\, U_{A_2}\right], \tag{2.108}$$

where the matrix $U_{A_2} = \mathrm{Id}_{A_1} \oplus -\mathrm{Id}_{A_2}$ is related to the transformation $(-1)^{F_{A_2}}$ in Eq. (2.84).

The connection between η and $\Gamma_A^{R_2}$ was applied in Ref. [81] to evaluate the negativity Hamiltonian on the lattice and compare it with the field-theoretical prediction in Eq. (2.91). In particular, in Ref. [81] the analytical negativity temperature $\beta^R_{\mathrm{loc}}(x)$ has been compared with the next-neighbour hopping term $\eta_{j,j+1}$ for the case of adjacent intervals, as we report in the inset of Fig. 2.4. While they are in good agreement with the local term of the field-theoretical prediction of Eq. (2.91) near the entangling points, a small deviation occurs as we move away from them. In the following we show that a perfect agreement also away from the entangling points is obtained by taking into account the higher hopping terms. This confirms the prediction in Eq. (2.91).

2.4.2 Continuum limit on the line

The continuum limit of the entanglement Hamiltonian of a single block for a free fermion infinite chain in its ground state has been first obtained in Ref. [133]. Then, the procedure introduced in this work has been successfully adapted to recover the other entanglement Hamiltonians in free systems [52, 135–137]. The core idea behind this limit is to express the model in terms of the low-energy fluctuations on top of the Fermi sea. This is done by introducing the continuous coordinate $x = is$ and linearising the fluctuations of the lattice fermions c_i around the two Fermi points k_F. In terms of the left- and right-moving fermions ψ_L and ψ_R which describe the scaling limit of the tight-binding model, the lattice fermion c_j reads

$$c_i \sim \sqrt{s}\left[e^{-\mathrm{i}k_F x}\psi_L(x) + e^{\mathrm{i}k_F x}\psi_R(x)\right], \tag{2.109}$$

where s is again the the lattice spacing, which acts as the expansion parameter. This expansion is the starting point of the limit studied in [133, 134] which we now review in the case of generic Fermi momentum k_F, since this will be useful also in later Chapters.

Let us divide the entanglement Hamiltonian kernel $h_{i,j}$ in Eq. (2.102) in matrix blocks $\left(h^{(\sigma,\zeta)}\right)_{i,j}$ such that $i \in A_\sigma, j \in A_\zeta$. As an example, for a subsystem made by the union of two disjoint segments $A = A_1 \cup A_2$, the EH kernel reads

$$h = \begin{pmatrix} h^{(1,1)} & h^{(1,2)} \\ h^{(2,1)} & h^{(2,2)} \end{pmatrix}, \tag{2.110}$$

where the diagonal blocks $h^{(1,1)}$ and $h^{(2,2)}$ describe hoppings within the first and second segment respectively, whereas the off-diagonal ones contain long-range hopping terms between the two segments. This structure facilitates the continuum limit because the diagonal and the off-diagonal blocks in the entanglement Hamiltonian matrix (2.110) provide respectively the local and the bi-local terms of (2.36), as discussed in [134].

Let us first consider the diagonal blocks $h^{(\sigma,\sigma)}$, which yield the local term. Following [133], one substitutes the linearisation in Eq. (2.109) in the expression of the lattice entanglement Hamiltonian in Eq. (2.102), obtaining

$$\begin{aligned} h^{(\sigma,\sigma)}_{i,i+r}\Big[c^\dagger_i c_{i+r} + c^\dagger_{i+r} c_i\Big] \approx\ & s\, h^{(\sigma,\sigma)}_{x,x+rs}\Big[e^{-\mathrm{i}k_F rs}\psi^\dagger_L(x)\,\psi_L(x+rs) + e^{\mathrm{i}k_F rs}\,\psi^\dagger_R(x)\,\psi_R(x+rs) + \\ & + e^{\mathrm{i}k_F(2x+rs)}\psi^\dagger_L(x)\,\psi_R(x+rs) + e^{-\mathrm{i}k_F(2x+rs)}\psi^\dagger_L(x)\,\psi_R(x+rs) + \text{h.c.}\Big], \end{aligned} \tag{2.111}$$

where we expressed also the matrix element $h^{(\sigma,\sigma)}_{x,x+rs}$ as a function of the continuous variable x. Since the massless Dirac field-theory presents conformal symmetry, one expects that in the continuum limit $s \to 0$ the right- and left-moving fermions ψ_R, ψ_L will decouple. From Eq. (2.111) we can understand that the decoupling mechanism is due to the phases: the terms proportional to the product of left- and right-movers are multiplied by a strongly oscillating phase $e^{\pm\mathrm{i}k_F(2x+rs)}$ and in the limit $s \to 0$, these phases will average to zero, leading to the decoupling between ψ_L and ψ_R [133]. Dropping the highly oscillating terms and expanding in powers of the lattice spacing s both the fields ψ_L, ψ_R and the matrix element $h^{(\sigma,\sigma)}_{x,x+rs}$ we find

$$\begin{aligned} & h^{(\sigma,\sigma)}_{i,i+r}\Big[c^\dagger_i c_{i+r} + c^\dagger_{i+r} c_i\Big] \approx \\ & \quad \approx s\left(h^{(\sigma,\sigma)}_{x-\frac{rs}{2},x+\frac{rs}{2}} + \frac{rs}{2}\partial_x h\right) 2\cos(k_F rs)\left(\psi^\dagger_L(x)\psi_L(x) + \psi^\dagger_R(x)\psi_R(x)\right) + \\ & \qquad + s\, h^{(\sigma,\sigma)}_{x-\frac{rs}{2},x+\frac{rs}{2}}\Big[\cos(k_F rs)\, r\, s\, \partial_x\left(\psi^\dagger_L(x)\psi_L(x) + \psi^\dagger_R(x)\psi_R(x)\right) + \\ & \qquad\qquad - \mathrm{i}\sin(k_F rs)\, r\, s\left(\psi^\dagger_L(x)\,\partial_x\psi_L(x) - \psi^\dagger_R(x)\,\partial_x\psi_R(x)\right) + \text{h.c.}\Big]. \end{aligned} \tag{2.112}$$

We now plug the expansion (2.112) into Eq. (2.102) and we promote the sum over the index i to an integral over x, sending $is \to x$, $s \to \mathrm{d}x$. Integrating by parts the operator in the third row of (2.112), this term cancels out with the one proportional to the derivative of the matrix element $\partial_x h$ in the second row [133]. In the second row, we recognise the number operator of the Dirac fermion $N(x)$

$$N(x,t) = :\Big[\psi^\dagger_R(x-t)\psi_R(x-t) + \psi^\dagger_L(x+t)\psi_L(x+t)\Big]:, \tag{2.113}$$

while in the last row the energy density $T_{00}(x)$ defined in Eq. (2.37). Thus, at leading order in the lattice spacing, we find that the diagonal blocks of the entanglement Hamiltonian can be written as [133]

$$\sum_i h^{(\sigma,\sigma)}_{i,i+r} \left[c^\dagger_i c_{i+r} + c^\dagger_{i+r} c_i\right] \sim \int \mathrm{d}x \left[\mathcal{S}^{\mathrm{loc}}(x)\, T_{00}(x) + \mathcal{C}^{\mathrm{loc}}(x)\, N(x)\right], \tag{2.114}$$

where we have introduced the weighted sums over the matrix elements [133]

$$\mathcal{S}^{\mathrm{loc}}(x) \equiv -\, 2\, s \sum_{r\geq 1} r\, \sin(k_F r s)\, h^{(\sigma,\sigma)}_{i-\frac{r}{2},i+\frac{r}{2}}\,, \tag{2.115}$$

$$\mathcal{C}^{\mathrm{loc}}(x) \equiv h^{(\sigma,\sigma)}_{i,i} +\, 2 \sum_{r\geq 1} \cos(k_F r s)\, h^{(\sigma,\sigma)}_{i-\frac{r}{2},i+\frac{r}{2}}\,. \tag{2.116}$$

Let us compare Eq. (2.114) with the field-theoretical predictions for the entanglement Hamiltonian on the plane in Eq. (2.36). Identifying the terms proportional to the energy density $T_{00}(x)$, in Ref. [133] it was verified numerically that in the case of a single interval, the sum $\mathcal{S}^{\mathrm{loc}}(x)$ in Eq. (2.115) correctly reproduces the prediction for the entanglement temperature $\beta_{\mathrm{loc}}(x)$. We remark that, according to (2.115), this continuum limit requires to sum over higher hoppings and not to consider only the next-neighbour element $h_{i,i+1}$, as one would expect from a naive discretisation of the stress-energy tensor in (2.36). Regarding the term in Eq. (2.114) proportional to the number operator $N(x)$, a remarkable simplification happens at half-filling (that we consider in this Chapter). Due to the checkerboard structure (see discussion below Eq. (2.103)), only the elements $h_{i,i+r}$ with r odd are non-vanishing. This implies that the expression (2.116) vanishes exactly at half-filling, guaranteeing that Eq. (2.114) does not depend on $N(x)$. Finally, specialising the sum in Eq. (2.115) to the half-filling case we have

$$\mathcal{S}^{\mathrm{loc}}(x) \equiv -\, 2s \sum_{\substack{r \text{ odd} \\ r\geq 1}} r\, (-1)^{\frac{r-1}{2}}\, h^{(\sigma,\sigma)}_{i-\frac{r-1}{2},i+\frac{r+1}{2}}\,. \tag{2.117}$$

In Ref. [134], the previous considerations have been extended in order to obtain the bi-local terms of the entanglement Hamiltonian (2.36) through a continuum limit. Let us recall that, when A is the union of disjoint intervals, the bi-local term in Eq. (2.36) (see also Eq. (2.38)) couples fermions evaluated in two different positions given by x and a certain conjugate point $\tilde{x}_p(x)$ satisfying Eq. (2.26) and belonging to a different interval. Thus for, e.g., $A = A_1 \cup A_2$ and $x \in A_1$ we have that $\tilde{x}_1 \in A_2$ and therefore the off-diagonal block $h^{(1,2)}_{i,j}$ in the lattice entanglement Hamiltonian matrix (2.110) must be considered. In analogy with the field-theoretical result, the non-zero matrix elements of this off-diagonal block turns out to be localised around the curve defined by $js = \tilde{x}_p(is)$ [132, 134]. However, despite the fact that the matrix elements decay as we move away from this curve, they remain non-zero even far from it, similarly to what happens for the diagonal blocks $h^{(\sigma,\sigma)}$ previously discussed. This necessary leads to take into account all the elements of the off-diagonal block in order to reproduce the correct result in the continuum limit [134].

Plugging the expression for $c_j^\dagger$ and c_j given by (2.109) into the entanglement Hamiltonian obtained from (2.102) and again dropping the strongly oscillating contributions, the term provided by the off-diagonal block $h^{(1,2)}$ reads [134]

$$\begin{aligned} c_i^\dagger h_{i,j}^{(1,2)} c_j \sim\, & s\, h_{i,j}^{(1,2)} \Big[e^{\mathrm{i}k_F(i-j)s} \psi_L^\dagger(x)\, \psi_L(y) + e^{\mathrm{i}k_F(j-i)s} \psi_R^\dagger(x)\, \psi_R(y) \\ & + e^{\mathrm{i}k_F(i+j)s} \psi_L^\dagger(x)\, \psi_R(y) + e^{-\mathrm{i}k_F(i+j)s} \psi_R^\dagger(x)\, \psi_L(y) \Big] \\ =\, & \mathrm{i}\, s\, \sin(k_F(j-i)s)\, h_{i,j}^{(1,2)} \Big[\psi_R^\dagger(x)\, \psi_R(y) - \psi_L^\dagger(x)\, \psi_L(y) \Big] \\ & + s\, \cos(k_F(j-i)s)\, h_{i,j}^{(1,2)} \Big[\psi_R^\dagger(x)\, \psi_R(y) + \psi_L^\dagger(x)\, \psi_L(y) \Big] . \end{aligned} \tag{2.118}$$

In the second-to-last row we recognise the bi-local operator $T_{\text{diag}}^{\text{bl}}(x, y, t = 0)$ defined in (2.38), which does not mix fields with different chiralities defined in Eq. (2.48), while the term in the last row is proportional to a different operator $j^{\text{bl}}(x, y) = j^{\text{bl}}(x, y, 0)$ with

$$\begin{aligned} j^{\text{bl}}(x, y, t) = \frac{1}{2} :\Big[& \Big(\psi_R^\dagger(x-t)\psi_R(y-t) + \psi_R^\dagger(y-t)\psi_R(x-t) \Big) \\ & + \Big(\psi_L^\dagger(x+t)\psi_L(y+t) + \psi_L^\dagger(y+t)\psi_L(x+t) \Big) \Big]: , \end{aligned} \tag{2.119}$$

which was already identified in Ref. [134].

In order to find the proper continuum limit, we now expand the field in position y around the conjugate point $\tilde{x}_p$, keeping only the term at leading order in s, obtaining [134]

$$\sum_i \sum_j c_i^\dagger h_{i,j}^{(1,2)} c_j \sim \int \mathrm{d}x \left[\mathcal{S}^{\text{diag}}(x)\, T_{\text{diag}}^{\text{bl}}(x, \tilde{x}_p) + \mathcal{C}^{\text{diag}}(x)\, j^{\text{bl}}(x, \tilde{x}_p) \right] , \tag{2.120}$$

where we have again promoted the sum over the row index i to an integral over x and we have introduced the sums [134]

$$\mathcal{S}^{\text{diag}}(x) \equiv \sum_{j \in A_2} \sin(k_F(j-i)s)\, h_{i,j}^{(1,2)}, \tag{2.121}$$

$$\mathcal{C}^{\text{diag}}(x) \equiv \sum_{j \in A_2} \cos(k_F(j-i)s)\, h_{i,j}^{(1,2)}. \tag{2.122}$$

Similar results are obtained for the other off-diagonal blocks in Eq. (2.110).

If we now compare the limit of the off-diagonal blocks in Eq. (2.120) with the bi-local terms of the field-theoretical entanglement Hamiltonian (2.36), we see that the sum $\mathcal{S}^{\text{diag}}(x)$ in Eq. (2.121) needs to reproduce the bi-local weight, since they are both proportional to the bi-local operator $T_{\text{diag}}^{\text{bl}}$ in Eq. (2.48). This was checked numerically in Ref. [134] for the case of two intervals. Therefore we see that, like for the local term, the whole block matrices

$h^{(1,2)}_{i,j}$ and $h^{(2,1)}_{i,j}$ must be used to recover the field theory prediction for the bi-local term, and not only the matrix elements around $\tilde{x}_p(x)$, as one could naively expect.

On the other hand, analogously to what happens in the local case, we expect that the sum $\mathcal{C}^{\mathrm{diag}}(x)$ (2.122) multiplying the new operator $j^{\mathrm{bl}}(x)$ (2.119) vanishes, since such an operator does not appear in the field-theoretical entanglement Hamiltonian (2.36). Also in the off-diagonal blocks, at half-filling $k_F = \frac{\pi}{2s}$, the checkerboard structure of the lattice entanglement kernel h implies that Eq. (2.122) vanishes identically, simplifying the calculations.

Also in this case, for convenience, we specialise the expression of Eq. (2.121) to the half-filling case, obtaining

$$\mathcal{S}^{\mathrm{diag}}(x) \equiv \sum_j (-1)^{(j-i-1)/2} h^{(1,2)}_{i,j}. \tag{2.123}$$

In the following, for simplicity we will always restrict ourselves to the case at half-filling.

Negativity Hamiltonian

The formulae (2.117) and (2.123) have been obtained in [133, 134] to find the continuum limit of the entanglement Hamiltonian for a multipartite geometry. We remark that, in the derivations of Eqs. (2.111) and (2.112) for the local part and of Eq. (2.118) for the bi-local one, only the expansion (2.109) of the lattice fermion c_i in terms of the low energy fluctuations ψ_L, ψ_R has been used. Such expansion is valid in general, not only for the entanglement Hamiltonian; hence the steps of the previous section can be repeated for the lattice negativity Hamiltonian (2.106), by replacing each block of $h_{i,j}$ with the corresponding block of the negativity kernel $\eta_{i,j}$, which for the case at half-filling under study also inherits a checkerboard structure. This allows us to find that the continuum limit of the lattice negativity Hamiltonian has a local term whose weight function can be read from Eq. (2.117), while the bi-local terms take different signs and imaginary factors in different intervals. In the special case of two intervals, this can be seen from Eq. (2.91), where the bi-local term is the imaginary part of N_A and the integral over $[a_2, b_2]$ has an additional minus sign due to the partial transposition. This tells us that, in order to compare the continuum limit of the lattice negativity Hamiltonian (at half-filling) with the field-theoretical prediction of Eq. (2.91), Eq. (2.123) must be modified as follows

$$\mathcal{S}^{\mathrm{diag}}(x) = \begin{cases} \mathrm{i} \sum_j (-1)^{(j-i-1)/2} \eta^{(1,2)}_{i,j} & x \in [a_1, b_1] \\ \\ -\,\mathrm{i} \sum_j (-1)^{(j-i-1)/2} \eta^{(2,1)}_{i,j} & x \in [a_2, b_2]\,. \end{cases} \tag{2.124}$$

Now we can study the continuum limit of (2.117) and (2.124) to check the field theory predictions for the negativity Hamiltonian, which is reported in Eqs. (2.91) to (2.93) for two disjoint intervals of arbitrary length, after a partial transposition of the second one.

In Fig. 2.4 we consider three different length ratios $\ell_2/\ell_1 = 0.5, 1, 1.5$ for two adjacent intervals (left panels) or two disjoint intervals separated by ℓ_1 sites. As for the continuum

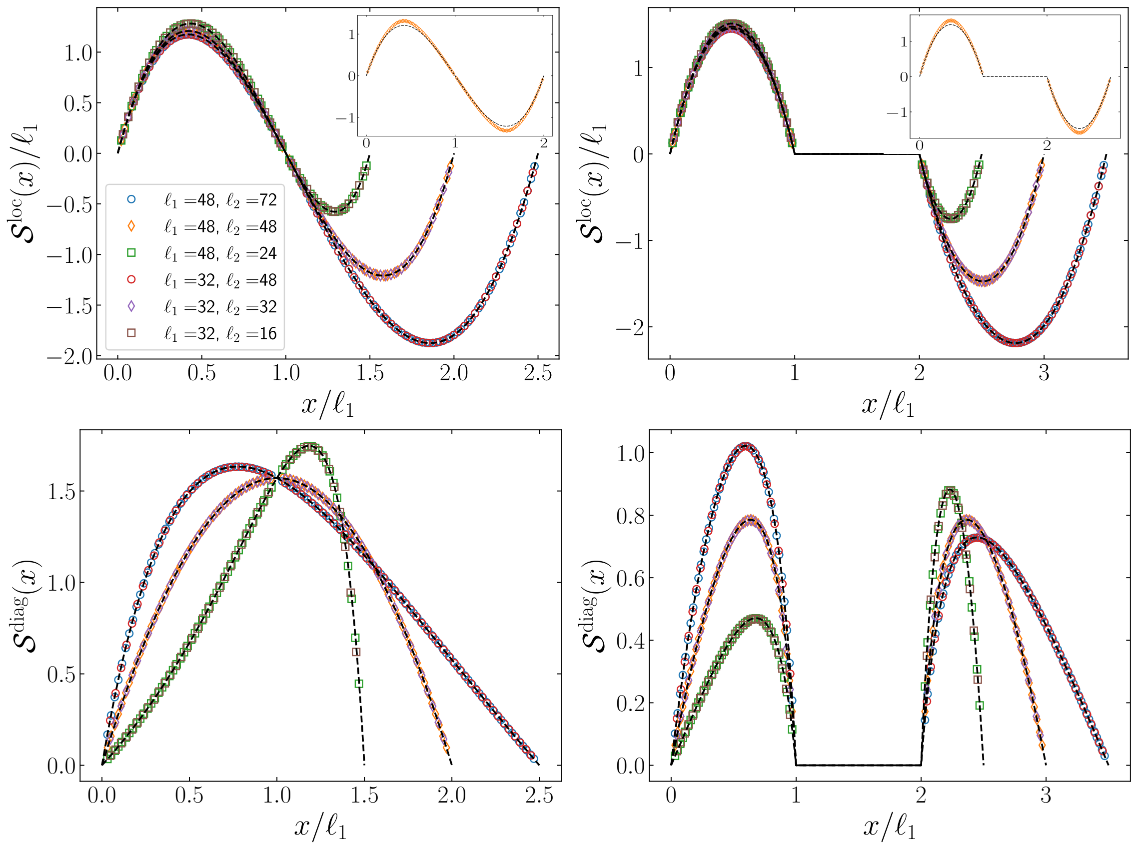

Figure 2.4: Benchmark of the analytical prediction for the negativity Hamiltonian of adjacent (left panels) and disjoint (right panels) blocks in the infinite chain for a Dirac fermion. We consider a subsystem $A = A_1 \cup A_2$, with $A_1 = [1, \ell_1] \cup A_2 = [\ell_1 + d, \ell_1 + \ell_2]$, where $d = 1, \ell_1$ on the left and right panels, respectively, for different length ratios $\ell_2/\ell_1 = 1.5, 1, 0.5$. In the top panels, the symbols are obtained from (2.117) while the dashed lines correspond to (2.92), rescaled by ℓ_1 in order to show the collapse for different sizes. The insets show that considering only the nearest neighbours does not provide a perfect agreement away from the entangling points. In the bottom panels, the symbols are obtained from (2.123) while the dashed line corresponds to the weight function in the bi-local term in (2.91).

limit of the diagonal blocks in Eq. (2.117), in the top panels we find that the sum $\mathcal{S}^{\rm loc}$ over the higher hoppings is in perfect agreement with the field-theoretical entanglement temperature (2.92), even away from the entangling points. We recall that in Ref. [81] only the nearest neighbour negativity Hamiltonian has been considered; hence this accurate test of the continuum limit, which involves also long-range hoppings, appeared for the first time in Ref. [84], on which this Chapter is based.

Regarding the non-local term of the negativity Hamiltonian, in Ref. [81] the numerical calculation of the bi-local weight function was limited to the simple case in which the two intervals have the same length and the main contribution to the bi-local term of Eq. (2.91) comes from the antidiagonal elements of η. However, for arbitrary lengths of the two intervals, it is even more difficult to select the matrix elements corresponding to the bi-local term and, as a consequence, a proper continuum limit is necessary to recover the field theory results. In the bottom left (bottom right) panel of Fig. 2.4, we compare $\mathcal{S}^{\rm diag}$ in Eq. (2.124) for adjacent (non-adjacent) intervals and different ratios of their lengths with the field-theoretical weight function $\beta^R_{\rm loc}(\tilde{x}^R)/(x-\tilde{x}^R)$ occurring in the bi-local term of the negativity Hamiltonian in Eq. (2.91). In all cases perfect agreement is obtained between the field theory expression (2.91) and the numerical results.

2.4.3 Continuum limit in the presence of a boundary

In the following we discuss how the continuum limit procedure described above is modified in the presence of a boundary. In Sec. 2.4.3 we review the case of the entanglement Hamiltonian of one interval considered in Ref. [134]. Then we apply this continuum limit procedure to the subsystem made by two intervals with the first one adjacent to the boundary (see Sec. 2.2.3 and Sec. 2.3.1), in order to recover numerically the weight functions occurring in the entanglement Hamiltonian (Sec. 2.4.3) and in the negativity Hamiltonian associated to the partial transposition of the second interval (Sec. 2.4.3).

Entanglement Hamiltonian: single interval

In order to describe the ingredients needed to benchmark the theoretical predictions of this manuscript, let us briefly review the result of Ref. [134], where the proper continuum limit of the lattice entanglement Hamiltonian for one single interval $A=[b,c]$ in the presence of the boundary has been studied. In this case the lattice entanglement Hamiltonian h consists of one single block and the corresponding field theoretical prediction in Eq. (2.66) is the sum of two terms: a local one proportional to the stress-energy tensor (2.37) and a bi-local one proportional to the operator $T^{\rm bl}_{\rm mix}$ in (2.51) that mixes fields with different chiralities. For simplicity, we will restrict ourselves to the half-filling case we will consider in the numerics.

As for the local part of the entanglement Hamiltonian, in Ref. [134] it has been found that the combination of the matrix elements of h to consider is

$$\mathcal{S}^{\rm loc}(x) \equiv -2s\sum_r r\,(-1)^{(r-1)/2} h_{i,i+r}\,, \tag{2.125}$$

which differs from Eq. (2.117) only up to higher order terms in the lattice spacing and may introduce slight deviations, as discussed in [135] for the harmonic chain.

For the continuum limit of the bi-local term, as discussed in Ref. [134], the correlator (2.101) for OBC corresponds to the vector phase condition (2.10) with scattering phase

$\alpha = \pi$, that is

$$\psi_R(x=0) = -\,\psi_L(x=0). \tag{2.126}$$

Therefore, using in Eq. (2.120) the bi-local operator in the vector phase of Eq. (2.66) and replacing this result in the expression of the lattice entanglement Hamiltonian (2.102), we obtain in the continuum limit (dropping the contributions that vanish at half-filling)

$$\begin{split}\frac{1}{2\pi}\sum_{i,j} c_i^\dagger h_{i,j} c_j \sim \frac{1}{2\pi}\int_A \mathrm{d}x\, \mathcal{S}^{\mathrm{loc}}(x)\, T_{00}(x) \\ + \frac{1}{2\pi}\int_A \mathrm{d}x\, \mathcal{S}^{\mathrm{mix}}(x)\, T^{\mathrm{bl}}_{\text{mix, vec}}(x,-\tilde{x},0;\alpha=\pi), \quad \text{with } -\tilde{x} = \frac{bc}{x},\end{split} \tag{2.127}$$

where $\mathcal{S}^{\mathrm{loc}}$ is given by Eq. (2.125) and we have introduced the sum over the columns of the matrix h

$$\mathcal{S}^{\mathrm{mix}}(x) \equiv \sum_j (-1)^{(i+j-1)/2} h_{i,j}. \tag{2.128}$$

For different boundary conditions, this expression takes a different form, as discussed in Ref. [134].

An important complication due to the presence of a boundary is that the non-diagonal bi-local operator and the local one are superimposed, making it difficult to distinguish their different weight functions. A solution to this problem was proposed in Ref. [134] by observing that, from Eqs. (2.117) and (2.128), the matrix elements $h_{i,j}$ contributing to the two weight functions have distinct oscillating phases that cannot be compensated at the same time. This allows us to isolate, for example, the local term by averaging the i-th term with its nearest neighbours as

$$\widetilde{\mathcal{S}}^{\mathrm{loc}}(i) = \frac{1}{4}\,\mathcal{S}^{\mathrm{loc}}(i-1) + \frac{1}{2}\,\mathcal{S}^{\mathrm{loc}}(i) + \frac{1}{4}\,\mathcal{S}^{\mathrm{loc}}(i+1), \tag{2.129}$$

because the unwanted contribution is an alternating function eliminated through such average. A similar strategy can be applied for $\mathcal{S}^{\mathrm{mix}}$. In Ref. [134], by using the average in Eq. (2.129) and the one corresponding to $\mathcal{S}^{\mathrm{mix}}$, it was checked numerically that the weight functions in the field-theoretical entanglement Hamiltonian (2.66) are obtained in the continuum limit.

Entanglement Hamiltonian: two intervals

Consider the subsystem A given by the union of two disjoint intervals in the semi-infinite chain. The corresponding entanglement Hamiltonian matrix h which has the block structure of Eq. (2.110), is visualised in Fig. 2.5 for the special case where the lengths of the intervals and their distance take the same value. The dashed lines display the position of the conjugate points. For the sake of simplicity, we focus on the case where the first interval is adjacent

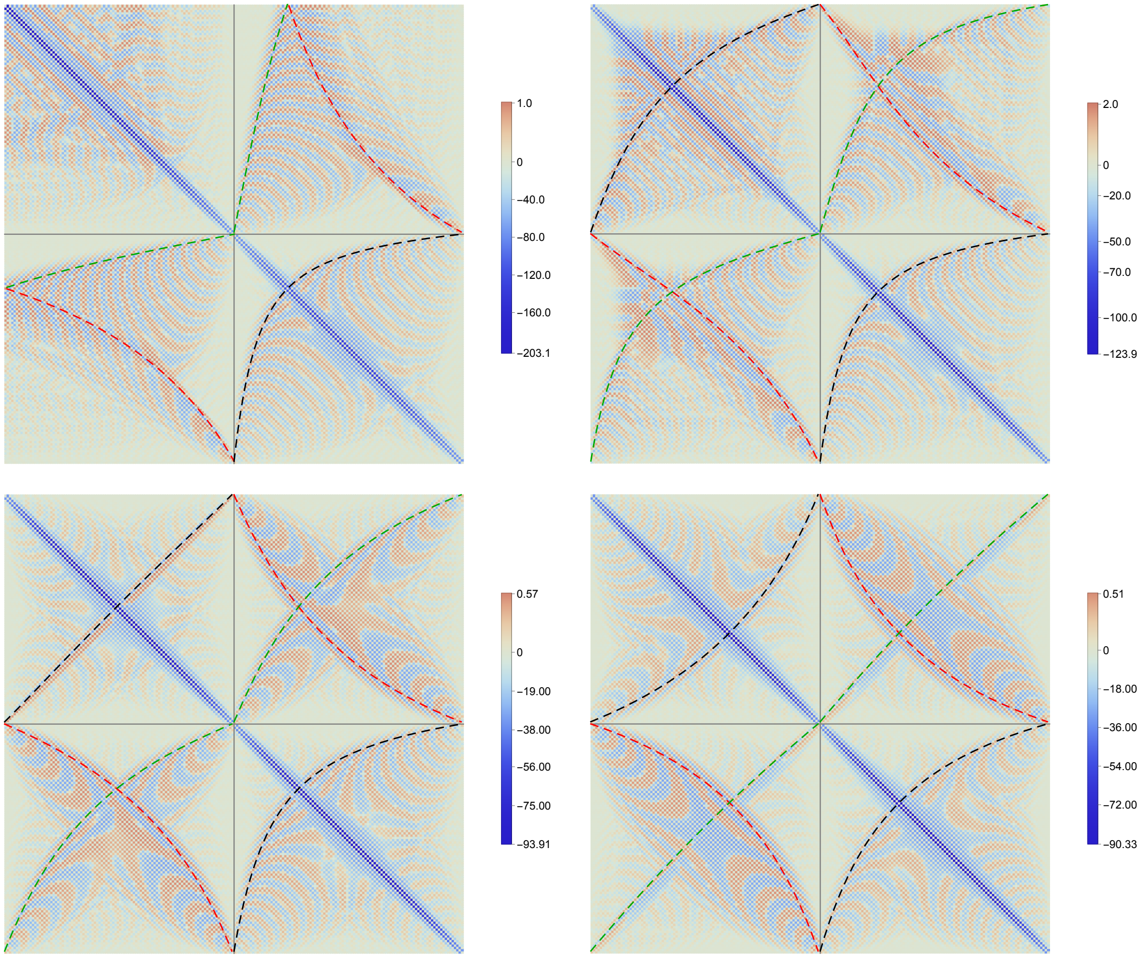

Figure 2.5: Matrix elements of the entanglement Hamiltonian matrix h for two disjoint intervals in the semi-infinite chain with OBC, made by $\ell_1 = \ell_2 = 100$ consecutive sites and separated by 100 consecutive sites. The distance between the boundary and the first interval is given by 0 (top left), 10 (top right), 100 (bottom left) and 1000 (bottom right) consecutive sites. The dashed lines correspond to the conjugate points (see Fig. 2.1).

to the boundary, namely $A = [0, a] \cup [b, c]$ (top left panel in Fig. 2.5). The corresponding field-theoretical results for the entanglement Hamiltonian are reported in Sec. 2.2.3.

In Fig. 2.6 we show numerical results about the local term, which corresponds to the blocks $h^{(1,1)}$ and $h^{(2,2)}$ (see Eq. (2.110)). The continuum limit is performed by employing Eq. (2.125) for the interval $[0, a]$ and Eq. (2.117) for $[b, c]$, both combined with the average over the neighbours as in Eq. (2.129). Different ratios $\ell_2/\ell_1 = 0.5, 1, 1.5$ are considered, where $\ell_1 = a, \ell_2 = c - b$ are the lengths of the two intervals, keeping the distance between

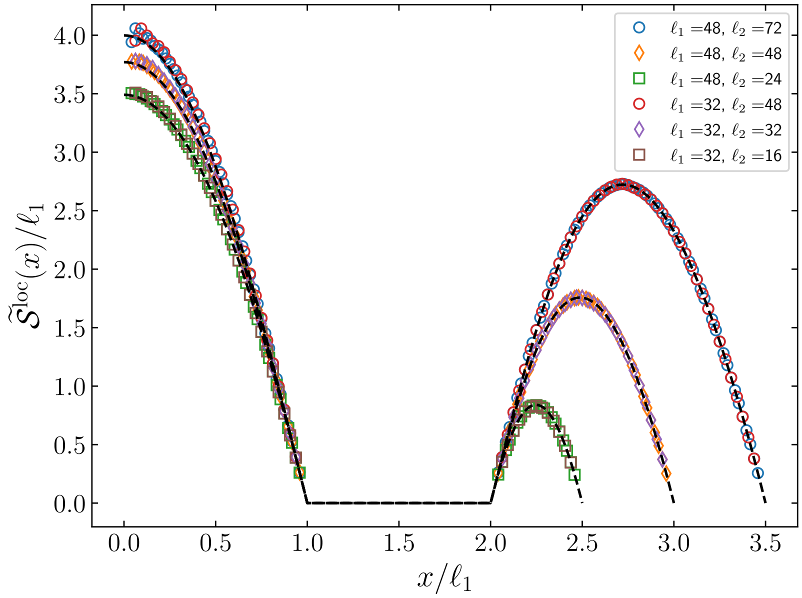

Figure 2.6: Local effective temperature of the entanglement Hamiltonian for the union of two disjoint intervals $A = [1, \ell_1] \cup [2\ell_1 + 1, 2\ell_1 + \ell_2]$ in the semi-infinite chain with OBC, for different values of the ratio $\ell_2/\ell_1 = 0.5, 1, 1.5$. The dashed line corresponds to the CFT prediction (2.57). The numerical data (symbols) are obtained by using (2.125) for the first interval and (2.117) for the second one by averaging over the neighbouring sites according to (2.129).

them $b - a$ fixed and equal to ℓ_1. The data are rescaled by ℓ_1 in order to show a collapse for different sizes. Perfect agreement with the field-theoretical entanglement temperature of Eq. (2.57) is obtained.

As for the bi-local terms, the entanglement Hamiltonian (2.61) contains the bi-local operator diagonal in the fermionic chiralities and also the one that mixes the fermionic chiralities, which are evaluated in different conjugate points obtained from $\tilde{x}_+$ and $\tilde{x}_-$ reported in Eq. (2.58). To understand how these two bi-local terms appear from the continuum limit of K_A, let us focus on the block $h^{(1,2)}$ as an example. Its continuum limit should produce bi-local terms in which the integration variable x is in $[0, a]$ and the conjugate point is in $[b, c]$. Identifying which terms appear in the limit of $h^{(1,2)}$ can therefore be done by selecting the conjugate points that map the first interval into the second. From the mappings in Eq. (2.60) (see also Fig. 2.3), we see that $\tilde{x}_+([0, a])$ is a subset of $[b, c]$ and, as a consequence, the bi-local diagonal continuum limit (2.123) with $h^{(1,2)}$ is proportional to the bi-local diagonal operator $T^{\rm bl}_{\rm diag}$ of Eq. (2.38) calculated in $\tilde{x}_+$. On the other hand, from Eq. (2.60) we see that $\tilde{x}_-([0, a])$ is a subset of the reflection of $[b, c]$ with respect to the boundary. Due to the presence of the boundary, these points are reflected (see Fig. 2.3) and therefore the bi-local mixed limit (2.128) for the block $h^{(1,2)}$ is proportional to the bi-local

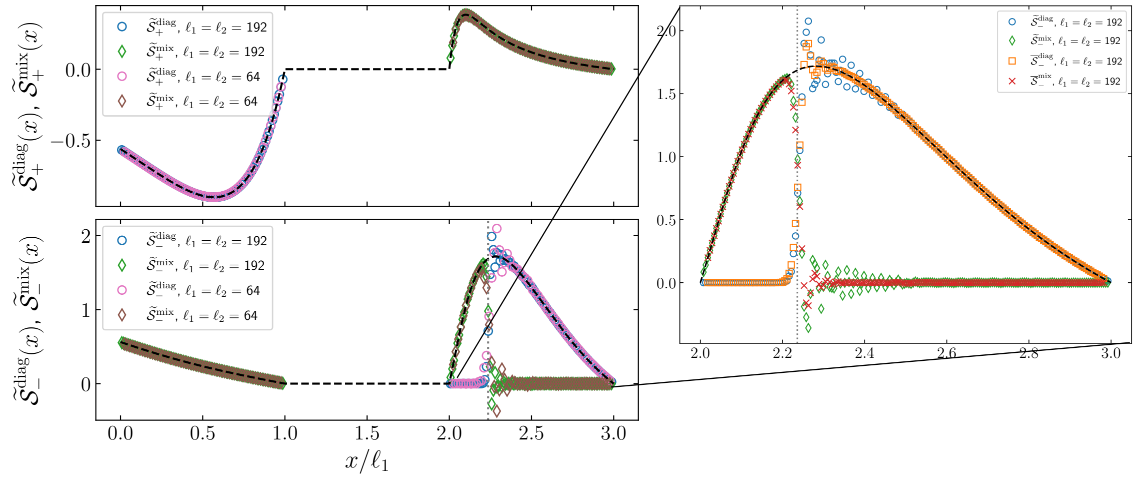

Figure 2.7: Scaling of the bi-local weights of the entanglement Hamiltonian as a function of x/ℓ_1 for the geometry $A=[1,\ell_1]\cup[2\ell_1+1,3\ell_1]$ in the presence of a boundary at $x=0$, with $\ell_1=64,192$. The top (bottom) panel shows the bi-local weight function relative to $\tilde{x}_+$ ($\tilde{x}_-$), while the different colours distinguish between the non-diagonal and diagonal operators according to the legend. The green/brown (blue/pink) symbols have been obtained by applying (2.129) to (2.128) ((2.123)). The dotted grey line indicates the self-conjugate point $x_{S,2}$ in (2.59), while the dashed ones represent the field theory prediction in (2.61). The zoom focuses on the oscillating terms around $x=x_{S,2}$, showing that a more refined averaging procedure (see Eq. (2.132)) suppresses them.

mixed operator $T^{\rm bl}_{\rm mix}$ of Eq. (2.51) evaluated in $-\tilde{x}_-$. Similar considerations can be applied to the other matrix blocks, and we finally identify that the continuum limits proportional to operators calculated in $\tilde{x}_+$ are

$$
\begin{aligned}
\mathcal{S}_+^{\rm diag}(x) &= \sum_j (-1)^{(j-i-1)/2} h_{i,j}^{(1,2)}, \qquad x\in[0,a]\,,\\
\mathcal{S}_+^{\rm mix}(x) &= \sum_j (-1)^{(i+j-1)/2} h_{i,j}^{(2,2)}, \qquad x\in[b,c]\,,
\end{aligned}
\tag{2.130}
$$

while those proportional to operators calculated in $\tilde{x}_-$

$$
\begin{aligned}
\mathcal{S}_-^{\rm diag}(x) &= \sum_j (-1)^{(j-i-1)/2} h_{i,j}^{(2,1)}, \qquad x\in[b,c]\,,\\
\mathcal{S}_-^{\rm mix}(x) &= \begin{cases} \sum_j (-1)^{(i+j-1)/2} h_{i,j}^{(1,2)}, & x\in[0,a]\\ \sum_j (-1)^{(i+j-1)/2} h_{i,j}^{(2,1)}, & x\in[b,c]\,. \end{cases}
\end{aligned}
\tag{2.131}
$$

In Fig. 2.7 we compare the two different limits (2.130) and (2.131) with the predicted bi-local weights $\beta_{\text{loc}}^{\text{sym}}(\tilde{x}_\pm)/(x-\tilde{x}_\pm)$ in Eq. (2.61) for intervals of equal length $\ell_1 = \ell_2 = 64$ and $\ell_1 = \ell_2 = 192$, showing their collapse for different system sizes. In the top panel, we consider the bi-local weight of the operators calculated in $\tilde{x}_+$, where the continuum limit is given by Eq. (2.130) combined with the average in Eq. (2.129). Both the diagonal part and the mixed one converge to the field-theoretical result of Eq. (2.61): the former to the prefactor of $T^{\text{bl}}_{\text{diag}}(x, \tilde{x}_+, 0)$, the latter to the prefactor of $T^{\text{bl}}_{\text{mix, vec}}(x, -\tilde{x}_+, 0; \pi)$.

In the bottom panel of the same figure, we repeat a similar analysis for the bi-local weight of the operators calculated in $\tilde{x}_-$, whose continuum limit is given by Eq. (2.131) with the average in Eq. (2.129) adapted to this quantity. We find also in this case a good agreement with the prefactor of $T^{\text{bl}}_{\text{diag}}(x, \tilde{x}_-, 0)$ (blue/pink) and of $T^{\text{bl}}_{\text{mix, vec}}(x, -\tilde{x}_+, 0; \pi)$ (green/brown) in our prediction in Eq. (2.61). Moreover, in the second interval, we observe a cross-over between the non-diagonal operator and the diagonal one, in correspondence of the point $x_{S,2}$ in Eq. (2.59) (dotted grey line), confirming what we found in Eq. (2.61). We remind that $x_{S,2}$ is a self-conjugate point, i.e. one of the zeroes of the function z_{sym}, which for the subsystem A under consideration is given by Eq. (2.56).

We can now explain the mechanism of this cross-over on the lattice. From the expression of $\mathcal{S}_-^{\text{mix}}(x)$ in Eq. (2.131), when $x \in [b, c]$, the phase of the matrix element $h_{i,j}$ is a smooth function for $x < x_{S,2}$ while it is strongly oscillating for $x > x_{S,2}$. The opposite happens for $\mathcal{S}_-^{\text{diag}}(x)$. The goal of the averaging procedure of Eq. (2.129) is precisely to eliminate the strongly oscillating contributions and therefore it makes possible to clearly see the cross-over. However, as we can see from Fig. 2.7, this averaging is not sufficient to completely remove the oscillations at the cross-over point, which moreover appear to be independent of the size of the subsystem. In the zoom of Fig. 2.7, we show that an additional averaging procedure which extends up to the next-to-nearest neighbours (i.e. not only nearest neighbours as in Eq. (2.129)) is sufficient to eliminate these residual oscillations. It is given by

$$\overline{S}_-^{\text{diag}}(i) \equiv \frac{1}{6}\widetilde{\mathcal{S}}_-^{\text{diag}}(i-2)+\frac{1}{6}\widetilde{\mathcal{S}}_-^{\text{diag}}(i-1)+\frac{1}{3}\widetilde{\mathcal{S}}_-^{\text{diag}}(i)+\frac{1}{6}\widetilde{\mathcal{S}}_-^{\text{diag}}(i+1)+\frac{1}{6}\widetilde{\mathcal{S}}_-^{\text{diag}}(i+2)\,, \quad (2.132)$$

(where $\widetilde{\mathcal{S}}_-^{\text{diag}}(i)$ is defined by the combination (2.129) with $\mathcal{S}_-^{\text{diag}}(i)$ instead of $\mathcal{S}_-^{\text{loc}}(i)$) and by the same combination for $\overline{S}_-^{\text{mix}}(i)$. As anticipated, the zoom of Fig. 2.7 shows that using (2.132), i.e. red and orange symbols, the oscillations are suppressed with respect to ones obtained through (2.129), i.e. green and blue symbols.

Negativity Hamiltonian

As we discussed in Sec. 2.4.2, also in the presence of the boundary the derivation of the continuum limit from the lattice negativity Hamiltonian is almost unmodified. Again, the only difference comes from the imaginary factors due to the partial time-reversal operation. For $A = [0, a] \cup [b, c]$, the appropriate factors can be read from the field-theoretical result

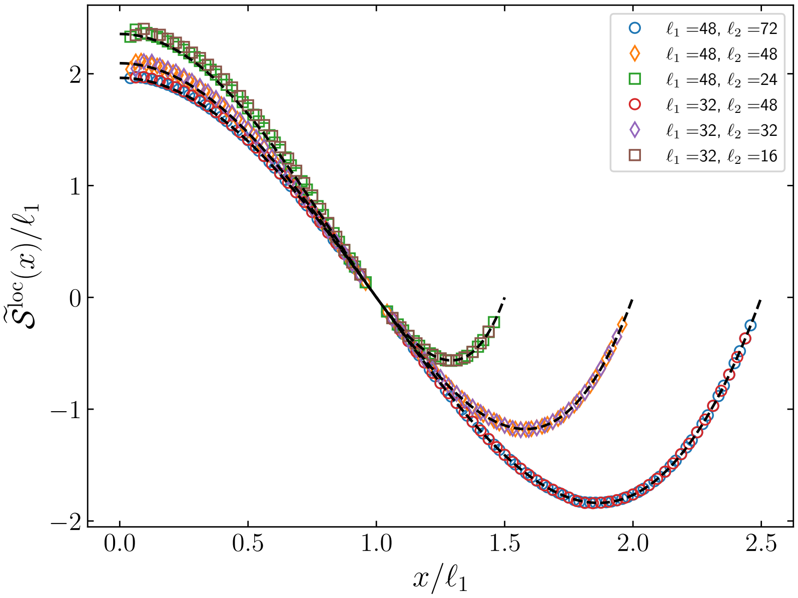

Figure 2.8: Inverse effective temperature of the negativity Hamiltonian, rescaled with ℓ_1 as a function of x/ℓ_1. The geometry we consider is $A = [1, \ell_1] \cup [\ell_1 + 1, \ell_1 + \ell_2]$ for different values of the ratio $\ell_1/\ell_2 = 0.5, 1, 1.5$ and with a boundary at $x = 0$. The data points are obtained by applying (2.129) to (2.125) for the first interval and to (2.117) for the second one. The dashed curves correspond to the CFT expression (2.95).

in Eq. (2.97). By properly modifying Eqs. (2.130) and (2.131) to take into account the transposition of the second interval, we find for the bi-local term calculated in $\tilde{x}^R_+$

$$\mathcal{S}^{\mathrm{diag}}_+(x) = \begin{cases} \mathrm{i}\sum_j (-1)^{(j-i-1)/2}\eta^{(1,2)}_{i,j}, & x \in [0, a] \\ -\mathrm{i}\sum_j (-1)^{(j-i-1)/2}\eta^{(2,1)}_{i,j}, & x \in [b, c]\,, \end{cases} \tag{2.133}$$

$$\mathcal{S}^{\mathrm{mix}}_+(x) = -\mathrm{i}\sum_j (-1)^{(i+j-1)/2}\eta^{(2,1)}_{i,j}, \qquad x \in [b, c]\,,$$

while for the one in $\tilde{x}^R_-$

$$\mathcal{S}^{\mathrm{mix}}_-(x) = \begin{cases} \mathrm{i}\sum_j (-1)^{(i+j-1)/2}\eta^{(1,2)}_{i,j}, & x \in [0, a] \\ \sum_j (-1)^{(i+j-1)/2}\eta^{(2,2)}_{i,j}, & x \in [b, c]\,. \end{cases} \tag{2.134}$$

We can now test our predictions for the negativity Hamiltonian in Eq. (2.97). Choosing $a = b = \ell_1, c = \ell_1 + \ell_2$, in Fig. 2.8, we use the continuum limit in Eq. (2.125) for the first interval adjacent to the boundary and Eq. (2.117) for the second one, together with the

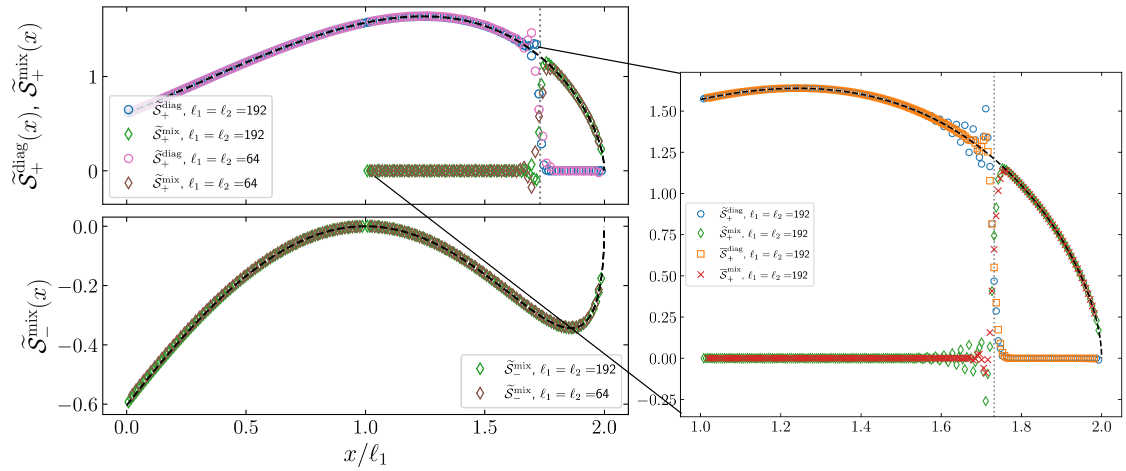

Figure 2.9: Weight functions of the bi-local terms in the negativity Hamiltonian as a function of x/ℓ_1 for the geometry $A = [1, \ell_1] \cup [\ell_1 + 1, 2\ell_1]$ in the presence of a boundary at $x = 0$ (see (2.97)) for $\ell_1 = 64$ and $\ell_1 = 192$. The bi-local weight functions for $\tilde{x}_+$ (top panel) and $\tilde{x}_-$ (bottom panel) are shown. The green/brown and blue/pink colours distinguish between the non-diagonal and diagonal operators respectively, by applying (2.129) to (2.133) and (2.134). The vertical dotted grey line indicates the self-conjugate point $x^R_{S,2}$ (see the text below (2.95)). The dashed curves correspond to the field-theoretical prediction (2.97) for the weight function of the bi-local terms. The zoom shows the suppression of the oscillations around $x = x^R_{S,2}$ using the more refined averaging procedure reported in (2.132).

average in Eq. (2.129). For all the different length ratios $\ell_2/\ell_1 = 0.5, 1, 1.5$, we find good agreement with the analytical prediction for $\beta^{R\,\rm sym}_{\rm loc}(x)$ in Eq. (2.95). The small discrepancy in the first interval can again be attributed to the effects of the sum along rows rather than along antidiagonals.

In Fig. 2.9 we benchmark the bi-local term of the negativity Hamiltonian with $\ell_2 = \ell_1$. In the top panel, we compare the continuum limit in Eq. (2.133) with $\beta^{R\,\rm sym}_{\rm loc}(\tilde{x}^R_+)/(x - \tilde{x}^R_+)$ in Eq. (2.97). The green/brown (blue/pink) symbols agree with the weight function that multiplies the operator $T^{\rm bl}_{\rm mix,\ vec}(x, -\tilde{x}^R_+, 0; \pi)$ ($T^{\rm bl}_{\rm diag}(x, \tilde{x}^R_+, 0)$). We also observe the cross-over between the diagonal and the non-diagonal operators in correspondence of the self-conjugate point $x^R_{S,2} = \sqrt{ca + bc - ab}$ (dotted grey line) (see discussion below Eq. (2.95)). The zoom shows also here that the use of the additional average (2.132) suppresses the oscillations around $x^R_{S,2}$ with respect to (2.129). Finally, in the bottom panel we compare the continuum limit in Eq. (2.134) with $\beta^{R\,\rm sym}_{\rm loc}(\tilde{x}^R_-)/(x - \tilde{x}^R_-)$ in Eq. (2.97), finding again good agreement.

2.5 Final remarks

In this Chapter, we have studied the entanglement Hamiltonian of a multi-interval subsystem A of a massless Dirac fermion on the half-line, generalising the result for the single interval found in Ref. [89]. The boundary condition can be implemented in two different ways, either preserving the charge (in the vector phase) or the helicity (axial phase). Interestingly, while the entanglement entropy of this geometry is identical in the two phases, the entanglement Hamiltonian distinguishes between them. The entanglement Hamiltonians can be written as a sum of a local operator proportional to the stress-energy tensor and a bi-local one, which mixes the two chiral components of the Dirac field with a non-trivial dependence on the phase (see Eqs. (2.52) and (2.53)). The latter operator is different for the two phases. We have worked out explicitly the case $A = [0, a] \cup [b, c]$, i.e. two intervals with one adjacent to the boundary, from which we have recovered some well know limits as a consistency check.

The multipartite geometry offers also an ideal setting to compute the negativity Hamiltonian for free fermions introduced in Ref. [81]. This is defined as the logarithm of the partially transposed reduced density matrix and represents an operatorial characterisation of entanglement in mixed states. After providing a construction scheme for a generic number of transposed intervals in the presence of a boundary, we focus on a tripartite geometry $[0, a] \cup [b, c]$, for which we report an explicit expression in Eq. (2.97).

We have also performed comparisons between our analytical predictions and the exact numerical computations in a free fermion chain by adapting the method discussed in Refs. [133–135] for other cases. As for the local part of the entanglement and negativity Hamiltonian, the field theoretical results are obtained through a proper continuum limit, which includes also the long-range hopping terms (see Figs. 2.6 and 2.8). The weight function of the bi-local terms is recovered by a proper sum of the matrix elements multiplied by an oscillatory factor (see Figs. 2.7 and 2.9). In both cases, the numerical results show a perfect agreement with field theory.

There are a number of generalisations of the results presented here that are worth mentioning as outlooks. The first obvious one would be to investigate what happens on the lattice for a generic boundary condition as recently done for one interval in Ref. [134]. Another generalisation concerns the calculation of the entanglement and negativity Hamiltonians in the presence of slowly varying inhomogeneities, resulting, e.g. from external trapping potential or inhomogeneous initial states out of equilibrium. In this setting the CFT approach in curved space [85] can be used to describe universal quantities and it has been already employed for some entanglement Hamiltonians [140] (an explicit example of this will be discussed in Chapter 6, based on Ref. [141]). An open problem is also the determination of entanglement and negativity Hamiltonians in the presence of a point-like defect which allows both reflection and transmission (a boundary condition is a purely reflective defect); the results for a single interval appeared already in Ref. [96]. Finally, another natural question is what happens in higher dimensional boundary systems and how to recover the continuum limit from the lattice (as in Ref. [137] for the bulk case).

Chapter 3

Finite temperature negativity Hamiltonians of the massless Dirac fermion

In the previous Chapter, we worked out explicitly the negativity Hamiltonian (see Eq. (1.23) and accompanying discussion) for the case of two intervals in the presence of a boundary. Another example of negativity Hamiltonian was presented in the earlier work [81], which considered two intervals on the plane, i.e., without boundaries. Both these results considers tripartite configurations of a pure state, but not a truly global mixed state. In this Chapter, based on Ref. [131], we fill this gap by computing the negativity Hamiltonian of several disjoint intervals at finite temperature in the massless Dirac CFT, both on a finite size system and on the infinite line. This was the first example of negativity Hamiltonian of a mixed state ever appeared in the literature.

3.1 Finite temperature entanglement Hamiltonian

In order to derive the expression of the negativity Hamiltonian, we use the construction introduced in Ref. [81] (reviewed in Sec. 2.3 of Chapter 2), where it was argued that the effect of the partial transposition amounts to exchange the extrema of the transposed interval in the expression of the entanglement Hamiltonian, taking into account that the fermionic field picks up an imaginary phase if it belongs to the transposed interval. Since this computation requires the knowledge of the entanglement Hamiltonian in the same geometry, in this section we present the known results for the finite temperature entanglement Hamiltonian of the free massless Dirac fermion in a multi-component region A, underlying the major differences with respect to the ground state presented in Sec. 2.2.1 of Chapter 2.

3.1.1 Entanglement Hamiltonian on the torus

Let us consider a free massless Dirac fermion on a circle of circumference L at finite temperature $1/\beta$, i.e., on a torus. In the imaginary time direction we impose anti-periodic (also called Neveu-Schwarz) boundary conditions, while in the spatial direction we choose either anti-periodic or periodic (Ramond) ones. Then, in a subsystem $A = [a_1, b_1] \cup \ldots \cup [a_n, b_n]$ composed of n intervals, the entanglement Hamiltonian is [142–144]

$$\begin{aligned} K_A(\beta, L) &= K_A^{\mathrm{loc}}(\beta, L) + K_A^{\mathrm{nl}}(\beta, L) \\ &= \int_A \mathrm{d}x\, \beta_{\mathrm{loc}}(x; \beta, L)\, T_{00}(x) + \sum_{(p,k)\neq(0,0)} (\pm 1)^k \int_A \mathrm{d}x\, \frac{\beta_{\mathrm{loc}}(\tilde{x}_{kp}; \beta, L)}{\frac{\beta}{\pi}\sinh\left[\frac{\pi}{\beta}\left(x - \tilde{x}_{kp} + kL\right)\right]}\, T^{\mathrm{bl}}(x, \tilde{x}_{kp}, t = 0)\,, \end{aligned} \tag{3.1}$$

where the signs $+$ and $-$ correspond, respectively, to the Ramond and Neveu-Schwarz sectors, $p \in \{0, \ldots, n-1\}, k \in \mathbb{Z}$. The Hamiltonian (3.1) presents a local part, $K_A^{\mathrm{loc}}(\beta, L)$, proportional to the energy density T_{00} (reported in Eq. (2.37) in Chapter 2) with a weight given by the local entanglement temperature $\beta_{\mathrm{loc}}(x) = 1/z'(x)$, where [142–144]

$$\begin{aligned} z(x; \beta, L) &= \log\left[-\prod_{i=1}^{n} \frac{\vartheta_1\left(\frac{\pi}{L}\left(x - a_i\right)|q\right)}{\vartheta_1\left(\frac{\pi}{L}\left(x - b_i\right)|q\right)}\right] + \frac{2\pi\ell}{\beta L}x \\ &= \log\left[-\prod_{i=1}^{n} \frac{\sigma(x - a_i)}{\sigma(x - b_i)}\right] - \frac{2\ell}{\mathrm{i}\beta}\zeta(\mathrm{i}\beta/2)\, x + \mathrm{const.} \end{aligned} \tag{3.2}$$

Here, $\ell = \sum_i b_i - a_i$ is the total length of the subsystem A and the additive constant term is only a shift which does not depend on x and, therefore, does not affect the expression for $\beta_{\mathrm{loc}}(x)$, that we report explicitly

$$\begin{aligned} \beta_{\mathrm{loc}}(x) &= \left[\frac{\pi}{L}\sum_{i=1}^{n}\left[\frac{\vartheta_1'\left(\frac{\pi}{L}\left(x - a_i\right)|q\right)}{\vartheta_1\left(\frac{\pi}{L}\left(x - a_i\right)|q\right)} - \frac{\vartheta_1'\left(\frac{\pi}{L}\left(x - b_i\right)|q\right)}{\vartheta_1\left(\frac{\pi}{L}\left(x - b_i\right)|q\right)}\right] + \frac{2\pi\ell}{\beta L}\right]^{-1} \\ &= \left[\sum_{i=1}^{n}\left(\zeta(x - a_i) - \zeta(x - b_i)\right) - \frac{2\ell}{\mathrm{i}\beta}\zeta(\mathrm{i}\beta/2)\right]^{-1}. \end{aligned} \tag{3.3}$$

In Eqs. (3.2) and (3.3), σ and ζ denote respectively Weierstrass' sigma and zeta functions and ϑ_1 is the Jacobi's elliptic theta function with nome $q = e^{\mathrm{i}\pi\tau}, \tau = \mathrm{i}\beta/L$ (see Sec. 3.B for their definitions). In particular, the expression in the first row of Eq. (3.2) is the result obtained in Ref. [142] while the one in the second row follows the conventions of Refs. [143, 144]. While it is not obvious that the two alternative expressions coincide, one can show they are identical by using the properties of Weierstrass functions reported in Sec. 3.B. In the rest of this Chapter we will adopt the conventions of Ref. [142] in terms of elliptic theta functions.

Regarding the non-local part $K_A^{\rm nl}(\beta, L)$ of Eq. (3.1), even in the case of one interval, this contains infinite terms proportional to the bi-local operator $T^{\rm bl}(x, y, t)$ [87] that we report in Eq. (2.48). Since in this Chapter we only consider the case without boundaries and the operator will always be diagonal in the chiral fermions, to ease the notation in the following we will drop the suffix "diag". As was the case for the EH on the plane in Eq. (2.36), the bi-local operator in (3.1) couples one point x with a single other conjugate point $\tilde{x}_{kp}$, given by the non-trivial solutions of the equations [142–144]

$$z(x; \beta, L) - z(\tilde{x}_{kp}; \beta, L) + \frac{2\pi k\ell}{\beta} = 0\,, \quad k \in \mathbb{Z}\,, \tag{3.4}$$

indexed by the integer k, which is the analogue of Eq. (2.26). One can see that for every fixed index k, Eq. (3.4) admits n solutions, indexed by $p = 0, \ldots, n-1$, each belonging to a different interval. In the following, we will use the index $p = 0$ to denote the solution of Eq. (3.4) such that $\tilde{x}_{k0}$ belongs to the same interval as x. With this convention, we see that for $k = 0$ Eq. (3.4) presents the trivial solution $y = \tilde{x}_{00} = x$, which does not contribute to the non-local part $K_A^{\rm nl}(\beta, L)$ (see Eq. (3.1)).

It is instructive to compare the entanglement Hamiltonian on the torus (3.1) with the one on the plane (2.36), i.e, of n intervals on the infinite line at zero temperature, that we reviewed in Sec. 2.2.1 of Chapter 2. The local part of Eq. (2.36) is in form analogous to the one of Eq. (3.1), with entanglement temperature $\beta_{\rm loc}(x) = 1/z'(x)$ equal to the inverse of the derivative of the function in Eq. (2.20). The main qualitative difference of the Hamiltonian (3.1) on the toric space-time with respect to Eq. (2.36) is the structure of the non-local part $K_A^{\rm nl}$. While on the plane the bi-local part $K_A^{\rm bl}$ in Eq. (2.36) only contains $n-1$ terms, now in Eq. (3.1) the the non-local part contains infinite terms, indexed by the integer k in Eq. (3.4). This is even more striking in the single interval case, where the entanglement Hamiltonian (1.13) on the plane is completely local since it is conformally equivalent to the Bisognano-Wichmann result (1.12) [31–34, 87], while the one on the torus remains highly non-local. This shows that in general the entanglement Hamiltonian on the torus (3.1) is much more non-local than the analogous configuration on the plane [142–144].

3.1.2 Finite temperature entanglement Hamiltonian on the infinite line

We will now review the known results for the finite temperature entanglement Hamiltonian on the infinite line, i.e., on an infinite cylinder of circumference β in the time direction. In Refs. [142–144], this Hamiltonian was obtained from the result on the torus (3.1) by taking the limit $L \to \infty$. Using the asymptotic expansion of the elliptic theta function ϑ_1 for $q = e^{\mathrm{i}\pi\tau}$, $\tau = \mathrm{i}\beta/L \to 0$ (see Eq. (3.104) of Sec. 3.B) in the expression (3.2) for the function

$z(x;\beta,L)$, we obtain

$$\begin{aligned} z(x;\beta,L) &\longrightarrow \log\left[-\prod_{i=1}^{n}\frac{\sinh\frac{\pi(x-a_i)}{\beta}\,e^{\frac{\pi}{\beta L}(2a_ix-a_i^2)}}{\sinh\frac{\pi(x-b_i)}{\beta}\,e^{\frac{\pi}{\beta L}(2b_ix-b_i^2)}}\right]+\frac{2\pi\ell}{\beta L}x \\ &= z(x;\beta)-\frac{\pi}{\beta L}\sum_{i=1}^{n}\left(2b_ix-2a_ix-b_i^2+a_i^2\right)+\frac{2\pi\ell}{\beta L}x = z(x;\beta)+\text{const}\,, \end{aligned} \tag{3.5}$$

where, using $\ell=\sum_i(b_i-a_i)$, the contributions proportional to x cancel and we have introduced [142–144]

$$z(x;\beta)=\log\left[-\prod_{i=1}^{n}\frac{\sinh\frac{\pi(x-a_i)}{\beta}}{\sinh\frac{\pi(x-b_i)}{\beta}}\right]. \tag{3.6}$$

The local term of Eq. (3.1) becomes proportional to the entanglement temperature [142–144]

$$\beta_{\text{loc}}(x;\beta)=\frac{1}{z'(x;\beta)}=\frac{\beta}{\pi}\left[\sum_{i=1}^{n}\left(\coth\frac{\pi(x-a_i)}{\beta}-\coth\frac{\pi(x-b_i)}{\beta}\right)\right]^{-1}. \tag{3.7}$$

In the non-local component $K_A^{\text{nl}}(\beta,L)$ of Eq. (3.1), instead, we can see that in this limit the denominator $\sinh(\pi(x-\tilde{x}_{kp}+kL)/\beta)$ diverges for all $k\neq 0$ [142–144]. For this reason, the only conjugate points that contribute in this limit are the $n-1$ non-trivial solutions of the equation [142–144]

$$z(x;\beta)=z(\tilde{x}_p;\beta)\,, \tag{3.8}$$

obtained as the limit of Eq. (3.4) with $k=0$. This was expected by the fact that the cylinder can be conformally mapped into the plane, where the entanglement Hamiltonian is written in Eq. (2.36), which only contains $n-1$ bi-local terms.

Putting all together, we find that the finite temperature entanglement Hamiltonian for a multi-component subsystem $A=[a_1,b_1]\cup\ldots\cup[a_n,b_n]$ on the infinite line is [142–144]

$$\begin{aligned} K_A(\beta) &= K_A^{\text{loc}}(\beta)+K_A^{\text{bl}}(\beta) \\ &= \int_A \mathrm{d}x\,\beta_{\text{loc}}(x;\beta)\,T_{00}(x)+\sum_{p=1}^{n-1}\int_A \mathrm{d}x\,\frac{\beta_{\text{loc}}(\tilde{x}_p;\beta)}{\frac{\beta}{\pi}\sinh\frac{\pi(x-\tilde{x}_p)}{\beta}}\,T^{\text{bl}}(x,\tilde{x}_p,t=0)\,, \end{aligned} \tag{3.9}$$

with entanglement temperature $\beta_{\text{loc}}(\tilde{x}_p;\beta)$ given by Eq. (3.7). When specialising to a subsystem A made up of one interval, the entanglement Hamiltonian in Eq. (3.9) is purely local and in agreement with the result of Ref. [33, 34], which reads

$$K_A(\beta)=\int_a^b \mathrm{d}x\,\frac{\beta}{\pi}\left[\coth\frac{\pi(x-a)}{\beta}+\coth\frac{\pi(x-b)}{\beta}\right]^{-1}T_{00}(x). \tag{3.10}$$

As we mentioned earlier, since the cylinder is conformally equivalent to the plane, an alternative derivation of the finite temperature entanglement Hamiltonian on the infinite line in Eqs. (3.6) and (3.9) consists in mapping the expressions (2.36) and (2.20) on the plane to the cylinder. We find it worthwhile to also present this additional derivation as a non-trivial check of the correctness of Eq. (3.9) and because we will adapt a similar trick later in the Chapter. We first present how to map the entanglement Hamiltonian from the plane to a generic geometry and we later specialise this procedure to the cylinder. Let us consider a multi-component subsystem $A = [a_1, b_1] \cup \ldots \cup [a_n, b_n]$ made up of n intervals in a geometry conformally isomorphic to the plane. In order to map it to the plane, it is convenient to switch to imaginary time $w = x + \mathrm{i}t$ and consider, for simplicity, only the holomorphic component. Let then $\xi(w)$ be the transformation from this geometry to the plane, with the subsystem A being mapped on the real line. On the complex plane, the holomorphic part of the entanglement Hamiltonian is given by the analytic continuation of Eq. (2.36)

$$K_A = \int_{\xi(A)} \mathrm{d}\xi \, \frac{T(\xi(w))}{\partial_\xi z(\xi(w))} + \sum_{i=1}^{n} \int_{\xi(A)} \mathrm{d}\xi \, \frac{1}{\xi(w) - \xi(\tilde{w}_p)} \frac{T^{\mathrm{bl}}(\xi(w), \xi(\tilde{w}_p))}{\partial_\xi z(\xi(\tilde{w}_p))} \,, \tag{3.11}$$

where the function $z(w) = z(\xi(w))$ is Eq. (2.20) evaluated in $\xi(w)$, i.e.

$$z(w) = z(\xi(w)) = \log \left[- \prod_{i=1}^{n} \frac{\xi(w) - \xi(a_i)}{\xi(w) - \xi(b_i)} \right] , \tag{3.12}$$

with $\xi(a_i), \xi(b_i)$ the extrema of the mapping $\xi(A)$ of the subsystem A on the plane, and the conjugate points $\tilde{w}_p$ are the solutions of $z(w) = z(\tilde{w}_p)$.

We first consider the mapping of the local part. Despite the fact that the holomorphic stress-energy tensor T is not a primary field, its transformation law only involves an additional function of w proportional to the Schwarzian derivative of $\xi(w)$. When integrated in the entanglement Hamiltonian, this simply gives a constant factor which can be reabsorbed in the overall normalisation and can therefore be neglected. Considering also the Jacobian, the holomorphic part transforms as

$$\begin{aligned} \int_{\xi(A)} \mathrm{d}\xi \, \frac{T(\xi(w))}{\partial_\xi z(\xi(w))} &= \int_A \xi'(w) \, \mathrm{d}w \, \frac{\xi'(w)^{-2} \, T(w)}{\partial_\xi z(\xi(w))} + \mathrm{const} \\ &= \int_A \mathrm{d}w \, \frac{T(w)}{z'(w)} + \mathrm{const} \equiv \int_A \mathrm{d}w \, \beta_{\mathrm{loc}}(w) \, T(w) + \mathrm{const} \,, \end{aligned} \tag{3.13}$$

where we see that in the original geometry the entanglement temperature $\beta_{\mathrm{loc}}(w)$ is given by the inverse of the derivative of Eq. (3.12) with respect to w.

In order to find the transformation of the bi-local part, it is necessary to understand how the bi-local operator in Eq. (2.48) transforms under conformal mappings. In complex

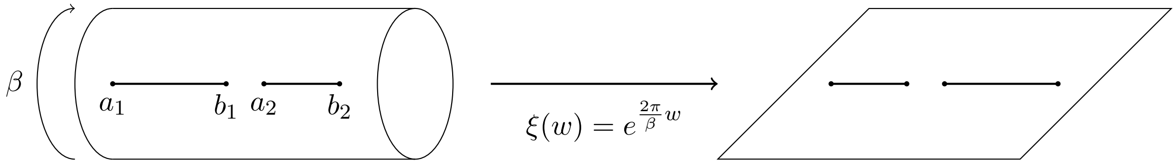

Figure 3.1: Conformal mapping from the infinite cylinder of circumference β described by the coordinate w to the plane, ξ, using the transformation $\xi(w) = e^{\frac{2\pi w}{\beta}}$. The segments $[a_1, b_1], [a_2, b_2]$ are mapped to the branch cuts on the left figure.

coordinates, the holomorphic bi-local operator takes the form

$$T^{\mathrm{bl}}(\xi,\zeta) = \frac{\mathrm{i}}{2} :\!\Big[\psi^\dagger(\xi)\psi(\zeta) - \psi^\dagger(\zeta)\psi(\xi)\Big]\!: . \tag{3.14}$$

Since the fermions $\psi, \psi^\dagger$ are primary fields of conformal dimension $(\frac{1}{2}, 0)$, under the conformal mapping $\xi(z)$ they transform as $\psi(z) = \left(\frac{\partial\xi}{\partial z}\right)^{1/2} \psi(\xi(z))$ (and analogously for the anti-holomorphic part). Replacing this transformation in Eq. (3.14) of the bi-local field, we find that in the original geometry it becomes

$$T^{\mathrm{bl}}(z,w) = \xi'(z)^{1/2}\, \xi'(w)^{1/2}\, T^{\mathrm{bl}}(\xi(z),\xi(w)) . \tag{3.15}$$

Using the transformation of the bi-local operator in the entanglement Hamiltonian in Eq. (3.11), we obtain for the holomorphic part

$$\begin{aligned} &\int_{\xi(A)} \mathrm{d}\xi\, \frac{1}{\xi(w)-\xi(\tilde{w}_p)} \frac{T^{\mathrm{bl}}(\xi(w),\xi(\tilde{w}_p))}{\partial_\xi z(\xi(\tilde{w}_p))} \\ &= \int_A \xi'(w)\mathrm{d}w\, \frac{1}{\xi(w)-\xi(\tilde{w}_p)} \frac{\xi'(w)^{-1/2}\,\xi'(\tilde{w}_p)^{-1/2}\, T^{\mathrm{bl}}(w,\tilde{w}_p)}{\xi'(\tilde{w}_p)^{-1}\, z'(\tilde{w}_p)} \\ &= \int_A \mathrm{d}w\, \frac{\xi'(w)^{1/2}\,\xi'(\tilde{w}_p)^{1/2}}{\xi(w)-\xi(\tilde{w}_p)} \frac{T^{\mathrm{bl}}(w,\tilde{w}_p)}{z'(\tilde{w}_p)} = \int_A \mathrm{d}w\, \frac{\xi'(w)^{1/2}\,\xi'(\tilde{w}_p)^{1/2}}{\xi(w)-\xi(\tilde{w}_p)}\, \beta_{\mathrm{loc}}(\tilde{w}_p)\, T^{\mathrm{bl}}(w,\tilde{w}_p) . \end{aligned} \tag{3.16}$$

Putting together both the local and the bi-local components, we find that the holomorphic entanglement Hamiltonian in the original geometry takes the form

$$K_A = \int_A \mathrm{d}w\, \beta_{\mathrm{loc}}(w)\, T(w) + \int_A \mathrm{d}w\, \frac{\xi'(w)^{1/2}\,\xi'(\tilde{w}_p)^{1/2}}{\xi(w)-\xi(\tilde{w}_p)}\, \beta_{\mathrm{loc}}(\tilde{w}_p)\, T^{\mathrm{bl}}(w,\tilde{w}_p), \tag{3.17}$$

and an analogous result can be also derived for the anti-holomorphic component.

In order to use the result of Eq. (3.17) for the finite temperature case, we recall that the cylinder is mapped into the plane under the transformation $\xi(w) = e^{\frac{2\pi}{\beta}w}$, depicted in

Fig. 3.1. In particular, at the time $t = 0$ in which we are interested in, the holomorphic and anti-holomorphic coordinate w coincides and the holomorphic and anti-holomorphic parts differ only in the operator. Substituting this mapping in Eq. (3.12), we reproduce the expression for $z(x;\beta)$ at finite temperature reported in Eq. (3.6), which gives the entanglement temperature $\beta_{\rm loc}(x;\beta)$ in Eq. (3.7). Regarding the bi-local part in Eq. (3.16), the weight function becomes

$$\frac{\xi'(w)^{1/2}\,\xi'(\tilde{w}_p)^{1/2}}{\xi(w)-\xi(\tilde{w}_p)}\,\beta_{\rm loc}(\tilde{w}_p) = \frac{\frac{2\pi}{\beta}e^{\frac{\pi}{\beta}(w-\tilde{w}_p)}}{e^{\frac{2\pi}{\beta}w}-e^{\frac{2\pi}{\beta}\tilde{w}_p}}\,\beta_{\rm loc}(\tilde{w}_p) = \frac{\beta_{\rm loc}(\tilde{w}_p)}{\frac{\beta}{\pi}\sinh\frac{\pi(w-\tilde{w}_p)}{\beta}}\,, \tag{3.18}$$

which is also in agreement with Eq. (3.9), as expected. Therefore, we have used an alternative path to provide the results for the entanglement Hamiltonian of a disjoint set of intervals on the infinite cylinder. We stress that we find instructive to give this derivation here because we will use it also to evaluate the thermal twisted negativity Hamiltonian defined in Eq. (2.87).

3.2 Finite temperature negativity Hamiltonian

In this section, we present the main analytical result of this Chapter, which is the field-theoretical prediction for the negativity Hamiltonian on a torus. In order to perform this computation, we show how to apply the construction of Ref. [81] reviewed in Sec. 2.3 to the finite temperature case and we use it in two explicit examples. In particular, we find that in some cases the structure of the negativity Hamiltonian is more local than the one of the corresponding entanglement Hamiltonian.

3.2.1 Negativity Hamiltonian on the torus

Recall from the discussion of Sec. 2.3 in Chapter 2 that, according to the procedure of Ref. [81], given the entanglement Hamiltonian in a certain geometry, the negativity Hamiltonian is obtained by exchanging the extrema of the reversed interval everywhere in the EH and by introducing appropriate imaginary units for every fermion in the reversed interval. We refer the reader to Sec. 3.A for a proper derivation of this result. This construction applies almost unmodified also to the negativity Hamiltonian on the torus, starting from the EH in Eqs. (3.1) and (3.2).

To fix the ideas, let us reverse a single interval $[a_j, b_j]$. We remind that in the function $z(x;\beta,L)$ in Eq. (3.2), it appears a term proportional to x and to the total length ℓ of the subsystem [142–144]. It is useful to write the subsystem length ℓ as $\ell = \sum_i (b_i - a_i)$, since in order to obtain the correct negativity Hamiltonian it is necessary to exchange the endpoints of the reversed interval also in this expression. If we call $\ell_1 = \sum_{j\in A_1}(b_j - a_j)$ the total length of the partially reversed subsystem A_1 (for us, $\ell_1 = b_j - a_j$) and $\ell_2 = \sum_{i\in A_2}(b_i - a_i)$

the total length of A_2, this procedure gives

$$z^R(x;\beta,L) = \log\left[-\frac{\vartheta_1\big(\frac{\pi}{L}\,(x-b_j)\,|q\big)}{\vartheta_1\big(\frac{\pi}{L}\,(x-a_j)\,|q\big)}\prod_{i\neq j}\frac{\vartheta_1\big(\frac{\pi}{L}\,(x-a_i)\,|q\big)}{\vartheta_1\big(\frac{\pi}{L}\,(x-b_i)\,|q\big)}\right] + \frac{2\pi x}{\beta L}\,(\ell_2-\ell_1)\,. \qquad (3.19)$$

Analogously, Eq. (3.4) which determines the position of the conjugate points becomes

$$z^R(x;\beta,L) - z^R(\tilde{x}^R_{kp};\beta,L) + \frac{2\pi k}{\beta}\,(\ell_2-\ell_1) = 0\,, \quad k\in\mathbb{Z}\,, \qquad (3.20)$$

where again we have exchanged ℓ with $\ell_2-\ell_1$. For $\ell_1\neq\ell_2$, the negativity Hamiltonian on the torus has a non-local structure analogous to the one of the corresponding entanglement Hamiltonian in Eq. (3.1), containing infinite terms coupling different points

$$\begin{aligned}\mathcal{N}_A(\beta,L) &= \mathcal{N}^{\text{loc}}_A(\beta,L) + \mathcal{N}^{\text{nl}}_A(\beta,L)\\ &= \int \mathrm{d}x\,\beta^R_{\text{loc}}(x;\beta,L)\,T_{00}(x)\\ &\quad + \sum_{(p,k)\neq(0,0)}(\pm1)^k\int_A \mathrm{d}x\,\frac{\beta^R_{\text{loc}}(\tilde{x}^R_{kp};\beta,L)\,\mathrm{i}^{\Theta_1(x)}(-\mathrm{i})^{\Theta_1(\tilde{x}^R_{kp})}}{\frac{\beta}{\pi}\sinh\Big[\frac{\pi}{\beta}\Big(x-\tilde{x}^R_{kp}+kL\Big)\Big]}\,T^{\text{bl}}\big(x,\tilde{x}^R_{kp},t=0\big)\,,\end{aligned} \qquad (3.21)$$

where $p\in\{0,\dots,n-1\}, k\in\mathbb{Z}$ and the function $\Theta_1(x)$ is equal to 1 only for $x\in A_1$, 0 otherwise

$$\Theta_1(x) = \begin{cases}1, & x\in A_1,\\ 0, & x\notin A_1.\end{cases} \qquad (3.22)$$

Analogously to what we did in Sec. 2.3, in Eq. (3.21) we have introduced the negativity temperature

$$\beta^R_{\text{loc}}(x;\beta,L) = \frac{1}{(z^R(x;\beta,L))'}, \qquad (3.23)$$

and, analogously to Eq. (3.1), the signs $+$ and $-$ correspond respectively to the Ramond and to the Neveu-Schwarz sectors.

On the other hand, when $\ell_1=\ell_2$, the dependence on the integer index k in Eq. (3.20) cancels out exactly and the solutions $\tilde{x}^R_{kp}$ with different k collapse on each another, giving a striking qualitative difference with respect to the entanglement Hamiltonian in Eq. (3.1). In Eq. (3.21), the bi-local terms with different k and same p are then calculated in the same conjugate point $\tilde{x}^R_p$, leading to a bi-local structure with only $n-1$ bi-local terms, similar to the one of the NH on the plane of Eq. (2.89)

$$
\begin{aligned}
&\mathcal{N}_A(\beta, L) = \mathcal{N}_A^{\mathrm{loc}}(\beta, L) + \mathcal{N}_A^{\mathrm{nl}}(\beta, L) \\
&= \int \mathrm{d}x\, \beta_{\mathrm{loc}}^R(x;\beta, L)\, T_{00}(x) \\
&\qquad + \sum_{p=1}^{n} \int_A \mathrm{d}x\, \beta_{\mathrm{loc}}^R(\tilde{x}_p^R;\beta, L)\, \frac{g_{\pm}^R(x-\tilde{x}_p^R)}{L}\, \mathrm{i}^{\Theta_1(x)}(-\mathrm{i})^{\Theta_1(\tilde{x}_{kp}^R)}\, T^{\mathrm{bl}}\big(x, \tilde{x}_p^R, t=0\big)\,.
\end{aligned}
\tag{3.24}
$$

In Eq. (3.24) we have introduced the (dimensionless) functions $g_{\pm}^R(z)$ defined by the infinite series

$$
g_{\pm}^R(z;\beta, L) = \frac{\pi L}{\beta} \sum_{k=-\infty}^{+\infty} \frac{(\pm 1)^k}{\sinh\Big[\frac{\pi}{\beta}\,(z+kL)\Big]}\,. \tag{3.25}
$$

In the Ramond sector (+ sign), Eq. (3.25) can be resummed to give

$$
g_{+}^R(z;\beta, L) = \psi_q\Big(-\frac{z}{L}\Big) - \psi_q\Big(1+\frac{z}{L}\Big) + \psi_q\bigg(1+\frac{z-\mathrm{i}\beta}{L}\bigg) - \psi_q\bigg(-\frac{z+\mathrm{i}\beta}{L}\bigg)\,, \qquad q = e^{\frac{\pi L}{\beta}}\,, \tag{3.26}
$$

where ψ_q denotes the q-digamma function (see Sec. 3.B for its definition), while in the Neveu-Schwarz sector (− sign) it reads

$$
\begin{aligned}
g_{-}^R(z;\beta, L) = \frac{1}{2}\Bigg[&\psi_{q^2}\Big(-\frac{z}{2L}\Big) - \psi_{q^2}\bigg(\frac{L-z}{2L}\bigg) + \psi_{q^2}\bigg(\frac{L+z}{2L}\bigg) - \psi_{q^2}\Big(\frac{z}{2L}+1\Big) \\
&+ \psi_{q^2}\bigg(\frac{L-z-\mathrm{i}\beta}{2L}\bigg) - \psi_{q^2}\bigg(\frac{L+z-\mathrm{i}\beta}{2L}\bigg) + \psi_{q^2}\bigg(\frac{2L+z-i\beta}{2L}\bigg) - \psi_{q^2}\bigg(-\frac{z+i\beta}{2L}\bigg)\Bigg].
\end{aligned}
\tag{3.27}
$$

To summarise, when the length of the reversed intervals is equal to the non-reversed one, the negativity Hamiltonian recovers a mild non-local structure given by a finite number of bi-local terms, while such a simplification does not arise in the entanglement Hamiltonian.

In the following we specialise to the case of n intervals lying on an infinite line at finite temperature (i.e. the space-time is a cylinder), and then we present explicit examples for the case of two intervals.

3.2.2 Finite temperature negativity Hamiltonian on the infinite line

The finite temperature negativity Hamiltonian on the infinite line can be obtained either by directly exchanging the extrema of the reversed interval in the related EH reported in Eqs. (3.6) and (3.9) or by taking the $L \to \infty$ limit of the negativity Hamiltonian in

Eq. (3.19), similarly to the limit reported in Eq. (3.5). By applying the exchanging procedure to Eq. (3.9), we find that the function $z(x;\beta)$ in Eq. (3.6) reduces to

$$z^R(x;\beta) = \log\left[-\frac{\sinh\frac{\pi(x-b_j)}{\beta}}{\sinh\frac{\pi(x-a_j)}{\beta}} \prod_{i\neq j} \frac{\sinh\frac{\pi(x-a_i)}{\beta}}{\sinh\frac{\pi(x-b_i)}{\beta}} \right], \tag{3.28}$$

and the $n-1$ conjugate points $\tilde{x}_p^R$ are found to be the non-trivial solutions of $z^R(x;\beta) = z^R(\tilde{x}_p^R;\beta)$. Thus, the finite temperature negativity Hamiltonian on the infinite line is

$$\begin{aligned}\mathcal{N}_A(\beta) &= \mathcal{N}_A^{\text{loc}}(\beta) + \mathcal{N}_A^{\text{bl}}(\beta) \\ &= \int_A \mathrm{d}x\, \beta_{\text{loc}}^R(x;\beta)\, T_{00}(x) + \sum_{p=1}^{n-1} \int \mathrm{d}x\, \frac{\beta_{\text{loc}}^R(\tilde{x}_p;\beta)\, \mathrm{i}^{\Theta_1(x)} (-\mathrm{i})^{\Theta_1(\tilde{x}_p^R)}}{\frac{\beta}{\pi}\sinh\frac{\pi\left(x-\tilde{x}_p^R\right)}{\beta}}\, T^{\text{bl}}\big(x, \tilde{x}_p^R, t=0\big)\ ,\end{aligned} \tag{3.29}$$

where the negativity temperature $\beta_{\text{loc}}^R(x;\beta)$ is given by

$$\begin{aligned}\beta_{\text{loc}}^R(x;\beta) = \frac{1}{z^{R\prime}(x;\beta)} = \frac{\beta}{\pi}\Bigg[&\coth\frac{\pi(x-b_j)}{\beta} - \coth\frac{\pi(x-a_j)}{\beta} \\ &+ \sum_{i\neq j}\left(\coth\frac{\pi(x-a_i)}{\beta} - \coth\frac{\pi(x-b_i)}{\beta}\right)\Bigg]^{-1},\end{aligned} \tag{3.30}$$

and the bi-local terms are calculated in the $n-1$ conjugate points obtained as the non-trivial solutions of $z^R(x;\beta) = z^R(\tilde{x}_p^R;\beta)$. As we also commented for the entanglement Hamiltonian, the negativity Hamiltonian only contains $n-1$ bi-local terms.

3.2.3 Tripartite geometry

As a first explicit example regarding the negativity Hamiltonian on the torus, we consider a tripartite geometry made up of two intervals $A_1 = [a_1, b_1]$, $A_2 = [a_2, b_2]$. Let us call $\ell_1 = b_1 - a_1$ the length of A_1 and $\ell_2 = b_2 - a_2$ the one of A_2, and let us reverse the interval A_1. Then, specialising Eq. (3.19) to this configuration we find

$$z^R(x;\beta,L) = \log\left[-\frac{\vartheta_1\big(\frac{\pi}{L}(x-b_1)\,|q\big)\,\vartheta_1\big(\frac{\pi}{L}(x-a_2)\,|q\big)}{\vartheta_1\big(\frac{\pi}{L}(x-a_1)\,|q\big)\,\vartheta_1\big(\frac{\pi}{L}(x-b_2)\,|q\big)} \right] + \frac{2\pi x}{\beta L}\,(\ell_2-\ell_1)\,, \tag{3.31}$$

while the conjugate point equation in Eq. (3.20) becomes

$$z^R(x;\beta,L) - z^R(\tilde{x}_k^R;\beta,L) + \frac{2\pi k}{\beta}\,(\ell_2-\ell_1) = 0\,, \quad k\in\mathbb{Z}\,. \tag{3.32}$$

We stress again that for $\ell_1 = \ell_2$, the non-local structure of the negativity Hamiltonian drastically simplifies since the solutions of Eq. (3.32) do not depend on the index k, leading to a single bi-local term. We can now also consider some interesting limits of Eq. (3.31).

Finite temperature on the infinite line: If the two intervals $A_1 = [a_1, b_1]$ and $A_2 = [a_2, b_2]$ lie on the infinite line, the function $z^R(x;\beta)$ in Eq. (3.31) becomes

$$z^R(x;\beta) = \log\left[\frac{\sinh\frac{\pi(x-b_1)}{\beta}\,\sinh\frac{\pi(x-a_2)}{\beta}}{\sinh\frac{\pi(x-a_1)}{\beta}\,\sinh\frac{\pi(b_2-x)}{\beta}}\right], \tag{3.33}$$

which gives the negativity temperature

$$\beta^R_{\mathrm{loc}}(x;\beta) = \frac{\beta}{\pi}\left[-\coth\frac{\pi(x-a_1)}{\beta} + \coth\frac{\pi(x-b_1)}{\beta} + \coth\frac{\pi(x-a_2)}{\beta} - \coth\frac{\pi(x-b_2)}{\beta}\right]^{-1}. \tag{3.34}$$

There is a single bi-local term, calculated in the conjugate point $\tilde{x}^R$

$$\tilde{x}^R = \frac{\beta}{2\pi}\log\left[\frac{2\,e^{\frac{2\pi}{\beta}x}\,\sinh\frac{\pi(\ell_2-\ell_1)}{\beta} + \left(e^{\frac{2\pi}{\beta}a_1} + e^{\frac{2\pi}{\beta}b_2}\right)e^{\frac{\pi}{\beta}(\ell_1-\ell_2)} - \left(e^{\frac{2\pi}{\beta}b_1} + e^{\frac{2\pi}{\beta}a_2}\right)e^{\frac{\pi}{\beta}(\ell_2-\ell_1)}}{e^{-\frac{\pi}{\beta}(a_1+b_1+a_2+b_2)}\left(e^{\frac{2\pi}{\beta}a_1} - e^{\frac{2\pi}{\beta}b_1} + e^{\frac{2\pi}{\beta}b_2} - e^{\frac{2\pi}{\beta}a_2}\right)e^{\frac{2\pi}{\beta}x} - 2\sinh\frac{\pi(\ell_2-\ell_1)}{\beta}}\right] \tag{3.35}$$

which is the only non-trivial solution of $z^R(x;\beta) = z^R(\tilde{x}^R;\beta)$. In particular, for $\ell_1 = \ell_2$ Eq. (3.35) reduces simply to $\tilde{x}^R = a_1 + b_2 - x$. The weight function of the bi-local operator reads

$$\beta^R_{\mathrm{bl}}(x;\beta) = \frac{\beta^R_{\mathrm{loc}}(\tilde{x}^R;\beta)}{\frac{\beta}{\pi}\sinh(\frac{\pi}{\beta}(x-\tilde{x}^R))}, \tag{3.36}$$

As a further cross-check of our result, it is interesting to consider the zero-temperature limit $\beta \to \infty$ of the negativity Hamiltonian. In this regime, we expect to retrieve the result for the tripartite configuration in the ground state which was obtained in Ref. [81] by directly applying the exchanging procedure to the entanglement Hamiltonian on the plane in in Eqs. (2.20) and (2.36). Indeed, we see that taking the limit $\beta \to \infty$ of $z^R(x;\beta)$ in Eq. (3.33), we reproduce the function on the plane found in [81]

$$z^R(x) = \log\left[\frac{(x-b_1)(x-a_2)}{(x-a_1)(b_2-x)}\right]. \tag{3.37}$$

Regarding the conjugate points, again we see that they are given by the single non-trivial solution of $z^R(x) = z^R(\tilde{x})$, with $z^R(x)$ in Eq. (3.37), finding the same conjugate point of [81]

$$\tilde{x}^R = \frac{(a_1b_2 - b_1a_2)x + (a_1+b_2)b_1a_2 - (b_1+a_2)a_1b_2}{(a_1-b_1+b_2-a_2)x + b_1a_2 - a_1b_2}, \tag{3.38}$$

as expected. Note that Eqs. (3.37) and (3.38) agree with the NH for two interval reported in Eq. (2.91) up to exchanging the two interval. This is just a matter of convention, since in Eq. (2.91) we reversed the second interval, while here we reversed the first one.

3.2.4 Bipartite geometry

We now study a bipartite geometry on the torus where $A_1 = [0, \ell_1]$ and the rest of the system is $A_2 = [\ell_1, L]$. Notice that, differently from the case studied above, now the union $A = A_1 \cup A_2$ of the reversed interval A_1 and A_2 is not a proper subset of the circle, but it covers all the system. Such a geometry can be obtained from the tripartite case of Sec. 3.2.3 by choosing $a_1 = 0$, $b_1 = a_2 = \ell_1$ and $b_2 = L$. Taking this limits in the function z^R in Eq. (3.31), we obtain

$$\begin{aligned} z^R(x;\beta,L) &= \log\left[-\frac{\vartheta_1\big(\frac{\pi}{L}(x-\ell_1)\,|q\big)^2}{\vartheta_1\big(\frac{\pi}{L}x|q\big)\,\vartheta_1\big(\frac{\pi}{L}(x-L)\,|q\big)}\right] + \frac{2\pi x}{\beta}\left(1-\frac{2\ell_1}{L}\right) \\ &= 2\log\left|\frac{\vartheta_1\big(\frac{\pi}{L}(x-\ell_1)\,|q\big)}{\vartheta_1\big(\frac{\pi}{L}x|q\big)}\right| + \frac{2\pi x}{\beta}\left(1-\frac{2\ell_1}{L}\right), \end{aligned} \tag{3.39}$$

where we have used the periodicity of the theta function $\vartheta_1(z-\pi|q) = -\vartheta_1(z|q)$, while Eq. (3.32) for the conjugate points becomes

$$z^R(x;\beta,L) - z^R(\tilde{x}^R_k;\beta,L) + \frac{2\pi k}{\beta}(L-2\ell_1) = 0\,, \quad k \in \mathbb{Z}\,. \tag{3.40}$$

The corresponding negativity temperature is provided by

$$\beta^R_{\text{loc}}(x;\beta,L) = \frac{1}{z^R(x;\beta,L)'}. \tag{3.41}$$

We again remark that for $\ell_1 = L/2$ the dependence in k drops out from Eq. (3.40), and therefore all the infinite non-local solutions collapse into a single bi-local term with weight given by

$$\beta^R_{\text{bl}}(x;\beta,L) = \beta^R_{\text{loc}}(\tilde{x}^R;\beta,L)\frac{g^R_{\pm}(x-\tilde{x}^R)}{L}, \tag{3.42}$$

where $g^R_{\pm}$ are given in Eqs. (3.26) and (3.27), respectively. This formula represents an important result of this Chapter, since a bipartite system at finite temperature is a neat example of mixed state: in this case, the negativity is a genuine entanglement measure, differently from the entanglement entropy which mixes both quantum and thermal correlations. Therefore, the result for the negativity Hamiltonian provides the first operatorial characterisation of a thermal state. Let us now consider some interesting limits also for this bipartite geometry.

Finite temperature on the infinite line: Finding the theoretical prediction for the bipartite negativity Hamiltonian on the infinite line is more subtle than in the tripartite case of Sec. 3.2.3 because now A_1 and A_2 cover the full infinite line. The geometry of interest is $A_1 = [0, \ell_1]$, $A_2 = [-\infty, 0] \cup [\ell_1, +\infty]$ where we reverse the interval A_1. We can obtain this geometry from a three interval configuration on the infinite line $A_1 = [0, \ell_1]$,

$A_2 = [-L/2, 0] \cup [\ell_1, \ell_1 + L/2]$, taking then the limit $L \to \infty$ [121]. Specialising the function $z^R(x;\beta)$ in Eq. (3.28) to this geometry and taking the $L \to \infty$ limit we find (up to x-independent terms)

$$\log\left[\left(\frac{\sinh\frac{\pi(\ell_1-x)}{\beta}}{\sinh\frac{\pi x}{\beta}}\right)^2 \frac{\sinh\frac{\pi(x+L/2)}{\beta}}{\sinh\frac{\pi(L/2+\ell_1-x)}{\beta}}\right] \longrightarrow \log\left[\left(\frac{\sinh\frac{\pi(\ell_1-x)}{\beta}}{\sinh\frac{\pi x}{\beta}}\right)^2 \frac{e^{\frac{\pi}{\beta}x}}{e^{\frac{\pi}{\beta}(\ell_1-x)}}\right] \tag{3.43}$$
$$= z^R(x;\beta) + \mathrm{const}\,,$$

where now $z^R(x;\beta)$ reads

$$z^R(x;\beta) = 2\log\left|\frac{\sinh\frac{\pi(\ell_1-x)}{\beta}}{\sinh\frac{\pi x}{\beta}}\right| + \frac{2\pi x}{\beta}\,. \tag{3.44}$$

This form differs from the one in Eq. (3.33) for the tripartite geometry, since now we find a term proportional to x. From this result we see that the negativity temperature is

$$\beta^R_{\mathrm{loc}}(x;\beta) = \frac{1}{z'(x)} = \frac{\beta}{2\pi}\left[1 + \coth\frac{\pi(x-\ell_1)}{\beta} - \coth\frac{\pi x}{\beta}\right]^{-1}\,. \tag{3.45}$$

Since the geometry is made of three intervals, the equation for the conjugate points obtained from Eq. (3.28), with $z^R(x;\beta) = z^R(y;\beta)$ is a polynomial of third order in y and one has the trivial solution $y = x$ and also two non-trivial solutions $y = \tilde{x}^R_\pm$, that in the limit $L \to \infty$ read

$$\begin{aligned}
\tilde{x}^R_+ = \frac{\beta}{2\pi}\log\Bigg[\frac{1}{8}\Bigg(&-4e^{\frac{2\pi\ell_1}{\beta}} + e^{\frac{4\pi\ell_1}{\beta}} + \left(e^{\frac{2\pi\ell_1}{\beta}} - 1\right)\sqrt{-6e^{\frac{2\pi\ell_1}{\beta}} + e^{\frac{4\pi\ell_1}{\beta}} + 4e^{\frac{2\pi(\ell_1-x)}{\beta}} + 4e^{\frac{2\pi x}{\beta}} - 3}\\
&+2e^{\frac{2\pi(\ell_1-x)}{\beta}} + 2e^{\frac{2\pi x}{\beta}} - 1\Bigg)\operatorname{csch}^2\left(\frac{\pi x}{\beta}\right)\Bigg],\\
\tilde{x}^R_- = \frac{\beta}{2\pi}\log\Bigg[\frac{1}{8}\Bigg(&-4e^{\frac{2\pi\ell_1}{\beta}} + e^{\frac{4\pi\ell_1}{\beta}} - \left(e^{\frac{2\pi\ell_1}{\beta}} - 1\right)\sqrt{-6e^{\frac{2\pi\ell_1}{\beta}} + e^{\frac{4\pi\ell_1}{\beta}} + 4e^{\frac{2\pi(\ell_1-x)}{\beta}} + 4e^{\frac{2\pi x}{\beta}} - 3}\\
&+2e^{\frac{2\pi(\ell_1-x)}{\beta}} + 2e^{\frac{2\pi x}{\beta}} - 1\Bigg)\operatorname{csch}^2\left(\frac{\pi x}{\beta}\right)\Bigg].
\end{aligned} \tag{3.46}$$

The bi-local inverse temperature corresponding to each conjugate point $\tilde{x}^R_\pm$ is

$$\beta^R_{\mathrm{bl}}(\tilde{x}^R_\pm;\beta) = \frac{\beta^R_{\mathrm{loc}}(\tilde{x}^R_\pm;\beta)}{\frac{\beta}{\pi}\sinh(\frac{\pi}{\beta}(x - \tilde{x}^R_\pm))}\,. \tag{3.47}$$

Another interesting limit we can study is when $\beta \to \infty$, i.e. the zero temperature case, in which the state becomes pure. From Eq. (3.45), the negativity temperature is given by

$$\beta^R_{\mathrm{loc}}(x;\infty) = \frac{(x-\ell_1)x}{2\ell_1}\,, \tag{3.48}$$

which is half of the weight function of the entanglement Hamiltonian for one single interval in the ground state in Eq. (1.13). The limit of Eq. (3.44) is

$$z^R(x;\infty) = 2\log\left|1-\frac{\ell_1}{x}\right|\,, \tag{3.49}$$

and the two conjugate point in Eq. (3.46) are

$$\begin{aligned}
\tilde{x}^R_+ &= \begin{cases} \frac{\beta}{\pi}\log\left|\frac{\ell_1-x}{x}\right|, & x<\ell_1/2\,,\\ \frac{x\ell_1}{2x-\ell_1}, & x>\ell_1/2\,,\end{cases}\\
\tilde{x}^R_- &= \begin{cases} \frac{x\ell_1}{2x-\ell_1}, & x<\ell_1/2\,,\\ \frac{\beta}{\pi}\log\left|\frac{\ell_1-x}{x}\right|, & x>\ell_1/2\,.\end{cases}
\end{aligned} \tag{3.50}$$

In the limit $\beta \to \infty$, the conjugate point $\tilde{x}^R_+$ ($\tilde{x}^R_-$) diverges as $\mathcal{O}(\beta)$ for $x<\ell_1/2$ ($x>\ell_1/2$), and the bi-local operators calculated in this point do not contribute because the fermionic field $\psi(x)$ vanish as $x\to\infty$ [84, 89]. In the other regions, instead, $\tilde{x}^R_+$ and $\tilde{x}^R_-$ are joined together to give the conjugate point $\tilde{x}^R = x\ell_1/(2x-\ell_1)$ in which the fermion does not vanish. Notice that, as expected, this conjugate point is precisely the only non-trivial solution of $z^R(x;\infty) = z^R(\tilde{x}^R;\infty)$ with $z^R(x;\infty)$ in Eq. (3.49). We can explicitly compute the weight functions of the bi-local operators as

$$\begin{aligned}
\frac{\beta^R_{\mathrm{loc}}(\tilde{x}^R_+;\beta)}{\frac{\beta}{\pi}\sinh\left[\frac{\pi}{\beta}(x-\tilde{x}^R_+)\right]} &= \begin{cases} \frac{|x|(\ell_1-x)}{\ell_1^2(2x-\ell_1)}, & x<\ell_1/2\,,\\ \frac{\ell_1}{4(\ell_1-2x)}, & x>\ell_1/2\,,\end{cases}\\
\frac{\beta^R_{\mathrm{loc}}(\tilde{x}^R_-;\beta)}{\frac{\beta}{\pi}\sinh\left[\frac{\pi}{\beta}(x-\tilde{x}^R_-)\right]} &= \begin{cases} \frac{\ell_1}{4(\ell_1-2x)}, & x<\ell_1/2\,,\\ \frac{x|\ell_1-x|}{\ell_1^2(2x-\ell_1)}, & x>\ell_1/2\,.\end{cases}
\end{aligned} \tag{3.51}$$

As we can see, considering only the bi-local weights calculated in the region in which the conjugate points in Eq. (3.50) remain finite, the bipartite negativity Hamiltonian at zero temperature is

$$\begin{aligned}
\mathcal{N}_A &= \mathcal{N}_A^{\mathrm{loc}} + \mathcal{N}_A^{\mathrm{loc}}\\
&= \int_{-\infty}^{+\infty} \mathrm{d}x\,\frac{(x-\ell_1)x}{2\ell_1}\,T_{00}(x) - \mathrm{i}\left(\int_{-\infty}^{0} - \int_{0}^{\ell_1} + \int_{\ell_1}^{+\infty}\right)\mathrm{d}x\,\frac{\ell_1}{4(\ell_1-2x)}\,T^{\mathrm{bl}}(x,\frac{x\ell_1}{2x-\ell_1})\,.
\end{aligned} \tag{3.52}$$

We remark that, although one of the imaginary bi-local operators of the negativity Hamiltonian does not vanish, as $\beta \to \infty$ the state becomes pure and $[\rho_A^{R_1}, (\rho_A^{R_1})^\dagger] = 0$ [112, 117]. As a consequence, we find

$$\sqrt{\rho_A^{R_1}(\rho_A^{R_1})^\dagger} = \left|\rho_A^{R_1}\right| = \frac{1}{Z} e^{-\pi(\mathcal{N}_A + \mathcal{N}_A^\dagger)} = \frac{1}{Z} e^{-2\pi \mathcal{N}_A^{\rm loc}}. \tag{3.53}$$

The local part of the negativity Hamiltonian can be also rewritten as

$$\mathcal{N}_A^{\rm loc} = \frac{1}{2}\left(\mathrm{Id}_{A_1} \otimes K_{A_2} - K_{A_1} \otimes \mathrm{Id}_{A_2}\right), \tag{3.54}$$

where Id_{A_2} and Id_{A_2} denote the identity operators on A_1 and A_2, respectively, and

$$K_{A_1} = \int_0^{\ell_1} dx \frac{x(\ell_1 - x)}{\ell_1} T_{00}(x), \qquad K_{A_2} = \int_{-\infty}^{0} dx \frac{x(x-\ell_1)}{\ell} T_{00}(x) + \int_{\ell_1}^{\infty} dx \frac{x(x-\ell_1)}{\ell_1} T_{00}(x), \tag{3.55}$$

are the entanglement Hamiltonians of the interval $A_1 = [0, \ell_1]$ (K_{A_1}) and of its complement (K_{A_2}). This result does not come as a surprise since a bipartite geometry at zero temperature is a pure state and one recovers that [117]

$$\mathrm{Tr}\left|\rho_A^{R_1}\right| = \mathrm{Tr}(\rho_{A_1}^{1/2})^2. \tag{3.56}$$

In other words, for a pure state the logarithmic negativity is equal to the Rényi entropy of order 1/2 defined in Eq. (1.7).

3.3 Numerical analysis

In this section we present exact numerical calculations on the lattice in order to compare them with our field-theoretical predictions. We compute both the lattice entanglement and lattice negativity Hamiltonians directly from the knowledge of the correlation matrix, using the relation for Gaussian states that we reviewed in the Introduction and in Sec. 2.4. For lattice fermions at finite temperature on the circle, C_A is known both for periodic and for anti-periodic boundary conditions [145, 146]. However recall that, as we have discussed in Sec. 2.4, comparing the lattice and negativity Hamiltonian with the analytical results is highly non-trivial, requiring a careful continuum limit [25, 52, 53, 55, 84, 132–137, 141]. We refer the reader to Sec. 2.4 for more details and for a derivation of this limiting procedure. In the following we apply the limiting procedure detailed in Sec. 2.4 to the finite temperature negativity Hamiltonian, obtaining good agreement between the lattice results and our predictions.

3.3.1 Lattice entanglement and negativity Hamiltonians for free fermions

On a circle of L sites, we again consider the tight-binding Hamiltonian

$$H = -\sum_i \left[c_i^\dagger c_{i+1} + c_{i+1}^\dagger c_i \right], \tag{3.57}$$

where the lattice fermions satisfy the canonical anti-commutation relations

$$\left\{ c_i, c_j^\dagger \right\} = \delta_{ij}, \qquad \left\{ c_i, c_j \right\} = \left\{ c_i^\dagger, c_j^\dagger \right\} = 0\,, \tag{3.58}$$

and we impose either anti-periodic boundary conditions $c_{L+1} = -c_1$, $c_{L+1}^\dagger = -c_1^\dagger$ or periodic ones $c_{L+1} = c_1$, $c_{L+1}^\dagger = c_1^\dagger$. We can write down the Hamiltonian (3.57) in the Fourier modes $c_k, c_k^\dagger$ and the dispersion relation of the tight-binding model (3.57) reads

$$H = \sum_k \varepsilon(k)\, c_k^\dagger c_k\,, \qquad \varepsilon(k) = -\cos\frac{2\pi k}{L}\,, \tag{3.59}$$

where the allowed momenta k depend on the boundary conditions, i.e., in the Neveu-Schwarz sector, the momenta are semi-integer

$$k = -\frac{L}{2} + \frac{1}{2}, \dots, -\frac{1}{2}, \frac{1}{2}, \dots, \frac{L}{2} - \frac{1}{2}\,, \quad \text{(NS)}, \tag{3.60}$$

while they are integer in the Ramond one

$$k = -\frac{L}{2} + 1, \dots, -1, 0, 1, \dots, \frac{L}{2}\,, \quad \text{(R)}. \tag{3.61}$$

Notice that, when L is divisible by 4, in the Ramond sector there are two zero-modes corresponding to the momenta $k = \pm\frac{L}{4}$. As discussed in [98, 142–144, 147], their presence is responsible for a non-local term in the ground state entanglement Hamiltonian. Choosing $L = (2 \mod 4)$ (i.e. divisible by 2 but not by 4), there are no zero-modes in the Ramond sector, while $k = \pm L/2$ correspond to two zero-modes in the Neveu-Schwarz sector. To simplify the discussion, in the following we will focus on the case in which L is a multiple integer of 4.

In terms of the energy $\varepsilon(k)$ in Eq. (3.59), the two-point correlation matrix at finite temperature β takes the form [121]

$$C_{i,j} = \frac{1}{L} \sum_{k=-\frac{L}{2}+\frac{1}{2}}^{\frac{L}{2}-\frac{1}{2}} \frac{e^{2\pi \mathrm{i} k r/L}}{1+e^{\beta\varepsilon(k)}} \quad \text{(NS)}, \qquad C_{i,j} = \frac{1}{L} \sum_{k=-\frac{L}{2}+1}^{\frac{L}{2}} \frac{e^{2\pi \mathrm{i} k r/L}}{1+e^{\beta\varepsilon(k)}} \quad \text{(R)}. \tag{3.62}$$

Since the finite temperature state is Gaussian, as we did in Sec. 2.4 we write the reduced density matrix as in Eq. (1.14),

$$\rho_A = \frac{1}{Z_A} e^{-2\pi K_A} = \frac{1}{Z_A} \exp\left\{ -\sum_{i,j} c_i^\dagger h_{i,j} c_j \right\}, \tag{3.63}$$

where $h_{i,j}$ plays the role of the matrix kernel of the entanglement Hamiltonian $2\pi K_A$. Similarly to what we did in Sec. 2.4 for the ground state, we compute the kernel $h_{i,j}$ directly from the two-point correlation matrix (3.62) using Peschel's formula (1.15) [41,108–111,148]. We refer the reader to Sec. 2.4 for more details.

As we also explained in Sec. 2.4, Eq. (1.15) can be generalised to compute the fermionic negativity Hamiltonian, both the standard Eq. (2.86) and the twisted one Eq. (2.87). The effect of the partial time reversal on the covariance matrix $\Gamma_A = \mathrm{Id}_A - 2C_A$ is to introduce an imaginary unit for every fermion in the reversed interval. The NH kernel η is then related to the reversed covariance matrix Γ_A^R via Eq. (2.107), while the kernel of the twisted NH $\widetilde{\eta}$ is given by Eq. (2.108). We again refer the reader to Sec. 2.4.

3.3.2 Continuum limit of the entanglement Hamiltonian

In Sec. 2.4 in Chapter 2, we also discussed in detail the continuum limit of the entanglement and negativity Hamiltonian in the ground state. Recall that the main problem of the comparison between the lattice results and the QFT expressions is that even when the field-theoretical EH is completely local (see e.g. Eq. (1.13) for one interval in the ground state or Eq. (3.10) at finite temperature), the corresponding lattice EH contains couplings between fermions at arbitrary distance [132, 133]. These higher couplings are not negligible and the QFT prediction for the entanglement and negativity temperatures can only be recovered by summing over the couplings at all distances [133]. In particular, writing the kernel of the lattice EH $h_{i,j}$ in Eq. (3.63) in matrix blocks $\left(h^{(\sigma,\zeta)}\right)_{i,j}$ such that $i \in A_\sigma, j \in A_\zeta$, it was found that the diagonal blocks reproduce the local part of the QFT prediction in Eq. (2.36), while the off-diagonal blocks yield the bi-local terms. For the local part we have (see Sec. 2.4 for the full derivation) [133]

$$\sum_i h_{i,i+r}^{(\sigma,\sigma)} \left[c_i^\dagger c_{i+r} + c_{i+r}^\dagger c_i\right] \sim \int \mathrm{d}x \left[\mathcal{S}^{\mathrm{loc}}(x)\, T_{00}(x) + \mathcal{C}^{\mathrm{loc}}(x)\, N(x)\right], \tag{3.64}$$

where $T_{00}(x)$ and $N(x)$ are the stress-energy (2.37) and the number operator (2.113) in the massless Dirac fermion QFT, respectively. The weights $\mathcal{S}^{\mathrm{loc}}(x)$ and $\mathcal{C}^{\mathrm{loc}}(x)$ in Eq. (3.64) are given by the expressions [133]

$$\mathcal{S}^{\mathrm{loc}}(x) \equiv -\,2\,s \sum_{r\geq 1} r\, \sin(k_F r s)\, h^{(\sigma,\sigma)}_{i-\frac{r}{2},i+\frac{r}{2}}\,, \tag{3.65}$$

$$\mathcal{C}^{\mathrm{loc}}(x) \equiv h_{i,i}^{(\sigma,\sigma)} +\, 2 \sum_{r\geq 1} \cos(k_F r s)\, h^{(\sigma,\sigma)}_{i-\frac{r}{2},i+\frac{r}{2}}\,. \tag{3.66}$$

Ref. [133, 134] also studied the finite temperature entanglement Hamiltonian in infinite size, observing that, in the case of a single interval, the sum $\mathcal{S}^{\mathrm{loc}}(x)$ in Eq. (3.65), correctly yields the local entanglement temperature $\beta_{\mathrm{loc}}(x)$ reported in Eq. (3.10). The term proportional to the number operator $N(x)$ in Eq. (3.64) instead vanishes identically at half-filling

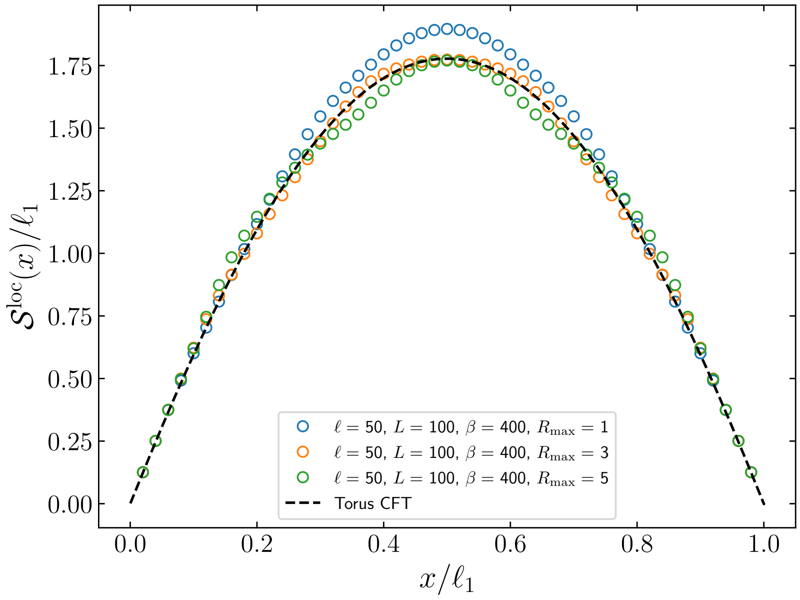

Figure 3.2: Local effective temperature of the entanglement Hamiltonian for one single interval of length $\ell = 50$ in a system of size $L = 100$ at finite temperature $\beta = 400$. Due to the presence of non-local terms, we introduce a cut-off, $R_{\max}$ in Eq. (3.65) to recover the continuum limit (symbols). The best agreement with the theoretical prediction in Eq. (3.1) is obtained for $R_{\max} = 3$.

$k_F = \frac{\pi}{2s}$. In this case, because of the particle-hole symmetry, the correlation matrix presents a checkerboard structure, inherited by the lattice entanglement Hamiltonian, which implies that Eq. (3.66) is identically zero.

We are now interested in extending the analysis of Sec. 2.4 to study free fermions on a torus, i.e. at finite temperature and size. The derivation of Ref. [133] reviewed in Eqs. (2.111), (2.112) and (3.64) relies on the fact that all the matrix elements in the diagonal blocks contribute to the local term of the field-theoretical entanglement Hamiltonian (3.64). However, we have observed that the field-theoretical EH in Eq. (3.1) contains infinite bi-local terms, even in the case of a single interval. This implies that summing over all matrix elements $\mathcal{S}^{\mathrm{loc}}(x)$ of Eq. (3.65) gives the wrong continuum limit, since we would be also including contributions that reproduce the bi-local terms of the entanglement Hamiltonian. It is therefore necessary to introduce a maximum cut-off $R_{\max}$ in the sum in Eq. (3.65), to only include the local contributions. We show this in Fig. 3.2 for the local part of the entanglement Hamiltonian of one interval of length $\ell = 50$ on the torus with $L = 100$ and $\beta = 400$. As we vary the cut-off $R_{\max}$, the agreement between the lattice bi-local weight in Eq. (3.65) and the theoretical prediction in Eq. (3.1) worsens. This non-local behaviour is also visible in Fig. 3.3, where we report the matrix plot of the entanglement Hamiltonian kernel h obtained via Eq. (1.15) for the case of a fermion on a torus at temperature $\beta = 500$

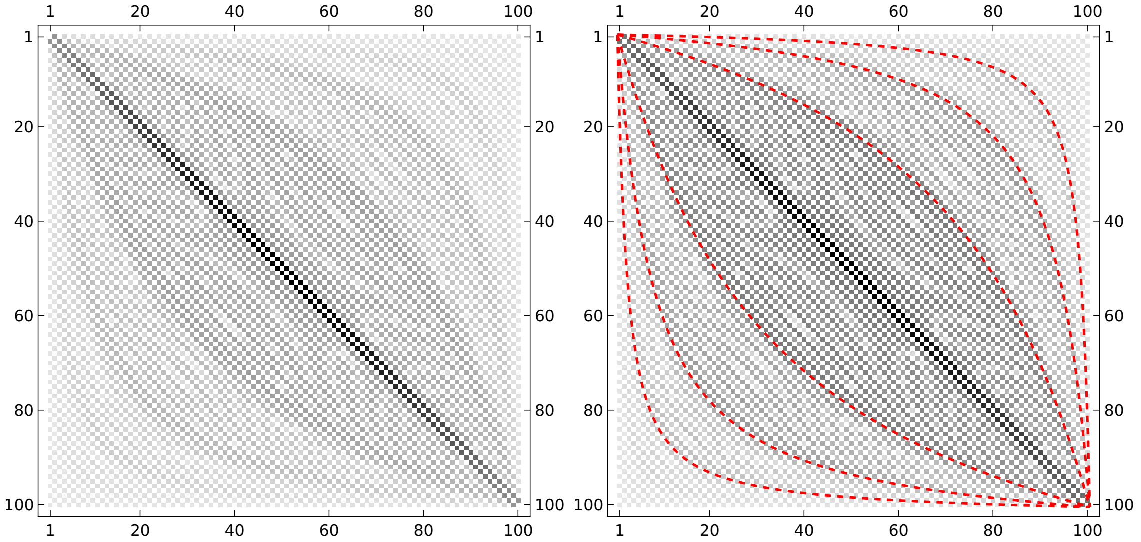

Figure 3.3: Matrix plot of the kernel of the lattice entanglement Hamiltonian for one interval of length $\ell = 100$ on a torus of length $L = 200$ and inverse temperature $\beta = 500$ in the Neveu-Schwarz sector. We see that besides the local part around the first sub-diagonal, there are bi-local terms coupling different points, localised around the solutions $\tilde{x}_k$ of Eq. (3.4) (red dashed lines) for $k = \pm 1, \pm 2, \pm 3$.

and system size $L = 200$ with anti-periodic boundary conditions. We see that besides the diagonal contributions, the matrix plot presents other terms located in the position of the conjugate points given by Eq. (3.4) for one interval.

The bi-local terms of a multi-interval entanglement Hamiltonian are instead provided by the limit of the off-diagonal blocks of the lattice EH kernel. We have (see Sec. 2.4) [134]

$$\sum_i \sum_j c_i^\dagger h_{i,j}^{(1,2)} c_j \sim \int \mathrm{d}x \left[\mathcal{S}^{\mathrm{bl}}(x)\, T^{\mathrm{bl}}(x, \tilde{x}_p) + \mathcal{C}^{\mathrm{bl}}(x)\, j^{\mathrm{bl}}(x, \tilde{x}_p) \right], \tag{3.67}$$

where $T^{\mathrm{bl}}(x, \tilde{x}_p)$ is the bi-local operator introduced in Eq. (2.48) and $j^{\mathrm{bl}}(x, \tilde{x}_p)$ is a different non-local operator defined in Eq. (2.119), both calculated in the conjugate point $\tilde{x}_p$. The limiting expressions $\mathcal{S}^{\mathrm{bl}}(x)$ and $\mathcal{C}^{\mathrm{bl}}(x)$ were found to be [134]

$$\mathcal{S}^{\mathrm{bl}}(x) \equiv \sum_{j \in A_2} \sin(k_F (j - i) s)\, h_{i,j}^{(1,2)}, \tag{3.68}$$

$$\mathcal{C}^{\mathrm{bl}}(x) \equiv \sum_{j \in A_2} \cos(k_F (j - i) s)\, h_{i,j}^{(1,2)}, \tag{3.69}$$

where from the comparison of Eq. (3.67) with the QFT prediction in, e.g., Eq. (2.36), we see that $\mathcal{S}^{\mathrm{bl}}(x)$ in Eq. (3.68) is expected to reproduce the bi-local weight and $\mathcal{C}^{\mathrm{bl}}(x)$ in

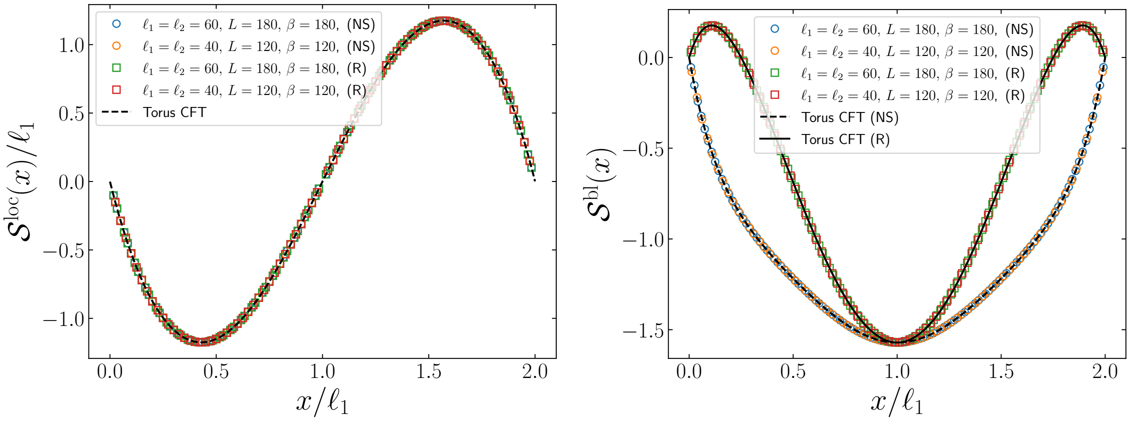

Figure 3.4: Benchmark of the analytical prediction for the negativity Hamiltonian of adjacent blocks of equal length on the torus for a Dirac fermion. In the left panels, the symbols are obtained from Eq. (3.65) while the dashed lines correspond to Eq. (3.23), rescaled by ℓ_1 in order to show the collapse for different sizes. In the right panel, we perform the same analysis for the bi-local part of the negativity Hamiltonian in the same geometry. The symbols are obtained from Eq. (3.70) while the dashed line corresponds to the weight function in the bi-local term in Eq. (3.26) and (3.27) for Ramond and Neveu-Schwarz boundary condition, respectively.

Eq. (3.69) is expected to vanish. Analogously to the local case, at half-filling the sum $\mathcal{C}^{\mathrm{bl}}(x)$ vanishes identically because of the checkerboard structure of the lattice entanglement kernel h, greatly simplifying the calculations.

3.3.3 Negativity Hamiltonian

In Sec. 2.4 we also argued that the limiting procedure of the lattice entanglement Hamiltonian $h_{i,j}$ is almost identical to the one of the lattice negativity Hamiltonian $\eta_{i,j}$ of Eqs. (2.106) and (2.107). Indeed, the limit only depends on the expansion of the lattice fermion of Eq. (2.109), which is identical also for the negativity Hamiltonian. The only difference is due to the presence of the imaginary factors $\mathrm{i}^{\Theta_1(x)}(-\mathrm{i})^{\Theta_1(\tilde{x}_p)}$ in Eq. (3.68).

Again for convenience we report here the results reviewed in Sec. 2.4 for the negativity temperature and the bi-local weight function, which we will use to check our predictions of Sec. 3.2. The weight function of the local term can be read from Eq. (3.65), while the bi-local terms take different signs and imaginary factors in different intervals. In order to compare the continuum limit of the lattice negativity Hamiltonian, in the special case of two intervals, Eq. (3.68) must be modified as follows (see Sec. 2.4)

$$\mathcal{S}^{\mathrm{bl}}(x) = \begin{cases} -\mathrm{i}\sum_j \sin(k_F(j-i)s)\,\eta^{(1,2)}_{i,j}, & x \in [a_1, b_1], \\ \mathrm{i}\sum_j \sin(k_F(j-i)s)\,\eta^{(2,1)}_{i,j}, & x \in [a_2, b_2]\,. \end{cases} \tag{3.70}$$

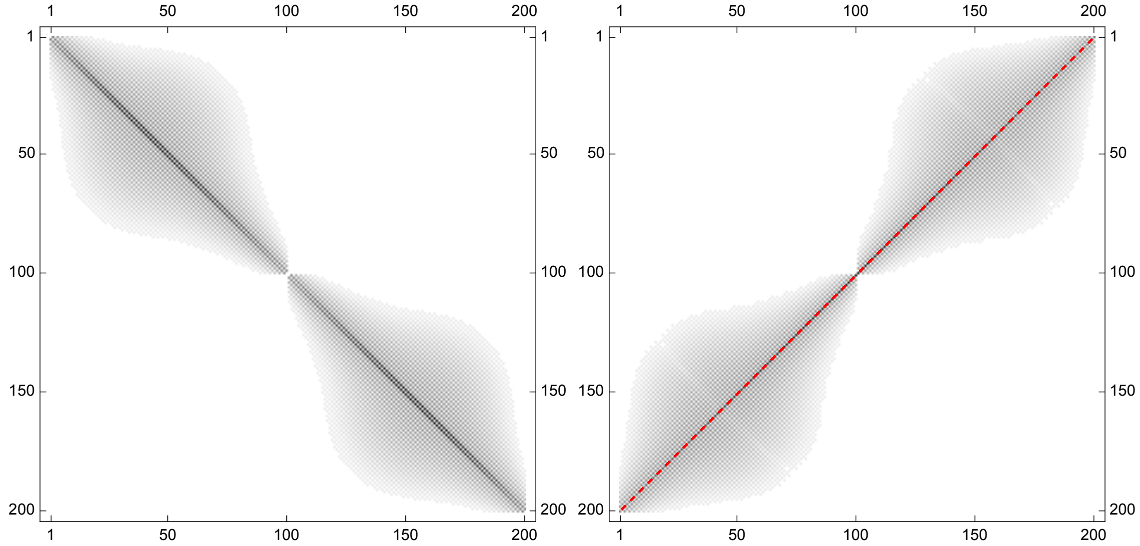

Figure 3.5: Matrix elements of the negativity Hamiltonian kernel η for two adjacent intervals of equal size, $\ell_1 = \ell_2 = 100$, in a system of size $L = 300$ and (inverse) temperature $\beta = 300$ with Neveu-Schwarz boundary conditions. The left panel corresponds to the real local part, while the right panel is the bi-local contribution. The dashed lines correspond to the only conjugate point obtained by solving Eq. (3.20).

Also for the negativity, at half-filling Eqs. (3.66) and (3.69) vanish identically. Now we can study the continuum limit of Eqs. (2.124) and (3.65) to check the field theory predictions for the negativity Hamiltonian, Eq. (3.21), for two disjoint intervals at finite temperature and size, in different regimes and both in a tripartite and bipartite geometry.

In Fig. 3.4 we consider two adjacent intervals of equal length $\ell_1 = \ell_2$, for several values of ℓ_1 and system size L and for different values of β, both with NS and R boundary conditions. In the left panel we find that the sum $\mathcal{S}^{\text{loc}}$ over the higher hoppings is in perfect agreement with the field-theoretical local effective inverse temperature in Eq. (3.31). In the right panel, we report a similar analysis for the non-local term of the negativity Hamiltonian for the same geometry: we compare $\mathcal{S}^{\text{bl}}$ in Eq. (3.70) with the field-theoretical weight function occurring in the bi-local term of the negativity Hamiltonian in Eq. (3.24), finding a good agreement. We stress that this geometry is quite interesting because the infinite non-local terms of the negativity Hamiltonian collapse on each other and we recover a bi-local structure, as we discussed in Sec. 3.2.1. This is also clear by studying the matrix plot of the kernel of the negativity Hamiltonian in Fig. 3.5 for two intervals of equal length, $\ell_1 = \ell_2 = 100$, $L = \beta = 300$, where the left panel corresponds to the real local part of Eq. (3.24) while the right panel describes the bi-local imaginary contribution. The structure differs from the one for the entanglement Hamiltonian shown in Fig. 3.3 and the dashed lines corresponds to the position of the single conjugate point.

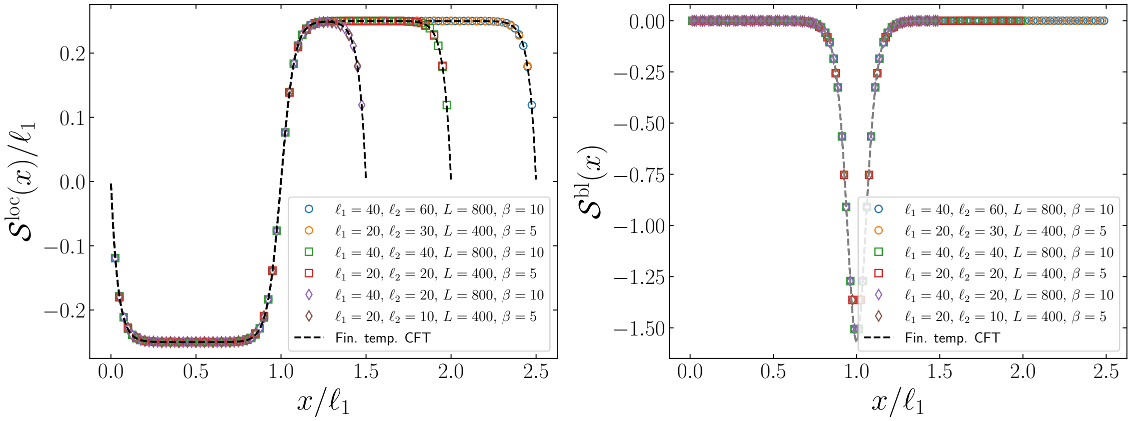

Figure 3.6: Local (left) and bi-local (right) inverse effective temperature of the negativity Hamiltonian, rescaled with ℓ_1 as a function of x/ℓ_1. The geometry we consider is $A = [1, \ell_1] \cup [\ell_1 + 1, \ell_1 + \ell_2]$ for different values of the ratio $\ell_1/\ell_2 = 0.5, 1, 1.5$. Here we fix the system size as $L/\ell_1 = 20$ and we rescale the inverse temperature β such that $\beta/\ell_1 = 1/4$. The data points are obtained by applying Eq. (3.65) (Eq. (3.70)) in the left (right) panel while the dashed curves correspond to the prediction in Eq. (3.34) (Eq. (3.36)).

In Fig. 3.6, we consider again two intervals for different ratios of the length $\ell_2/\ell_1 = 0.5, 1, 1.5$, with $\beta/\ell_1 = 1/4$. Here the system size is $L = 20\,\ell_1$, but since $L \gg \beta$, this amounts to study a thermal tripartite geometry on the infinite line, whose analytical predictions are reported in Eq. (3.29). Indeed, both the left and the right panels confirm what we find analytically in Eqs. (3.34) and (3.36) for the local and bi-local terms of the negativity Hamiltonian, respectively.

Before concluding the section, we want to check also the results for a bipartite geometry found in Sec. 3.2.4. In the top panels of Fig. 3.7, we consider a bipartition of a system of size L into two intervals of equal length, $\ell_1 = \ell_2 = L/2$, at inverse temperature $\beta = L$. This choice is particularly convenient because from Eq. (3.40) we can deduce that the infinite non-local terms are suppressed. Both the local and the bi-local component of the negativity Hamiltonian are in good agreement with Eq. (3.41) and Eq. (3.42), respectively. In the bottom panels, we consider a different geometry, $A = [-\ell_2/2, 0] \cup [1, \ell_1] \cup [\ell_1 + 1, \ell_1 + \ell_2/2] = A_1 \cup A_2 \cup A_3$, with $\ell_2 = L - \ell_1$ and we perform a partial transpose operation with respect to the middle interval $A_2 = [1, \ell_1]$. Since now A consists of three intervals, in the limit $L \to \infty$, we have two conjugate points $\tilde{x}^R_\pm$ given by Eq. (3.46). We can find the continuum limit by studying

$$\begin{aligned}
\mathcal{S}^{\rm bl}_{+}(x) &\equiv (-\mathrm{i})^{\delta_{\sigma,2}}(\mathrm{i})^{\delta_{\zeta,2}} \sum_{j\in A_\zeta} \sin(k_F(j-i)s)\, \eta^{(\sigma,\zeta)}_{i,j}, \quad (\sigma,\zeta) \in \{(1,3),(2,3),(3,2)\}, \\
\mathcal{S}^{\rm bl}_{-}(x) &\equiv (-\mathrm{i})^{\delta_{\sigma,2}}(\mathrm{i})^{\delta_{\zeta,2}} \sum_{j\in A_\zeta} \sin(k_F(j-i)s)\, \eta^{(\sigma,\zeta)}_{i,j}, \quad (\sigma,\zeta) \in \{(1,2),(2,1),(3,1)\}.
\end{aligned} \tag{3.71}$$

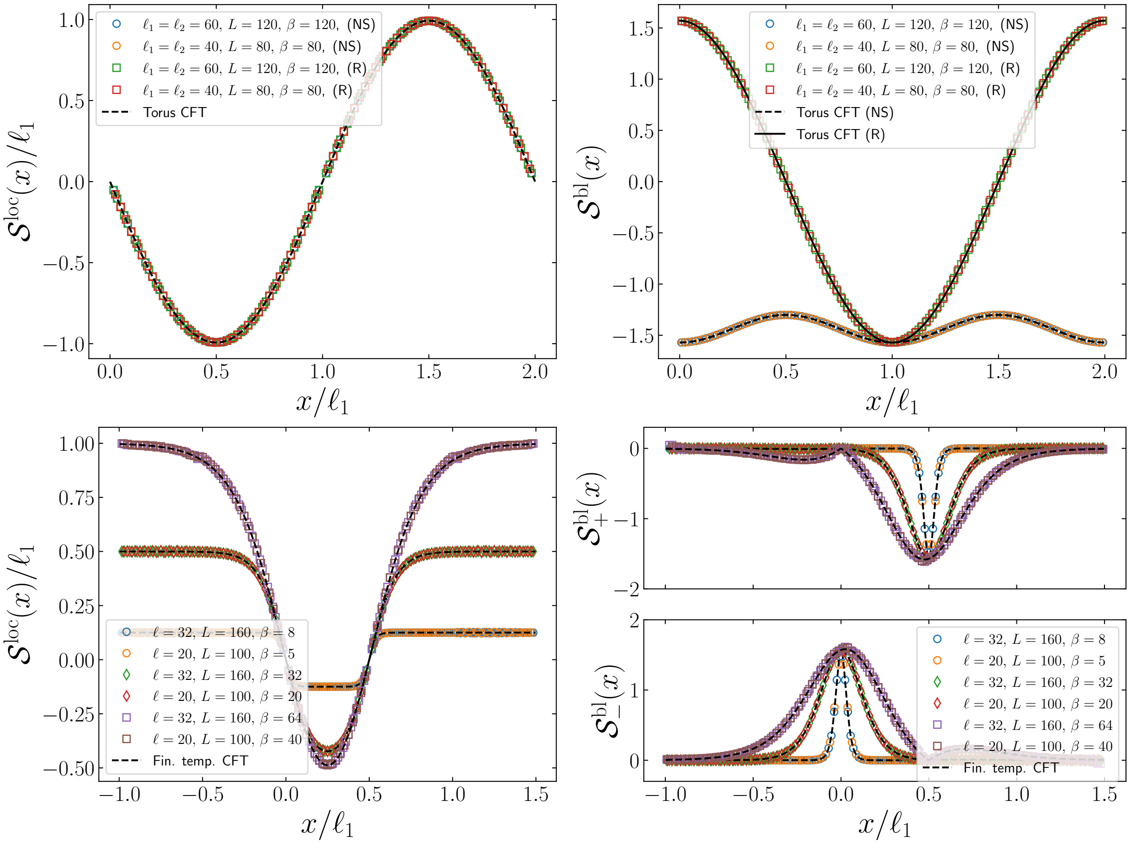

Figure 3.7: Top panels: Local and bi-local weight functions of the negativity Hamiltonian in the left and right panel, respectively. The geometry we are considering is a bipartition of a system of size L into two intervals of equal length, $\ell_1 = \ell_2 = L/2$, at inverse temperature $\beta = L$. The dashed line corresponds to Neveu-Schwarz boundary conditions, while the solid line describes a system with Ramond boundary conditions. The theoretical prediction are Eq. (3.41) (left) and Eq. (3.42) (right). Bottom panels: same analysis as above, for the geometry $A = [-\ell_2/2, 0] \cup [1, \ell_1] \cup [\ell_1 + 1, \ell_1 + \ell_2/2]$, with $\ell_2 = L - \ell_1$ and $A_2 = [1, \ell_1]$. It corresponds to a bipartite case, where now we fix $L \gg \beta$, such that in the left panel we can use our theoretical prediction in Eq. (3.45)(left) and Eq. (3.47) (right).

We observe a good agreement with Eq. (3.45) for the local part (left) and Eq. (3.47) for the bi-local weight (right).

3.3.4 Twisted negativity Hamiltonian

While for the entanglement and negativity Hamiltonians we presented both known and novel field-theoretical predictions and we could compare them with the continuum limit of the lattice results, for the twisted negativity Hamiltonian defined in Eq. (2.87), there are no field theory results. To avoid confusion with the notation, we stress that we define the negativity Hamiltonian related to $\rho_A^{R_1}$ as $\mathcal{N}_A$ and the one related to $\rho_A^{\widetilde{R}_1}$ as $\widetilde{\mathcal{N}}_A$. The advantage of studying $\rho_A^{\widetilde{R}_1}$ is that it is an Hermitian operator, so the logarithmic negativity recovers its original meaning of measure of the negativeness of the eigenvalues. Although we do not manage to derive its form theoretically, we perform a numerical study on the lattice using the limiting procedure described in Sec. 3.3.2. This allows us to identify which operators appear in the continuum limit of the lattice twisted negativity Hamiltonian and we can formulate a conjecture for the local weight functions in the case of two identical intervals on the plane. We comment that this approach allows us to identify all the operators appearing in $\widetilde{\mathcal{N}}_A$, contrarily to the analysis done in Ref. [81], where only the nearest neighbour negativity Hamiltonian has been considered.

Twisted negativity Hamiltonian on the plane

Let us first consider the twisted negativity Hamiltonian of the ground state on the infinite line, i.e, on the plane. The geometry under analysis $A = A_1 \cup A_2, A_1 = [-\ell, 0], A_2 = [0, \ell]$ consists of two adjacent intervals of identical length ℓ, and we perform a partial transpose operation on the first one, A_1.

As we did for $\mathcal{N}_A$, the continuum limit of $\widetilde{\mathcal{N}}_A$ is identical to the one of the entanglement Hamiltonian described in Sec. 3.3.2, since it depends only on the expansion of the lattice fermion in Eq. (2.109). However, differently from all the cases considered so far, we have numerically checked that even at half-filling $k_F = \frac{\pi}{2s}$, the twisted negativity kernel $\widetilde{\eta}$ in Eq. (2.108) does not present a checkerboard structure. For this reason, also the terms proportional to the sums $\mathcal{C}^{\mathrm{loc}}(x)$ in Eq. (3.66) and $\mathcal{C}^{\mathrm{bl}}(x)$ in Eq. (3.69) have to be computed. This is the first difference with respect to Ref. [81], where the study of only the nearest neighbour terms prevented them from finding the operator $\mathcal{C}^{\mathrm{bl}}(x)$. This also confirms that, in order to recover the continuum limit correctly, a careful treatment of the long-range hoppings has to be taken into account. Therefore, besides the energy density $T_{00}(x)$ in Eq. (2.37) and the bi-local operator $T^{\mathrm{bl}}(x, y)$ in Eq. (2.48), the continuum limit will contain also an imaginary local chemical potential term proportional to the number operator $N(x)$ in Eq. (2.113) and a term proportional to the operator $j^{\mathrm{bl}}(x, y)$ defined in Eq. (2.119). Although we cannot derive the form of the weight functions of these operators explicitly, we provide a conjecture that very accurately matches numerical data on the lattice. Indeed, the twisted negativity Hamiltonian reads

$$\begin{aligned}\widetilde{\mathcal{N}}_A = \int \mathrm{d}x\, \beta^R_{\mathrm{loc}}(x)\, T_{00}(x) + \mathrm{i} \int \mathrm{d}x\, \tilde{\mu}(x)\, N(x) \\ + \int \mathrm{d}x\, \tilde{\beta}_{\mathrm{bl}}(x)\, T^{\mathrm{bl}}(x, \tilde{x}^R_p) + \mathrm{i} \int \mathrm{d}x\, \tilde{\mu}_{\mathrm{bl}}(x)\, j^{\mathrm{bl}}(x, \tilde{x}^R)\end{aligned} \tag{3.72}$$

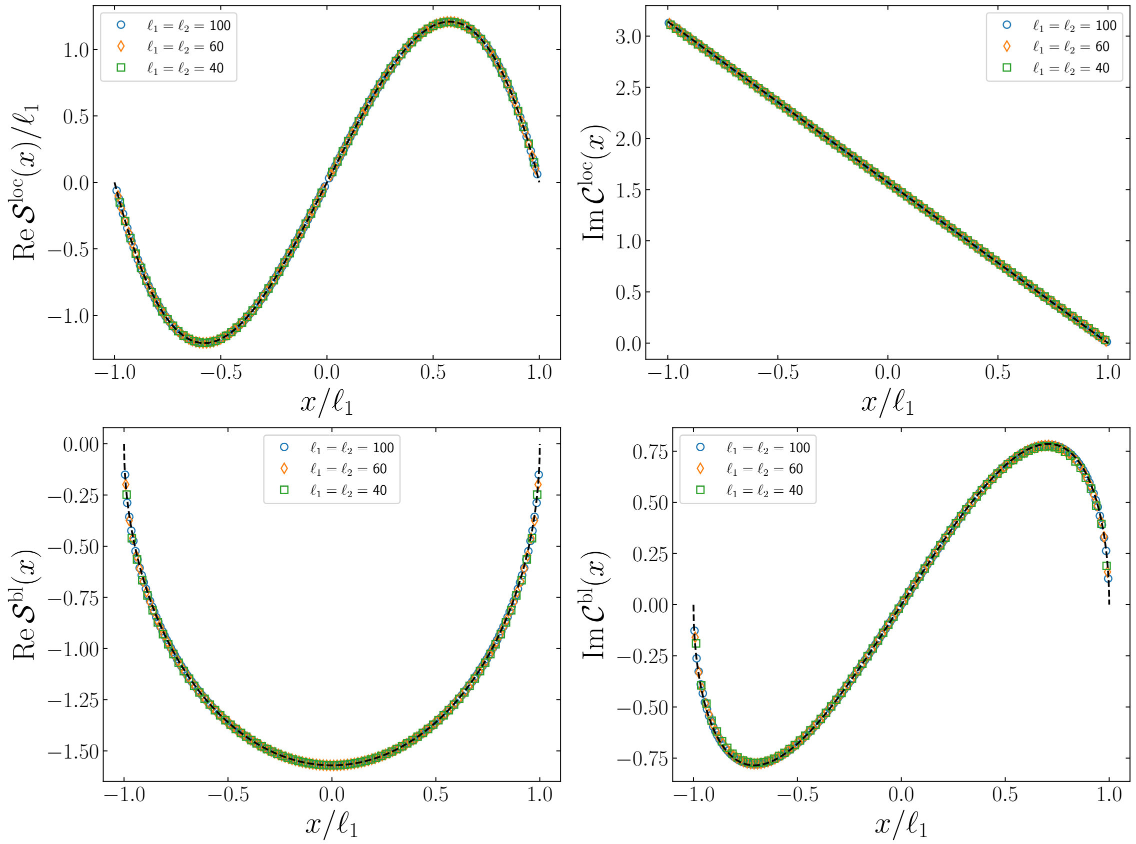

Figure 3.8: Benchmark of the analytic prediction for the twisted negativity Hamiltonian $\widetilde{\mathcal{N}}_A$ for two adjacent intervals of equal length on the infinite line. The symbols correspond to the numerical data obtained using Eqs. (3.65) and (3.66) for the top left and right panel, respectively, and Eqs. (3.68) and (3.69) for the bottom left and right. The solid lines are our analytical conjectures in Eqs. (3.73) (top left) and (3.74) (top right) for the local terms and in Eqs. (3.75) (bottom left) and (3.76) (bottom right) in the bi-local part.

where the inverse negativity temperature $\beta^R_{\mathrm{loc}}(x)$ is given by

$$\beta^R_{\mathrm{loc}}(x) = \frac{1}{z^{R\prime}(x)}, \tag{3.73}$$

with $z^R(x)$ given in Eq. (2.88), i.e. its functional form is the same as for $\mathcal{N}_A$. Despite being localised around the same conjugate point $\tilde{x}^R$ in Eq. (3.38) as the negativity Hamiltonian $\mathcal{N}_A$, the other weight functions are different and we report them here

$$\tilde{\mu}(x) = \frac{1}{4}\left(1 - \frac{x}{\ell}\right), \tag{3.74}$$

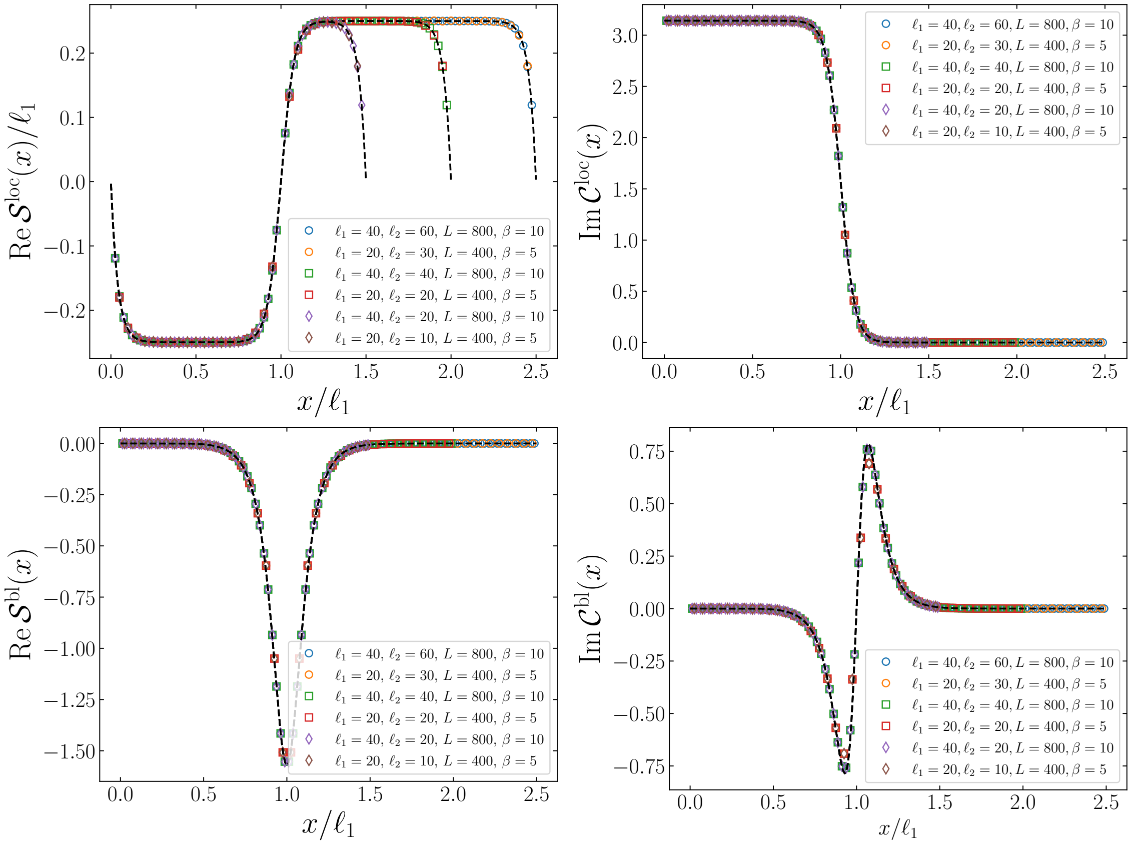

Figure 3.9: Same benchmark of the analytic prediction for the twisted negativity Hamiltonian $\widetilde{\mathcal{N}}_A$ as in Fig. 3.8 but at finite temperature. The geometry we consider is $A = [1, \ell_1] \cup [\ell_1 + 1, \ell_1 + \ell_2]$ for different values of the ratio $\ell_1/\ell_2 = 0.5, 1, 1.5$. The system size is fixed as $L/\ell_1 = 20$ and we rescale the inverse temperature β such that $\beta/\ell_1 = 1/4$. The analytical predictions have been obtained by doing a conformal mapping from the plane to an infinite cylinder of circumference β in Eq. (3.79).

$$\tilde{\beta}_{\mathrm{bl}}(x) = -\frac{1}{4}\sqrt{1 - \frac{x^2}{\ell^2}}, \tag{3.75}$$

$$\tilde{\mu}_{\mathrm{bl}}(x) = \frac{1}{4}\frac{x}{\ell}\sqrt{1 - \frac{x^2}{\ell^2}}. \tag{3.76}$$

The weight function of the number operator $N(x)$ is the same that was conjectured in [81], while the weight functions for $T^{\mathrm{bl}}(x, \tilde{x}^R)$ and $j^{\mathrm{bl}}(x, \tilde{x}^R)$ are different and, we stress again, in order to recover them, it is important to sum over all the elements of the kernel of the negativity Hamiltonian, as done in Eq. (3.68). We also benchmark the analytical predictions from Eq. (3.72) in Fig. 3.8. The good agreement between the lattice computations and Eq. (3.72) supports our conjecture.

Our prediction for equal intervals can be mapped into a geometry with adjacent intervals of different length using a Möbius transformation. For $A = A_1 \cup A_2, A_1 = [a,b], A_2 = [b,c]$, the Möbius transformation

$$\xi(z) = \frac{(z-b)(c-a)\ell}{(z-b)(a-2b+c)+2(b-a)(c-b)}\,, \tag{3.77}$$

maps A into the subsystem $\xi(A_1) = [-\ell, 0], \xi(A_2) = [0,\ell]$, for which Eq. (3.72) is valid. In order to properly apply the transformation, we also need to consider the Jacobians arising from the transformation of the fields. As discussed in Sec. 3.1, to understand the transformations of the fields it is convenient to pass to Euclidean time and consider, for example, only the holomorphic component. Under this conformal mapping, the operators appearing in Eq. (3.72) transform as

$$\begin{aligned} N(z) &= \xi'(z)\, N(\xi(z)), \\ T^{\mathrm{bl}}(z,w) &= \xi'(z)^{1/2}\, \xi'(w)^{1/2}\, T^{\mathrm{bl}}(\xi(z),\xi(w)), \\ j^{\mathrm{bl}}(z,w) &= \xi'(z)^{1/2}\, \xi'(w)^{1/2}\, j^{\mathrm{bl}}(\xi(z),\xi(w)), \end{aligned} \tag{3.78}$$

where we have used that the fermions $\psi, \psi^\dagger$ transform as $\psi(z) = \left(\frac{\partial\xi}{\partial z}\right)^{1/2} \psi(\xi(z))$ (and analogously for the anti-holomorphic part). Therefore, taking into account Eq. (3.78) and the Jacobians of the transformation, we obtain the following expression for the twisted negativity Hamiltonian of two intervals of arbitrary length on the infinite line

$$\begin{aligned} \widetilde{\mathcal{N}}_A = &\int \mathrm{d}x\, \beta^R_{\mathrm{loc}}(x)\, T_{00}(x) + \mathrm{i}\int \mathrm{d}x\, \tilde{\mu}(\xi(x))\, N(x) \\ &+ \int \mathrm{d}x\, \tilde{\beta}_{\mathrm{bl}}(\xi(x)) \sqrt{\frac{\xi(x)}{\xi(\tilde{x}^R)}}\, T^{\mathrm{bl}}(x,\tilde{x}^R) + \mathrm{i}\int \mathrm{d}x\, \tilde{\mu}_{\mathrm{bl}}(x) \sqrt{\frac{\xi(x)}{\xi(\tilde{x}^R)}}\, j^{\mathrm{bl}}(x,\tilde{x}^R), \end{aligned} \tag{3.79}$$

where $\beta^R_{\mathrm{loc}}(x) = 1/\partial_x z^R(\xi(x))$ with z^R given by Eq. (2.88). By doing another conformal mapping $\xi(x) \to e^{\frac{2\pi}{\beta}x}$ in Eq. (3.79), we can obtain the result for two intervals on the infinite line at finite temperature, as shown in Fig. 3.1. We report a check of our conjecture in Fig. 3.9 for different ratios of the length $\ell_2/\ell_1 = 0.5, 1, 1.5$, with $\beta/\ell_1 = 1/4$ and $L = 20\,\ell_1$. Beyond the good agreement, we observe that the weight function of the number operator $N(x)$ drastically changes: the linear behaviour in x found at $T = 0$ becomes a kink interpolating from π for $x < \ell_1$ to 0 for larger x. To summarise, starting from our conjecture for the twisted negativity Hamiltonian for two intervals of equal size on the infinite line, through a series of conformal mappings, we are able to find an expression also for the finite temperature case, which is a concrete example of a global mixed state.

3.4 Final remarks

In this Chapter we have continued the analysis initiated in the previous one and in Ref. [81] about the study of the negativity Hamiltonian, i.e. an operatorial characterisation of entanglement in mixed states. The most relevant novelty introduced here is the study of the entanglement in thermal states, which represent genuine examples of globally mixed states. We studied the negativity Hamiltonian of free massless Dirac fermions on a torus, for an arbitrary set of disjoint intervals at generic temperature. The structure of the negativity Hamiltonian exhibits a pattern similar to the entanglement Hamiltonian found in the same geometry in Ref. [142, 143]: in addition to a local term, each point is non-locally coupled to an infinite but discrete set of other points. However, contrarily to what happens for the entanglement Hamiltonian, when the reversed and non-reversed subsystems have the same length, the bi-local solutions collapse on each other and we find only a finite number of bi-local terms, which couple each point only to another one in each other interval.

We also analysed in detail the negativity Hamiltonian in a bipartite configuration. If the state is pure, the relation between the entanglement entropy and the negativity is well-known [77] and we retrieve it here. If the temperature is different from zero, a bipartite system is the first non-trivial example in which the negativity becomes essential to proper detect the quantum correlations. Also in this case, we found an infinite number of bi-local contributions, which reduce to one single bi-local solution only in the case of infinite system size. Our analytical findings are supported by exact numerical computations in a free-fermion chain.

Another main result presented in this Chapter is the negativity Hamiltonian computed from the twisted partial transpose, cf. Eq (2.84). Through a careful numerical analysis, we identified the local and bi-local operators and their weight functions for two intervals on the infinite line both at zero and finite temperature. It would be interesting to derive analytically the conjectured formulae for the twisted negativity Hamiltonian, e.g. using the methods discussed in Sec. 3.A.

This study about the negativity Hamiltonian adds an important contribution to the operatorial characterisation of the mixed state entanglement, but there is still much work to do. For example, a challenging task is to exploit the mild non-locality of the negativity Hamiltonian together with the Hamiltonian reconstruction methods already used in [36–38] to reconstruct the negativity spectrum. Similarly, it is still an open problem to derive the conformal negativity spectrum [149] from the negativity Hamiltonian, as instead done for the entanglement spectrum in Ref. [150]. Another interesting direction is the study of the negativity Hamiltonian in higher dimensional systems, following what has been done for the entanglement Hamiltonian [137]. Finally, it would be also interesting to study whether one can define a notion of modular flow [23, 97, 151] for the partial transpose reduced density matrix and its eventual connections with the negativity Hamiltonian.

3.A The resolvent method for the negativity Hamiltonian

In Ref. [87], the field-theoretical prediction for the kernel H_A of the entanglement Hamiltonian on the plane in Eq. (2.36) was obtained from the knowledge of the *resolvent* of the Green function C_A restricted to the subsystem (see also [98, 142–144, 147, 151]). In this appendix we show how to generalise the resolvent method of Ref. [87] to the negativity Hamiltonian in the case of multiple intervals on the plane, confirming the validity of the construction of Ref. [81] reviewed in Sec. 2.3 that we have used in Secs. 2.3 and 3.2.

For our purposes, we recast the resolvent method in terms of the partially reversed covariance matrix $\Gamma_A^{R_1}$. To fix the ideas, we present the calculation for chiral fermions. Applying the partial reversal procedure in Eq. (2.105) to the Green function we find

$$\Gamma_A^{R_1}(x,y) = -\frac{1}{\mathrm{i}\pi}\mathcal{P}\frac{1}{x-y}\,\mathrm{i}^{\Theta_1(x)}\,\mathrm{i}^{\Theta_1(y)}\,, \tag{3.80}$$

where the function $\Theta_1(x)$, defined in Eq. (3.22), is equal to 1 only for $x \in A_1$, 0 otherwise and $\mathcal{P}$ denotes Cauchy's principal value. Recall from the main text that the kernel of the negativity Hamiltonian can be related via Peschel's formula in Eq. (2.107) to the reversed covariance matrix $\Gamma_A^{R_1}$. To apply Eq. (2.107) in the continuum theory, we first consider a single eigenvalue g of $\Gamma_A^{R_1}$. For the entanglement Hamiltonian, in [87] it was used the fact that the spectrum of the Green function is real and contained in $[0,1]$. In the case of the negativity Hamiltonian, we can use the knowledge that the eigenvalues of $\Gamma_A^{R_1}$ are contained in the unit complex disc $|g|<1$ [120], as depicted in Fig. 3.10. Then, Peschel's formula for the single eigenvalue can be rewritten using Cauchy's theorem as

$$\log[1+g]-\log[1-g] = \frac{1}{2\pi\mathrm{i}}\oint_{\mathcal{C}}\mathrm{d}z\left[\frac{1}{z-g}-\frac{1}{z+g}\right]\log(1+z)\,, \tag{3.81}$$

where the branch cut of the logarithm is taken to go from $-\infty$ to -1. Since $|g|<1$, the contour of integration $\mathcal{C}$ in Eq. (3.81) can always be taken to avoid the branch cut (see Fig. 3.10) and therefore can be deformed continuously to integrate along the branch cut and on a small circle at infinity. Denoting the upper and lower branches of the complex logarithm as $\log^+$ and $\log^-$ respectively, and using the fact that the difference of the two branches is $\log^+ - \log^- = 2\pi\mathrm{i}$ we find for every eigenvalue g of $\Gamma_A^{R_1}$

$$\begin{aligned}\log[1+g]-\log[1-g] &= \frac{1}{2\pi\mathrm{i}}\int_{-\infty}^{-1}\mathrm{d}z\left[\frac{1}{z-g}-\frac{1}{z+g}\right]\left[\log^+(1+z)-\log^-(1+z)\right]\\ &= -\int_1^{\infty}\mathrm{d}z\left[\frac{1}{g-z}+\frac{1}{g+z}\right].\end{aligned} \tag{3.82}$$

Since this holds for every eigenvalue, it holds also for the operator, leading finally to the expression for the kernel of the negativity Hamiltonian

$$N_A(x,y) = \frac{1}{2\pi}\log\left[\frac{\mathrm{Id}_A+\Gamma_A^{R_1}}{\mathrm{Id}_A-\Gamma_A^{R_1}}\right] = -\frac{1}{2\pi}\int_1^{\infty}\mathrm{d}\zeta\,\left[R(\zeta;x,y)+R(-\zeta;x,y)\right], \tag{3.83}$$

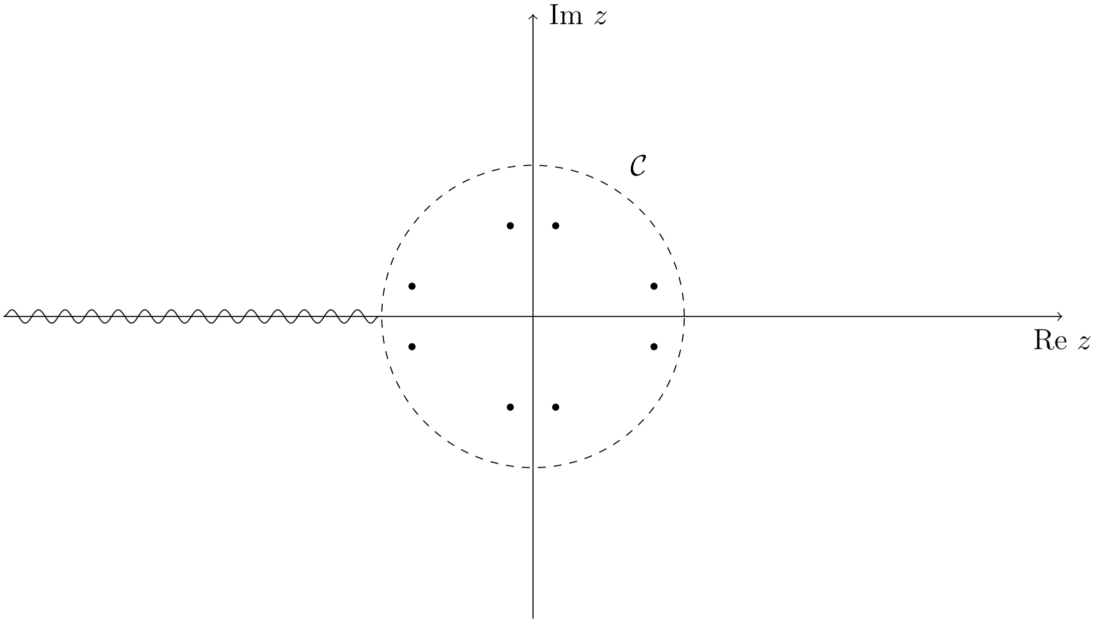

Figure 3.10: Representation of the contour of integration in Eqs. (3.81). The dashed line represents the contour $\mathcal{C}$ around the poles (small black dots), while the wavy line denotes the branch cut of $\log(1+z)$.

where we have introduced the resolvent of the partially reversed covariance matrix of Eq. (3.80)

$$R(\zeta;x,y)=\frac{1}{\Gamma_A^{R_1}-\zeta\mathrm{Id}_A}=\left[-\frac{1}{\mathrm{i}\pi}\mathcal{P}\frac{\mathrm{i}^{\Theta_1(x)}\,\mathrm{i}^{\Theta_1(y)}}{x-y}-\zeta\delta(x-y)\right]^{-1}. \tag{3.84}$$

Note that throughout this appendix, $2\pi N_A(x,y)$ corresponds to the continuum limit of η defined in Eq. (2.106).

In order to find the explicit form of the resolvent in Eq. (3.84), we need to solve a singular integral equation. By construction, the resolvent (3.84) satisfies

$$-\zeta R(\zeta;x,y)-\frac{\mathrm{i}^{\Theta_1(y)}}{\mathrm{i}\pi}\mathcal{P}\int\mathrm{d}z\,\frac{R(\zeta;x,z)\,\mathrm{i}^{\Theta_1(z)}}{z-y}=\delta(x-y)\,. \tag{3.85}$$

Multiplying both sides by $(-)\mathrm{i}^{\Theta_1(y)}$

$$\zeta R(\zeta;x,y)\,\mathrm{i}^{\Theta_1(y)}+\frac{(-1)^{\Theta_1(y)}}{\mathrm{i}\pi}\mathcal{P}\int\mathrm{d}z\,\frac{R(\zeta;x,z)\,\mathrm{i}^{\Theta_1(z)}}{z-y}=(-)\mathrm{i}^{\Theta_1(y)}\,\delta(x-y)\,, \tag{3.86}$$

we see that Eq. (3.86) has the form of a *characteristic singular integral equation* [99]

$$a(y)\phi(y)+\frac{b(y)}{\mathrm{i}\pi}\mathcal{P}\int\mathrm{d}z\,\frac{\phi(z)}{z-y}=f(y)\,, \tag{3.87}$$

in the unknown function $\phi(y) = \mathrm{i}^{\Theta_1(y)} R(\zeta; x, y)$, with the identification $a = \zeta$, $b(y) = (-1)^{\Theta_1(y)}$ and $f(y) = (-)\mathrm{i}^{\Theta_1(y)}\,\delta(x-y)$. Comparing Eq. (3.86) with the analogous one for the entanglement Hamiltonian in Ref. [87], we see that the most important difference is the presence of the function $b(y) = (-1)^{\Theta_1(y)}$ in front of the Cauchy kernel, which changes sign if the interval is reversed. Now, we show that this function is precisely responsible for the inversion of the extrema a_j, b_j of the partially reversed intervals in the expression of the negativity Hamiltonian.

To solve Eq. (3.86), we introduce [99]

$$G(y) = \frac{a(y)-b(y)}{a(y)+b(y)} = \frac{\zeta-(-1)^{\Theta_1(y)}}{\zeta+(-1)^{\Theta_1(y)}} = \left[\frac{\zeta-1}{\zeta+1}\right]^{(-1)^{\Theta_1(y)}}, \tag{3.88}$$

and the solution of Eq. (3.87) will be expressed in terms of the function [99]

$$\begin{aligned}
\omega(y) &= \sqrt{a^2(y)-b^2(y)}\, \exp\left\{\frac{1}{2\pi i}\mathcal{P}\int \mathrm{d}z\, \frac{\log G(z)}{z-y}\right\} \\
&= \sqrt{\zeta^2-1}\, \exp\left\{\frac{1}{2\pi i}\log\frac{\zeta-1}{\zeta+1}\,\mathcal{P}\int \mathrm{d}z\, \frac{(-1)^{\Theta_1(z)}}{z-y}\right\} \\
&= \sqrt{\zeta^2-1}\, \exp\left\{-\frac{1}{2\pi i}\log\frac{\zeta-1}{\zeta+1}\left[\sum_{i\in A_2}\log\left|\frac{y-a_i}{y-b_i}\right| - \sum_{j\in A_1}\log\left|\frac{y-a_j}{y-b_j}\right|\right]\right\} \\
&= \sqrt{\zeta^2-1}\, \exp\left\{-\frac{z^R(y)}{2\pi i}\log\frac{\zeta-1}{\zeta+1}\right\},
\end{aligned} \tag{3.89}$$

where z^R is precisely the function in Eq. (2.88), obtained by exchanging the extrema a_j, b_j of the reversed intervals in the expression of Eq. (2.20). As we can see, the factor $(-1)^{\Theta_1(z)}$ in the second row of Eq. (3.89) is responsible for the exchange of the extrema in Eq. (2.88).

The general solution of the characteristic singular equation (3.87) is [99]

$$\phi(y) = \frac{1}{a^2(y)-b^2(y)}\left[a(y)f(y) - \frac{b(y)\omega(y)}{\mathrm{i}\pi}\,\mathcal{P}\int \mathrm{d}z\, \frac{f(z)}{(z-y)\,\omega(z)}\right], \tag{3.90}$$

which specialised to our Eq. (3.86) gives

$$\begin{aligned}
R(\zeta; x, y) &= \frac{(-\mathrm{i})^{\Theta_1(y)}}{\zeta^2-1}\left[-\zeta\,\delta(x-y)\,\mathrm{i}^{\Theta_1(y)} - \frac{(-1)^{\Theta_1(y)}\omega(y)}{\mathrm{i}\pi}\,\mathcal{P}\int \mathrm{d}z\, \frac{\delta(x-z)\,(-)\mathrm{i}^{\Theta_1(z)}}{(z-y)\,\omega(z)}\right] \\
&= \frac{1}{1-\zeta^2}\left[\zeta\,\delta(x-y) - \frac{1}{\mathrm{i}\pi}\,\frac{\omega(y)}{\omega(x)}\,\mathcal{P}\frac{1}{(x-y)}\,\mathrm{i}^{\Theta_1(x)}\mathrm{i}^{\Theta_1(y)}\right] \\
&= \frac{1}{1-\zeta^2}\left[\zeta\,\delta(x-y) - \frac{1}{\mathrm{i}\pi}\,\mathcal{P}\frac{1}{(x-y)}\,\mathrm{i}^{\Theta_1(x)}\mathrm{i}^{\Theta_1(y)}\, \exp\left\{\frac{1}{2\pi i}\log\frac{\zeta-1}{\zeta+1}\left[z^R(x)-z^R(y)\right]\right\}\right].
\end{aligned} \tag{3.91}$$

If we compare the resolvent for the negativity Hamiltonian on the plane in Eq. (3.86) with the one obtained in the context of the entanglement Hamiltonian in [87], we see that the main differences are the presence of the imaginary factors $\mathrm{i}^{\Theta_1(x)}\mathrm{i}^{\Theta_1(y)}$ and the substitution of the function (2.20) with the one in Eq. (2.88) where the extrema of the reversed intervals are exchanged.

With the knowledge of the resolvent in Eq. (3.91), we can finally obtain the kernel of the negativity Hamiltonian by substituting it in Eq. (3.83). Changing variables as $s = \frac{1}{2\pi}\log\frac{\zeta-1}{\zeta+1}$ we find, formally

$$N_A(x,y) = -\frac{\mathrm{i}}{2\pi}\int_{-\infty}^{+\infty}\mathrm{d}s\,\frac{e^{-\mathrm{i}\,s\left[z^R(x)-z^R(y)\right]}}{x-y}\,\mathrm{i}^{\Theta_1(x)}\mathrm{i}^{\Theta_1(y)} = -\mathrm{i}\,\frac{\delta\big(z^R(x)-z^R(y)\big)}{x-y}\,\mathrm{i}^{\Theta_1(x)}\mathrm{i}^{\Theta_1(y)}\,. \tag{3.92}$$

In the formal expression of the kernel $N_A(x,y)$, the Dirac delta is calculated in the solution of the equation $z^R(x) = z^R(y)$. However, when dealing with the trivial solution $y = x$ which corresponds to the local part of the kernel, Eq. (3.92) is proportional to the product of distributions $\delta(x-y)/(x-y)$ with coincident singular support. As discussed in Ref. [87], such an expression is ambiguous and it is necessary to regularise it. Following Ref. [87], the product is the distribution T that satisfies the algebraic distributional equation $(x-y)T = \delta(x-y)$, whose solution is $T = -\partial_x\delta(x-y) + \kappa\,\delta(x-y)$, where κ is an arbitrary constant which is fixed by requiring that the local part of N_A is Hermitian [87]. For this reason, we find it more convenient to explicitly antisymmetrise the kernel in the variables x and y, which cancels the $\kappa\,\delta(x-y)$ contribution.

We also use the fact that the function z^R in Eq. (2.88) has the property that it is monotonically decreasing in the reversed intervals A_1 and monotonically increasing outside, which implies for its derivative

$$\left|\big(z^R(x)\big)'\right| = (-1)^{\Theta_1(x)}\,\big(z^R(x)\big)' \equiv \frac{(-1)^{\Theta_1(x)}}{\beta^R_{\mathrm{loc}}(x)}\,. \tag{3.93}$$

Then, by replacing Eq. (3.93) in the term of Eq. (3.92) corresponding to the trivial solution $y = x$ we find

$$\begin{aligned} N_A^{\mathrm{loc}}(x,y) &= -\frac{\mathrm{i}}{2}\left[\frac{(-1)^{\Theta_1(y)}}{\left|\big(z^R(y)\big)'\right|}\frac{\delta(x-y)}{x-y} - \frac{(-1)^{\Theta_1(x)}}{\left|\big(z^R(x)\big)'\right|}\frac{\delta(y-x)}{y-x}\right] \\ &= \frac{\mathrm{i}}{2}\Big[\beta^R_{\mathrm{loc}}(y)\,\partial_x\delta(y-x) - \beta^R_{\mathrm{loc}}(x)\,\partial_y\delta(x-y)\Big]\,, \end{aligned} \tag{3.94}$$

which, when plugged in the expression for the negativity Hamiltonian reproduces the local part

$$\begin{aligned} \mathcal{N}_A^{\mathrm{loc}} &= \int_A \mathrm{d}x\int_A \mathrm{d}y\,\psi^\dagger(x)\,N_A^{\mathrm{loc}}(x,y)\,\psi(y) \\ &= \int_A \mathrm{d}x\,\beta^R_{\mathrm{loc}}(x)\left[-\frac{\mathrm{i}}{2}:\!\Big(\partial_x\psi^\dagger(x)\psi(x) - \psi^\dagger(x)\partial_x\psi(x)\Big)\!:\right]\,. \end{aligned} \tag{3.95}$$

The $n-1$ non-trivial solutions $y=\tilde{x}_p^R$ of the equation $z^R(y)=z^R(x)$ instead give rise to the bi-local terms. Explicitly anti-symmetrising the expression in the variables x, y gives

$$\begin{aligned} N_A^{\mathrm{bl}}(x,y) &= -\frac{\mathrm{i}}{2}\frac{1}{x-y}\sum_{p=1}^{n-1}\left[\frac{\delta(y-\tilde{x}_p^R)}{\left|\big(z^R(\tilde{x}_p^R)\big)'\right|}+\frac{\delta(x-\tilde{y}_p^R)}{\left|\big(z^R(\tilde{y}_p^R)\big)'\right|}\right]\mathrm{i}^{\Theta_1(x)}\mathrm{i}^{\Theta_1(y)} \\ &= -\frac{\mathrm{i}}{2}\sum_{p=1}^{n-1}\Bigg[\mathrm{i}^{\Theta_1(x)}(-\mathrm{i})^{\Theta_1(\tilde{x}_p^R)}\frac{\beta^R_{\mathrm{loc}}(\tilde{x}_p^R)}{x-\tilde{x}_p^R}\,\delta(y-\tilde{x}_p^R) \\ &\qquad\qquad -\mathrm{i}^{\Theta_1(y)}(-\mathrm{i})^{\Theta_1(\tilde{y}_p^R)}\frac{\beta^R_{\mathrm{loc}}(\tilde{y}_p^R)}{y-\tilde{y}_p^R}\,\delta(x-\tilde{y}_p^R)\Bigg]\,, \end{aligned} \tag{3.96}$$

leading to the bi-local part of the negativity Hamiltonian

$$\begin{aligned} \mathcal{N}_A^{\mathrm{bl}} &= \int_A \mathrm{d}x\int_A \mathrm{d}y\,\psi^\dagger(x)\,N_A^{\mathrm{bl}}(x,y)\,\psi(y) \\ &= \sum_{p=1}^{n-1}\int \mathrm{d}x\,\frac{\beta^R_{\mathrm{loc}}(\tilde{x}_p^R)}{x-\tilde{x}_p^R}\,\mathrm{i}^{\Theta_1(x)}(-\mathrm{i})^{\Theta_1(\tilde{x}_p^R)}\,\left[-\frac{\mathrm{i}}{2}\,{:}\Big(\psi^\dagger(x)\psi(\tilde{x}_p^R)-\psi^\dagger(\tilde{x}_p^R)\psi(x)\Big){:}\right]\,. \end{aligned} \tag{3.97}$$

This resolvent procedure could be analogously extended to the case on the cylinder or on the torus considered in Sec. 3.2. Therefore, we can formally justify not only the construction introduced in Ref. [81] to compute the negativity Hamiltonian on the plane, but also at finite temperature or size, proving the correctness of the results found in this Chapter.

3.B Mathematical identities

We report here the main mathematical tools we have used throughout the Chapter. The Weierstrass zeta function is defined by [152]

$$\zeta(x)=\frac{1}{z}+\sum_{\lambda\neq 0}\left(\frac{1}{z+\lambda}-\frac{1}{\lambda}+\frac{z}{\lambda^2}\right). \tag{3.98}$$

It enters in the class of elliptic functions and it is quasiperiodic, i.e. it satisfies

$$\zeta(x+P_i)=\zeta(x)+2\zeta(P_i/2), \tag{3.99}$$

where P_i, $i=1,2$, are the fundamental periods. In the case of interest for us, $P_1=L$ and $P_2=i\beta$. In order to prove the equality in Eq. (3.3), we have used the following representation of the Weierstrass zeta function through Jacobi functions

$$\zeta(x)=\frac{2x\pi}{L\beta}-\mathrm{i}\frac{2x\zeta(\mathrm{i}\beta/2)}{\beta}+\frac{\pi}{L}\frac{\vartheta_1'\big(\frac{\pi}{L}x|q\big)}{\vartheta_1\big(\frac{\pi}{L}x|q\big)}. \tag{3.100}$$

For completeness, we also report here the definition of the Weierstrass sigma function used in Eq. (3.2)

$$\sigma(x) = x \prod_{\lambda \neq 0} \left[\left(1 + \frac{x}{\lambda}\right) e^{-\frac{x}{\lambda} + \frac{1}{2}(\frac{x}{\lambda})^2} \right]. \tag{3.101}$$

Also the equality in Eq. (3.2) can be proven by using the following property

$$\sigma(x) = \frac{L}{\pi} e^{\zeta(L/2)\frac{x^2}{L}} \frac{\vartheta_1\left(\frac{\pi}{L}x \middle| q\right)}{\vartheta_1'\left(0 \middle| q\right)}. \tag{3.102}$$

We also define the Jacobi theta functions $\theta_1(z|u)$ [152]

$$\theta_1(u|q) = = \sum_{k=-\infty}^{\infty} (-1)^{k-1/2} q^{\left(k+\frac{1}{2}\right)^2} e^{\mathrm{i}(2k+1)u}, \tag{3.103}$$

which satisfies the following asymptotic behaviour in the limit $\tau \to 0$

$$\vartheta_1\left(u \middle| q\right) \sim \frac{2\,\mathrm{i}}{\sqrt{-\mathrm{i}\tau}} e^{-\mathrm{i}\left(\pi^2+4u^2\right)/4\pi\tau} \sin\left(\frac{u}{\tau}\right) = 2\left(\frac{L}{\beta}\right)^{1/2} e^{-\frac{L}{4\pi\beta}\left(\pi^2+4u^2\right)} \sinh\left(\frac{uL}{\beta}\right). \tag{3.104}$$

This expansion turns out to be useful to recover Eq. (3.5).

Finally, we remind here the definition for the $q-$digamma function [153] used in Eqs. (3.26) and (3.27)

$$\psi_q(x) = \begin{cases} -\log(1-q) + \log q \sum_{n=1}^{\infty} \frac{q^{nx}}{1-q^n}, & 0 < q < 1, \\ -\log(q-1) + \log q \left(x - \frac{1}{2} - \sum_{n=1}^{\infty} \frac{q^{-nx}}{1-q^{-n}}\right), & q > 1. \end{cases} \tag{3.105}$$

Chapter 4

Entanglement Hamiltonian in the non-Hermitian SSH model

In the Introduction and in Chapters 2 and 3 we have presented several examples of analytic results for the entanglement Hamiltonian in Hermitian models. Recall from the Introduction that, on the one hand, in quantum field theory many systems are captured by the Bisognano-Wichmann theorem (1.12) and its corollaries for CFT (see, e.g., Eq. (1.13) and related discussion). On the other hand, in lattice integrable models the EH is directly related to the corner transfer matrix through Eq. (1.17) and presents a sort of lattice Bisognano-Wichmann behaviour (1.19).

Despite the wealth of results for unitary models, nothing is known for non-Hermitian theories. In particular, since one of the hypothesis of the Bisognano-Wichmann theorem (1.12) is that the Hilbert space carries a unitary representation of the Poincaré group [23, 26, 27], it is not obvious how to adapt to non-unitary CFTs this theorem and its corollary (1.13). Non-Hermitian models [154, 155] have recently attracted a lot of interest for several reasons, including but not restricted to the study of the PT-symmetric systems [156–160], optical phenomena [161, 162] and the study of open systems [163–165] and measurement induced transitions [166–170]. It is then very natural to explore the entanglement properties within this class of systems.

A pioneering study was carried out in Ref. [171], where the authors have studied the entanglement entropy and the entanglement spectrum in a non-Hermitian fermionic lattice model, the non-Hermitian Su-Schrieffer-Heeger (SSH) model at criticality (reviewed in Sec. 4.1). Remarkably, it was observed that the entanglement entropies obey the logarithmic dependence on the subsystem length (1.9) typical of critical systems [20–22], but with a negative central charge $c = -2$ (see also [172]). Later, in Ref. [173], the analysis has been extended to the symmetry resolved entanglement entropies. In this Chapter (based on Ref. [174]) we move a step further, conducting an exploratory and thorough numerical investigation of the EH in the non-Hermitian Su-Schrieffer-Heeger model, both in the gapped

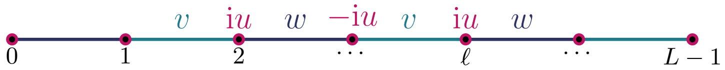

Figure 4.1: Schematic representation of the nH-SSH model, described by Eq. (4.1). The nearest neighbours hoppings have alternating strengths v and w. The imaginary chemical potential is set to iu on the even sites and $-$iu on the odd sites.

phase and at criticality. In the gapped phase we observe that the lattice EH has a structure analogous to the one of integrable lattice models reported in Eq. (1.19). At the critical point, we instead find an additional term not accounted for in the Bisognano-Wichmann corollary in Eq. (1.13), which is responsible for the negativeness of the entanglement entropies.

4.1 The non-Hermitian Su–Schrieffer–Heeger model

Before presenting our results, in this section we review the non-Hermitian model that we study in this Chapter. We consider the non-Hermitian SSH (nH-SSH) chain with PT-symmetry on a discrete circle of $L = 2N$ sites, described by the Hamiltonian

$$H = \sum_{j\in\mathbb{Z}_N} \left(-w\, c^\dagger_{2j} c_{2j+1} - v\, c^\dagger_{2j-1} c_{2j} + \text{h.c.} \right) + \mathrm{i}u \sum_{j\in\mathbb{Z}_N} \left(c^\dagger_{2j} c_{2j} - c^\dagger_{2j+1} c_{2j+1} \right), \tag{4.1}$$

with $u, v, w > 0$. A schematic representation of this Hamiltonian is depicted in Fig. 4.1. We assume quasi-periodic boundary conditions, i.e., $c_{j+L} = e^{\mathrm{i}\delta} c_j$, with $0 < \delta \ll 1$. The reason for this choice will be explained later. The model is a fermionic chain with nearest neighbours hoppings, which have alternating strength on even-odd links. The staggered imaginary chemical potential breaks the hermiticity of the Hamiltonian. Notice that our conventions match those in Ref. [172] after setting $v_1 = 0$ and $v_2 = v$ and identifying their up (down) sites with our even (odd) ones.

The Hamiltonian becomes block diagonal after a Fourier transform of the lattice operators, performed separately on the even and odd sites

$$\tilde{c}_{k,\mathrm{e}} = \frac{1}{\sqrt{N}} \sum_{j\in\mathbb{Z}_N} e^{-\mathrm{i}kj} c_{2j}\,, \qquad \tilde{c}_{k,\mathrm{o}} = \frac{1}{\sqrt{N}} \sum_{j\in\mathbb{Z}_N} e^{-\mathrm{i}kj} c_{2j+1}\,, \tag{4.2}$$

with

$$k \in \frac{2\pi}{N} \left(\mathbb{Z}_N + \frac{\delta}{2\pi} \right), \tag{4.3}$$

where the shift in momentum space is due to the δ-twisted boundary conditions. The Hamiltonian then becomes

$$H = \sum_k \begin{pmatrix} \tilde{c}^\dagger_{k,\mathrm{e}} & \tilde{c}^\dagger_{k,\mathrm{o}} \end{pmatrix} \begin{pmatrix} \mathrm{i}u & -w - ve^{-\mathrm{i}k} \\ -w - ve^{\mathrm{i}k} & -\mathrm{i}u \end{pmatrix} \begin{pmatrix} \tilde{c}_{k,\mathrm{e}} \\ \tilde{c}_{k,\mathrm{o}} \end{pmatrix}, \tag{4.4}$$

Figure 4.2: Phase diagram of the nH-SSH model, explained in the main text. The orange circle and the green square mark the points in parameter space for which we study the EH, reported in Sec. 4.2.1 and Sec. 4.2.2 respectively.

and the eigenvalues of the matrix in Eq. (4.4) are the single-particle energies.

Varying the relative strengths of the parameters u, v, w, the model admits three different gapped phases [171]. If $v - w \in (-u, u)$, the PT symmetry is broken so that the energy spectrum is complex and the eigenvalues appear in complex conjugate pairs. In the two phases $v - w > u$ or $v - w < -u$, the PT symmetry is unbroken and the energy spectrum is real. The latter two phases are distinguished by topological properties, as discussed in Ref. [175]. The resulting phase diagram is given in Fig. 4.2.

Two critical points occur for $v - w = \pm u$. In these cases, the single-particle spectrum is $\epsilon_{\pm,k} = \pm\sqrt{2vw(1+\cos k)}$ and the gap closes at $k = \pi$, leading locally to a linear spectrum with speed of sound

$$c_S = \sqrt{vw}. \tag{4.5}$$

Moreover, at $k = \pi$ the kernel of the Hamiltonian (4.4) is not diagonalisable, as it is made of a 2×2 Jordan block. This is called an *exceptional point* in momentum space. The exceptional point occurs because, as $k \to \pi$, the two eigenspaces become more and more collinear, and they perfectly coincide at $k = \pi$.

Finally, since the Hamiltonian is a linear combination of terms of the form $c_i^\dagger c_j$, it is invariant under the $U(1)$ generated by

$$Q = \sum_{j \in \mathbb{Z}_{2N}} c_j^\dagger c_j \,. \tag{4.6}$$

In this Chapter, we will investigate the ground-state of the system in the PT-unbroken trivial phase and the critical point between the PT-unbroken trivial phase and the PT-broken phase, marked in Fig. 4.2 with a orange circle and a green square, respectively. In Ref. [171], the latter point has been identified with the fermionic bc-ghost CFT with central charge $c = -2$, which we review in the following section.

4.1.1 bc-ghost CFT

The bc-ghost CFTs are a family of theories governed by the following action [100, 176–179]

$$S = \int \mathrm{d}^2 z \left(b\,\bar{\partial} c + \bar{b}\,\partial \bar{c}\right), \tag{4.7}$$

where b and c are anticommuting holomorphic fields and $\bar{b}$ and $\bar{c}$ are the corresponding anti-holomorphic fields. The different members of this family are distinguished by the value of the central charge and by the conformal dimension of the fields c and b. In particular, the CFT which describes the nH-SSH critical point is the one with central charge $c = -2$ [171], in which the fields have conformal weight $h_b = 1, h_c = 0$. All these theories have a conserved current $J = :cb:$ so that the field c has charge 1 and b has charge -1, independently of the specific realisation and central charge.

The CFT with $c = -2$ is one of the simplest instances of a logarithmic CFT [178], incorporating reducible but not indecomposable representations of the Virasoro algebra. Specifically, the fields c and the identity field share the same conformal weights, leading to the formation of a 2-dimensional Jordan block in the Virasoro modes L_0 and $\bar{L}_0$. This phenomenon occurs exclusively in the untwisted sector of the theory, which corresponds to periodic boundary conditions on a cylinder. In the scenario where δ-twisted boundary conditions are adopted, the fields acquire a phase factor $e^{\mathrm{i}2\pi\delta}$ as they move around the non-contractible loop of the cylinder. Consequently, the identity field is no longer part of the spectrum, and the system's ground state becomes associated with the twist field σ_δ [178]. The conformal dimension of σ_δ is given by $h_{\sigma_\delta} = \delta(\delta - 1)/2$, which is negative for $\delta \neq 0$. This implies that for $\delta \neq 0$, there is no Jordan block for L_0 and $\bar{L}_0$, effectively eliminating the logarithmic singularities [178]. It is noteworthy that the presence of the Jordan block in periodic boundary conditions and its absence in the twisted sectors draws a further analogy with the nH-SSH model.

4.1.2 Left-right ground-state

Before concluding this brief review, we would like to emphasise the states that are the focus of this Chapter. First, in both of the cases we consider (see Fig. 4.2), the Hamiltonian has a real spectrum, thus there is a well defined notion of a ground state as the eigenstate with minimum energy eigenvalue. We denote by $|R\rangle$ the right ground state of the Hamiltonian, defined by $H|R\rangle = E_{gs}|R\rangle$, while we denote with $\langle L|$ the left ground-state, defined by $\langle L| H = E_{gs}\langle L|$. Since the Hamiltonian is non-Hermitian, the left ground state is not the "bra" of the right ground state, in other words, $|L\rangle \neq |R\rangle$.

We consider the density matrix $\rho = |R\rangle\langle L|$, which we call the left-right ground state [171–173, 180–184]. Indeed, this can be seen as the zero-temperature limit of the thermal state $e^{-\beta H}/Z$ and therefore is the most natural object to be studied in field theory. The density matrix ρ is positive semi-definite but not Hermitian and therefore the reduced density matrix ρ_A is not positive semi-definite. This means that the entanglement entropy between a subsystem and its complement can be negative. Indeed, the entanglement entropy scales as $c/3\log\ell$, with $c = -2$ [171].

The symmetry-resolved entanglement, relative to the $U(1)$ symmetry (4.6), at the critical point has been studied in Ref. [173]. Of relevance for this Chapter, it has been understood that the eigenvalues of the reduced density matrix are either positive or negative depending on the sign of the charge sector, namely $\operatorname{sign}\lambda_q = (-1)^{q-\langle Q_A\rangle}$, where λ_q stands for an eigenvalue of ρ_A in the charge sector q of Q_A (i.e. the charge (4.6) restricted to A). We will show in Sec. 4.2.2 that we can identify the source of this behaviour in the form of the EH.

4.1.3 Correlation function

A key object in the analysis of the EH of the left-right ground state is the two-point correlation matrix C with entries [171, 173]

$$C_{2j+a,2l+b} = \langle L|c^\dagger_{2j+a}c_{2l+b}|R\rangle = \frac{1}{N}\sum_k e^{-\mathrm{i}k(j-l)}\mathcal{G}(k)_{ab}\,, \quad a,b\in\{0,1\}, \tag{4.8}$$

with

$$\mathcal{G}(k) = \frac{1}{2}\begin{pmatrix} 1-\cos(2\xi_k) & -\sqrt{\frac{\eta_k^*}{\eta_k}}\sin(2\xi_k) \\ -\sqrt{\frac{\eta_k}{\eta_k^*}}\sin(2\xi_k) & 1+\cos(2\xi_k)\end{pmatrix}, \tag{4.9}$$

where $2\xi_k = \tan^{-1}(|\eta_k|/(iu))$, $\eta_k = -w - ve^{-ik}$. Due to the dimerization of the hopping amplitudes v, w, the correlation matrix C presents a block structure. In the thermodynamic limit $L\to\infty$, C is a block Toeplitz matrix generated by the symbol $\mathcal{G}$.

4.2 Lattice entanglement Hamiltonians of the non-Hermitian SSH model

This section contains the main results of this Chapter, the numerical lattice EH in the non-Hermitian SSH model and an analytic conjecture for its behaviour. In order to compute numerically the lattice EH we again use the known relation between fermionic Gaussian states and the correlation matrix, analogously to what we did in Secs. 2.4 and 3.3 in the previous Chapters. Indeed, since the Hamiltonian (4.1) is quadratic, the ground state is Gaussian [171, 173]. Analogously to what we did in the previous Chapters, we write the reduced density matrix as

$$\rho_A = \frac{1}{Z_A}\exp\left\{-\sum_{i,j\in A} c_i^\dagger k^A_{i,j} c_j\right\}, \tag{4.10}$$

where $k^A_{i,j}$ is the kernel of the EH, i.e., the single-particle EH, which can be then obtained from the reduced correlation matrix using Peschel's formula $k^A = \log\left[C_A^{-1} - \mathbb{I}\right]^T$ reported in Eq. (1.15) [108–110]. Importantly, while Eq. (1.15) was initially derived for Hermitian models, as discussed in Refs. [171, 173] it remains valid in the non-Hermitian one under consideration. In Refs. [171, 173] the restricted correlation matrix of the non-Hermitian SSH model was used for the computation of the entanglement spectrum and the entropies. In the following we will compute the kernel of the EH using the correlation matrix (4.8).

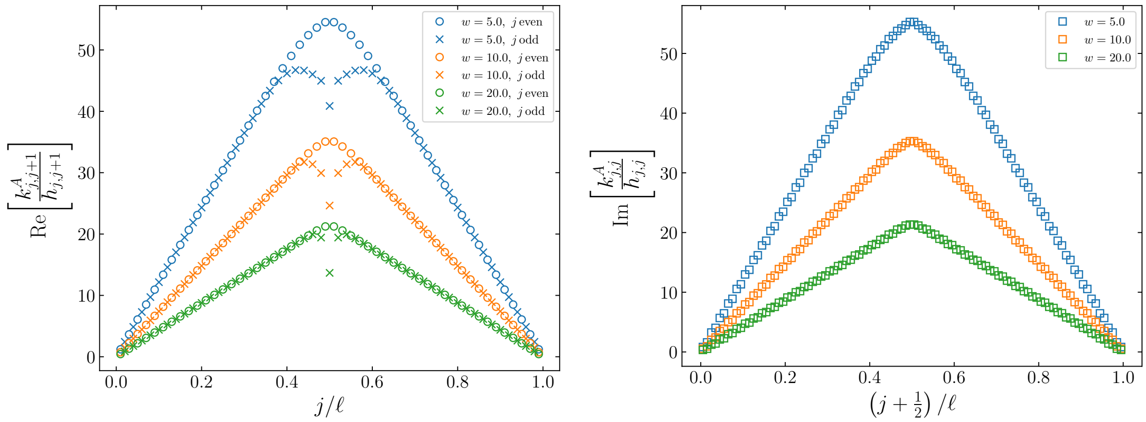

(a) Real part of the nearest-neighbour coupling $k^A_{j,j+1}$. **(b)** Imaginary part of the chemical potential $k^A_{j,j}$.

Figure 4.3: Entanglement temperature in the gapped phase $w - v > u$. In both plots we fix $v = u = 1$ and we consider different values of $w = 5, 10$ and 20 and we take a subsystem of length $\ell = 100$ in a full system of total length $L = 2000$. In the left plot we report, as a function of j/ℓ, the real part of the ratio of the nearest-neighbour EH coupling $k^A_{j,j+1}$ with the coupling $(h_{j,j+1})$, i.e. $-w$ for even j (circles) and $-v$ for odd j (crosses). The purpose of this ratio is to isolate the entanglement temperature. Apart from a small region in the center of the interval, the ratio follows the expected triangular shape (see discussion below Eq. (4.11)). In the right plot we report the imaginary part of the ratio between the staggered imaginary chemical potential $k^A_{j,j}$ with $+u$ $(-u)$ for even (odd) site j. Again, up to a small finite size oscillation, the ratio follows the predicted triangular shape.

We also recall that the numerical computation of the formula (1.15) suffers from numerical instabilities and must be conducted at high precision. In our study we used the `python` library `mpmath` [139] and the software `Mathematica`, keeping up to 500 digits.

In rest of this section, we present the results for the EH of an interval $A = [0, \ell]$ in the left-right ground state. We first study the topologically trivial gapped phase $w - v > u$ with periodic boundary conditions and we compare with the known results in unitary integrable lattice models [52]. We then consider the critical point $w - v = u$ with a small twisting of the boundary conditions $\delta = 10^{-7}$, which as we explained in Sec. 4.1 is described by the $c = -2$ *bc*-ghost CFT. We compare the results with the continuum prediction from unitary CFTs and we use our observations to formulate a conjecture for the EH of an interval in the ground state of the *bc*-ghost theory.

4.2.1 Entanglement Hamiltonian in the trivial gapped phase

Before studying the non-Hermitian model, it is instructive to first recall the known results in unitary gapped lattice models, in order to compare them with ours. As we reported in Eq. (1.19) in the Introduction, in certain integrable models the EH in the half-space follows

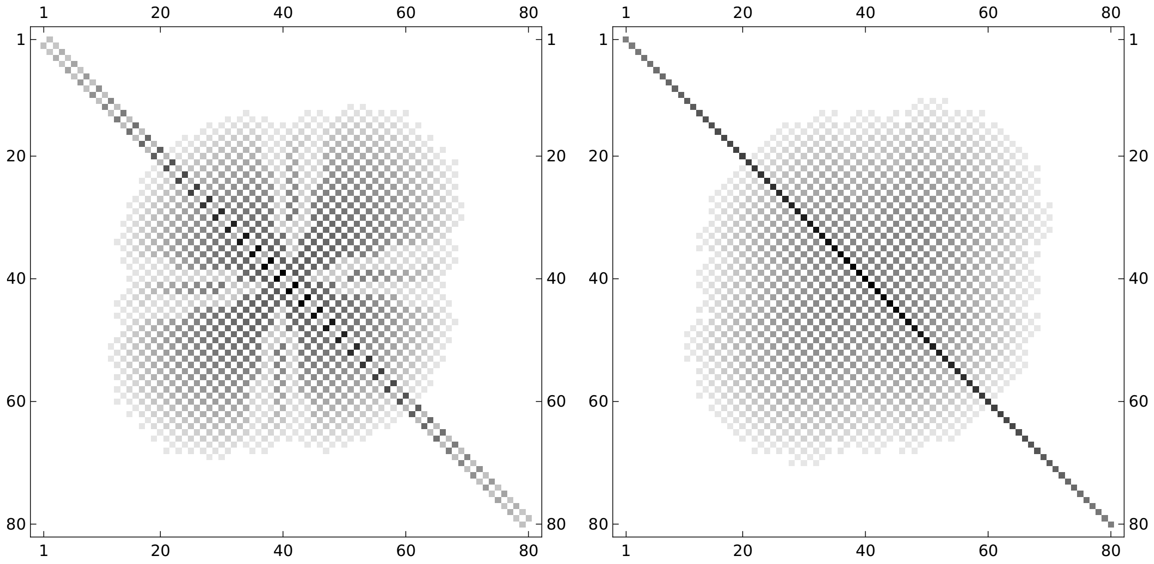

(a) Real part of the EH kernel k^A. **(b)** Imaginary part of the EH kernel k^A.

Figure 4.4: Matrix plot of the EH kernel k^A in the gapped phase $w - v > u$ with $w = 20$, $v = 2$ and $u = 2$, for an interval of length $\ell = 80$ in a system of length $L = 2000$. Left (Right): Absolute value of the real (imaginary) part of k^A. Consistently with the Tetel'man-Thacker behaviour (4.11), near the two endpoints the only non-vanishing elements of the EH are the imaginary chemical potential (main diagonal in the right plot) and the coupling between nearest-neighbours (first sub-diagonals in the left plots). The latter couplings (left) display the alternating value between the odd and even sites (see Eq. (4.11)). In the middle of the interval, the EH deviates from Eq. (4.11) and also couplings at higher distances are non-zero.

the structure recognised by Tetel'man, Itoyama and Thacker, i.e., the EH is proportional to the Hamiltonian density with a local temperature equal to the lattice site, analogous to a lattice Bisognano-Wichmann behaviour [25, 48, 49, 58, 59, 61]. If we instead consider a finite interval, in the general case there are very few known analytic results. If the gap is sufficiently large, however, in Ref. [52] it was observed via numerical computations that near the two endpoints of the interval the EH follows the half-space result of Eq. (1.19), only deviating from this behaviour in the middle of the interval, which give rise to a characteristic triangular entanglement temperature.

This triangular behaviour has been observed in several Hermitian models, such as the Hermitian Su-Schrieffer-Heeger model (or dimerised hopping chain) and the harmonic chain [52]. Its physical interpretation is that, for short-range correlated systems, the EH density is affected only by the closest boundary, as the contribution from the furthest one is exponentially suppressed. Then the EH density behaves as the one of a semi-infinite subsystem (see Eq. (1.19)) and the RDM effectively factorises [185]. This argument is independent of unitarity and holds also for the non-hermitian model under consideration.

It is therefore natural to wonder if this factorisation holds also for the non-Hermitian model under study. Another important consequence of Eq. (1.19) is that in unitary lattice integrable modes, the half-space lattice EH does not couple fermions at distances larger than those in the corresponding lattice Hamiltonian. Correspondingly, within an interval, it was noted that near the endpoints, the EH does not exhibit higher couplings, only manifesting them in the crossover region at the center [52].

Let us now consider the non-Hermitian SSH model. Assuming that the structure of the EH in Eq. (1.19) holds also for this theory, from the Hamiltonian in Eq. (4.1) we can conjecture that the half-space lattice EH takes the form

$$\begin{aligned} K_A \propto \sum_{j=0}^{+\infty} \Bigg[(2j)\, w \left(c^\dagger_{2j} c_{2j+1} + c^\dagger_{2j+1} c_{2j} \right) + (2j+1)\, v \left(c^\dagger_{2j-1} c_{2j} + c^\dagger_{2j} c_{2j-1} \right) + \\ + \mathrm{i} \left(2j + \frac{1}{2} \right) u\, c^\dagger_{2j} c_{2j} - \mathrm{i} \left(2j + \frac{3}{2} \right) u\, c^\dagger_{2j+1} c_{2j+1} \Bigg], \end{aligned} \tag{4.11}$$

with some unknown proportionality constant. Since we cannot access numerically the full EH of the half-space, in order to test the conjecture in Eq. (4.11) we study the EH of an interval $[0, \ell]$ in a finite system of length $L \gg \ell$. In analogy with the unitary case, we expect that for a sufficiently large gap, near the endpoints the EH will follow the half-space result in Eq. (4.11), with a crossover in the middle of the interval, giving rise to the typical triangular shape.

In Fig. 4.3 we report the results of the numerical calculation of the lattice EH in the gapped phase, for an interval of length $\ell = 100$ in a system of total length $L = 2000$ with periodic boundary conditions. We fix the parameters $v = u = 1$ and we study different gaps by varying the value of w, in particular we take $w = 5, 10$ and 20. The plots report the ratio between the kernel of the EH, k^A, obtained from Eq. (1.15) and the one of the Hamiltonian h in Eq. (4.1) as a function of the lattice site. On the left, in Fig. 4.3b we report the real part of the nearest-neighbour coupling $k^A_{j,j+1}$, divided by $(-w)$ for j even (circles) and by $(-v)$ for j odd (crosses). Dividing by these coupling constants, we isolate the entanglement temperature, which is expected to follow the triangular shape (see Eq. (4.11) and discussion below). Indeed we see that, apart from a small crossover region in the center of the interval, the nearest-neighbour coupling follows the expected behaviour for all values of w that we considered. This behaviour is completely analogous to what was observed in Ref. [52] for the dimerised hopping chain. The novel result is reported in the right plot, in Fig. 4.3b, where we show the staggered imaginary chemical potential $k^A_{j,j}$, divided by u for j even and by $(-u)$ for j odd. Again, the role of this division is to isolate the entanglement temperature, which should agree with the one obtained from the nearest-neighbour coupling. Indeed we observe that, apart from a small oscillation due to finite size effects, the imaginary chemical potential follows the same triangular shape as the nearest-neighbour coupling, as expected from our conjecture in Eq. (4.11).

As a further check, in Fig. 4.4 we report the matrix plots of the real (left plot) and of the imaginary parts (right plot) of the single-particle EH k^A. According to our conjecture in Eq. (4.11), the half-space EH does not couple fermions at distances higher than one, similarly to what happens for unitary integrable models in Eq. (1.19). In the left plot in Fig. 4.4a, we see that near the endpoints the only non-zero elements of the real part of the EH kernel are the nearest-neighbour couplings $k^A_{j,j+1}$ and $k^A_{j,j-1}$. The higher couplings are non-zero only in a crossover region in the middle of the interval, as expected. This behaviour is again completely analogous to what was observed in Ref. [52] for the dimerised hopping chain. The new results are given by the imaginary part, shown in the right plot in Fig. 4.4b. We see that also the imaginary part follows the expected behaviour, with only the main diagonal k^A being significantly different from zero near the endpoints. This confirms the validity of our local conjecture in Eq. (4.11) for the half space EH in the non-Hermitian SSH model. We remark that this is the first observation of a Bisognano-Wichmann like behaviour in a non-Hermitian model.

Before concluding this section, we wish to comment on the proportionality constant in Eq. (4.11), i.e., the slope of the triangles in Fig. 4.3. This constant is actually related to the velocity of the excitations in the gapped model. In Ref. [52], the analogous proportionality constant in the dimerised hopping chain was computed analytically using the knowledge of the exact corner transfer matrix. It would be interesting to obtain analytically the CTM in the non-Hermitian SSH model, which would refine our conjecture (4.11) for the half-space EH. This computation would not only allow us to predict the slope of the linearly increasing entanglement temperature, but it could also provide a quantitative understanding of the finite size oscillations of the chemical potential in Fig. 4.3b which are not captured by Eq. (4.11). This is however a rather involved calculation which goes beyond the scope of this Chapter.

4.2.2 Entanglement Hamiltonian at the critical point

In this section we study the EH at the critical point $w - v = u$ (green square in Fig. 4.2). As discussed in Sec. 4.1, at the critical point and for periodic boundary conditions, the lattice Hamiltonian (4.1) presents a Jordan block. Then, to treat the system numerically we need to introduce a small twisting of the boundary conditions δ [171, 173]. In all the following discussion we fix $\delta = 10^{-7}$. In full analogy to the study we performed for the gapped phase in Sec. 4.2.1, we compute numerically the lattice EH kernel k^A using Eq. (1.15), performing all calculations at high precision. However, at the critical point there is an additional subtlety. In Ref. [171] it was shown that at criticality all eigenvalues ν_j of the correlation matrix are real and lie outside of the interval $[0, 1]$. As a consequence, the matrix appearing inside the logarithm in Eq. (1.15) has all negative eigenvalues (see also Ref. [173]). This is susceptible to numerical instabilities, giving an imaginary part of the logarithm which (unphysically) oscillates wildly between $+\mathrm{i}\pi$ and $-\mathrm{i}\pi$. In this Chapter we always fix it to be equal to $+\mathrm{i}\pi$.

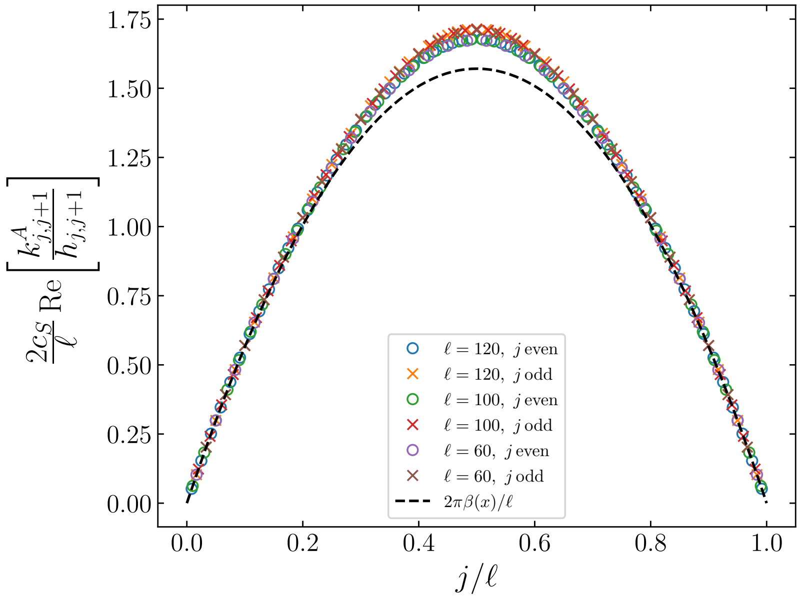

Figure 4.5: Real part of the ratio of the EH nearest-neighbour coupling $k^A_{j,j+1}$ with the coupling w (v) for j even (odd), rescaled by $2c_S/\ell$, where ℓ is the length of the interval and c_S is the speed of sound (4.5). The circles represent even sites and the crosses are odd sites. For all lengths considered we observe a perfect collapse. The black dashed parabola is the field theory prediction for the local temperature $2\pi\beta_{\mathrm{loc}}(x)$ in Eq. (1.13), divided by ℓ. Near the endpoints of the interval we find a very good agreement between the lattice result and the field theory. The deviation in the middle of the interval is due to the contribution of higher couplings, analogously to what happens in Hermitian lattice models.

Before presenting our result for the critical non-Hermitian SSH model, we remind the reader of what occurs in the case of critical unitary models. As we discussed in Sec. 2.4, the lattice EH of an interval in the ground state is much more non-local than the QFT result (1.13), presenting couplings between fermions at arbitrary distances [53–55, 132]. Contrast this behaviour with the one for gapped integrable models that we have seen in Sec. 4.2.1, where the lattice EH only contains next-neighbour couplings. In the critical case, all these higher couplings contribute to the continuum energy density and, in order to recover the CFT entanglement temperature $\beta_{\mathrm{loc}}(x)$ in Eq. (1.13), it is necessary to perform a careful continuum limit which takes into account all of these higher contributions [133–135]. This limit has been reviewed in detail in Sec. 2.4 and we refer the reader to that section. While this limiting procedure has allowed to reconstruct the CFT EH in several systems (see, e.g., Refs. [133–135, 137] and Chapters 2, 3 and 6 for some applications), it is however highly dependent on the lattice model and, to date, it is only understood in the case of free massless lattice fermions and the harmonic chain.

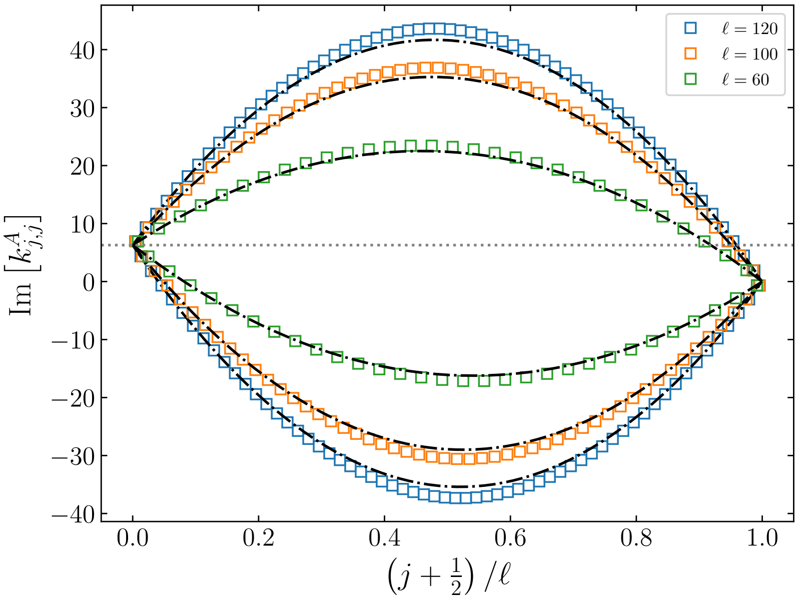

Figure 4.6: Imaginary chemical potential $k^A_{j,j}$ at criticality $w - v = u$ for different lengths of the interval $\ell = 60, 100$ and 120. The black dash-dotted curves are reported in Eq. (4.13) and are obtained as the sum of the naive field theory prediction for the entanglement temperature in Eq. (1.13) and of the conjectured form of the novel term in Eq. (4.12). Close to the endpoints we observe a perfect agreement which becomes slightly worse in the middle of the interval.

Considering now the non-Hermitian SSH model, in Figs. 4.5 and 4.6, we report the numerical lattice EH, obtained from Eq. (1.15) with a choice of parameters $w = 1.5$, $v = 1$ and $u = w - v = 0.5$ and different interval lengths $\ell = 60, 100$ and 120 in a total system of length $L = 2000$. In Fig. 4.5 we plot the real part of the nearest-neighbour coupling $k^A_{j,j+1}$, divided by $(-w)$ for j even and by $(-v)$ for j odd, analogously to what we have done in the massive case. We further make the quantity dimensionless by multiplying it by $2c_S/\ell$, where c_S is the speed of sound (4.5) in the critical lattice model. Indeed, notice that if we reintroduce the dimensions, k^A is dimensionless, while w and v have the dimensions of an inverse time. We observe a perfect collapse for all the lengths considered. The black dashed line in Fig. 4.5 is the parabolic entanglement temperature $2\pi\beta_{\mathrm{loc}}(x)$ for unitary CFTs reported in Eq. (1.13), divided by the length of the interval ℓ. While near the endpoints we find a good agreement, we see a deviation in the middle of the interval. Similarly to what happens for unitary lattice models, the origin of this discrepancy is the presence of higher couplings which in the continuum limit give contributions to the continuum energy density. We expect that a proper continuum limit should exactly reproduce the parabola in Eq. (1.13) (as for Hermitian free fermions [133]), but this is beyond our goals.

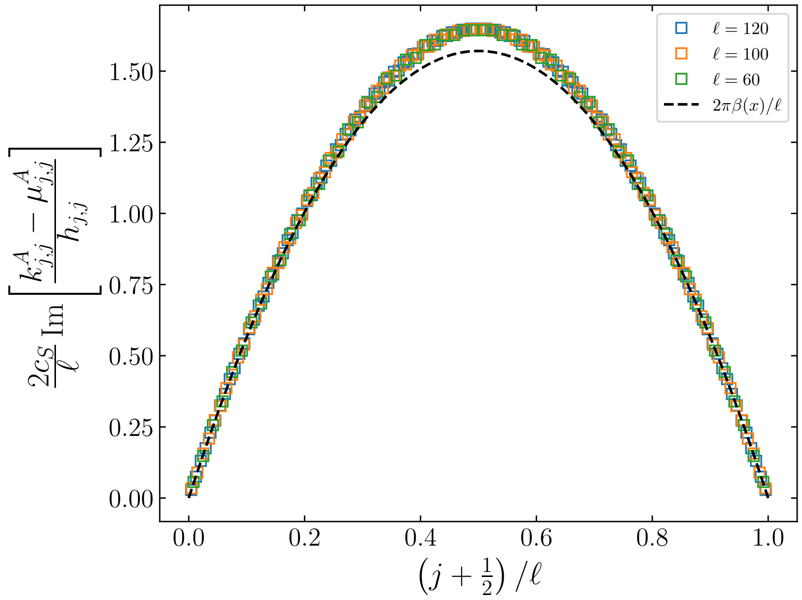

Figure 4.7: Imaginary part of $(k^A_{j,j} - \mu^A_{j,j})/h_{j,j}$ (i.e. the difference between the EH chemical potential and $\mu^A_{j,j}$ in Eq. (4.12), all in units of $h_{j,j}$), rescaled with $2c_S/\ell$, where c_S is the speed of sound in Eq. (4.5). We consider intervals of length $\ell = 60, 100$ and 120 in a system of total length $L = 2000$, with parameters $w = 1.5$, $v = 1$ and $u = w - v = 0.5$. For all ℓ, we observe a perfect collapse, suggesting that we have successfully isolated the scaling part. The black dashed curve is the CFT prediction for the entanglement temperature $2\pi\beta_{\mathrm{loc}}$ in Eq. (1.13) divided by ℓ. Analogously to the nearest-neighbour coupling in Fig. 4.5, the agreement is perfect at the endpoints and is slightly worse in the middle of the interval, due to the contribution of higher order couplings.

In Fig. 4.6 we instead report the staggered imaginary chemical potential (the alternating sign with respect to Fig. 4.3b is due to not having divided by either u or $(-u)$). This quantity displays the most significant difference with respect to the Hermitian case. For all the lengths ℓ of the interval, at the left endpoint $j/\ell = 0$ the chemical potential takes the value $2\pi\mathrm{i}$ (grey dotted line), while at the right one $j/\ell = 1$ it vanishes. Based on this observation, we conjecture that besides the approximate parabolic result, at the critical point appears an additional term of the form

$$\sum_{j=0}^{\ell} \mu^A_{j,j}\, c^\dagger_j c_j = 2\pi\mathrm{i} \sum_{j=0}^{\ell} \left(1 - \frac{\left(j+\frac{1}{2}\right)}{\ell}\right) c^\dagger_j c_j, \tag{4.12}$$

i.e., a chemical potential term which interpolates linearly between $2\pi\mathrm{i}$ and 0. We remark that, differently from the parabolic entanglement temperature $\beta_{\mathrm{loc}}(x)$ in Eq. (1.13), this novel term does not scale with the system size. In order to check Eq. (4.12), in Fig. 4.6 we compare the two curves (dash-dotted black lines)

$$\frac{\pi\,(\pm u)}{c_S}\left(\frac{(\ell-x)x}{\ell}\right)+2\pi\left(1-\frac{x}{\ell}\right), \tag{4.13}$$

with the imaginary part of the EH chemical potential term for $\ell = 60, 100$ and 120. Near the endpoints we find a perfect match for all the lengths considered, while the agreement gets slightly worse in the middle of the interval, but still acceptable.

To facilitate the comparison, we extract the part of the EH chemical potential that scales with the length of the interval by subtracting the conjectured form $\mu^A_{j,j}$ in Eq. (4.12) from the numerical result for $k^A_{j,j}$. We then divide by u for j even and by $(-u)$ for j odd to isolate the entanglement temperature and we rescale with $2c_S/\ell$ to make the quantity dimensionless. The result of this procedure is reported in Fig. 4.7. For all the values of the length considered we observe a perfect collapse, which suggests that the novel non-scaling term $\mu^A_{j,j}$ takes indeed the conjectured form (4.12). The black dashed curve is again the parabolic CFT prediction for the entanglement temperature in Eq. (1.13) divided by ℓ. Once again, we have a perfect agreement near the endpoints of the interval, while we observe a deviation in the middle. This deviation is always due to the presence of contributions from higher couplings.

Summing up our findings, recalling from Sec. 4.1 that the critical point is described by the $c = -2$ bc-ghost CFT, we propose that the continuum limit of the difference $(k^A - \mu^A)$ must reproduce the continuum CFT enatnglement Hamiltonian in Eq. (1.13). Meanwhile, the continuum limit associated with the new chemical potential term μ^A in Eq. (4.12) will yield

$$\sum_{j=0}^{\ell}\mu^A_{j,j}\,c_j^\dagger c_j \sim 2\pi\mathrm{i}\int_0^\ell \mathrm{d}x\left(1-\frac{x}{\ell}\right)J(x)+\text{irrelevant operators}, \tag{4.14}$$

where $J(x) = {:}cb{:}(x)$ is the ghost number operator. Putting all together, we conjecture that the EH of the $c = -2$ bc-ghost CFT would take the form

$$K_A=\int_0^\ell \mathrm{d}x\,\frac{x\,(\ell-x)}{\ell}\,T_{00}(x)+2\pi\mathrm{i}\int_0^\ell \mathrm{d}x\left(1-\frac{x}{\ell}\right)J(x)\,, \tag{4.15}$$

which is one of the main results of this Chapter. Comparing the proposed EH with the result for unitary CFTs in Eq. (1.13), the main difference is the presence of the imaginary term proportional to the ghost number $J(x)$. Nevertheless, since this term is again the integral of a local operator, our conjecture (4.15) retains a local structure. Notice that, since the conformal dimension of the ghost number operator $J(x)$ is $\Delta_J = 1$, the local weight $(1 - x/\ell)$ is dimensionless and it does not scale with the system size, as we observed on the lattice.

In order to understand the role played by the term μ^A in Eq. (4.12), in Fig. 4.8 we compare the single-particle entanglement spectrum, i.e., the eigenvalues of k^A, with the

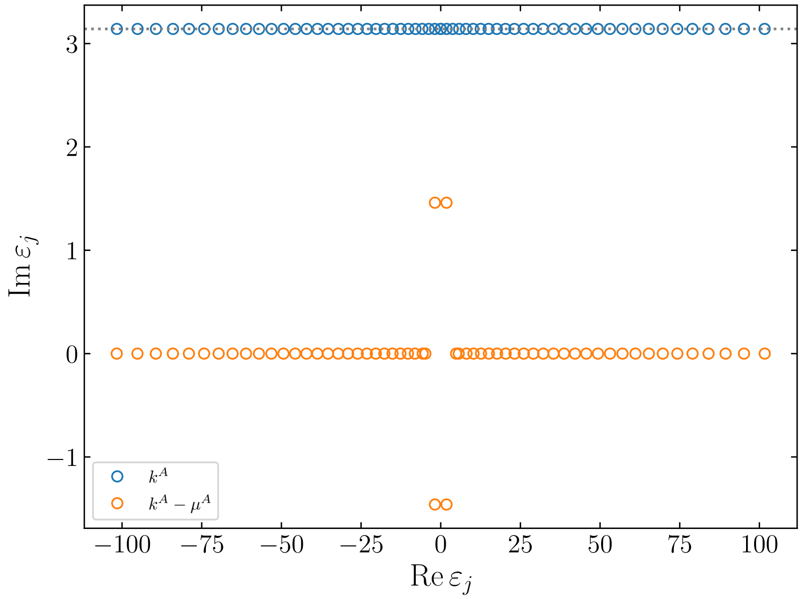

Figure 4.8: Spectra of the single-particle EH k^A (blue) and of the difference $(k^A - \mu^A)$ (orange), where μ^A is given by Eq. (4.12). The data are for an interval of length $\ell = 120$, in a system of size $L = 2000$, and couplings $w = 1.5$, $v = 1$ and $u = w - v = 0.5$. All eigenvalues of the EH have imaginary part equal to π (gray dotted line). Subtracting μ^A has the net effect of making almost all the eigenvalues real.

eigenvalues of the matrix $(k^A - \mu^A)$. All the eigenvalues ε_j of the single-particle EH (blue circles) possess an imaginary part equal to π, a feature previously identified in Ref. [173]. As already mentioned, this imaginary part is due to the fact that the eigenvalues ν_j of the correlation matrix all belong to $(-\infty, 0) \cup (1, +\infty)$, which, using Eq. (1.15), leads to [173]

$$\varepsilon_j = \log \left| \frac{1 - \nu_j}{\nu_j} \right| + \mathrm{i}\pi \,. \tag{4.16}$$

As discussed in Sec. 4.1.2, the impact of the imaginary part in Eq. (4.16) on the many-body spectrum of the reduced density matrix is to impart an alternating sign to the eigenvalues of ρ_A depending on the charge sector, i.e., the number of ghosts, according to [173]

$$\rho_A = (-1)^{Q_A - \langle Q_A \rangle} \, |\rho_A| \,, \tag{4.17}$$

which in turn is responsible for the negative sign of the entanglement entropy. On the other hand, in Fig. 4.8 we see that the eigenvalues of $(k^A - \mu^A)$ (orange circles) are almost all real. We can therefore argue that the novel operator μ^A in Eq. (4.12) (and its continuum limit (4.14) in the bc-ghost CFT) is the one responsible for the alternating sign of the entanglement spectrum. Without the operator μ^A, the reduced density matrix ρ_A would be positive defined and, as a consequence, the entanglement entropy would be positive too.

4.3 Final remarks

In this Chapter we have have studied the ground state EH in the non-Hermitian SSH model, considering the left-right density matrix $\rho = |R\rangle \langle L|$. We studied both the topologically trivial gapped phase and the critical point. In the gapped phase, the EH assumes the typical triangular shape (see Eq. (4.11) and discussion) that was already observed in Ref. [52] for unitary integrable gapped models. Near the endpoints of the interval, the entanglement temperature grows linearly with the lattice site, according to the half-space prediction in Eq. (4.11). Remarkably, we observe that the same behaviour is true for the imaginary part of the EH. This is the first example of a lattice Bisognano-Wichmann like behaviour in a non-Hermitian model.

At the critical point, described by the *bc*-ghost CFT, we find a departure from the parabolic EH in Eq. (1.13) predicted by the Bisognano-Wichmann theorem for unitary CFTs. In addition to a term proportional to the energy density with a parabolic entanglement temperature, we observe a term proportional to the number operator $c_i^\dagger c_i$ with an imaginary chemical potential interpolating between $2\pi\mathrm{i}$ and 0, cf. Eq. (4.12). This operator has a profound effect on the entanglement spectrum. As depicted in Fig. 4.8, removing the operator in Eq. (4.12) ensures that almost all the eigenvalues are real. As discussed in Ref. [173], the imaginary part of the single-particle entanglement spectrum in Eq. (4.16) is responsible for the negativeness of the entanglement entropy. If the operator in Eq. (4.12) were not present, the entanglement entropy would be positive. Based on these results, we formulate a conjecture given by Eq. (4.15) for the EH in the *bc*-ghost CFT. Such a conjecture consists of a term analogous to the Bisognano-Wichmann EH in Eq. (1.13) and of an imaginary chemical potential term proportional to the ghost number $J(x)$.

The work in this Chapter paves the way for future investigations into the EHs of non-Hermitian models. Three open problems emerges very naturally. Firstly, in the gapped phase, it would be interesting to derive analytically the CTM. As discussed in Sec. 4.2.1, this would determine the slope of the triangular entanglement temperature in Fig. 4.3 and could validate the lattice Bisognano-Wichmann behaviour. Secondly, it is desirable to analytically derive the EH at the critical point, akin to the work done for free massless fermions in Ref. [87]. Thirdly, the robustness of our findings remains uncertain, such as whether the conjectured form of the EH withstands the presence of relevant interactions. Other unexplored research directions include understanding the EH for non-Hermitian systems that lack a real Hamiltonian spectrum.

Part II

Entanglement in integrable models

Chapter 5

Entanglement entropy along a massless renormalisation flow: the tricritical to critical Ising crossover

This second part of the thesis, is devoted to the behaviour of entanglement in 1+1-dimensional integrable QFTs. Integrable QFTs have the remarkable property that the scattering matrix factorises as the product of two-particle scattering. As we will discuss in more detail later, in integrable models, factorised scattering makes it possible to analytically determine form factors of quantum fields via the *form factor bootstrap program* [186, 187]. Using the spectral expansion of correlation function, this makes in turn possible to compute correlators as expansion in form factors. Recall from the Introduction that the entanglement entropies can be computed from the partition function on a replicated manifold (see Eq. (1.10)). As recognised in Refs. [22, 103, 188], this partition function is given by the correlators of particular kind of fields, the branch-point twist fields $\mathcal{T}, \widetilde{\mathcal{T}}$ (reviewed in Sec. 5.2), opening the opportunity to compute the entropies in integrable models as a spectral expansion of expansion of twist fields form factors [188–191]. This program has been successfully applied in several systems, see e.g. Refs. [188–190, 192–206]. In an analogous fashion, the symmetry resolved entanglement entropies (1.30) can be obtained from correlators of composite twist fields, given by the fusion of the twist fields with an operator which introduces an appropriate Aharonov-Bohm flux.

In this Chapter we investigate the ground state Rényi entanglement entropies in the massless QFT associated to the renormalisation group that connects the tricritical and critical Ising theories by perturbing the former with a relevant field. This theory is the simplest member of the well-known family of massless renormalisation group flows that have as UV and IR fixed points two consecutive A-series unitary conformal minimal models [207–211]. Entanglement entropies are a particularly interesting quantity to study in this context due to their behaviour along RG flows. In the renormalisation group picture of QFTs as perturbed

CFTs, an important result in two dimensions is the Zamolodchikov c-theorem [212, 213], which describes the loss of information about the short-distance degrees of freedom along the flow. In Refs. [193, 194], it was recognised that the scaling dimension of branch-point twist fields (obtained from the Δ-sum rule [214], see Sec. 5.6) provides another quantity with the same qualitative behaviour as the Zamolodchikov c-function. This Δ-function monotonically decreases with the distance and it is equal to the scaling dimension of the twist fields at the IR and UV fixed points of the flow. A different c-function can also be directly constructed from the entanglement entropy [215].

In the theory under study, the form factor bootstrap program has been first successfully applied in Ref. [216] to obtain correlators of order and disorder fields. Here we extend it to the branch point twist fields, both standard and composite, and we obtain explicit expressions for the two- and four-particle form factors. To this end, we follow the same strategy as in the massive case, we write the set of form factor bootstrap equations that take into account the particular exchange properties of the twist fields and we propose a general ansatz for their solution. Furthermore, we also derive the two and four-particle form factors along the massless flow from the roaming limit of the sinh-Gordon ones. By analytically continuing the scattering matrix of the sinh-Gordon model, one can find the Zamolodchikov's staircase model [217], a two-dimensional integrable scattering theory that describes a renormalisation group flow which interpolates between the successive A-series unitary conformal minimal models. It has been shown [218, 219] that the form factors of different fields in the tricritical-critical Ising model flow can be obtained as roaming limits of certain form factors of the sinh-Gordon theory. We show here that a similar property holds for the twist field form factors. We also study the Δ-function associated to the standard and the composite twist fields along the flow, finding that it is monotonic and correctly reproduces their scaling dimension at the fixed points. Finally, we use the form factors of the standard twist field to compute the leading contribution to the $n = 2, 3$-Rényi entropies and we compare them with the expected value in both the ultraviolet and the infrared.

5.1 The massless RG flow from the tricritical to the critical Ising theory

In this Chapter, we review the theory that we investigate in this Chapter, the massless renormalisation group flow that connects the tricritical and critical Ising CFTs. These CFTs are respectively the unitary minimal models $\mathcal{M}_4$ and $\mathcal{M}_3$ [209–211] with central charges [100, 101]

$$c_{\mathrm{UV}} = \frac{7}{10}\,, \quad \text{and} \quad c_{\mathrm{IR}} = \frac{1}{2}\,, \tag{5.1}$$

and with Kac tables reported in Table 5.1. The massless RG flow, usually denoted as A_2, is the simplest member of the infinite family of massless theories A_p that interpolate between two consecutive A-series diagonal conformal minimal models $\mathcal{M}_{p+2} \to \mathcal{M}_{p+1}$ with central

3	3/2	3/5	1/10	0
2	7/16	3/80	3/80	7/16
1	0	1/10	3/5	3/2
s/r	1	2	3	4

(a) $\mathcal{M}_4$, $c = \frac{7}{10}$

2	1/2	1/16	0
1	0	1/16	1/2
s/r	1	2	3

(b) $\mathcal{M}_3$, $c = \frac{1}{2}$

Table 5.1: Kac tables of the tricritical (Table 5.1a) and critical (Table 5.1b) Ising CFTs [100, 101]. In each case, we report the conformal dimension of the primary fields $\phi_{r,s}$ of the theory. The vertical and horizontal axes correspond to the s and r indices respectively.

charges

$$c_{\mathrm{UV}} = 1 - \frac{6}{(p+2)\,(p+3)}\,, \qquad \text{and} \qquad c_{\mathrm{IR}} = 1 - \frac{6}{(p+1)\,(p+2)}\,. \tag{5.2}$$

This family of integrable RG trajectories is obtained by deforming the UV CFT $\mathcal{M}_{p+2}$ with its relevant field $\phi_{1,3}$ [207–211]. In particular, in the tricritical Ising CFT, $\phi_{1,3}$ corresponds to the vacancy density field with conformal dimension $h_{1,3} = \frac{3}{5}$ (see Table 5.1a) [209–211]. In the Euclidean formalism, the action $\mathcal{A}_{\mathrm{flow}}$ of this flow takes the form

$$\mathcal{A}_{\mathrm{flow}} = \mathcal{A}_{\mathcal{M}_4} + \lambda \int \mathrm{d}^2x\, \phi_{1,3}(\mathbf{x})\,, \tag{5.3}$$

where λ is a dimensionful coupling and, importantly, λ is positive, since for negative coupling a different massive integrable theory is obtained. Several other families of massless integrable flows have been identified as well [220–227].

The masslessness of the flow described by Eq. (5.3) can be understood by recalling that the tricritical Ising CFT $\mathcal{M}_4$ is one of the simplest examples of superconformal theory [228–230]. The deformation with the vacancy field $\phi_{1,3}$ leads to a spontaneous supersymmetry breaking [231] which gives rise to right- and left-moving massless Goldstone fermions $\psi, \bar{\psi}$ and ensures that the theory has vanishing mass gap.

In Ref. [231], it was shown that the low energy behaviour of the massless flow is described by the effective Lagrangian

$$\mathcal{L}_{\mathrm{eff}} = \frac{1}{2\pi}\left(\psi\bar{\partial}\psi + \bar{\psi}\partial\bar{\psi}\right) - \frac{1}{\pi^2 M^2}\left(\psi\partial\psi\right)\left(\bar{\psi}\bar{\partial}\bar{\psi}\right) + \dots\,, \tag{5.4}$$

that is, the $T\bar{T}$ deformation of the critical Ising model. Notice that the Majorana fermions $\psi, \bar{\psi}$ of the Ising model are now identified with the Goldstone fermions of the massless flow A_2, which are the only stable particles in this theory [232]. It is worth stressing that the massless flow at low-energies is described by a $T\bar{T}$-deformed CFT. Such theories have been studied in great detail [233–246] and hence they provide non-trivial benchmarking for some of our results.

The massless flow (5.3) as well as the effective Lagrangian (5.4) possess a mass scale M, which plays the role of the momentum scale at which non-trivial scattering happens between the fermions. We can parameterise the energy and momenta of the right- and left-moving Goldstone fermions in terms of a rapidity variable θ and of this mass scale M as [232]

$$\begin{aligned} E_R(\theta) &= \frac{M}{2}e^{\theta}\,, \qquad E_L(\theta) = \frac{M}{2}e^{-\theta}\,, \\ p_R(\theta) &= \frac{M}{2}e^{\theta}\,, \qquad p_L(\theta) = -\frac{M}{2}e^{-\theta}\,. \end{aligned} \tag{5.5}$$

Since the massless fermions are the only stable particles, they form a complete basis of asymptotic states, which in the rapidity parameterisation read as

$$|\theta_1, \ldots \theta_r, \theta'_1, \ldots \theta'_l\rangle_{r,l} = \psi(\theta_1)\ldots\psi(\theta_r)\,\bar{\psi}(\theta'_1)\ldots\bar{\psi}(\theta'_l)\,|0\rangle\,, \tag{5.6}$$

which contains r right-moving and l left-moving fermions. If the rapidities are ordered as $\theta_1 > \theta_2 > \ldots > \theta_r$ and $\theta'_l > \ldots > \theta'_2 > \theta'_1$, then the set of states (5.6) corresponds to in-states, whereas the opposite ordering results in out-states. Different orderings are linked by scattering processes between the particles. Since the theory is integrable, the scattering of particles is completely elastic, preserves particle number and rapidity, and is fully characterised by the two-body S-matrices. Since the scattering of the particles is diagonal, the S-matrices are scalars and functions of the rapidity difference of the particles. In particular [232]

$$\begin{aligned} S_{\mathrm{RR}} &= S_{\mathrm{LL}} = -1\,, \\ S_{\mathrm{RL}}(\theta) &= S_{\mathrm{LR}}^{-1}(-\theta) = \tanh\left(\frac{\theta}{2} - \frac{\mathrm{i}\pi}{4}\right)\,, \end{aligned} \tag{5.7}$$

that is, only the scattering between left- and right-movers is non-trivial.

The massless flow (5.3) has been the subject of numerous studies. These involve its description in terms of the thermodynamic Bethe ansatz [209–211], or the determination of form factors, i.e., the matrix elements of the off-critical versions of the UV scaling fields, as well as certain correlation functions [216]. At the level of the free energy and form factors [218, 219], the massless flow can also be recovered from the staircase model [217, 220], which we shall introduce in Sec. 5.5. The model also shows interesting properties in inhomogeneous out-of-equilibrium situations as studied in [247] via generalised hydrodynamics.

To complete the brief review of this massless flow, we discuss its symmetry properties. Both the UV and IR limiting CFTs enjoy a spin-flip $\mathbb{Z}_2$ symmetry under which the perturbing field also transforms trivially. Consequently, the massless flow inherits this symmetry as well. This fact can be made more transparent using the Landau-Ginzburg formalism, which allows the identification of the multicritical Ising CFTs with a Lagrangian [100, 101]. In particular, the tricritical and critical Ising models can be described by the following actions in terms of the bosonic field φ

$$\mathcal{A}_{\mathrm{tri}} = \int \mathrm{d}^2x\, \frac{1}{2}\,(\partial_\mu\varphi\,\partial^\mu\varphi) + g\,:\varphi^6:\,, \qquad \mathcal{A}_{\mathrm{crit}} = \int \mathrm{d}^2x\, \frac{1}{2}\,(\partial_\mu\varphi\,\partial^\mu\varphi) + g'\,:\varphi^4:\,, \tag{5.8}$$

where :: denotes normal ordering of the fields. The perturbing field of the UV theory $\phi_{1,3}$ corresponds to $:\varphi^4:$ [100, 101], which means that the action of the massless flow can be equivalently written as

$$\mathcal{A}_{\text{flow}} = \int \mathrm{d}^2x \, \frac{1}{2} \left(\partial_\mu \varphi \, \partial^\mu \varphi\right) + \tilde{\lambda} :\varphi^4: + g :\varphi^6: , \tag{5.9}$$

in which the invariance under the spin-flip $\mathbb{Z}_2$ symmetry, which maps $\varphi \to -\varphi$, is explicit.

Given the presence of a global $\mathbb{Z}_2$ symmetry, a relevant question is whether the ground state entanglement entropy along the massless flow (5.3) can be resolved with respect to it. It is not immediately obvious if a reduced density matrix of the ground state of the theory commutes with the charge operator associated with the $\mathbb{Z}_2$ symmetry. While for a continuous symmetry this is ensured by Noether theorem, in the case of discrete symmetries, the existence of a local charge density is not guaranteed. In order to justify the existence of such a local $\mathbb{Z}_2$ charge, we can appeal to the defect line formalism. As understood in recent years, global symmetries in QFT are implemented by topological defects [248, 249], which, in the case of CFT minimal models, correspond to the Verlinde lines operators. In particular, the spin-flip $\mathbb{Z}_2$ symmetry is implemented by the Verlinde line associated with the primary operator ε. Such a defect line can be restricted to the subsystem A, with two disorder operators μ inserted at the end-points [248, 249] (which we discuss in more detail in the next section). This formalism has been very recently used to study the symmetry resolution of entanglement in CFTs with respect to both continuous and discrete finite groups in Ref. [250]. Since the operators ε and μ exist along the entire massless flow, the previous construction may be extended outside the fixed points.

5.2 Entanglement entropy and Branch Point Twist Fields in QFT

In this section, we review the computation of the entanglement entropies in QFT as correlators of branch point twist fields. As we described in the Secs. 1.1 and 1.4 of the Introduction, in QFT the non-trivial task of computing entanglement entropies can be naturally formulated via the path integral approach. The main idea is that the moments of the reduced density matrix $\mathrm{Tr}(\rho_A^n)$ and the charged moments $\mathrm{Tr}(\rho_A^n e^{i\alpha Q_A})$ can be regarded as partition functions of the QFT on a Riemann surface consisting of n replicas of the space-time that are sewed along the subsystem A in a cyclical way [21, 22], as depicted in Fig. 1.1.

Alternatively, one can take n copies of the QFT under analysis and quotient them by the $\mathbb{Z}_n$ symmetry associated to the cyclic exchange of the copies. In $(1+1)$-dimensional relativistic QFTs, there exist local fields in the n-replica theory, called branch points twist fields (BPTF), that implement the boundary conditions imposed on the fields in the path integral on the n-sheeted Riemann surface. These twist fields can be generalised to cases in which the boundary conditions also involve additional phases, such as in the calculation of the charged moments $\mathrm{Tr}(\rho_A^n e^{i\alpha Q_A})$, in which an Aharonov-Bohm flux is introduced between the sheets of the Riemann surface. In this setup, the corresponding twist fields are called composite BPTFs and they were originally introduced in other context [194, 195]. Both types of fields are associated with particular symmetries of the replicated theory, which allows us to discuss them on the same ground. Therefore, for our purposes it is useful to distinguish the following twist fields:

1) the disorder field μ associated with the $\mathbb{Z}_2$ spin-flip symmetry of the massless flow;

2) the standard BPTFs, $\mathcal{T}_n$ and its conjugate $\widetilde{\mathcal{T}}_n$, which are associated with the cyclic and the inverse cyclic permutation symmetry $\mathbb{Z}_n$ among the copies in the n-replica massless flow. These fields play a central role in the computation of the entanglement entropy;

3) the $\mathbb{Z}_2$-composite BPTFs, denoted as $\mathcal{T}_n^\mu$ and $\widetilde{\mathcal{T}}_n^\mu$, which are the result of fusing the former fields
$$\mathcal{T}_n^\mu(\mathbf{x}) = :\mathcal{T}_n\,\mu:(\mathbf{x})\,, \qquad \widetilde{\mathcal{T}}_n^\mu(\mathbf{x}) = :\widetilde{\mathcal{T}}_n\,\mu:(\mathbf{x}). \tag{5.10}$$
Therefore, they are associated both with the $\mathbb{Z}_n$ symmetry under the cyclic permutation of the replicas and with the global $\mathbb{Z}_2$ spin-flip symmetry present in the massless flow. These composite fields play the analogous role of the BPTF in the computation of the symmetry resolved entanglement entropies [82].

These twist fields are typically non-local or semi-local with respect to other quantum fields of the theory, in particular with respect to the fundamental field or to the interpolating field, which is associated with particle creation/annihilation. Non-locality can be formulated by non-trivial equal-time exchange relations between the two fields. Let us first consider the disorder operator μ and an operator $\mathcal{O}_i$ living in the copy i of the replicated theory. Since the disorder field introduces an Aharonov-Bohm flux in the region $y^1 > x^1$, the exchange relations of these two operators can be written as

$$\mathcal{O}_i(\mathbf{y})\mu(\mathbf{x}) = \begin{cases} e^{\mathrm{i}\kappa_{\mathcal{O}}\pi}\,\mu(\mathbf{x})\,\mathcal{O}_i(\mathbf{y})\,, & \text{for } y^1 > x^1, \\ \mu(\mathbf{x})\,\mathcal{O}_i(\mathbf{y})\,, & \text{otherwise.} \end{cases} \tag{5.11}$$

We refer to $\kappa_{\mathcal{O}}$ as the charge of the operator $\mathcal{O}$ with respect to the $\mathbb{Z}_2$ spin-flip symmetry. In particular, the Goldstone fermions $\psi, \bar{\psi}$ which generate the asymptotic states (5.6) have charge $\kappa_\psi = 1$, i.e., they are odd under the spin-flip transformation.

The action of the standard BPTFs when winding around a field is to cyclically map it from one replica to the next, as encoded in the equal time exchange relation

$$\mathcal{O}_i(\mathbf{y})\mathcal{T}_n(\mathbf{x}) = \begin{cases} \mathcal{T}_n(\mathbf{x})\,\mathcal{O}_{i+1}(\mathbf{y})\,, & \text{for } y^1 > x^1\,, \\ \mathcal{T}_n(\mathbf{x})\,\mathcal{O}_i(\mathbf{y})\,, & \text{otherwise.} \end{cases} \tag{5.12}$$

In the case of the composite BPTFs, the winding around them further adds a phase $e^{i\kappa_{\mathcal{O}}\pi}$. When considering discrete groups, as the $\mathbb{Z}_2$ spin-flip symmetry of the tricritical-critical massless flow, we must be careful on how we include this phase. Differently from the continuous $U(1)$ symmetry discussed in Refs. [251, 252] and in the Introduction, here we cannot distribute the flux uniformly in all the copies by inserting a phase $e^{i\kappa_{\mathcal{O}}\pi/n}$ when moving between replicas since this operation in not compatible with the properties of the $\mathbb{Z}_2$ field μ. This issue can be addressed in two different ways. The first possibility is to insert a phase $e^{i\kappa_{\mathcal{O}}\pi}$ between all the copies; this corresponds to consider the exchange relation

$$\mathcal{O}_i(\mathbf{y})\mathcal{T}^{\mu}_n(\mathbf{x}) = \begin{cases} e^{\mathrm{i}\kappa_{\mathcal{O}}\pi}\,\mathcal{T}^{\mu}_n(\mathbf{x})\,\mathcal{O}_{i+1}(\mathbf{y})\,, & \text{for } y^1 > x^1\,,\\ \mathcal{T}^{\mu}_n(\mathbf{x})\,\mathcal{O}_i(\mathbf{y})\,, & \text{otherwise.}\end{cases} \tag{5.13}$$

This approach was applied in Ref. [253], but it is only legitimate when we take an odd number of replicas $n = 1, 3, 5, 7, \ldots$ in which the identity $e^{i\pi n} = -1$ clearly holds. The other approach consists of introducing the flux only between the last and the first replicas, in such a way that the phase $e^{i\pi\kappa_{\mathcal{O}}}$ only appears when a particles moves from the n-th copy to the 1-st one, that is

$$\mathcal{O}_i(\mathbf{y})\mathcal{T}^{\mu}_n(\mathbf{x}) = \begin{cases} \mathcal{T}^{\mu}_n(\mathbf{x})\,\mathcal{O}_{i+1}(\mathbf{y})\,, & \text{for } y^1 > x^1 \text{ and } i \neq n\,,\\ e^{\mathrm{i}\kappa_{\mathcal{O}}\pi}\,\mathcal{T}^{\mu}_n(\mathbf{x})\,\mathcal{O}_{i+1}(\mathbf{y})\,, & \text{for } y^1 > x^1 \text{ and } i = n\,,\\ \mathcal{T}^{\mu}_n(\mathbf{x})\,\mathcal{O}_i(\mathbf{y})\,, & \text{otherwise.}\end{cases} \tag{5.14}$$

This choice introduces a slight asymmetry between the replicas, but it is applicable to any number n of replicas. In Sec. 5.4, we discuss in more detail the effect of the two conventions (5.13) and (5.14), showing that they provide the same results for the correlation functions under analysis.

Analogous exchange relations can be formulated for the Hermitian conjugate fields $\widetilde{\mathcal{T}}$ and $\widetilde{\mathcal{T}}^{\mu}$, with the difference that they move the field from the replica i to $i-1$. In the following discussion, whenever we wish to treat both the standard and the composite twist fields at the same time, we use the notation $\mathcal{T}^{\tau}_n$, $\widetilde{\mathcal{T}}^{\tau}_n$, where τ refers either to 'μ' for the composite or to the identity for the standard BPTF.

Using the (composite) BPTFs, one can switch from a path-integral to an operator formulation of both the neutral and charged moments of ρ_A, which can be defined in terms of multi-point functions of the standard or the composite BPTFs in the replicated QFT inserted at the end-points of subsystem A. In particular, when A consists of a single interval, $A = [0, \ell]$, we have

$$\mathrm{Tr}(\rho_A^n) \sim \langle 0|\,\mathcal{T}_n(0)\widetilde{\mathcal{T}}_n(\ell)\,|0\rangle\,, \tag{5.15}$$

and

$$\mathrm{Tr}\big(\rho_A^n\, e^{\mathrm{i}\pi Q_A}\big) \sim \langle 0|\,\mathcal{T}^{\mu}_n(0)\widetilde{\mathcal{T}}^{\mu}_n(\ell)\,|0\rangle\,. \tag{5.16}$$

The twist field formalism is especially useful at criticality, where conformal invariance fixes the properties of both the standard $\mathcal{T}_n$ and the composite branch point twist field $\mathcal{T}^{\mu}_n$.

In particular, in a unitary CFT with central charge c, the standard twist fields $\mathcal{T}_n$, $\widetilde{\mathcal{T}}_n$ are known to be primary operators with conformal dimension [18, 22]

$$h_{\mathcal{T}} = \frac{c}{24}\left(n - \frac{1}{n}\right), \tag{5.17}$$

which correctly reproduces the entanglement entropy in Eq. (1.9). We remind the reader that, in the A-diagonal unitary minimal models $\mathcal{M}_p$, the central charge is given by Eq. (5.2).

In order to identify the conformal dimension of the composite twist fields $\mathcal{T}_n^{\mu}$, $\widetilde{\mathcal{T}}_n^{\mu}$, one can use the fact that they are the fusion of $\mathcal{T}_n$, $\widetilde{\mathcal{T}}_n$ with the disorder field μ as shown in Eq. (5.10). In the tricritical and critical Ising models, the field μ is the Kramers-Wannier dual of the spin field $\sigma = \phi_{2,2}$ and has the same conformal dimension reported in the Kac table in Table 5.1 [100, 101]

$$h_{\mu}^{\mathrm{UV}} = h_{\sigma}^{\mathrm{UV}} = \frac{3}{80}, \qquad h_{\mu}^{\mathrm{IR}} = h_{\sigma}^{\mathrm{IR}} = \frac{1}{16}, \tag{5.18}$$

where we denote with UV the tricritical and with IR the critical Ising models respectively. Knowing the dimension of the disorder field, the one of the composite twist fields $\mathcal{T}_n^{\mu}$, $\widetilde{\mathcal{T}}_n^{\mu}$ is obtained as [82]

$$h_{\mathcal{T}^{\mu}} = h_{\mathcal{T}} + \frac{h_{\mu}}{n}. \tag{5.19}$$

In particular, for the tricritical and critical Ising models, Eq. (5.19) gives respectively

$$h_{\mathcal{T}^{\mu}}^{\mathrm{UV}} = \frac{1}{240}\left(7n + \frac{2}{n}\right), \quad \text{and} \quad h_{\mathcal{T}^{\mu}}^{\mathrm{IR}} = \frac{1}{48}\left(n + \frac{2}{n}\right). \tag{5.20}$$

The use of CFT techniques has provided exact results for $\mathrm{Tr}(\rho_A^n)$ in many different situations [18, 22]. On the other hand, away from criticality, the exact determination of the correlation functions of Eqs. (5.15) and (5.16) is known to be an extremely difficult task, except in the case of free theories [198, 254]. In integrable QFTs, however, the form factor (FF) bootstrap approach provides a powerful tool to systematically investigate and construct (truncated) multi-point functions via form factors, namely matrix elements of generic local operators between the vacuum and the multi-particle states [186, 187]. Although, in principle, all these matrix elements can be analytically computed, their resummation is an unsolved problem. Nevertheless, the multi-point correlation functions at large distances are generically dominated by the first few (lower-particle) form factors. For this reason this technique applies efficiently to the infrared properties of these theories as was first shown in Ref. [188] in the case of BPTFs and entanglement. As we shall see in this Chapter, the above considerations do not hold in massless theories, i.e., when the IR limit of the QFT is described by a non-trivial CFT as well. However, we show that it is possible to identify a subset of terms in the form factor expansion whose resummation reproduces the IR CFT results, while the remaining contributions yield non-trivial predictions for the behaviour of the entropies along the flow.

5.2.1 Form factors and spectral representations of BPTF correlation functions

From the knowledge of the exchange relations (5.12) satisfied by the BPTFs, one can formulate bootstrap equations for their FF in integrable QFTs [188–190], generalising the standard form factor program for local fields [186, 187], which for the tricritical-critical Ising flow (5.3) has been investigated in Ref. [216].

Let us consider the two-point correlation function of the (composite) BPTFs in the ground state of the theory and insert the set of asymptotic states (5.6), which form a complete basis,

$$\begin{aligned}&\langle 0|\, \mathcal{T}_n^{\tau}(x)\widetilde{\mathcal{T}}_n^{\tau}(x')\,|0\rangle \\ &=\sum_{k=0}^{\infty}\sum_{\{\gamma\},\{\nu\}}\int\prod_{i=1}^{k}\mathrm{d}\theta_i\ \langle 0|\,\mathcal{T}_n^{\tau}(x)\,|\theta_1,\ldots\theta_k\rangle^{\nu_1\ldots\nu_k}_{\gamma_1\ldots\gamma_k}\times{}^{\nu_1\ldots\nu_k}_{\gamma_1\ldots\gamma_k}\langle\theta_1,\ldots\theta_k|\,\widetilde{\mathcal{T}}_n^{\tau}(x')\,|0\rangle\,,\end{aligned} \tag{5.21}$$

where $\tau = 0, \mu$ corresponds to the standard or the $\mathbb{Z}_2$-composite BPTF respectively. In the multi-particle states

$$|\theta_1,\ldots,\theta_k\rangle^{\nu_1\ldots\nu_k}_{\gamma_1\ldots\gamma_k}\,, \tag{5.22}$$

of the n-replica theory, the subindex $\gamma_i = R, L$ specifies if the particle with rapidity θ_i is a right- (R) or left-mover (L). Moreover, each particle is labelled by an extra index ν_i which indicates the copy where the particle lives; therefore, it takes values from 1 to n and it is identified up to $\nu_i \sim \nu_i + n$.

In the n-replica theory, the S-matrix connects non-trivially only particles living on the same replica, while particles in different copies do not interact and no scattering events occur between them. In light of this, the S-matrix of the replicated model takes the form [188]

$$S^{\nu_i,\nu_j}_{\gamma_i,\gamma_j}(\theta) = \begin{cases} S_{\gamma_i\gamma_j}(\theta), & \nu_i = \nu_j,\\ 1, & \nu_i \neq \nu_j,\end{cases} \tag{5.23}$$

where $S_{\gamma_i,\gamma_j}(\theta)$ is the S matrix of the original theory, which for the massless flow (5.3) is reported in Eq. (5.7).

Since the vacuum of the theory is invariant under space and time translations, we can rewrite the spectral expansion in Eq. (5.21) as

$$\begin{aligned}&\langle 0|\, \mathcal{T}_n^{\tau}(x-x')\widetilde{\mathcal{T}}_n^{\tau}(0)\,|0\rangle \\ &=\sum_{k=0}^{\infty}\sum_{\{\gamma\},\{\nu\}}\int\prod_{i=1}^{k}\mathrm{d}\theta_i\ \langle 0|\,e^{\mathrm{i}H(x_0-x_0')-\mathrm{i}P(x_1-x_1')}\mathcal{T}_n^{\tau}(0)e^{-\mathrm{i}H(x_0-x_0')+\mathrm{i}P(x_1-x_1')}\,|\theta_1,\ldots\theta_k\rangle^{\nu_1\ldots\nu_k}_{\gamma_1\ldots\gamma_k}\times \\ &\qquad\times{}^{\nu_1\ldots\nu_k}_{\gamma_1\ldots\gamma_k}\langle\theta_1,\ldots\theta_k|\,\widetilde{\mathcal{T}}_n^{\tau}(0)\,|0\rangle\end{aligned}$$

$$
\begin{aligned}
&= \sum_{k=0}^{\infty} \sum_{\{\gamma\},\{\nu\}} \int \prod_{i=1}^{k} \mathrm{d}\theta_i \, \langle 0 | \, \mathcal{T}_n^{\tau}(0) \, | \theta_1, \dots \theta_k \rangle^{\nu_1 \dots \nu_n}_{\gamma_1 \dots \gamma_k} \; e^{-\mathrm{i} \sum_i E_i (x_0 - x_0') + \mathrm{i} \sum_i p_i (x_1 - x_1')} \\
&\qquad\qquad \times {}^{\nu_1 \dots \nu_k}_{\gamma_1 \dots \gamma_k} \langle \theta_1, \dots \theta_k | \, \widetilde{\mathcal{T}}_n^{\tau}(0) \, | 0 \rangle ,
\end{aligned}
\tag{5.24}
$$

where E_i and p_i are the single particle energies and momenta reported in Eq. (5.5). The elementary FFs of a generic (semi-)local operator $\mathcal{O}(x,t)$ are their matrix elements between the vacuum and the asymptotic multi-particle states (5.22), i.e.

$$
F^{\mathcal{O}|\nu_1 \dots \nu_k}_{\gamma_1 \dots \gamma_k}(\theta_1, \dots, \theta_k) = \langle 0 | \, \mathcal{O}(0,0) \, | \theta_1, \dots \theta_k \rangle^{\nu_1 \dots \nu_k}_{\gamma_1 \dots \gamma_k} \, . \tag{5.25}
$$

Using the definition (5.25) of the FFs in the spectral sum representation in Eq. (5.24), we finally obtain the following expansion of the twist field correlator

$$
\langle 0 | \, \mathcal{T}_n^{\tau}(\mathbf{x}) \widetilde{\mathcal{T}}_n^{\tau}(0) \, | 0 \rangle = \sum_{k=0}^{\infty} \sum_{\{\gamma\},\{\nu\}} \int \prod_{i=1}^{k} \mathrm{d}\theta_i \left| F^{\mathcal{T}_\tau | \nu_1 \dots \nu_k}_{\gamma_1 \dots \gamma_k}(\theta_1, \dots, \theta_k; n) \right|^2 \exp\left(-\ell \sum_i^k E_i \right) , \tag{5.26}
$$

where we switched to the Euclidean formalism for simplicity and ℓ denotes the Euclidean distance. We can see from the above formula that the computation of the twist field correlation functions can be naturally formulated by means of FFs via the insertion of a complete set of asymptotic multi-particle states. Crucially, the form factors in integrable QFTs can often be determined exactly, giving access to the corresponding correlation functions. In the following, we review some basic properties of the twist field FFs and present the bootstrap equations from which their analytic expressions can be obtained.

5.3 Form factors of the branch point twist field in the massless flow

Given the exchange properties of the standard BPTFs (5.11), it is possible to write down the bootstrap equations for the form factors (5.25) associated with these fields in integrable QFTs. Relying on earlier works [188–190], we can immediately specify these equations for our massless theory (5.3). If we denote the FFs of $\mathcal{T}_n$ by $F^{\mathcal{T}|\underline{\nu}}_{\underline{\gamma}}(\underline{\theta}; n)$, then their bootstrap equations can be written as [188–190]

$$
F^{\mathcal{T}|\underline{\nu}}_{\underline{\gamma}}(\underline{\theta}; n) = S^{\nu_i \nu_{i+1}}_{\gamma_i \gamma_{i+1}}(\theta_{i,i+1}) \, F^{\mathcal{T}| \dots \nu_{i-1} \nu_{i+1} \nu_i \nu_{i+2} \dots}_{\dots \gamma_{i-1} \gamma_{i+1} \gamma_i \gamma_{i+2} \dots}(\dots \theta_{i+1}, \theta_i, \dots ; n), \tag{5.27}
$$

$$
F^{\mathcal{T}|\underline{\nu}}_{\underline{\gamma}}(\theta_1 + 2\pi \mathrm{i}, \theta_2, \dots, \theta_k; n) = F^{\mathcal{T}|\nu_2 \nu_3 \dots \nu_k \hat{\nu}_1}_{\gamma_2 \gamma_3 \dots \gamma_k \gamma_1}(\theta_2, \dots, \theta_k, \theta_1; n), \tag{5.28}
$$

$$
-\mathrm{i} \operatorname*{Res}_{\theta_0' = \theta_0 + \mathrm{i}\pi} F^{\mathcal{T}|\nu_0 \nu_0 \underline{\nu}}_{\bar{\gamma}_0 \gamma_0 \underline{\gamma}}(\theta_0', \theta_0, \underline{\theta}; n) = F^{\mathcal{T}|\underline{\nu}}_{\underline{\gamma}}(\underline{\theta}; n), \tag{5.29}
$$

$$-\mathrm{i}\underset{\theta_0'=\theta_0+\mathrm{i}\pi}{\mathrm{Res}} F^{\mathcal{T}|\nu_0\hat{\nu}_0\underline{\nu}}_{\bar{\gamma}_0\gamma_0\underline{\gamma}}(\theta_0',\theta_0,\underline{\theta};n) = -\prod_{l=1}^{k} S^{\hat{\nu}_0\nu_l}_{\gamma_0\gamma_l}(\theta_{0l})\,F^{\mathcal{T}|\underline{\nu}}_{\underline{\gamma}}(\underline{\theta};n), \tag{5.30}$$

where we introduced

$$\bar{\gamma}_i = \gamma_i, \qquad \hat{\nu}_i = \nu_i + 1, \tag{5.31}$$

and $\bar{\gamma}_i$ denotes the anti-particle of γ_i (which coincides with the particle in the theory under consideration). Here $\underline{\theta}$ and $\underline{\gamma}$, $\underline{\nu}$ are shorthands for $(\theta_1,\theta_2,\ldots,\theta_k)$ and $(\gamma_1,\gamma_2,\ldots,\gamma_k)$, $(\nu_1,\nu_2,\ldots,\nu_k)$ respectively, with $\gamma = R, L$ and $\bar{R} = R$, $\bar{L} = L$. In the argument of the S-matrices, $\theta_{ij} = \theta_i - \theta_i$.

In the massless flow (5.3), two particles of any type cannot form a bound state. It is also easy to see that the one-particle FFs of BPTF are vanishing. The reason for this is that these fields are neutral w.r.t. the $\mathbb{Z}_2$ charge. This implies that only FFs with an even number of R and an even number of L particles are non-vanishing and, consequently, the odd-particle FFs are zero.

Moreover, relativistic invariance imposes that

$$F^{\mathcal{T}|\underline{\nu}}_{\underline{\gamma}}(\theta_1+\Lambda,\ldots,\theta_k+\Lambda;n) = e^{\Sigma\Lambda}F^{\mathcal{T}|\underline{\nu}}_{\underline{\gamma}}(\underline{\theta};n) = F^{\mathcal{T}|\underline{\nu}}_{\underline{\gamma}}(\underline{\theta};n)\,, \tag{5.32}$$

where Σ is the Lorentz spin, which is $\Sigma = 0$ for the twist field.

Another important property of form factors which will be useful in our analysis is the cluster property, studied in detail in Ref. [214] and recognised in different models, see e.g. [193, 255–258]. In the limit in which the difference between the particle rapidities diverges, the form factors factorise in the product of form factors with a lower number of particles. In our model, the clusterisation of the different particle species can be phrased as

$$\lim_{\Lambda\to\infty} F^{\mathcal{T}|\underline{\nu},\underline{\nu}'}_{\underline{R},\underline{L}}(\underline{\theta}+\Lambda,\underline{\theta}'-\Lambda;n) = \langle\mathcal{T}_n\rangle^{-1}F^{\mathcal{T}|\underline{\nu}}_{\underline{R}}(\underline{\theta};n)F^{\mathcal{T}|\underline{\nu}'}_{\underline{L}}(\underline{\theta}';n)\,, \tag{5.33}$$

where $\underline{\theta}$ and $\underline{\nu}$ stand for the rapidities and replica indices of the 'R' particles, and $\underline{\theta}'$ and $\underline{\nu}'$ for the 'L' particles. The cluster property for particles of the same species is instead written as

$$\lim_{\Lambda\to\infty} F^{\mathcal{T}|\underline{\nu}_1+\underline{\nu}_2,\underline{\nu}'}_{\underline{R}_1+\underline{R}_2,\underline{L}}(\underline{\theta}_1+\Lambda,\underline{\theta}_2-\Lambda,\underline{\theta}'-\Lambda;n) = \langle\mathcal{T}_n\rangle^{-1}F^{\mathcal{T}|\underline{\nu}_1}_{\underline{R}_1}(\underline{\theta}_1;n)F^{\mathcal{T}|\underline{\nu}_1,\underline{\nu}'}_{\underline{R}_2,\underline{L}}(\underline{\theta}_2,\underline{\theta}';n)\,, \tag{5.34}$$

with an analogous expression for the clustering of 'L' particles.

Let us now use the previous axioms to construct a set of solutions of the bootstrap equations (5.27)-(5.30) for the BPTF form factors. To fix the ideas, we first place every particle on the first replica $\nu_i = 1$. A convenient ansatz for the form factors is [216]

$$\begin{aligned} F^{\mathcal{T}}_{\underline{R},\underline{L}}(\underline{\theta},\underline{\theta}';n) = H^{\mathcal{T}}_{r,l}Q^{\mathcal{T}}_{r,l}(\underline{x},\underline{y};n) \prod_{1\leqslant i<j\leqslant r}\frac{f_{RR}(\theta_i-\theta_j;n)}{(x_i-\omega x_j)(x_j-\omega x_i)}\times \\ \times\prod_{i=1}^{r}\prod_{j=1}^{l} f_{RL}(\theta_i-\theta_j';n)\prod_{1\leqslant i<j\leqslant l}\frac{f_{LL}(\theta_i'-\theta_j';n)}{(y_i-\omega y_j)(y_j-\omega y_{ji})}, \end{aligned} \tag{5.35}$$

where we have r right-moving and l left-moving particles and we have defined $x_i = e^{\theta_i/n}$, $y_i = e^{-\theta'_i/n}$ and $\omega = e^{\mathrm{i}\pi/n}$. Notice that we simplified our notation by omitting the reference to the replica indices. In the ansatz (5.35), $Q^{\mathcal{T}}_{r,l}$ are polynomials of their variables and $f_{RR} = f_{LL}$ and f_{RL} are the minimal form factors. In Eq. (5.35), the kinematical singularity of the FF (see Eq. (5.29)) comes entirely from the denominators and therefore the cyclic permutation and the exchange axioms, Eqs. (5.27) and (5.28), are automatically satisfied requiring the following identities for the minimal form factors:

$$\begin{aligned} f_{RR}(\theta;n) &= -f_{RR}(-\theta;n)\,, \\ f_{RR}(2\pi n\mathrm{i}+\theta;n) &= f_{RR}(-\theta;n)\,. \end{aligned} \tag{5.36}$$

By prescribing that the minimal form factor f_{RR} has no poles and has the mildest asymptotic behaviour, we end up with the unique solution

$$f_{RR}(\theta;n) = \sinh\left(\frac{\theta}{2n}\right), \tag{5.37}$$

and $f_{RR} = f_{LL}$, which is identical to the minimal form factor of the massive Ising theory [188].

For f_{RL}, the defining equations are

$$\begin{aligned} f_{RL}(\theta;n) &= S_{RL}(\theta) f_{LR}(-\theta;n)\,, \\ f_{RL}(2\pi n\mathrm{i}+\theta;n) &= f_{LR}(-\theta;n)\,, \end{aligned} \tag{5.38}$$

whose solution can be explicitly given based on the knowledge of the Fourier representation of the non-trivial S-matrix S_{RL} in Eq. (5.7). In particular, we can write the solution as

$$f_{RL}(\theta;n) = \exp\left[\frac{\theta}{4n} - \int_0^\infty \frac{dt}{t}\frac{\sin^2\left(\frac{(\mathrm{i}\pi n-\theta)t}{2\pi}\right)}{\sinh(nt)\cosh\frac{t}{2}}\right], \tag{5.39}$$

using an integral representation, or, alternatively, in terms of a mixed product integral representation

$$\begin{aligned} f_{RL}(\theta;n) = \exp\!\left(\frac{\theta}{4n}\right) &\left[\prod_{k=0}^{m} \frac{\Gamma\left(\frac{2k+n+\frac{3}{2}}{2n}\right)^2 \Gamma\left(\frac{\frac{\mathrm{i}\theta}{\pi}+2k+\frac{1}{2}+2n}{2n}\right)\Gamma\left(\frac{-\frac{\mathrm{i}\theta}{\pi}+2k+\frac{1}{2}}{2n}\right)}{\Gamma\left(\frac{2k+n+\frac{1}{2}}{2n}\right)^2 \Gamma\left(\frac{\frac{\mathrm{i}\theta}{\pi}+2k+\frac{3}{2}+2n}{2n}\right)\Gamma\left(\frac{-\frac{\mathrm{i}\theta}{\pi}+2k+\frac{3}{2}}{2n}\right)}\right]\times \\ &\times \exp\left(\int_0^\infty \mathrm{d}t\, \frac{e^{-(2m+2)t}\sinh^2\left(\frac{1}{2}t\left(n+\frac{\mathrm{i}\theta}{\pi}\right)\right)}{t\cosh\left(\frac{t}{2}\right)\sinh(nt)}\right), \end{aligned} \tag{5.40}$$

which is more convenient for numerical evaluation. Notice that, for $n = 1$, the minimal form factor (5.39) reduces to the known result for a single replica obtained in Ref. [216].

Moreover, it is bounded, that is, $f_{RL}(\theta,n) \to 0$ when $\theta \to -\infty$, and $f_{RL}(\theta,n) \to \mathcal{N}_n^{-1}$ when $\theta \to \infty$. Therefore, it is customary to normalise it such that

$$\lim_{\theta\to\infty} \tilde{f}_{RL}(\theta;n) = 1\,. \tag{5.41}$$

In order to fix this normalisation along the massless flow, we compute the value $\mathcal{N}_n^{-1}$ of f_{RL} in the limit $\theta \to \infty$, which reads

$$\mathcal{N}_n^{-1} = e^{\mathrm{i}\pi/4}\,2^{1/4}\exp\!\left(\frac{1}{8}\int_{-\infty}^{+\infty}\frac{\mathrm{d}t}{t}\frac{1}{\sinh(nt)}\left[1-\frac{1}{\cosh t\cosh(nt)}\right]\right) = e^{\mathrm{i}\pi/4}\,2^{1/4}\,e^{G_n/\pi}\,, \tag{5.42}$$

where we have defined the sequence

$$G_n = \frac{\pi}{8}\int_{-\infty}^{+\infty}\frac{\mathrm{d}t}{t}\frac{1}{\sinh(nt)}\left[1-\frac{1}{\cosh t\cosh(nt)}\right], \tag{5.43}$$

which is equal to Catalan's constant G for $n = 1$, recovering the normalisation for f_{RL} found in the non-replicated theory in Ref. [216]. With the choice

$$\tilde{f}_{RL}(\theta;n) = \mathcal{N}_n f_{RL}(\theta;n)\,, \tag{5.44}$$

we fix all the constants in the form factors for the massless flow. An important property that the f_{RL} minimal form factor satisfies is

$$\mathcal{N}_n f_{RL}(\theta+\mathrm{i}\pi;n)\,\mathcal{N}_n f_{RL}(\theta;n) = \left(1-e^{-\frac{\mathrm{i}\pi}{2n}}e^{-\frac{\theta}{n}}\right)^{-1}, \tag{5.45}$$

which shall be very useful in the rest of the section.

The ansatz (5.35), with the definitions for the minimal FFs f_{RR} (5.37) and f_{RL} (5.40), satisfies all the axioms for the BPTF FFs. The eventual determination of $F^{\mathcal{T}}_{\underline{R},\underline{L}}(\underline{\theta},\underline{\theta'};n)$ can be done recursively. In fact, by applying the residue axiom in Eq. (5.29) to the ansatz (5.35), one can derive recursive equations for the unknown $Q^{\mathcal{T}}_{r,l}(\underline{x},\underline{y};n)$ functions that relate $Q^{\mathcal{T}}_{r+2,l}(\underline{x},\underline{y};n)$ or $Q^{\mathcal{T}}_{r,l+2}(\underline{x},\underline{y};n)$ to $Q^{\mathcal{T}}_{r,l}(\underline{x},\underline{y};n)$, that is, to $Q^{\mathcal{T}}_{r,l}$ functions with fewer particles. In the next subsections and in Sec. 5.A.1, we explicitly demonstrate how the determination of higher-particle FFs is carried out by solving the recursive equations for the polynomials $Q^{\mathcal{T}}_{r,l}$.

5.3.1 Two-particle form factors and form factors with only one species

Since the Lorentz spin of the BPTFs is zero, their two-particle FFs only depend on one rapidity variable (5.32), that is, the rapidity difference $\theta_1-\theta_2$. Recall that, because of the spin-flip symmetry, we can only have 'RR' and 'LL' form factors, which means that these quantities coincide with those of the massive Ising QFT (c.f. Eqs. (5.35) and (5.37)) up to the vacuum expectation value $\langle\mathcal{T}_n\rangle$. These quantities, nevertheless, can also be easily obtained from the bootstrap equations (5.27), (5.28). For the two-particle form factors, they imply that

$$F^{\mathcal{T}|\nu_i\nu_j}_{\gamma_i\gamma_j}(\theta;n) = S^{\nu_i\nu_j}_{\gamma_i\gamma_j}(\theta) F^{\mathcal{T}|\nu_j\nu_i}_{\gamma_j\gamma_i}(-\theta;n) = F^{\mathcal{T}|\nu_j\nu_i}_{\gamma_j\gamma_i}(2\pi\mathrm{i}n-\theta;n)\,. \tag{5.46}$$

In this case, the kinematic residue equation (5.29),

$$-\mathrm{i}\,\underset{\theta=\mathrm{i}\pi}{\mathrm{Res}}\, F^{\mathcal{T}|\nu\nu}_{\gamma\gamma}(\theta;n) = \langle\mathcal{T}_n\rangle, \tag{5.47}$$

connects the two-particle FFs and the vacuum expectation value of the twist field. We can therefore write

$$F^{\mathcal{T}|11}_{\gamma\gamma}(\theta;n) = \frac{\langle\mathcal{T}_n\rangle \sin\frac{\pi}{n}}{2n\sinh\frac{\mathrm{i}\pi+\theta}{2n}\sinh\frac{\mathrm{i}\pi-\theta}{2n}}\,\frac{\sinh(\theta/(2n))}{\sinh(\mathrm{i}\pi/(2n))}\,. \tag{5.48}$$

If this formula is recast in the form of the ansatz (5.35), then we have the equivalent expression

$$\begin{aligned} F^{\mathcal{T}}_{2,0}(\theta_1-\theta_2;n) &= -\mathrm{i}\,\langle\mathcal{T}_n\rangle\frac{4\,\omega}{n}\cos\left(\frac{\pi}{2n}\right)\frac{x_1\,x_2\,f_{RR}(\theta_1-\theta_2;n)}{(x_1-\omega x_2)(x_2-\omega x_1)} \\ &= H^{\mathcal{T}}_{2,0}\,Q^{\mathcal{T}}_{2,0}(x_1,x_2)\,\frac{f_{RR}(\theta_1-\theta_2;n)}{(x_1-\omega x_2)(x_2-\omega x_1)}, \end{aligned} \tag{5.49}$$

in which we identify

$$H^{\mathcal{T}}_{2,0} = -\mathrm{i}\langle\mathcal{T}_n\rangle\frac{4\,\omega}{n}\cos\left(\frac{\pi}{2n}\right)\,, \tag{5.50}$$

$$Q^{\mathcal{T}}_{2,0}(x_1,x_2) = \sigma_2(x_1,x_2) = x_1x_2, \tag{5.51}$$

where σ_j is the fully symmetric polynomial of degree j in the variables x_1 and x_2. Since in the formula above both particles live in the first replica, we slightly changed the notation, namely we denote the form factor corresponding to two right-moving particles living in the first replica $F^{\mathcal{T}|11}_{RR}$ as $F^{\mathcal{T}}_{2,0}$. In the following, we shall use this convention whenever all the particles are on the first replica. The 'LL' form factor can be obtained by replacing x_1 and x_2 by y_1 and y_2 in Eq. (5.49).

From $F^{\mathcal{T}|11}_{\gamma\gamma}(\theta;n)$, we can obtain the form factors $F^{\mathcal{T}|jk}_{\gamma\gamma}(\theta;n)$ corresponding to particles in different replicas from [188]

$$F^{\mathcal{T}|jk}_{\gamma\gamma}(\theta;n) = \begin{cases} F^{\mathcal{T}|11}_{\gamma\gamma}(2\pi-\mathrm{i}(k-j)-\theta;n), & \text{if } k>j, \\ F^{\mathcal{T}|11}_{\gamma\gamma}(2\pi-\mathrm{i}(j-k)+\theta;n), & \text{otherwise.} \end{cases} \tag{5.52}$$

The form factors $\tilde{F}$ of the antitwist field $\widetilde{\mathcal{T}}_n$ can be simply obtained from those of $\mathcal{T}_n$ through the relation [188]

$$\tilde{F}^{\mathcal{T}|jk}_{\gamma\gamma}(\theta;n) = F^{\mathcal{T}|n-j,n-k}_{\gamma\gamma}(\theta;n)\,. \tag{5.53}$$

As we already said, the only non-vanishing FFs with higher-particle number are those containing an even number of 'R' and 'L' particles. It is easy to see that, in the particular case of form factors only containing an even number of particles of the same type, that is, the 'RR...RR' and 'LL...LL' form factors, they exactly coincide with the standard BPTF FFs of the massive Ising theory up to the vacuum expectation value $\langle\mathcal{T}_n\rangle$, similarly to the two-particle case discussed above. These form factors can be easily obtained from the two-particles ones. In particular, the form factor with $2k$ particles of the same type is given by

$$F_{\gamma\dots\gamma}^{\mathcal{T}|\nu_1\dots\nu_{2k}}(\theta_1,\dots,\theta_{2k};n)=\langle\mathcal{T}_n\rangle\,\mathrm{Pf}(W)\,, \tag{5.54}$$

for $\nu_1\geq\nu_2\geq\dots\geq\nu_{2k}$. Here $\mathrm{Pf}(W)$ is the Pfaffian of the $2k\times 2k$ anti-symmetric matrix W with entries

$$W_{lm}=\frac{1}{\langle\mathcal{T}_n\rangle}\begin{cases}F_{\gamma\gamma}^{\mathcal{T}|\nu_l\nu_m}(\theta_l-\theta_m;n)\,, & m>l,\\ (-1)^{\delta_{\nu_l,\nu_m}+1}\,F_{\gamma\gamma}^{\mathcal{T}|\nu_l\nu_m}(\theta_l-\theta_m;n)\,, & m<l.\end{cases} \tag{5.55}$$

If the ordering of the indices ν_i is not the canonical one, using the exchange axiom (5.27) one can reshuffle the particles and their rapidities to satisfy $\nu_1\geq\nu_2\geq\dots\geq\nu_{2k}$ and apply (5.54). In particular, for the 'RRRR' or 'LLLL' FFs with all the particles in the same replica, we have the simple formula

$$\begin{aligned}F_{4,0}^{\mathcal{T}}(\theta_1,\theta_2,\theta_3,\theta_4;n)=\langle\mathcal{T}_n\rangle^{-1}\big[&F_{2,0}^{\mathcal{T}}(\theta_1-\theta_2;n)F_{2,0}^{\mathcal{T}}(\theta_3-\theta_4;n)\\ &-F_{2,0}^{\mathcal{T}}(\theta_1-\theta_3;n)F_{2,0}^{\mathcal{T}}(\theta_2-\theta_4;n)+F_{2,0}^{\mathcal{T}}(\theta_1-\theta_4;n)F_{2,0}^{\mathcal{T}}(\theta_2-\theta_3;n)\big]\,.\end{aligned} \tag{5.56}$$

5.3.2 Solution for the four particle 'RRLL' form factor

The first non-vanishing form factors that contain both 'R' and 'L' particles appear at the four-particle level: $F_{RRLL}^{\mathcal{T}|\nu_1\nu_2\nu_3\nu_4}$ with any permutation of 'R' and 'L'. Similarly to the other FFs previously discussed, it is sufficient to determine only the 'RRLL' form factor with all the particles on the first replica. Using then the exchange relation (5.27) we can readily obtain any other sequence of the particle species, and, applying the cyclic permutation axiom (5.28), we can obtain FFs for particles living on different replicas. Following the notation introduced for the form factors with all the particles on the first replica, we will denote $F_{RRLL}^{\mathcal{T}|1111}$ as $F_{2,2}^{\mathcal{T}}$. In this case, the ansatz (5.35) takes the form

$$\begin{aligned}F_{2,2}^{\mathcal{T}}(\theta_1,\theta_2,\theta_1',\theta_2';n)=H_{2,2}^{\mathcal{T}}\,Q_{2,2}^{\mathcal{T}}(x_1,x_2,y_1,y_2;n)&\frac{f_{RR}(\theta_1-\theta_2;n)}{(x_1-\omega x_2)(x_2-\omega x_1)}\times\\ \times\prod_{i=1}^{2}\prod_{j=1}^{2}f_{RL}(\theta_i-\theta_j';n)&\frac{f_{LL}(\theta_1'-\theta_2';n)}{(y_1-\omega y_2)(y_2-\omega y_1)}\,.\end{aligned} \tag{5.57}$$

Applying now the residue axiom (5.29) to Eq. (5.57), we can derive recursive equations for the $H^{\mathcal{T}}_{2,2}$ normalisation factor and the $Q^{\mathcal{T}}_{2,2}$ function. The detailed solution of this equation for the case of four-particles (RRLL) is presented in Sec. 5.A.1 and here we report the results of the calculations.

The normalisation factor reads

$$H^{\mathcal{T}}_{2,2} = -\langle \mathcal{T}_n \rangle \mathcal{N}_n^4 \left[\frac{4\,\omega}{n} \cos\left(\frac{\pi}{2n}\right)\right]^2 , \tag{5.58}$$

where $\mathcal{N}_n$ is given by Eq. (5.42), while for the polynomial $Q^{\mathcal{T}}_{2,2}$ we obtain

$$\begin{aligned} Q^{\mathcal{T}}_{2,2}(x_1,x_2,y_1,y_2;n) &= 1 - \frac{1}{2\cos\frac{\pi}{2n}} \sigma_1(x_1,x_2)\sigma_1(y_1,y_2) + \sigma_2(x_1,x_2)\sigma_2(y_1,y_2) \\ &= 1 - \frac{1}{2\cos\frac{\pi}{2n}} \left(x_1+x_2\right)\left(y_1+y_2\right) + x_1x_2y_1y_2, \end{aligned} \tag{5.59}$$

where $\sigma_i, i = 1, 2$ denotes the completely symmetrical polynomial of degree i in two variables. Using these results, the final solution for the full FF is

$$\begin{aligned} F^{\mathcal{T}}_{2,2}(\theta_1,\theta_2,\theta'_1,\theta'_2;n) = &- \mathcal{N}_n^4 \left[\frac{4\,\omega}{n}\cos\left(\frac{\pi}{2n}\right)\right]^2 \left[1 - \frac{1}{2\cos\frac{\pi}{2n}}\left(x_1+x_2\right)\left(y_1+y_2\right) + x_1x_2y_1y_2\right] \times \\ &\times \frac{f_{RR}(\theta_1-\theta_2;n)}{(x_1-\omega x_2)(x_2-\omega x_1)} \prod_{i=1}^{2}\prod_{j=1}^{2} f_{RL}(\theta_i-\theta'_j;n) \frac{f_{LL}(\theta'_1-\theta'_2;n)}{(y_1-\omega y_2)(y_2-\omega y_1)} , \end{aligned} \tag{5.60}$$

which we can also rewrite as

$$\begin{aligned} &F^{\mathcal{T}}_{2,2}(\theta_1,\theta_2,\theta'_1,\theta'_2;n) = \\ &= -2\,\mathcal{N}_n^4\, e^{-\frac{\theta_1+\theta_2-\theta'_1-\theta'_2}{2n}} \left[\cosh\left(\frac{\theta_1+\theta_2-\theta'_1-\theta'_2}{2n}\right) - \frac{\cosh\left(\frac{\theta_1+\theta_2}{2n}\right)\cosh\left(\frac{\theta'_1+\theta'_2}{2n}\right)}{\cos\frac{\pi}{2n}}\right] \times \\ &\qquad \times F^{\mathcal{T}}_{2,0}(\theta_1,\theta_2;n) \prod_{i=1}^{2}\prod_{j=1}^{2} f_{RL}(\theta_i-\theta'_j;n)\, F^{\mathcal{T}}_{0,2}(\theta'_1,\theta'_2;n)\,. \end{aligned} \tag{5.61}$$

We remark that the form factor in Eq. (5.60) is one of the main results of this Chapter. As we will show in Sec. 5.6, it will provide the leading correction to the IR expressions for the entanglement entropy.

5.4 Form factors of the $\mathbb{Z}_2$-composite branch point twist field in the massless flow

In this section, we derive the bootstrap equations for the form factors of the $\mathbb{Z}_2$-composite BPTFs associated with the disorder field μ along the massless flow (5.3) and we obtain their explicit solution for the two and four-particle cases. Similarly to the standard BPTFs discussed in Sec. 5.3, from the exchange properties of the $\mathbb{Z}_2$-composite twist fields (5.13) or (5.14), we can easily write down their form factor bootstrap equations. Importantly, these equations include the non-trivial phase $e^{i\pi\kappa_{\mathcal{O}}}$ in the monodromy properties due to the insertion of the disorder field μ. The asymptotic states (5.22) that enter in the definition of the twist field FFs are constructed from the fields ψ, $\bar{\psi}$, which are odd under the $\mathbb{Z}_2$ transformation, i.e. $\kappa_\psi = 1$, and therefore we must take into account a phase $e^{i\pi}$ when moving between replicas. However, as we discussed around Eqs. (5.13) and (5.14), we have two different ways to introduce it, either as a whole phase $e^{i\pi}$ in each replica, which is valid only for odd n, or inserting it only in the last one. These two approaches lead to slightly different form factor bootstrap equations. In this section, we comment both choices. In particular, we will show that the two conventions give the same result for the form factors up to some (-1) factors which do not influence the final physical result.

Let us denote as $F^{\mathcal{T}^\mu|\underline{\nu}}_{\underline{\gamma}}(\underline{\theta},n)$ the form factors of the composite twist fields $\mathcal{T}^\mu_n$. If we introduce the phase $e^{\mathrm{i}\pi}$ on the last replica only, that is taking the exchange relations (5.14), the bootstrap equations take the form

$$F^{\mathcal{T}^\mu|\underline{\nu}}_{\underline{\gamma}}(\underline{\theta};n) = S^{\nu_i\nu_{i+1}}_{\gamma_i\gamma_{i+1}}(\theta_{i,i+1})\, F^{\mathcal{T}^\mu|\ldots\nu_{i-1}\nu_{i+1}\nu_i\nu_{i+2}\ldots}_{\ldots\gamma_{i-1}\gamma_{i+1}\gamma_i\gamma_{i+2}\ldots}(\ldots\theta_{i+1},\theta_i,\ldots;n)\,, \tag{5.62}$$

$$F^{\mathcal{T}^\mu|\underline{\nu}}_{\underline{\gamma}}(\theta_1+2\pi\mathrm{i},\theta_2,\ldots,\theta_k;n) = F^{\mathcal{T}^\mu|\nu_2\nu_3\ldots\nu_k\hat{\nu}_1}_{\gamma_2\gamma_3\cdots\gamma_k\gamma_1}(\theta_2,\ldots,\theta_k,\theta_1;n)\times\begin{cases}-1, & \nu_1=n,\\ 1, & \text{otherwise},\end{cases} \tag{5.63}$$

$$-\mathrm{i}\underset{\theta_0'=\theta_0+\mathrm{i}\pi}{\mathrm{Res}} F^{\mathcal{T}^\mu|\nu_0\nu_0\underline{\nu}}_{\bar{\gamma}_0\gamma_0\underline{\gamma}}(\theta_0',\theta_0,\underline{\theta};n) = F^{\mathcal{T}^\mu|\underline{\nu}}_{\underline{\gamma}}(\underline{\theta};n)\,, \tag{5.64}$$

$$-\mathrm{i}\underset{\theta_0'=\theta_0+\mathrm{i}\pi}{\mathrm{Res}} F^{\mathcal{T}^\mu|\nu_0\hat{\nu}_0\underline{\nu}}_{\bar{\gamma}_0\gamma_0\underline{\gamma}}(\theta_0',\theta_0,\underline{\theta};n) = -\prod_{l=1}^{k} S^{\hat{\nu}_0\nu_l}_{\gamma_0\gamma_l}(\theta_{0l})\, F^{\mathcal{T}^\mu|\underline{\nu}}_{\underline{\gamma}}(\underline{\theta};n)\times\begin{cases}-1, & \nu_0=n,\\ 1, & \text{otherwise}.\end{cases} \tag{5.65}$$

On the other hand, if we introduce the same flux between all the copies, we have

$$F^{\mathcal{T}^\mu|\underline{\nu}}_{\underline{\gamma}}(\underline{\theta};n) = S^{\nu_i\nu_{i+1}}_{\gamma_i\gamma_{i+1}}(\theta_{i,i+1})\, F^{\mathcal{T}^\mu|\ldots\nu_{i-1}\nu_{i+1}\nu_i\nu_{i+2}\ldots}_{\ldots\gamma_{i-1}\gamma_{i+1}\gamma_i\gamma_{i+2}\ldots}(\ldots\theta_{i+1},\theta_i,\ldots;n), \tag{5.66}$$

$$F^{\mathcal{T}^\mu|\underline{\nu}}_{\underline{\gamma}}(\theta_1+2\pi\mathrm{i},\theta_2,\ldots,\theta_k;n) = -F^{\mathcal{T}^\mu|\nu_2\nu_3\ldots\nu_k\hat{\nu}_1}_{\gamma_2\gamma_3\cdots\gamma_k\gamma_1}(\theta_2,\ldots,\theta_k,\theta_1;n), \tag{5.67}$$

$$-\mathrm{i}\underset{\theta_0'=\theta_0+\mathrm{i}\pi}{\mathrm{Res}} F^{\mathcal{T}^\mu|\nu_0\nu_0\underline{\nu}}_{\bar{\gamma}_0\gamma_0\underline{\gamma}}(\theta_0',\theta_0,\underline{\theta};n) = F^{\mathcal{T}^\mu|\underline{\nu}}_{\underline{\gamma}}(\underline{\theta};n), \tag{5.68}$$

$$-\mathrm{i}\underset{\theta_0'=\theta_0+\mathrm{i}\pi}{\mathrm{Res}} F^{\mathcal{T}^\mu|\nu_0\hat{\nu}_0\underline{\nu}}_{\bar{\gamma}_0\gamma_0\underline{\gamma}}(\theta_0',\theta_0,\underline{\theta};n) = \prod_{l=1}^{k} S^{\hat{\nu}_0\nu_l}_{\gamma_0\gamma_l}(\theta_{0l})\, F^{\mathcal{T}^\mu|\underline{\nu}}_{\underline{\gamma}}(\underline{\theta};n), \tag{5.69}$$

where notations are the same as for the standard BPTF discussed in Sec. 5.3; in particular, we recall that $\gamma_i = R, L$. Both the Lorentz spin and the $\mathbb{Z}_2$ charge of the composite BPTFs are zero. Observe that the phase (-1) in Eqs. (5.67) and (5.69) as well as in Eqs. (5.63) and (5.65) is due to the non-trivial monodromy of the fields ψ, $\bar{\psi}$ with $\mathcal{T}_n^{\mu}$ (compare with the analogous axioms for the standard BPTF in Eqs. (5.28) and (5.30)).

Similarly to the standard BPTF, only FFs with an even number of 'R' and 'L' particles are non-vanishing and, consequently, the odd-particle FFs are zero. Additionally, the FFs of the composite BPTF satisfy the momentum space clustering property in the same form as the FFs of the standard BPTF in Eqs. (5.33) and (5.34).

Analogously to what we have done in Sec. 5.3, let us assume the following ansatz for the composite twist field FFs in which, for simplicity, we place every particle in the first replica

$$\begin{aligned} F_{r,l}^{\mathcal{T}^{\mu}}(\underline{\theta}, \underline{\theta}'; n) = H_{r,l}^{\mathcal{T}^{\mu}}\, Q_{r,l}^{\mathcal{T}^{\mu}}(\underline{x}, \underline{y}; n) \prod_{1 \leqslant i < j \leqslant r} \frac{f_{RR}^{\mu}(\theta_i - \theta_j; n)}{(x_i - \omega x_j)(x_j - \omega x_i)} \times \\ \times \prod_{i=1}^{r} \prod_{j=1}^{l} f_{RL}^{\mu}(\theta_i - \theta_j'; n) \prod_{1 \leqslant i < j \leqslant l} \frac{f_{LL}^{\mu}(\theta_i' - \theta_j'; n)}{(y_i - \omega y_j)(y_j - \omega y_i)}, \end{aligned} \tag{5.70}$$

where we have r right-mover and l left-mover particles, and $x_i = e^{\theta_i/n}$, $y_i = e^{-\theta_i'/n}$ and $\omega = e^{\mathrm{i}\pi/n}$ as previously. The cyclic permutation and the exchange axioms can automatically be satisfied if the equalities

$$f_{\gamma\gamma}^{\mu}(2\pi \mathrm{i} n - \theta; n) = -f_{\gamma\gamma}^{\mu}(\theta; n) = f_{\gamma\gamma}^{\mu}(-\theta; n)\,, \tag{5.71}$$

are imposed, that is, the minimal form factors satisfy the non-trivial monodromy due to the insertion of the external flux. The solution of Eq. (5.71) can be easily obtained from the standard minimal form factor in Eq. (5.37) by simply introducing a factor $2\cosh(\theta/2n)$ which changes the monodromy properties [253]

$$f_{\gamma\gamma}^{\mu}(\theta; n) = 2\cosh\left(\frac{\theta}{2n}\right) f_{\gamma\gamma}(\theta; n) = \sinh\left(\frac{\theta}{n}\right). \tag{5.72}$$

For $f_{RL}^{\mu}(\theta; n)$ instead we have two possible choices. We might either choose the unaltered equation without the '-1' monodromy

$$f_{RL}^{\mu}(\theta; n) = S_{RL}(\theta)\, f_{LR}^{\mu}(-\theta; n)\,, \tag{5.73}$$

with the solution $f_{RL}^{\mu} = f_{RL}$, or we can also introduce the monodromy

$$f_{RL}^{\mu}(2\pi \mathrm{i} n - \theta; n) = -f_{LR}^{\mu}(\theta; n) = -S_{LR}(\theta)\, f_{LR}^{\mu}(-\theta; n)\,, \tag{5.74}$$

such that the solution becomes

$$f_{RL}^{\mu}(\theta; n) = e^{\theta/(2n)} f_{RL}(\theta; n)\,. \tag{5.75}$$

As we will later see in Sec. 5.5, the exponential factor in Eq. (5.75) also appears in the roaming limit approach. Importantly, the two choices for the minimal form factor f^{μ}_{RL} in Eqs. (5.73) and (5.75) are completely equivalent because for the composite BPTFs the number of 'R' and 'L' particles is always even. This implies that, in a FF, we always have the product of an even number of f^{μ}_{RL} terms, which implies that the (-1) phases always mutually cancel. In order to connect in a clearer way with the roaming limit that we later discuss in Sec. 5.5, we choose Eq. (5.75) as the minimal form factors in the ansatz (5.70) for the composite BPTF. If we had taken (5.73), we would have got different expressions for the functions $Q^{\mathcal{T}^{\mu}}_{r,l}$, which would differ only by products of x_i and y_j with the same integer powers.

We remark that, in contrast to what happened in Sec. 5.3, the ansatz (5.70) does not guarantee that $Q^{\mathcal{T}^{\mu}}_{r,l}$ is actually a polynomial. In fact, as we will explicitly show, this function is in general a rational function. The reason for this is the monodromy changing factor introduced in the minimal form factors in Eqs. (5.72) and (5.75). These terms possess additional zeros that cancel out with the denominator of the function $Q^{\mathcal{T}^{\mu}}_{r,l}$, guaranteeing that the pole structure remains compatible with the bootstrap axioms.

5.4.1 Two-particle form factors and form factors with only one species

Similarly to the standard BPTFs, for the composite BPTFs the only non vanishing form factors at the two-particle level are those containing a pair of 'R' or 'L' particles, which coincide with the analogous expressions of the massive Ising QFT [188]. Alternatively, they can easily be obtained from the bootstrap equations, either from Eqs. (5.62), (5.63) or from Eqs. (5.66), (5.67). For the two-particle form factors, the bootstrap equations imply that

$$F^{\mathcal{T}^{\mu}|\nu_i\nu_j}_{\gamma_i\gamma_j}(\theta;n) = S^{\nu_i\nu_j}_{\gamma_i\gamma_j}(\theta)F^{\mathcal{T}|\nu_j\nu_i}_{\gamma_j\gamma_i}(-\theta;n) = -F^{\mathcal{T}^{\mu}|\nu_j\nu_i}_{\gamma_j\gamma_i}(2\pi \mathrm{i} n-\theta;n)\,. \tag{5.76}$$

The kinematic residue equations (5.64) or (5.68) relate the FFs to the vacuum expectation value of $\mathcal{T}^{\mu}_n$ as

$$-\mathrm{i}\,\underset{\theta=\mathrm{i}\pi}{\mathrm{Res}}\,F^{\mathcal{T}^{\mu}|\nu\nu}_{\gamma\gamma}(\theta;n) = \langle\mathcal{T}^{\mu}_n\rangle. \tag{5.77}$$

The solution for the equations above can be immediately written by plugging in the two-particle FF of the standard twist field (5.48) the minimal form factor of Eq. (5.72) that takes into account the non-trivial monodromy of $\mathcal{T}^{\mu}_n$, obtaining

$$F^{\mathcal{T}^{\mu}|11}_{\gamma\gamma}(\theta;n) = \frac{\langle\mathcal{T}^{\mu}_n\rangle\sin\frac{\pi}{n}}{2n\sinh\frac{\mathrm{i}\pi+\theta}{2n}\,\sinh\frac{\mathrm{i}\pi-\theta}{2n}}\,\frac{\sinh(\theta/n)}{\sinh(\mathrm{i}\pi/n)}\,, \tag{5.78}$$

where, for simplicity, we have placed every particle on the first replica. Notice that Eq. (5.78) is not in the form of our ansatz (5.70), but it can be recast accordingly as

$$F^{\mathcal{T}^{\mu}}_{2,0}(\theta_1-\theta_2;n) = \langle\mathcal{T}_n\rangle\frac{\mathrm{i}\,\omega}{n}\frac{2x_1x_2}{(x_1-\omega x_2)(x_2-\omega x_1)}\sinh\left(\frac{\theta_1-\theta_2}{n}\right), \tag{5.79}$$

where an analogous expression for the 'LL' form factor holds upon replacing x_i with y_i. Since in the above formula each particle lives on the first replica, we again used the simplified notation to denote the FF, namely we write $F^{\mathcal{T}^\mu}_{2,0}$ which indicates that we have two right-moving particles on the first replica. In the following, we shall use this convention whenever all the particles are on the first replica.

The two-particle FFs with arbitrary replica indices can be straightforwardly obtained from the result (5.79) with all the particles on the first replica. Importantly, the different flux convention in Eqs. (5.62)-(5.65) or in Eqs. (5.66)-(5.69) only differ in some (-1) factors. In particular, if the flux is only inserted on one replica, we have

$$F^{\mathcal{T}^\mu|jk}_{\gamma\gamma}(\theta;n) = \begin{cases} F^{\mathcal{T}^\mu|11}_{\gamma\gamma}(2\pi\mathrm{i}(k-j)-\theta;n)\,, & \text{if } k>j,\\ F^{\mathcal{T}^\mu|11}_{\gamma\gamma}(2\pi\mathrm{i}(j-k)+\theta;n)\,, & \text{otherwise.}\end{cases} \tag{5.80}$$

The FFs of the anti-twist field $\widetilde{\mathcal{T}}^\mu_n$ denoted by $\widetilde{F}^{\mathcal{T}^\mu}_{\underline{a}}(\underline{\theta},n)$ can be simply written as [251]

$$\widetilde{F}^{\mathcal{T}^\mu|jk}_{\gamma\gamma}(\theta;n) = F^{\mathcal{T}^\mu|n-j,n-k}_{\gamma\gamma}(\theta;n)\,. \tag{5.81}$$

If the flux is instead introduced on each replica, we have

$$F^{\mathcal{T}^\mu|jk}_{\gamma\gamma}(\theta;n) = (-1)^{(k-j)}\begin{cases} F^{\mathcal{T}^\mu|11}_{\gamma\gamma}(2\pi\mathrm{i}(k-j)-\theta;n)\,, & \text{if } k>j,\\ F^{\mathcal{T}^\mu|11}_{\gamma\gamma}(2\pi\mathrm{i}(j-k)+\theta;n)\,, & \text{otherwise,}\end{cases} \tag{5.82}$$

while the FFs of the anti-twist field $\widetilde{\mathcal{T}}^\mu_n$ satisfy Eq. (5.81). In the computation of the symmetry resolved entropy, the additional factor $(-1)^{k-j}$ always cancels out, leading to the same value for both choices.

Similarly to the treatment of the standard BPTFs, it is easy to see that, in the particular case of form factors that only contain an even number of particles of the same type —that is the 'RR...RR' and 'LL...LL' form factors—, they exactly coincide with the $\mathbb{Z}_2$-composite BPTF FFs of the massive Ising theory [188], as occurs in the two-particle case discussed above. Assuming that $\nu_1 \geq \nu_2 \geq \ldots \geq \nu_{2k}$, they can be written in terms of a Pfaffian involving the two-particle FFs as

$$F^{\mathcal{T}^\mu|\nu_1\ldots\nu_{2k}}_{\gamma,\ldots,\gamma}(\theta_1,\ldots,\theta_{2k};n) = \langle\mathcal{T}^\mu_n\rangle\,\mathrm{Pf}(W^\mu)\,, \tag{5.83}$$

where W^μ is an anti-symmetric matrix with entries

$$W^\mu_{lm} = \frac{1}{\langle\mathcal{T}^\mu_n\rangle}\begin{cases} F^{\mathcal{T}^\mu|\nu_l\nu_m}_{\gamma\gamma}(\theta_l-\theta_m;n)\,, & m>l,\\ (-1)^{\delta_{\nu_l,\nu_m}+1}\,F^{\mathcal{T}^\mu|\nu_l\nu_m}_{\gamma\gamma}(\theta_l-\theta_m;n)\,, & m<l.\end{cases} \tag{5.84}$$

For a different ordering of the replica indices ν_i, we can apply the exchange axiom (5.62) to reorder them in the form $\nu_1 \geq \nu_2 \geq \ldots \geq \nu_{2k}$ and then use Eq. (5.83).

In particular, for the four-particle 'RRRR' or 'LLLL' FF with all particles on the same replica, Eq. (5.83) takes the form

$$\begin{aligned} F_{4,0}^{\mathcal{T}^\mu}(\theta_1,\theta_2,\theta_3,\theta_4;n) = \langle \mathcal{T}_n^\mu\rangle^{-1}\left[F_{2,0}^{\mathcal{T}^\mu}(\theta_1-\theta_2;n))F_{2,0}^{\mathcal{T}^\mu}(\theta_3-\theta_4;n)\right. \\ \left. -F_{2,0}^{\mathcal{T}^\mu}(\theta_1-\theta_3;n)F_{2,0}^{\mathcal{T}^\mu}(\theta_2-\theta_4;n)+F_{2,0}^{\mathcal{T}^\mu}(\theta_1-\theta_4;n)F_{2,0}^{\mathcal{T}^\mu}(\theta_2-\theta_3;n)\right]. \end{aligned} \tag{5.85}$$

5.4.2 Solution for the four particle 'RRLL' form factor

To obtain the first non-zero form factors that couple right- and left-moving particles, we have to move to the four-particle level, in which we find $F_{RRLL}^{\mathcal{T}^\mu|\nu_1\nu_2\nu_3\nu_4}$ and all the possible permutations of 'R' and 'L'. As for the standard BPTFs, it is sufficient to determine only the 'RRLL' form factor with all the particles on the first replica. In fact, using the exchange relation (5.62) we can directly get any other sequence of the particle species and, applying the cyclic permutation axiom (5.63), we can find the FFs for particles living on different replicas. If we denote the form factor $F_{RRLL}^{\mathcal{T}^\mu|1111}$ as $F_{2,2}^{\mathcal{T}^\mu}$, then it reads

$$\begin{aligned} F_{2,2}^{\mathcal{T}^\mu}(\theta_1,\theta_2,\theta_1',\theta_2';n) = H_{2,2}^{\mathcal{T}^\mu}\, Q_{2,2}^{\mathcal{T}^\mu}(x_1,x_2,y_1,y_2;n)\frac{f_{RR}^\mu(\theta_1-\theta_2;n)}{(x_1-\omega x_2)(x_2-\omega x_1)}\times \\ \times\prod_{i=1}^{2}\prod_{j=1}^{2} f_{RL}^\mu(\theta_i-\theta_j';n)\frac{f_{LL}^\mu(\theta_1'-\theta_2';n)}{(y_1-\omega y_2)(y_2-\omega y_1)}, \end{aligned} \tag{5.86}$$

according to the ansatz (5.70).

Applying now the residue axiom to Eq. (5.86) we can derive recursive equations for the normalisation factors $H_{2,2}^{\mathcal{T}^\mu}$ and the $Q_{2,2}^{\mathcal{T}^\mu}$ functions in a similar way as we did for the standard BPTFs in Sec. 5.3.2. In Sec. 5.A.2, we find the solution for the functions $H_{2,2}^{\mathcal{T}^\mu}$,

$$H_{2,2}^{\mathcal{T}^\mu} = -4\langle\mathcal{T}_n^\mu\rangle\mathcal{N}_n^4\,, \tag{5.87}$$

and $Q_{2,2}^{\mathcal{T}^\mu}$,

$$\begin{aligned} Q_{2,2}^{\mathcal{T}^\mu}(x_1,x_2,y_1,y_2;n) &= Q_{2,2}^{\mathcal{T}^\mu}(x_1,x_2,y_1,y_2;n)^{(0)} + Q_{2,2}^{\mathcal{T}^\mu}(x_1,x_2,y_1,y_2;n)^{(k)} \\ &= \frac{\omega^2}{n^2}\frac{1+x_1x_2y_1y_2}{x_1x_2y_1y_2}+ \\ &\quad -\frac{2\omega^2\cos\frac{\pi}{2n}}{n^2}\frac{\left(x_1x_2(y_1+y_2)^2+y_1y_2(x_1+x_2)^2-2x_1x_2y_1y_2(\cos\left(\frac{\pi}{n}\right)+1)\right)}{(x_1x_2y_1y_2)(x_1+x_2)(y_1+y_2)}. \end{aligned} \tag{5.88}$$

As we explain in Sec. 5.A.2, the set of equations that allows to obtain $Q_{2,2}^{\mathcal{T}^\mu}$ recursively is under-determined. This ambiguity in the solution can be fixed by requiring that the form factor $F_{2,2}^{\mathcal{T}^\mu}$ reduces to the one of the disorder field μ in the single replica limit $n \to 1$. One can further check that the normalisation term $H_{2,2}^{\mathcal{T}^\mu}$ also matches the one of μ in that limit. In Sec. 5.6, we use the Δ-sum rule to provide an additional test of the validity of our solution.

5.5 Roaming limit of twist field form factors

In the previous sections, we computed the form factors of the twist fields along the tricritical Ising massless flow directly from the solution of their bootstrap equations. In this section, in order to provide a non-trivial check of our expressions, we present an alternative derivation based on the roaming limit of the sinh-Gordon model. After reviewing the general notions of this approach, we will then use it to recover the form factors in the massless flow as the limit of those in the sinh-Gordon theory.

Let us first briefly introduce the sinh-Gordon (ShG) model. This theory is defined via the Euclidean action

$$\mathcal{A}_{\text{ShG}} = \int \mathrm{d}^2x \left\{ \frac{1}{2} \left[\partial\phi(x)\right]^2 + \frac{\mu^2}{g^2} :\!\cosh[g\phi(x)]\!: \right\}. \tag{5.89}$$

This is the simplest interacting integrable relativistic QFT and has been the subject of an intense research activity since many decades, see, e.g., [101, 257, 259–265]. The spectrum of the model consists of multi-particle states of a massive bosonic particle with the dispersion relation $E = m\cosh\theta, p = m\sinh\theta$, where m is the particle mass. The two-particle S-matrix is given by [259]

$$S_{\text{ShG}}(\theta) = \frac{\tanh\frac{1}{2}\left(\theta - \mathrm{i}\frac{\pi}{2}B\right)}{\tanh\frac{1}{2}\left(\theta + \mathrm{i}\frac{\pi}{2}B\right)}, \tag{5.90}$$

where B is defined in terms of the coupling g appearing in the action in Eq. (5.89) as

$$B(g) = \frac{2g^2}{8\pi + g^2}. \tag{5.91}$$

For the ShG model, the form factors of various operators are known [255, 257, 260], including the standard and the $\mathbb{Z}_2$-composite BPTFs in the n-replica theory [188, 193, 253].

It was observed in Ref. [217] that the S-matrix of the sinh-Gordon model can be analytically continued from the self-dual point $B = 1$ to complex values

$$B(\theta_0) = 1 + \mathrm{i}\frac{2}{\pi}\theta_0, \tag{5.92}$$

and the resulting S-matrix defines a new perfectly valid scattering theory, which has been called the staircase or roaming trajectories model. Using Bethe ansatz, it was found that, as the real parameter θ_0 increases, the c-function shows a ‘staircase’ of defined plateaux with values equal to the central charges of the $\mathcal{M}_p$ unitary diagonal minimal models and, in the intervals between the plateaux, the flow was found to approximate the A_p massless crossovers $\mathcal{M}_{p+2} \to \mathcal{M}_{p+1}$ generated by the perturbing field $\phi_{1,3}$ discussed in Sec. 5.1. Therefore, in the roaming limit $\theta_0 \to \infty$, the staircase model describes a renormalisation group flow that passes by the successive minimal models $\mathcal{M}_p$. The final point of the flow is a massive Ising theory.

In another work [218], it was shown that the c-function defined by the c-theorem [212,213] using a spectral series in terms of the form factors of the trace of the stress-energy tensor Θ [255, 260] presents the same behaviour. In addition, it was explicitly demonstrated that the FFs of the stress-energy tensor for the A_p massless flows can be reconstructed from those of the ShG model. Importantly, for this construction to work, the rapidities in the FFs have to be also shifted by $\pm k\theta_0/2$ with specific integers k. A follow-up publication targeted specifically the A_2 tricritical-critical Ising flow (5.3), and showed that the form factors of the order and disorder operators along the flow can also be obtained via the roaming limit of the appropriate ShG FFs and, although not published, the correspondence holds for the ε field of the flow as well. As we have said, the staircase model also incorporates the massive Ising field theory, which is regarded in this context as a flow from the critical Ising fixed point to a massive one, and where the consecutive RG flows between the multicritical Ising CFTs terminate. Accordingly, it was demonstrated in Ref. [261] that the FFs of the massive Ising theory can be obtained from the ShG FFs by merely taking the limit of Eq. (5.92), i.e., scaling the rapidity variables within the FFs. In contrast, for other than the A_2 flow and massive Ising QFT, only the FFs of the field Θ were found to be reproduced by the roaming limiting procedure, and hence the validity of this approach is not a priori obvious and well understood.

Regarding the replicated staircase model, in Ref. [193] the form factors of the standard BPTFs in the sinh-Gordon have been computed up to the four-particle order. While the explicit roaming limit of these form factors was not carried out, they were used in the computation of the conformal dimension of the BPTFs applying the Δ-sum rule [214], which we discuss in more detail in Sec. 5.6. In particular, it was found that the two-particle contribution correctly reproduces the first 'step' of the staircase, from the critical Ising CFT to the massive theory, while the four-particle one gives the result for the massless flow A_2 from tricritical to critical Ising [193]. This result reveals that the roaming limit also holds for the branch point twist fields of the replicated theory. In the following, we make a step further, by explicitly performing the roaming limit of the form factors of both the standard and the composite BPTFs up to the four-particle order, showing that they reduce to the exact expressions in the A_2 flow (5.3) obtained via the bootstrap program in Secs. 5.3 and 5.4. Proving the correspondence in the first few non-trivial particle levels provides strong evidence that the roaming limit for standard and composite BPTFs is valid for any (composite) BPTF form factors in the A_2 massless flow.

In the ShG model, the k-particle form factors of the BPTFs can be parameterised in the usual fashion, that is [193],

$$F_k^{\mathcal{T}^\tau}(\underline{\theta}, B; n) = H_k^{\mathcal{T}^\tau} Q_k^{\mathcal{T}^\tau}(\underline{x}, B; n) \prod_{1\leqslant i<j\leqslant k} \frac{f^\tau_{\mathrm{ShG}}(\theta_i - \theta_j, B; n)}{(x_i - \omega x_j)(x_j - \omega x_i)}\,, \tag{5.93}$$

where each particle is put on the first replica and the superscript $\tau = 0, \mu$ denotes the standard or the composite BPTF respectively. The minimal form factor for the standard twist field $f_{\mathrm{ShG}}(\theta; n)$ is given by

$$f_{\mathrm{ShG}}(\theta, B; n) = \exp\left[-2\int_0^\infty dt \frac{\sinh\left(\frac{tB}{4}\right)\sinh\left(\frac{t(2-B)}{4}\right)}{t\sinh(nt)\cosh\left(\frac{t}{2}\right)}\cosh\left(\frac{\mathrm{i}t\,(\theta - \mathrm{i}\pi n)}{\pi}\right)\right], \tag{5.94}$$

while the one for the composite field is obtained by including an appropriate monodromy changing factor

$$f^\mu_{\mathrm{ShG}}(\theta, B; n) = 2\cosh\left(\frac{\theta}{2n}\right) f_{\mathrm{ShG}}(\theta, B; n)\,, \tag{5.95}$$

analogously to what we have done in Eq. (5.72) for the massless flow. The minimal FF f_{ShG} in Eq. (5.94) is normalised in such a way that $f_{\mathrm{ShG}}(\pm\infty, B; n) = 1$. The roaming limit construction of the twist field FFs in the massless flow can then be formulated as

$$\frac{1}{\langle \mathcal{T}^\tau_{n,\mathrm{flow}}\rangle} F_{r,l}^{\mathcal{T}^\tau}\left(\underline{\theta}, \underline{\theta'}; n\right) = \lim_{\theta_0\to\infty} \frac{1}{\langle \mathcal{T}^\tau_{n,\mathrm{ShG}}\rangle} F_{r+l}^{\mathcal{T}^\tau}\left(\underline{\theta} + \theta_0/2, \underline{\theta'} - \theta_0/2, B(\theta_0); n\right), \tag{5.96}$$

where we split the rapidities in the sinh-Gordon FF into r right-moving ($\underline{\theta}$) and l left-moving ($\underline{\theta'}$) ones, which we shift by θ_0 and $-\theta_0$ respectively. The function $B(\theta_0)$ is defined in Eq. (5.92). In the rest of this section, we explicitly demonstrate the validity of the limit in Eq. (5.96) up to the four-particle level.

Let us first focus on the ShG minimal FFs. Based on Ref. [218], it can be shown that, in the roaming limit (5.96), the minimal form factor in Eq. (5.94) reduces to

$$\begin{aligned} f_{\mathrm{ShG}}(\theta, B(\theta_0); n) &\longrightarrow e^{-\frac{\theta_0}{2n}}\left[-2\mathrm{i}\sinh\left(\frac{\theta}{2n}\right)\right], \\ f_{\mathrm{ShG}}(\mathrm{i}\pi, B(\theta_0); n) &\longrightarrow e^{-\frac{\theta_0}{2n}}\, 2\sin\left(\frac{\pi}{2n}\right), \\ f_{\mathrm{ShG}}(\theta + \theta_0, B(\theta_0); n) &\longrightarrow \mathcal{N}_n\, f_{RL}(\theta; n)\,, \end{aligned} \tag{5.97}$$

where f_{RL} is the minimal form factor (5.40) in the massless flow and the normalisation constant $\mathcal{N}_n$ was found in Eq. (5.42). Similarly, for the composite twist field one has

$$\begin{aligned} f^\mu_{\mathrm{ShG}}(\theta, B(\theta_0); n) &\longrightarrow e^{-\frac{\theta_0}{2n}}\left[-2\mathrm{i}\sinh\left(\frac{\theta}{n}\right)\right], \\ f^\mu_{\mathrm{ShG}}(\mathrm{i}\pi, B(\theta_0); n) &\longrightarrow e^{-\frac{\theta_0}{2n}}\, 2\sin\left(\frac{\pi}{n}\right), \\ f^\mu_{\mathrm{ShG}}(\theta + \theta_0, B(\theta_0); n) &\longrightarrow e^{\frac{\theta_0}{2n}}\mathcal{N}_n\, f^\mu_{RL}(\theta; n) = e^{\frac{\theta_0+\theta}{2n}}\mathcal{N}_n\, f_{RL}(\theta; n)\,, \end{aligned} \tag{5.98}$$

with f^{μ}_{RL} given by Eq. (5.75). Note that, according to the definition (5.96), only the above cases are the relevant limits for the minimal form factor. Some of them involve an exponential factor $e^{\pm\theta_0/(2n)}$ but we anticipate that similar factors originate from other terms of the entire FF and they eventually cancel.

From Eqs. (5.97) and (5.98), it is easy to see that the roaming limit in the two-particle case correctly reproduces the form factors of the massless flow. This is clearer when the two-particle ShG FF is rewritten as a function of the rapidity difference as

$$F_2^{\mathcal{T}^\tau}(\theta, B; n) = \frac{\langle \mathcal{T}^\tau_{n,\mathrm{ShG}}\rangle \sin\frac{\pi}{n}}{2n\sinh\frac{i\pi+\theta}{2n}\sinh\frac{i\pi-\theta}{2n}}\frac{f^\tau_{\mathrm{ShG}}(\theta, B; n)}{f^\tau_{\mathrm{ShG}}(i\pi, B; n)}\,. \tag{5.99}$$

In the limit (5.96) this expression reproduces either Eq. (5.48) (for the standard BPTF) or Eq. (5.78) (for the composite BPTF) for the 'RR' and 'LL' cases, while it vanishes in the 'RL' case because of the diverging denominator.

5.5.1 Roaming limit of the four-particle FFs of the standard BPTF

It is also not difficult to show that the four-particle 'RRRR' and 'LLLL' FFs are provided by the roaming limit (5.96). If we consider the standard BPTFs, using as $Q_4^{\mathcal{T}}$ the polynomial determined in [193] and reviewed in Sec. 5.B.1, we can proceed in the following way. According to Eq. (5.96), the 'RRRR' or 'LLLL' form factors that only contain right or left movers are given by

$$\begin{aligned}\frac{1}{\langle \mathcal{T}_{n,\mathrm{flow}}\rangle}&F^{\mathcal{T}}_{4,0\ \mathrm{tri}}(\theta_1,\theta_2,\theta_3,\theta_4;n) = \\ &= \lim_{\theta_0\to\infty}\frac{1}{\langle \mathcal{T}_{n,\mathrm{ShG}}\rangle}F^{\mathcal{T}}_{4\ \mathrm{ShG}}(\theta_1+\theta_0/2,\theta_2+\theta_0/2,\theta_3+\theta_0/2,\theta_4+\theta_0/2,B(\theta_0);n)\,.\end{aligned} \tag{5.100}$$

In this limit, the denominator of the ShG FF (5.93) does not change but acquires the diverging factor $e^{6\theta_0/n}$,

$$\frac{1}{\prod_{i<j}(x_j-\omega x_i)(x_i-\omega x_j)} \longrightarrow e^{-6\theta_0/n}\frac{1}{\prod_{i<j}(x_j-\omega x_i)(x_i-\omega x_j)}\,, \tag{5.101}$$

whereas for the polynomial $Q_4^{\mathcal{T}}$ we obtain the following lengthy expression

$$\begin{aligned}&Q_4^{\mathcal{T}}(x_1,x_2,x_3,x_4,B;n) \longrightarrow \\ &e^{8\theta_0/n}\times 2e^{\frac{3(\theta_1+\theta_2+\theta_3+\theta_4)}{n}}\left\{\cosh\left(\frac{\theta_1+\theta_2-\theta_3-\theta_4}{n}\right)+2\cosh\left(\frac{\theta_1-\theta_2}{n}\right)\cosh\left(\frac{\theta_3-\theta_4}{n}\right)+\right.\\ &+\left(1-2\cos\frac{\pi}{n}\right)\left[\cosh\left(\frac{\theta_1-\theta_2}{n}\right)+\cosh\left(\frac{\theta_1-\theta_3}{n}\right)+\cosh\left(\frac{\theta_1-\theta_4}{n}\right)+\cosh\left(\frac{\theta_2-\theta_3}{n}\right)\right.\\ &\left.\left.+\cosh\left(\frac{\theta_2-\theta_4}{n}\right)+\cosh\left(\frac{\theta_3-\theta_4}{n}\right)\right]+2-\cos\frac{\pi}{n}+\cos\frac{2\pi}{n}+\cos\frac{3\pi}{n}\right\}\,,\end{aligned} \tag{5.102}$$

which diverges exponentially as $e^{8\theta_0/n}$ when $\theta_0 \to \infty$. In addition, taking into account the limit of the minimal form factor reported in Eq. (5.97), we have

$$\prod_{i<j} f_{\mathrm{ShG}}(\theta_i - \theta_j, B; n) \longrightarrow e^{-3\theta_0/n} \left[-2^6 \prod_{i<j} \sinh\left(\frac{\theta_i - \theta_j}{2n}\right) \right], \tag{5.103}$$

and for the normalisation factor $H_n^{\mathcal{T}}$, we find

$$H_n^{\mathcal{T}} = \left(\frac{2\sin(\pi/n)\omega^2}{n f^{\mathrm{ShG}}(i\pi, B; n)}\right)^2 \omega^2 \longrightarrow e^{\theta_0/n} \left(\frac{\sin(\pi/n)\omega^2}{n\sin(\pi/2n)}\right)^2 \omega^2 = e^{\theta_0/n} \left(\frac{4\, e^{\mathrm{i}\frac{6\pi}{n}}}{n^2} \cos^2\!\left(\frac{\pi}{2n}\right)\right). \tag{5.104}$$

Counting the divergent factors $e^{\theta_0/n}$ in the final expressions of Eqs. (5.101), (5.102), (5.103) and (5.104), we can conlude that the 'RRRR' ('LLLL') roaming limit form factor of the ShG twist field is finite. In fact, putting all the above results together it is straightforward to check that the limit (5.100) works and Eq. (5.56) is exactly reproduced.

Turning to the case of the 'RRLL' form factor, we have to consider

$$\begin{aligned} &\frac{1}{\langle \mathcal{T}_{n,\mathrm{flow}} \rangle} F^{\mathcal{T}}_{2,2\ \mathrm{tri}}\big(\theta_1, \theta_2, \theta_1', \theta_2'; n\big) = \\ &= \lim_{\theta_0 \to \infty} \frac{1}{\langle \mathcal{T}_{n,\mathrm{ShG}} \rangle} F^{\mathcal{T}}_{4\ \mathrm{ShG}}\big(\theta_1 + \theta_0/2, \theta_2 + \theta_0/2, \theta_1' - \theta_0/2, \theta_2' - \theta_0/2, B(\theta_0); n\big). \end{aligned} \tag{5.105}$$

For the denominator, the limit gives

$$\frac{1}{\prod_{i<j}(x_j - \omega x_i)(x_i - \omega x_j)} \longrightarrow e^{-4\theta_0/n} \frac{y_1^2 y_2^2}{x_1^4 x_2^4 \omega^4 (x_1 - \omega x_2)(x_2 - \omega x_1)(y_1 - \omega y_2)(y_2 - \omega y_1)}, \tag{5.106}$$

whereas for the polynomial $Q_4^{\mathcal{T}}$ we obtain the following expression

$$\begin{aligned} &Q_4^{\mathcal{T}}(x_1, x_2, x_3, x_4, B; n) \longrightarrow \\ &e^{4\theta_0/n} \times e^{\frac{4(\theta_1+\theta_2)}{n}} \left(-\frac{\left(e^{\theta_1/n} + e^{\theta_2/n}\right)\left(e^{\theta_1'/n} + e^{\theta_2'/n}\right) e^{\frac{2(\theta_1'+\theta_2')+i\pi}{2n}}}{1+\omega} + e^{\frac{\theta_1+\theta_2+\theta_1'+\theta_2'}{n}} + e^{\frac{2(\theta_1'+\theta_2')}{n}} \right), \end{aligned} \tag{5.107}$$

which we can rewrite as

$$Q_4^{\mathcal{T}}(x_1, x_2, x_3, x_4, B; n) \longrightarrow e^{4\theta_0/n} \times x_1^4 x_2^4 \left(-\frac{(x_1 + x_2)(y_1 + y_2)\, e^{\frac{i\pi}{2n}}}{(1+\omega) y_1^2 y_2^2} + \frac{x_1 x_2}{y_1 y_2} + \frac{1}{y_1^2 y_2^2} \right). \tag{5.108}$$

For the product of the minimal FFs, we find

$$\prod_{i<j} f_{\mathrm{ShG}}(\theta_i-\theta_j,B;n) \longrightarrow e^{-\theta_0/n}\left[-2^2\mathcal{N}_n^4\sinh\!\left(\frac{\theta_1-\theta_2}{2n}\right)\sinh\!\left(\frac{\theta_1'-\theta_2'}{2n}\right)\prod_{i<j} f_{RL}(\theta_i-\theta_j')\right]. \tag{5.109}$$

The limit of the normalisation factor $H_n^{\mathcal{T}}$ gives the same result as in Eq. (5.104). Combining (5.106), (5.108), (5.109), and the normalisation (5.104), it is immediate to see that the divergent exponential factors e^{θ_0} mutually cancel and that the roaming limit yields Eq. (5.60), confirming the validity of Eq. (5.105).

5.5.2 Roaming limit of the four-particle FFs of the composite BPTF

Unlike the four-particle form factor of the standard twist field, the one of the composite twist field was not previously known in the sinh-Gordon theory. In Sec. 5.B.2, we compute this form factor by constructing and solving the bootstrap equations, starting from the usual ansatz in Eq. (5.93). Notice that, as we discuss in Sec. 5.B.2, now the function $Q_k^{\mathcal{T}^\mu}$ is not a polynomial but a rational function. At the four-particle level, the explicit expressions of the normalisation $H_4^{\mathcal{T}^\mu}$ and of the polynomial $Q_4^{\mathcal{T}^\mu}$ are reported in Sec. 5.B.2 in Eq. (5.200) and in Eqs. (5.208), (5.209), respectively.

Let us first consider the form factors ‘RRRR’ and ‘LLLL’, containing only either right- or left-moving particles. Following Eq. (5.96), we see that we need to compute the limit of $F_4^{\mathcal{T}^\mu}(\underline{\theta}+\theta_0/2, B(\theta_0); n)$. As in Sec. 5.5.1 for the standard twist field, we study separately this limit for the different terms that constitute the composite ShG form factor in Eq. (5.93). Applying the limit of the minimal composite form factor reported in Eq. (5.98), we have

$$\begin{aligned}\prod_{1\leqslant i<j\leqslant 4} f^{\mu}_{\mathrm{ShG}}(\theta_i-\theta_j,B(\theta_0);n) &\longrightarrow e^{-3\theta_0/n}\left[-2^6\prod_{1\leqslant i<j\leqslant 4}\sinh\!\left(\frac{\theta_i-\theta_j}{n}\right)\right]\\ &= e^{-3\theta_0/n}\left[-\prod_{1\leqslant i<j\leqslant 4}\frac{(x_i+x_j)\,(x_i-x_j)}{x_i x_j}\right],\end{aligned} \tag{5.110}$$

where we have rewritten it in terms of $x_i = e^{\theta_i/n}$. It is convenient to take the limit of the function $Q_4^{\mathcal{T}^\mu}$, reported in Eqs. (5.208), (5.209), and of the denominator of the ansatz (5.93) together with the one of the minimal form factor. We find that this limit reproduces the form factor in Eq. (5.85) up to a normalisation with an exponential $e^{-\theta_0/n}$

$$
\begin{aligned}
&Q_4^{\mathcal{T}^\mu}(x_1,x_2,x_3,x_4,B(\theta_0)\,;n)\prod_{1\leqslant i<j\leqslant 4}\frac{f^{\mu}_{\text{ShG}}(\theta_i-\theta_j,B(\theta_0);n)}{(x_i-\omega x_j)\,(x_j-\omega x_i)}\longrightarrow\\
&\longrightarrow\frac{e^{-\theta_0/n}}{\omega^6\,(1+\omega)^2}\Bigg[-\left(\frac{x_1}{x_1-\omega x_4}+\frac{x_4}{\omega x_1-x_4}\right)\left(\frac{x_2}{x_2-\omega x_3}+\frac{x_3}{\omega x_2-x_3}\right)+\\
&\quad+\left(\frac{x_1}{x_1-\omega x_3}+\frac{x_3}{\omega x_1-x_3}\right)\left(\frac{x_2}{x_2-\omega x_4}+\frac{x_4}{\omega x_2-x_4}\right)+\\
&\quad-\left(\frac{x_1}{x_1-\omega x_2}+\frac{x_2}{\omega x_1-x_2}\right)\left(\frac{x_3}{x_3-\omega x_4}+\frac{x_4}{x_3-\omega x_4}\right)\Bigg]=\frac{e^{-\theta_0/n}\,n^2}{\omega^6\,(1+\omega)^2}F^{\mathcal{T}^\mu}_{4,0}(\theta_1,\theta_2,\theta_3\theta_4)\,.
\end{aligned}
\tag{5.111}
$$

Finally, we see that the normalisation term $H_n^{\mathcal{T}^\mu}$, whose explicit expression is given in Eq. (5.200), becomes

$$
\frac{H_4^{\mathcal{T}^\mu}(B(\theta_0))}{\langle\mathcal{T}^{\mu}_{\text{ShG}}\rangle}=\left(\frac{2\,(1+\omega)\sin\frac{\pi}{n}}{n\,f^{\mu}_{\text{ShG}}(\mathrm{i}\pi;n)}\right)^2\omega^6\longrightarrow e^{\theta_0/n}\,\frac{\omega^6\,(1+\omega)^2}{n^2}\,,
\tag{5.112}
$$

cancelling precisely the multiplicative factor in Eq. (5.111), such that the roaming limit correctly reproduces the ‘RRRR’ (or ‘LLLL’) form factor in Eq. (5.85), as expected.

Considering now the ‘RRLL’ form factor, we can see that it can be obtained from the limit of Eq. (5.96) in the particular case

$$
\frac{F^{\mathcal{T}^\mu}_{2,2\ \text{flow}}(\theta_1,\theta_2,\theta_1',\theta_2';n)}{\langle\mathcal{T}^{\mu}_{\text{flow}}\rangle}=\lim_{\theta_0\to\infty}\frac{F^{\mathcal{T}^\mu}_{4\ \text{ShG}}(\theta_1+\theta_0/2,\theta_2+\theta_0/2,\theta_1'-\theta_0/2,\theta_2'-\theta_0/2,B(\theta_0);n)}{\langle\mathcal{T}^{\mu}_{\text{ShG}}\rangle}\,.
\tag{5.113}
$$

The joint limit of the denominator of the ansatz (5.93) and of the polynomial $Q_4^{\mathcal{T}^\mu}$ reported in Eqs. (5.208), (5.209) gives

$$
\begin{aligned}
&\frac{Q^{\mathcal{T}^\mu}_{4\ \text{ShG}}(x_1,x_2,x_3,x_4)}{\prod_{1\leqslant i<j\leqslant 4}(x_i-\omega x_j)\,(x_j-\omega x_i)}\longrightarrow\\
&\longrightarrow e^{-2\theta_0/n}\frac{n^2}{\omega^6\,(1+\omega)^2}\frac{Q^{\mathcal{T}^\mu}_{2,2\ \text{flow}}(x_1,x_2,y_1,y_2)}{(x_1-\omega x_2)\,(x_2-\omega x_1)\,(y_1-\omega y_2)\,(y_2-\omega y_1)},
\end{aligned}
\tag{5.114}
$$

where $Q^{\mathcal{T}^\mu}_{2,2\ \text{flow}}$ is the polynomial in the massless flow of Eq. (5.88). The normalisation $H_4^{\mathcal{T}^\mu}$ has the same limit as in Eq. (5.112) and, recalling the limit of the composite minimal form factors in Eq. (5.98), we have

$$
\begin{aligned}
&f^{\mu}_{\text{ShG}}(\theta_1-\theta_2,B(\theta_0);n)\prod_{i,j=1,2}f^{\mu}_{\text{ShG}}\big(\theta_i-\theta_j',B(\theta_0);n\big)\,f^{\mu}_{\text{ShG}}\big(\theta_1'-\theta_2',B(\theta_0);n\big)\longrightarrow\\
&\longrightarrow e^{\theta_0/n}\left[-4\,\mathcal{N}_n^4\,\sinh\!\Big(\frac{\theta_1-\theta_2}{n}\Big)\prod_{i,j=1,2}f^{\mu}_{RL}(\theta;n)\,\sinh\!\Big(\frac{\theta_1'-\theta_2'}{n}\Big)\right].
\end{aligned}
\tag{5.115}
$$

Putting all together, we find that the limit of the 'RRLL' form factor is again finite as expected,

$$\begin{aligned}
&\lim_{\theta_0\to\infty} \frac{F_{4\,\mathrm{ShG}}^{\mathcal{T}^\mu}(\theta_1+\theta_0/2,\theta_2+\theta_0/2,\theta_1'-\theta_0/2,\theta_2'-\theta_0/2,B(\theta_0);n)}{\langle \mathcal{T}^\mu_{\mathrm{ShG}}\rangle}\\
&=-\,4\,\mathcal{N}_n^4\,Q^{\mathcal{T}^\mu}_{2,2\ \mathrm{flow}}(x_1,x_2,y_1,y_2)\,\frac{\sinh\frac{\theta_1-\theta_2}{n}}{(x_1-\omega x_2)\,(x_2-\omega x_1)}\prod_{i,j=1,2} f^\mu_{RL}(\theta;n)\,\frac{\sinh\frac{\theta_1'-\theta_2'}{n}}{(y_1-\omega y_2)\,(y_2-\omega y_1)}\\
&=\frac{F^{\mathcal{T}^\mu}_{2,2\ \mathrm{flow}}(\theta_1,\theta_2,\theta_1',\theta_2';n)}{\langle \mathcal{T}^\mu_{\mathrm{flow}}\rangle}\,,
\end{aligned} \tag{5.116}$$

confirming the validity of the roaming limit also for the composite twist field $\mathcal{T}_n^\mu$.

5.6 Standard and symmetry resolved entropies for the massless flow

In this section, we use the form factors computed in the previous sections to study the behaviour of the correlation functions of the standard and composite twist fields. After calculating the running dimension of the field along the renormalisation flow, we investigate the entanglement entropy, comparing it with expected results.

5.6.1 Running dimension from the Δ-sum rule

As we discussed in Sec. 5.1, the model under examination interpolates between the tricritical Ising CFT $\mathcal{M}_4$ in the UV and the Ising CFT $\mathcal{M}_3$ in the IR, providing the simplest example of a massless renormalisation flow between two A-series diagonal minimal models [209–211]. In both fixed points, the properties of the standard twist field $\mathcal{T}_n$ and the $\mathbb{Z}_2$ composite one $\mathcal{T}_n^\mu$ are known from conformal invariance [22], as we reviewed in Sec. 5.2. In particular, the conformal dimension of the standard twist field is given by Eq. (5.17) while the dimension of the composite one is in Eqs. (5.19), (5.20) for the fixed points of interest.

The knowledge of the exact conformal dimensions of the fields in the IR and the UV fixed points of the massless flow provides a non-trivial check of the correctness of the form factors via the Δ-sum rule [214]. Let us start by considering the twist field $\mathcal{T}_n$. Along a renormalisation group flow, the difference of conformal dimensions of the field $\mathcal{T}_n$ in the IR and in the UV is given by an integral of the two-point function between $\mathcal{T}_n$ and the trace of the stress-energy tensor Θ [214]

$$h_{\mathcal{T}}^{\mathrm{UV}}-h_{\mathcal{T}}^{\mathrm{IR}}=-\frac{1}{2\langle\mathcal{T}_n\rangle}\int_0^{+\infty}\mathrm{d}t\,t\,\langle\Theta(0)\,\mathcal{T}_n(t)\,\rangle\,. \tag{5.117}$$

In order to compute the Δ-sum rule (5.117), we expand the two-point function in form factors, analogously to what we did in Eq. (5.24) for the correlator of twist fields. The resulting spectral expansion of Eq. (5.117) involves the form factors of the twist field and the ones of the trace Θ, which in the case of the (non-replicated) massless tricritical flow have been obtained in [216]. In particular, in a massless model, all the form factors of Θ containing either only left- ('L') or right-movers ('R') identically vanish. When considering the replicated theory, we have to take the sum of Θ in each the copy. Therefore, the only non-vanishing form factors are the ones with identical replica indices $F_{r,l}^{\Theta|11\ldots1} = F_{r,l}^{\Theta}$. After integrating out the distance t in the spectral expansion of the Δ-sum rule (5.117), we finally find [188, 214]

$$h^{\mathrm{UV}} - h^{\mathrm{IR}} = -\frac{n}{2\langle\mathcal{T}_n\rangle}\sum_{r,l\ \mathrm{even}}\int_{-\infty}^{+\infty}\frac{\prod_{i=1}^{r}\mathrm{d}\theta_i\prod_{j=1}^{l}\mathrm{d}\theta'_j}{r!\,l!\,(2\pi)^{r+l}}\,\frac{1}{2\,E^2}\,F_{r,l}^{\Theta}(\theta_1,\ldots)\left(F_{r,l}^{\mathcal{T}|11\ldots1}(\theta_1,\ldots)\right)^*, \tag{5.118}$$

where E is the energy (reported in Eq. (5.5) for a massless model).

The leading non-trivial form factor of Θ is the four-particle 'RRLL' one, coupling two right- and two left-movers [216]

$$F_{2,2}^{\Theta}(\theta_1,\theta_2;\theta'_1,\theta'_2) = \frac{4\pi M^2}{\gamma^2}\sinh\frac{\theta_1-\theta_2}{2}\prod_{i,j=1,2} f_{\mathrm{RL}}(\theta_i-\theta'_j)\,\sinh\frac{\theta'_1-\theta'_2}{2}\,, \tag{5.119}$$

where γ is Euler-Mascheroni's constant and $f_{\mathrm{RL}}(\theta) = f_{\mathrm{RL}}(\theta; n=1)$ is the minimal form factor in Eq. (5.40) for a single replica $n = 1$. Since all form factors have an even number of left- and right-moving particles, Eq. (5.119) is the only contribution at the four-particle level [216]. We can then consider the approximation

$$h^{\mathrm{UV}} - h^{\mathrm{IR}} \approx -\frac{n}{2\langle\mathcal{T}_n\rangle}\int_{-\infty}^{+\infty}\frac{\mathrm{d}\theta_1\mathrm{d}\theta_2\mathrm{d}\theta'_1\mathrm{d}\theta'_2}{2\times 2\,(2\pi)^4}\,\frac{1}{2\,E^2}\,F_{2,2}^{\Theta}(\theta_1,\theta_2,\theta'_1,\theta'_2)\left(F_{2,2}^{\mathcal{T}|1111}\left(\theta_1,\theta_2,\theta'_1,\theta'_2;n\right)\right)^*, \tag{5.120}$$

where $F_{2,2}^{\Theta}$ is given in Eq. (5.119) and $F_{2,2}^{\mathcal{T}|1111}$ is the twist field FF that we obtained in Eqs. (5.60) and (5.61). Analogous expressions hold for the Δ-sum rule of the composite twist field $\mathcal{T}_n^{\mu}$, replacing $F_{2,2}^{\mathcal{T}|1111}$ with the form factor $F_{2,2}^{\mathcal{T}^{\mu}|1111}$ of the composite field reported in Eqs. (5.86) to (5.88).

In Table 5.2, we compare the exact difference of conformal dimensions of both the standard and the composite twist fields with the result of the Δ-sum rule at the four-particle order (5.120) for $n = 2, 3, 4$ replicas. The integral in Eq. (5.120) has been computed numerically using the Divonne routine of the library CUBA [266] for the software *Mathematica*, using a cut-off $\theta_j \in [-60, 60]$ for the rapidities. Already at the four-particle order we find a good agreement between the exact CFT result and the Δ-sum rule, confirming the

	BPTF $h^{\mathrm{UV}}_{\mathcal{T}} - h^{\mathrm{IR}}_{\mathcal{T}}$		composite TF $h^{\mathrm{UV}}_{\mathcal{T}^\mu} - h^{\mathrm{IR}}_{\mathcal{T}^\mu}$	
n	CFT	Δ-sum rule	CFT	Δ-sum rule
2	0.0125	0.0125	0	0.0002
3	$0.0\overline{2}$	0.0223	$0.013\overline{8}$	0.0138
4	0.03125	0.0313	0.025	0.0249

Table 5.2: Comparison of the difference of the conformal dimensions in the UV and IR fixed points $h^{\mathrm{UV}} - h^{\mathrm{IR}}$ with the results of the Δ-sum rule, for both the standard twist field $\mathcal{T}_n$ and the composite one $\mathcal{T}_n^\mu$. The 'CFT' columns collect the exact result fixed by conformal invariance in Eqs. (5.17), (5.20), while 'Δ-sum rule' is the result of the Δ-sum rule truncated at four-particle order, reported in Eq. (5.120). The column 'n' indicates the number of replicas. We can see that at the four-particle order we already find good agreement for all the number of replicas considered.

correctness of the form factors computed in Secs. 5.3 and 5.4 and the relatively small weight carried by the higher order FFs. This is consistent with Ref. [193], where it was found that, for the staircase model (reviewed in Sec. 5.5), the four-particle contribution obtained in the roaming limit reproduces the difference in conformal dimensions of the standard twist field along the massless flow (5.3).

The Δ-sum rule (5.117) can be modified to give a *running* dimension of the (composite) twist fields along the flow [193, 227]

$$h(\ell) - h^{\mathrm{IR}} = -\frac{1}{2\langle \mathcal{T}_n \rangle} \int_{\ell}^{\infty} \mathrm{d}t\, t \left\langle \Theta(0)\, \mathcal{T}_n(t) \right\rangle , \tag{5.121}$$

where now the integral over the distance t starts from a finite length ℓ. As we did before in Eq. (5.118), we expand the two-point function in form factors and we integrate over the distance t, obtaining [193, 227]

$$\begin{aligned} h(\ell) - h^{\mathrm{IR}} = -\frac{n}{2\langle \mathcal{T}_n \rangle} \sum_{r,l \text{ even}} \int_{-\infty}^{+\infty} \frac{\prod_{i=1}^{r} \mathrm{d}\theta_i \prod_{j=1}^{l} \mathrm{d}\theta'_j}{r!\, l!\, (2\pi)^{r+l}}\, \frac{(1+\ell\, E)\, e^{-\ell\, E}}{2\, E^2} \times \\ \times F^{\Theta}_{r,l}(\theta_1, \ldots) \left(F^{\mathcal{T}|11\ldots1}_{r,l}(\theta_1, \ldots) \right)^{*} , \end{aligned} \tag{5.122}$$

where again, in the massless flow, the leading contribution is given by the 'RRLL' form factors,

$$\begin{aligned} h(\ell) - h^{\mathrm{IR}} \approx -\frac{n}{2\langle \mathcal{T}_n \rangle} \int_{-\infty}^{+\infty} \frac{\mathrm{d}\theta_1 \mathrm{d}\theta_2 \mathrm{d}\theta'_1 \mathrm{d}\theta'_2}{2 \times 2\, (2\pi)^4}\, \frac{(1+\ell\, E)\, e^{-\ell\, E}}{2\, E^2} \times \\ \times F^{\Theta}_{2,2}(\theta_1, \theta_2, \theta'_1, \theta'_2) \left(F^{\mathcal{T}|1111}_{2,2}\left(\theta_1, \theta_2, \theta'_1, \theta'_2; n\right) \right)^{*} . \end{aligned} \tag{5.123}$$

A running Δ-theorem (5.121) can also be formulated for the composite twist field by considering the appropriate form factor $F^{\mathcal{T}^\mu|1111}_{2,2}$ of that operator obtained in Eqs. (5.86)-(5.88).

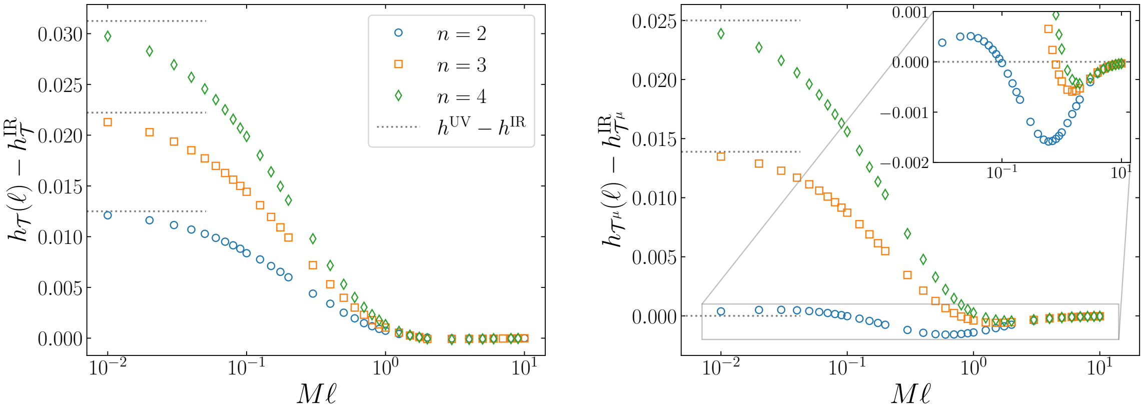

(a) Branch point twist field $\mathcal{T}_n$

(b) Composite twist field $\mathcal{T}_n^{\mu}$

Figure 5.1: Semi-logarithmic plot of the running conformal dimension $h_{\mathcal{T}^{\tau}}$ obtained using the Δ-sum rule at four-particle order reported in Eq. (5.123). In the plot on the left, we show the result for the standard twist field $\mathcal{T}_n$, while on the right for the composite one $\mathcal{T}_n^{\mu}$. The dotted gray lines indicate the exact difference between the UV and IR conformal dimension obtained from Eq. (5.17) in the plot on the left and from Eqs. (5.20) in the plot on the right. As expected, for small distances ℓ, the running conformal dimension approaches the exact UV results, as also reported in Table 5.2. On the left, we see that the one of the standard twist field decreases monotonically, consistently with its behaviour as an entropic c-function. On the right, in the inset we zoom on the running dimension of the composite twist field (for $n = 2$ we have $h_{\mathcal{T}^{\mu}}^{\mathrm{UV}} = h_{\mathcal{T}^{\mu}}^{\mathrm{IR}}$). The running dimension of the composite field is not monotonic along the flow.

In Ref. [194], it was argued that the running dimension $h(\ell)$ of the branch point twist field $\mathcal{T}_n$ provides an entropic c-function which is monotonically decreasing along the flow. In Fig. 5.1a we report the result of the numerical integration of the running Delta theorem in Eq. (5.123) for the standard branch point twist field $\mathcal{T}_n$ taking $n = 2, 3, 4$ replicas. We observe that, already at the four-particle order, the running dimension monotonically decreases with ℓ for all the number of replicas considered. In Fig. 5.1b, we plot the running dimension of the composite twist field $\mathcal{T}_n^{\mu}$ at four-particle order. In particular for $n = 2$ replicas, the dimensions of the twist fields and of the charge operator conspire to give the same ultraviolet and infrared conformal dimensions for the composite twist field. Remarkably, we see that along the flow the running dimension varies and is not monotonic in ℓ, differently from the standard twist field. In the inset, we zoom in the region of small running dimension which shows that also for larger number of replicas n the behaviour is non-monotonic.

5.6.2 Cumulant expansion of the entanglement entropy

As a main result of this Chapter, in this section we discuss the form factor expansion of the entanglement entropy along the massless renormalisation group flow. As we will show, the formal expressions require a suitable regularisation, after which the form factors containing particles with the same chirality reproduce the logarithmic entanglement entropy of the infrared Ising CFT, while those that include particles of different chirality provide the corrections along the flow.

Instead of studying the correlator of the twist field, we find more convenient to directly apply its form factor expansion to the Rényi entanglement entropies defined in Eq. (1.7). Plugging in Eq. (5.15) the spectral series (5.26) of the twist field correlator and expanding the logarithm for the Rényi entropy order by order in the number of particles, we obtain the cumulant expansion [192, 267]

$$S_n(M\ell) = \frac{1}{1-n}\log\left\langle \mathcal{T}_n(0)\,\widetilde{\mathcal{T}}_n(\ell)\right\rangle \approx \frac{2}{1-n}\log\langle\mathcal{T}_n\rangle + \frac{1}{1-n}\sum_{r,l\ \text{even}} c^{\mathcal{T}}_{r,l}(M\ell;n)\,, \tag{5.124}$$

where, in analogy with Ref. [267], we have introduced the cumulants

$$c^{\mathcal{T}}_{r,l}(M\ell;n) = \sum_{j,j'}\int_{-\infty}^{+\infty}\frac{\prod_{i=1}^{r}\mathrm{d}\theta_i\prod_{k=1}^{l}\mathrm{d}\theta'_k}{r!\,l!\,(2\pi)^{r+l}}\; f^{\mathcal{T}|j_1\dots j'_1\dots}_{r,l}\big(\theta_1,\dots,\theta'_1,\dots;n\big)\,e^{-\frac{M\ell}{2}\left(\sum_i e^{\theta_i}+\sum_k e^{-\theta'_k}\right)}. \tag{5.125}$$

In the integral in Eq. (5.125), $f^{\mathcal{T}|j_1\dots}_{r,l}$ denotes the connected part of the square of the form factor $\left|F^{\mathcal{T}|j_1\dots}_{r,l}\right|^2$, obtained by subtracting all the possible clusterisations for large rapidities [192, 267]. Recall from the discussion around Eqs. (5.33), (5.34) that, due to the clustering property, at large rapidity differences between the particles, the form factor factorises in the product of form factors with less particles. For example, up to the four-particle level, the connected components take the form

$$f^{\mathcal{T}|j_1j_2}_{2,0}(\theta_1,\theta_2;n) = \frac{1}{\langle\mathcal{T}_n\rangle^2}\left|F^{\mathcal{T}|j_1j_2}_{2,0}(\theta_1,\theta_2;n)\right|^2, \tag{5.126}$$

$$\begin{aligned} f^{\mathcal{T}|j_1j_2j_3j_4}_{4,0}(\theta_1,\theta_2,\theta_3,\theta_4;n) = {} & \frac{1}{\langle\mathcal{T}_n\rangle^2}\left|F^{\mathcal{T}|j_1j_2j_3j_4}_{4,0}(\theta_1,\theta_2,\theta_3,\theta_4;n)\right|^2 + \\ & - f^{\mathcal{T}|j_1j_2}_{2,0}(\theta_1,\theta_2;n)\;f^{\mathcal{T}|j_3j_4}_{2,0}(\theta_3,\theta_4;n) - f^{\mathcal{T}|j_1j_3}_{2,0}(\theta_1,\theta_3;n)\;f^{\mathcal{T}|j_2j_4}_{2,0}(\theta_2,\theta_4;n) + \\ & - f^{\mathcal{T}|j_1j_4}_{2,0}(\theta_1,\theta_4;n)\;f^{\mathcal{T}|j_2j_3}_{2,0}(\theta_2,\theta_3;n)\,, \end{aligned} \tag{5.127}$$

$$\begin{aligned} f^{\mathcal{T}|j_1j_2j'_1j'_2}_{2,2}\big(\theta_1,\theta_2,\theta'_1,\theta'_2;n\big) = {} & \frac{1}{\langle\mathcal{T}_n\rangle^2}\left|F^{\mathcal{T}|j_1j_2j'_1j'_2}_{2,2}\big(\theta_1,\theta_2,\theta'_1,\theta'_2;n\big)\right|^2 + \\ & - f^{\mathcal{T}|j_1j_2}_{2,0}(\theta_1,\theta_2;n)\;f^{\mathcal{T}|j'_1j'_2}_{0,2}\big(\theta'_1,\theta'_2;n\big)\,. \end{aligned} \tag{5.128}$$

By definition, the connected form factors $f^{\mathcal{T}|j_1\dots}_{r,l}$ vanish for large rapidities. As we will see, this improves the convergence of the integral in Eq. (5.125).

In the expansion (5.124), we recognise two different kinds of cumulants. Those containing only form factors diagonal in the chiralities, $c^{\mathcal{T}}_{r,0}$, $c^{\mathcal{T}}_{0,l}$, which we will call non-interacting cumulants, and the ones that couple left- and right-movers, which we will call interacting. In the rest of the section, we treat the two kinds of terms separately since, as we will see, they give different contributions to the entanglement entropy (5.124).

Non-interacting cumulants

Let us first focus on the non-interacting cumulants. As we saw in Sec. 5.3, in the massless flow, the form factors containing either only right- or only left-movers are identical to those of the massive Ising theory except for the vacuum expectation value $\langle\mathcal{T}_n\rangle$, implying that their connected components are identical $f^{\mathcal{T}|j_1\dots j_k}_{k,0} = f^{\mathcal{T}|j_1\dots j_k}_{0,k} = f^{\mathcal{T}|j_1\dots j_k}_{k,\text{ Ising}}$. Given this identity, we can analyse them by applying the same strategy as in Ref. [192] for the massive Ising theory, which we also report in Sec. 5.C.

Using the Pfaffian structure of the form factors in Eq. (5.54), it was shown that the non-interacting cumulants $c^{\mathcal{T}}_{r,0}$ have the general expression [190, 192, 198, 268]

$$c^{\mathcal{T}}_{k,0}(M\ell;n) = \frac{n}{k\,(2\pi)^k} \sum_{j_2,\dots,j_k=1}^{n} \int_{-\infty}^{+\infty} \prod_{i=1}^{k} \mathrm{d}\theta_i\, e^{-\ell\, E(\theta_1,\dots)} \Big[w(-\theta_{12} + 2\pi \mathrm{i} j_2)\, w(\theta_{1,k} + 2\pi \mathrm{i} j_k) \times \\ \times \prod_{l=1}^{k/2-1} w(-\theta_{2l,2l+1} + 2\pi\mathrm{i}\,(j_{2l} - j_{2l+1}))\, w(\theta_{2l+1,2l+2} + 2\pi\mathrm{i}\,(j_{2l+1} - j_{2l+2})) \Big], \tag{5.129}$$

where $\theta_{ij} = \theta_i - \theta_j$, we have summed over j_1, and we have introduced the notation

$$w(\theta) = \frac{1}{\langle\mathcal{T}_n\rangle} F^{\mathcal{T}|11}_{2,0}(\theta;n)\,. \tag{5.130}$$

From the form of Eq. (5.129), with all terms cyclically connected [192, 268], it is clear why they are known as fully connected. Importantly, Eq. (5.129) holds for both the massless tricritical-critical flow and for the massive Ising theory. The only difference between the cumulants in these two models is the form of the energy E appearing in the exponential factor. This difference has however a major effect in the integral in Eq. (5.129).

For simplicity, we can start by analysing the two-right-mover cumulant $c^{\mathcal{T}}_{2,0}$. The generalisation to higher particles will be straightforward. In our massless flow, as already recognised in Ref. [216] for a different correlation function, the two-fold integral in Eq. (5.129) is IR divergent due to the absence of a mass gap. In fact, in the relative and center-of-mass coordinates, $\theta_{12} = \theta_1 - \theta_2$ and $A = (\theta_1 + \theta_2)/2$, the energy (5.5) of two right-moving particles takes the form

$$E(\theta_1,\theta_2) = \frac{M}{2}\left(e^{\theta_1} + e^{\theta_2}\right) = M e^{A} \cosh\frac{\theta_{12}}{2}\,. \tag{5.131}$$

For right-movers, the IR region $E \to 0$ corresponds to large and negative center-of-mass rapidity $A \to -\infty$. Since the form factors do not depend on A, we see that the integrand of Eq. (5.129) tends to a non-zero constant for $A \to -\infty$, leading to a divergence when the integral in A is performed.

In order to cure this IR divergence, we introduce a cut-off Λ in the center-of-mass rapidity A. Since the form factors do not depend on A, the resulting integral can be cast in terms of the exponential integral function $\mathrm{Ei}(x)$,

$$\begin{aligned} c^{\mathcal{T}}_{2,0}(M\ell,\Lambda;n) &= \frac{n}{2\,(2\pi)^2}\sum_{j_2}\int_{-\infty}^{+\infty}\mathrm{d}\theta_{12}\,f_2^{\mathcal{T}|1j_2}(\theta_{12};n)\int_{-\log\Lambda}^{+\infty}\mathrm{d}A\,e^{-M\ell\,e^{A}\cosh\frac{\theta_{12}}{2}} \\ &= \frac{n}{2\,(2\pi)^2}\sum_{j_2}\int_{-\infty}^{+\infty}\mathrm{d}\theta_{12}\,f_2^{\mathcal{T}|1j_2}(\theta_{12};n)\,(-)\,\mathrm{Ei}\biggl(-\frac{M\ell}{\Lambda}\cosh\frac{\theta_{12}}{2}\biggr)\,. \end{aligned} \tag{5.132}$$

We see that Λ plays the role of a cut-off at large distances with $M\ell \ll \Lambda$. In this limit, using the expansion

$$\mathrm{Ei}(-x) \underset{x\ll 1}{\approx} \log x + \gamma + \mathcal{O}(x)\,, \tag{5.133}$$

we obtain a logarithmic dependence in the interval length ℓ,

$$c^{\mathcal{T}}_{2,0}(M\ell,\Lambda;n) \approx -\frac{z_2(n)}{2}\,\log\biggl(\frac{M\ell}{\Lambda}\biggr) + \text{const}, \tag{5.134}$$

where z_2 is the function

$$z_2(n) = \frac{n}{(2\pi)^2}\sum_{j_2}\int_{-\infty}^{+\infty}\mathrm{d}\theta_{12}\,f_2^{\mathcal{T}|1j_2}(\theta_{12};n)\,. \tag{5.135}$$

Remarkably, up to an additive constant and the large distance cut-off Λ, the sum of the left- and right-moving two-particle cumulants in our massless flow, $c^{\mathcal{T}}_{2,0} + c^{\mathcal{T}}_{0,2}$, is equal to the UV limit of the two-particle cumulant of the massive Ising model (cf. Eq. (5.216) in Sec. 5.C). This is consistent with the expectation that, in the IR, the contributions of the interacting cumulants vanish because the flow leads to the critical Ising fixed point. As such, we expect that for large distances the non-interacting cumulants completely reproduce the logarithmic entanglement entropy of the Ising CFT.

Moving to higher particle cumulants $c^{\mathcal{T}}_{r,0}$, we expect a similar structure. In the presence of more than two particles, a convenient set of coordinates is again provided by the center-of-mass rapidity $A = \frac{1}{k}\sum_{j=1}^{k}\theta_j$ and the difference between the rapidities $\theta_{j,j+1} = \theta_j - \theta_{j+1}$, with Jacobian equal to one. For convenience, we further define the rapidities in the center-of-mass frame of reference

$$\xi_j = \theta_j - A, \qquad \xi_k = -\sum_{j=1}^{k-1}\xi_j\,, \tag{5.136}$$

which can be shown to depend only on the rapidity differences. In the massless flow, the r-fold integral in Eq. (5.129) is divergent in the large negative center-of-mass rapidity region $A \to -\infty$. It is important to stress a subtle point. Due to the clustering property (see Eqs. (5.33) and (5.34)), the integral of the form factor is divergent in the direction of the sum of any two rapidities θ_j. However, in the cumulants, the non-connected factorised component is subtracted as in, e.g., Eqs. (5.127) and (5.128), guaranteeing that the integral of the connected part converges in those directions. The only remaining divergence is the one in the direction of large negative center-of-mass A, as it happens for the two-particle cumulant (5.132).

In the center-of-mass coordinates defined before Eq. (5.136), the energy of r right-moving particles in the massless flow takes the form

$$E(\theta_1, \dots, \theta_r) = \frac{M}{2} \sum_j e^{\theta_j} = \frac{M}{2}\, e^{A} \sum_j e^{\xi_j(\theta_{12}, \dots)} \,. \tag{5.137}$$

As already done in Eq. (5.132) for the two-particle case, we again introduce a cut-off Λ on the large negative center-of-mass rapidity A and we write the integral over it in terms of the exponential integral function $\mathrm{Ei}(x)$,

$$\begin{aligned} c^{\mathcal{T}}_{r,0}(M\ell, \Lambda; n) &= \frac{n}{r!\,(2\pi)^r} \sum_j \int_{-\infty}^{+\infty} \prod_{j=1}^{r-1} \mathrm{d}\theta_{j,j+1}\, f^{\mathcal{T}}_r(\theta_{12}, \dots; n) \int_{-\infty}^{+\infty} \mathrm{d}A\, e^{-\frac{M}{2}\ell\, e^{A} \sum_j e^{\xi_j}} \\ &= \frac{n}{r!\,(2\pi)^r} \sum_j \int_{-\infty}^{+\infty} \prod_{j=1}^{r-1} \mathrm{d}\theta_{j,j+1}\, f^{\mathcal{T}}_r(\theta_{12}, \dots; n)\ (-)\,\mathrm{Ei}\left(\frac{1}{2} \frac{M\ell}{\Lambda} \sum_j e^{\xi_j} \right) . \end{aligned} \tag{5.138}$$

In the large cut-off limit $\Lambda \gg M\ell$, we can approximate the cumulant using the expansion of the exponential integral in Eq. (5.133), obtaining the expected logarithmic behaviour

$$c^{\mathcal{T}}_{r,0}(M\ell, \Lambda; n) \approx -\frac{z_r(n)}{2} \log\frac{M\ell}{\Lambda} + \mathrm{const}\,, \tag{5.139}$$

with $z_k(n)$ equal to

$$\begin{aligned} z_k(n) &= \frac{2n}{k!\,(2\pi)^k} \sum_j \int_{-\infty}^{+\infty} \prod_{j=1}^{k-1} \mathrm{d}\theta_{j,j+1}\, f^{\mathcal{T}}_k(\theta_{12}, \dots; n) \\ &= \frac{2n}{k\,(2\pi)^k} \sum_{j_2, \dots, j_k = 1}^{n} \int_{-\infty}^{+\infty} \prod_{i=1}^{k} \mathrm{d}\theta_i \Big[w(-\theta_{12} + 2\pi\mathrm{i} j_2)\, w(\theta_{1,k} + 2\pi\mathrm{i} j_k) \times \\ &\qquad \times \prod_{l=1}^{k/2-1} w(-\theta_{2l,2l+1} + 2\pi\mathrm{i}\,(j_{2l} - j_{2l+1}))\, w(\theta_{2l+1,2l+2} + 2\pi\mathrm{i}\,(j_{2l+1} - j_{2l+2})) \Big] . \end{aligned} \tag{5.140}$$

As happens with the two-particle cumulants, the sum $c^{\mathcal{T}}_{r,0} + c^{\mathcal{T}}_{0,r}$ in the massless flow coincides with the UV limit of the r-particle cumulant of the massive Ising theory up to additive constants (see Eq. (5.220) in Sec. 5.C). In Ref. [192], the resummation of the $z_r(n)$ terms is carried out. Taking Eq. (5.139) and applying their result,

$$\sum_{k \text{ even}} z_k(n) = 4h^{\text{IR}}_{\mathcal{T}} = \frac{1}{12}\left(n - \frac{1}{n}\right), \tag{5.141}$$

we find that

$$\sum_{r \text{ even}} c^{\mathcal{T}}_{r,0}(M\ell, \Lambda; n) + \sum_{l \text{ even}} c^{\mathcal{T}}_{0,l}(M\ell, \Lambda; n) \approx \frac{1}{12}\left(n - \frac{1}{n}\right) \log\frac{M\ell}{\Lambda} + \text{const.} \tag{5.142}$$

This shows that, up to additive constants, the sum of the non-interacting left- and right-movers contribution to the entanglement entropy (5.124) in the massless flow gives the entropy of the Ising CFT in the IR fixed point.

Interacting cumulants

As shown in the previous discussion, the non-interacting cumulants contribute to the entropy of the IR Ising CFT; hence the corrections for smaller distances are provided by the interacting cumulants $c^{\mathcal{T}}_{r,l}$, which couple left- and right-movers. In this section, we study the only interacting cumulant at four-particle level, namely $c^{\mathcal{T}}_{2,2}$

$$\begin{aligned} c^{\mathcal{T}}_{2,2}(M\ell; n) &= \frac{n}{2 \times 2\,(2\pi)^4} \sum_{j_2, j_3, j_4} \int_{-\infty}^{+\infty} \mathrm{d}\theta_1 \mathrm{d}\theta_2 \mathrm{d}\theta_3 \mathrm{d}\theta_4 \, f^{\mathcal{T}|1 j_2 j_3 j_4}_{2,2}\big(\theta_1, \theta_2, \theta'_1, \theta'_2; n\big) \times \\ &\qquad\qquad\qquad\qquad \times e^{-\frac{M\ell}{2}\left(e^{\theta_1} + e^{\theta_2} + e^{-\theta'_1} + e^{-\theta'_2}\right)} \\ &= \frac{n}{2 \times 2\,(2\pi)^4} \sum_{j_2, j_3, j_4} \int_{-\infty}^{+\infty} \mathrm{d}\theta_1 \mathrm{d}\theta_2 \mathrm{d}\theta_3 \mathrm{d}\theta_4 \left[\frac{1}{\langle \mathcal{T}_n \rangle^2} \left| F^{\mathcal{T}|1 j_2 j_3 j_4}_{2,2}\big(\theta_1, \theta_2, \theta'_1, \theta'_2; n\big)\right|^2 + \right. \\ &\qquad \left. - \frac{1}{\langle \mathcal{T}_n \rangle^4} \left| F^{\mathcal{T}|1 j_2}_{2,0}(\theta_1, \theta_2; n)\right|^2 \left| F^{\mathcal{T}| j_3 j_4}_{0,2}\big(\theta'_1, \theta'_2; n\big)\right|^2 \right] e^{-\frac{M\ell}{2}\left(e^{\theta_1} + e^{\theta_2} + e^{-\theta'_1} + e^{-\theta'_2}\right)}, \end{aligned} \tag{5.143}$$

where the 'RRLL' form factor $F^{\mathcal{T}}_{2,2}$ is given in Eq. (5.60). As for the non-interacting cumulants, the integral of $F^{\mathcal{T}}_{2,2}$ is divergent in the IR limit. However, unlike the previous discussion, now the subtraction of the clusterisation in the connected component $f^{\mathcal{T}|1 j_2 j_3 j_4}_{2,2}$ ensures that the cumulant is convergent and a regularisation is not needed.

In Fig. 5.2, we report the result of the numerical integration of the cumulant $c^{\mathcal{T}}_{2,2}$ for different values of $M\ell$ and for $n = 2, 3$ replicas, performed using the Divonne routine of the library CUBA [266]. In the UV region $M\ell \ll 1$, we expect a leading logarithmic behaviour,

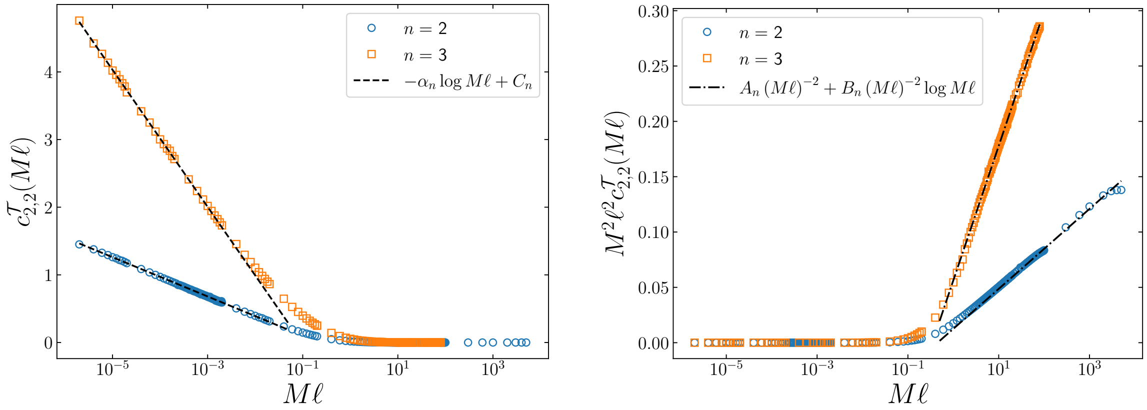

(a) Cumulant $c^{\mathcal{T}}_{2,2}$.

(b) Cumulant $c^{\mathcal{T}}_{2,2}$ times $M^2\ell^2$.

Figure 5.2: Semi-logarithmic plots of the cumulant $c^{\mathcal{T}}_{2,2}$ in Eq. (5.143) for $n = 2, 3$ replicas as a function of $M\ell$. On the left, the dashed line is the curve $-\alpha_n \log(M\ell) + C_n$, which provides the leading logarithmic behaviour in the UV regime $M\ell \ll 1$. The parameters α_n, C_n are obtained from numerical best fit of the points and are reported in Eqs. (5.144), (5.145). On the right, we plot the product of the cumulant times $M^2\ell^2$. The dash-dotted line represents the leading IR ($M\ell \gg 1$) behaviour $c^{\mathcal{T}}_{2,2} \simeq A_n\ (M\ell)^{-2} + B_n\ (M\ell)^{-2}\log(M\ell)$, with parameters A_n, B_n obtained from the best fit shown in Eqs. (5.152), (5.153).

since the sum of the interacting and non-interacting form factors should reproduce the logarithmic entanglement entropy of the tricritical Ising UV fixed point. In Fig. 5.2a, we plot the interacting cumulant $c^{\mathcal{T}}_{2,2}$ in Eq. (5.143) for $n = 2, 3$ replicas and we compare it with the fit of the numerical points to a logarithmic function $-\alpha_n \log M\ell + C_n$. We perform the fit for $M\ell \leqslant 2 \times 10^{-4}$ when $n = 2$ and for $M\ell \leqslant 6 \times 10^{-4}$ when $n = 3$, obtaining the parameters

$$\alpha_2 \approx 0.13, \quad C_2 \approx -0.19, \qquad \text{for } n = 2,\ M\ell \leqslant 2 \times 10^{-4}, \tag{5.144}$$

$$\alpha_3 \approx 0.44, \quad C_3 \approx -1.03, \qquad \text{for } n = 3,\ M\ell \leqslant 6 \times 10^{-4}. \tag{5.145}$$

From Fig. 5.2a, we see that for $M\ell \ll 1$ the cumulant is in good agreement with the expected logarithmic behaviour.

To understand the behaviour in the IR ($M\ell \gg 1$), recall from the general introduction of Sec. 5.1 that, near the IR fixed point, the effective theory describing the massless flow is the $T\bar{T}$ deformation of the critical Ising CFT, as shown in Eq. (5.4). The entanglement entropies of generic $T\bar{T}$-deformed CFTs have been heavily studied in recent years, see e.g. [233–246]. In particular, in Ref. [235], the entropy of an interval of length ℓ in a system of finite size L has been computed perturbatively for a generic $T\bar{T}$-deformed CFT. Let the deformed action be

$$\mathcal{A}_{T\bar{T}} = \mathcal{A}_{\text{CFT}} + g \int \mathrm{d}^2 z\, T\bar{T}\,, \tag{5.146}$$

where the $T\bar{T}$ coupling g has dimensions of an inverse mass squared, $g \propto M^{-2}$. The first perturbative correction to the Rényi entanglement entropy of the IR CFT was found to be [235]

$$(1-n)\,\delta S_n^{(1)}(\ell, L, g) = -\frac{\pi c^2 g}{36}\frac{\left(n^2-1\right)^2}{n^3}\left[\frac{1}{16\,\epsilon^2} - \frac{\left(11\cos\frac{2\pi\ell}{L}+19\right)}{24\left(\frac{L}{\pi}\sin\frac{\pi\ell}{L}\right)^2} + \frac{\cos\frac{\pi\ell}{L}\,\log\frac{L\sin\frac{\pi\ell}{L}}{2\pi\epsilon}}{\left(\frac{L}{\pi}\sin\frac{\pi\ell}{L}\right)^2}\right], \tag{5.147}$$

where ϵ is a non-universal UV cut-off. Here we are interested in the entanglement entropy in the thermodynamic limit $L \to \infty$ of Eq. (5.147),

$$(1-n)\,\delta S_n^{(1)}(\ell, g) = -\frac{\pi c^2 g}{36}\frac{\left(n^2-1\right)^2}{n^3}\left[\frac{1}{16\,\epsilon^2} - \frac{5}{4}\frac{1}{\ell^2} + \frac{\log\frac{\ell}{2\epsilon}}{\ell^2}\right] + \mathcal{O}\left(g^2\ell^{-4}\right). \tag{5.148}$$

Comparing the effective Lagrangian (5.4) with the generic one in Eq. (5.146) and taking into account that in our case $T = -\frac{1}{2}\psi\partial\psi$ and $\bar{T} = -\frac{1}{2}\bar{\psi}\bar{\partial}\bar{\psi}$, we can conclude that $g = -\frac{4}{\pi^2 M^2}$. Therefore, since the central charge of our IR point is $c = \frac{1}{2}$, Eq. (5.148) specialised to our massless flow gives

$$(1-n)\,\delta S_n^{(1)}(\ell, M) = \frac{1}{36\pi}\frac{\left(n^2-1\right)^2}{n^3}\left[\frac{1}{16M^2\epsilon^2} - \frac{5}{4}\frac{1}{M^2\ell^2} + \frac{\log\frac{\ell}{2\epsilon}}{M^2\ell^2}\right] + \mathcal{O}\left(M^{-4}\ell^{-4}\right). \tag{5.149}$$

Observe that in the prediction of Eq. (5.149) the leading correction is of the form $A_n\,\ell^{-2} + B_n\,\ell^{-2}\log\ell$. The coefficient A_n is not universal due to the presence of the UV cutoff ϵ, while the factor B_n is. In particular, for $n = 2, 3$ replicas, its numerical value is

$$B_2 = \frac{1}{32\pi} = 0.00995\ldots, \qquad \text{for } n = 2, \tag{5.150}$$

$$B_3 = \frac{16}{243\pi} = 0.02096\ldots, \qquad \text{for } n = 3. \tag{5.151}$$

Note also that the leading correction in Eqs. (5.147), (5.148), (5.149) is non-zero only for $n \geqslant 2$ Rényi entropies, while it vanishes in the replica limit $n \to 1$ [235].

It is worthwhile to compare the first-order perturbative prediction in Eq. (5.149) with the leading correction that we obtain here from the form factor cumulant expansion (5.124), which is given by the interacting cumulant $c_{2,2}^{\mathcal{T}}$. In Fig. 5.2b we study this cumulant for $n = 2, 3$ replicas as a function of $M\ell$ and we perform a best fit of the numerical points to a function $A_n\,\ell^{-2} + B_n\,\ell^{-2}\log\ell$, for $M\ell \geqslant 50$ when $n = 2$ and for $M\ell \geqslant 20$ when $n = 3$. We obtain

$$A_2 \approx 0.013, \quad B_2 \approx 0.016, \qquad \text{for } n = 2,\ M\ell \geqslant 50, \tag{5.152}$$

$$A_3 \approx 0.056, \quad B_3 \approx 0.053, \qquad \text{for } n = 3,\ M\ell \geqslant 20. \tag{5.153}$$

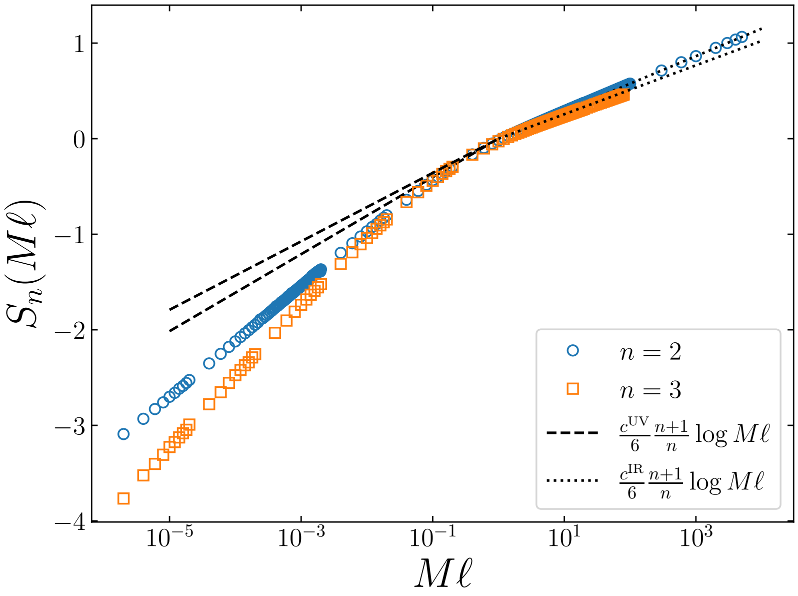

Figure 5.3: Semi-logarithmic plot of the Rényi entanglement entropy along the tricritical-critical Ising massless flow as a function of $M\ell$ for Rényi indices $n = 2$ and 3. The dots have been obtained using the truncated cumulant expansion (5.124), including the first 30 non-interacting cumulants $c^{\mathcal{T}}_{r,0}, c^{\mathcal{T}}_{0,l}$ and the leading interacting cumulant $c^{\mathcal{T}}_{2,2}$. The curves indicate the expected behaviour of the entropy when approaching the IR ($M\ell \gg 1$, dotted curves) and UV ($M\ell \ll 1$, dashed curves) regimes. In the IR, the truncated cumulant expansion agrees with the asymptotic behaviour, while in the UV it deviates. The reason of this mismatch is that we are only considering the leading interacting cumulant in the expansion (5.124) of the entropy.

For large distances, we find a good qualitative agreement with the functional form predicted in Eq. (5.149). However, while for $n = 2$ replicas the numerical result of the fit for B_2 is close to the predicted value in Eq. (5.150), this is not the case for $n = 3$. A possible explanation of this discrepancy is that the higher-particle interacting cumulants $c^{\mathcal{T}}_{r,l}$, which we are neglecting, also contribute to the term $\log \ell/\ell^2$ and their contribution depends on the number of replicas n.

Entanglement entropy

Finally, we can put together the results obtained in Secs. 5.6.2 and 5.6.2 to get the total entanglement. In Fig. 5.3, we consider the Rényi entanglement entropy in the massless flow as a function of $M\ell$ for $n = 2$ and 3. The results in this figure (represented as symbols) have been obtained with the cumulant expansion (5.124), including the first 30 non-interacting cumulants $c^{\mathcal{T}}_{r,0}$ and $c^{\mathcal{T}}_{0,l}$ and the leading interacting cumulant $c^{\mathcal{T}}_{2,2}$. In the plot, we also report the expected behaviour of the entanglement entropy when approaching the UV (dashed curves) and IR (dotted curves) fixed points. When approaching the IR, $M\ell \gg 1$, we find a very good agreement between the truncated cumulant expansion and the expected IR asymptotics for both values of n. In the UV, $M\ell \ll 1$, while the truncated expansion presents a behaviour compatible with a logarithmic divergence in $M\ell$, it does not quantitatively agree with the UV entropy. This is expected, since the UV limit is the regime where the higher-particle interacting cumulants $c^{\mathcal{T}}_{r,l}$ contribute more significantly and here we are only considering the four-particle one, $c^{\mathcal{T}}_{2,2}$. It would be interesting to include higher order terms, but this is a challenging task due to the difficulty of computing higher-particle cumulants, which involve an increasing number of multidimensional integrals. Nevertheless, in the light of Fig. 5.3, we can conclude that only including the leading interacting cumulant is enough to qualitatively observe the crossover between the IR and UV regimes.

Before concluding this section, let us comment on the symmetry resolved entanglement entropy. Also in this case, a cumulant expansion analogous to Eq. (5.124) holds true, by replacing the form factors with the appropriate ones for the composite twist field that we have determined in Sec. 5.4. In particular, the expansion of the symmetry resolved entanglement entropy contains both the non-interacting cumulants reproducing the Ising CFT and the interacting ones providing the corrections, analogously to what happens for the standard entropy. The symmetry resolved entropy in the massive Ising model has been recently studied in Ref. [268] where it was found that (differently from what happens for the standard BPTF) the cumulants of the composite twist fields are divergent although the theory is massive; consequently a regularisation was required. This fact suggests that, also for the massless flow, the regularisation employed for the total entropy is not sufficient to find a finite result for the composite twist field. Resolving such a regularisation is a problem that goes beyond the scope of this Chapter and we hope to return on the issue in the future.

5.7 Final remarks

In this Chapter, based on Ref. [269], we investigated the ground state Rényi entanglement entropies of a single interval in the massless QFT associated to the renormalisation group flow connecting the tricritical and critical Ising CFTs. The corresponding two-point correlation function of branch points twist fields admits a form factor expansion along the flow. We showed that these form factors can be calculated in two different and independent ways. On the one hand, we have directly applied the bootstrap approach of Ref. [188] for massive integrable QFTs: based on the symmetries of the theory and the exchange properties of the twist fields, we obtained a set of equations for the form factors and we found a general ansatz that solves them. Alternatively, we obtained the form factors using the Zamolodchikov's staircase model, an extension of the sinh-Gordon theory with complex couplings that includes the tricritical-critical renormalisation flow. In this framework, the form factors of several fields in this massless flow have been obtained as the roaming limit of those in the sinh-Gordon theory. We showed that the same strategy works for the branch points twist fields; we derived explicit expressions for the two and four-particle form factors, from which the higher-particle ones can be recursively derived. The two approaches gave identical results, confirming the validity of the roaming limit.

The form factor expansion of the entanglement entropy can be rearranged order by order in the number of particles in terms of cumulants, which are given by the connected part of the form factors. In this cumulant expansion, we distinguished free and interacting cumulants. The former only contain particles of the same chirality and give the entropy of the IR Ising CFT. In fact, we found that, after a proper regularisation, they are equal to those that appear in the massive Ising theory. On the other hand, the interacting cumulants, which contain particles with different chiralities, describe the behaviour of the entanglement entropy along the flow. In particular, we checked that the lowest-particle interacting cumulant yields in the UV limit the expected logarithmic behaviour in the subsystem size. The IR limit can be described by a $T\bar{T}$ deformation of the Ising CFT. We showed that the lowest-particle interacting cumulant expansion approaching the IR point qualitatively reproduces the result for a generic $T\bar{T}$ perturbation at first order [235]. However, we could not obtain a quantitative agreement since the two expansions are organised in a different way. It would be interesting to compute higher particle form factors, to confirm that the agreement improves.

The massless flow (5.3) that we studied here is also connected with the $SU(3)_2$-homogeneous sine-Gordon (HSG) model [225]. As shown in Refs. [193, 226, 227], along the renormalisation group flow, the central charge and the twist field dimension of this theory present two plateaux, analogously to the behaviour of the staircase model considered here. For certain values of the parameters, it was shown that one of these plateaux corresponds to the massless flow from tricritical to critical Ising [193, 226]. Since the form factors of the standard twist field in the $SU(3)_2$-HSG model have been obtained in Ref. [193] up to the four-particle order, it would be interesting to recover our results from an appropriate limit of the HSG expressions.

The massless flow connecting the tricritical and critical Ising CFTs enjoys a global $\mathbb{Z}_2$ symmetry. In this Chapter, we also considered the composite branch point twist fields associated to this symmetry. Their two-point functions give the charged moments of the reduced density matrix from which one can determine the symmetry-resolved entanglement entropy. Similarly to the standard twist fields, we obtained their bootstrap equations, which now include the non-trivial monodromy due to the insertion of the charge, and we found a general ansatz for their solution, which allows to obtain the higher-particle form factors recursively. We further derived them as the roaming limit of the composite twist field form factors of the sinh-Gordon theory. Remarkably, the latter were neither known in the previous literature, a gap which we also filled here.

Finally, we mention that, as we explained in Sec. 5.1, the flow (5.3) is the simplest example of the infinite family of massless renormalisation flows A_p, with $p \geqslant 2$, that interpolate between the unitary diagonal minimal models $\mathcal{M}_{p+2} \to \mathcal{M}_{p+1}$, all of which possess a global $\mathbb{Z}_2$ symmetry. A natural continuation of the work in this Chapter would be to study the form factor of both the standard and the composite twist fields in these flows and use them to study the (symmetry-resolved) entanglement entropies. The additional complication of these models is the presence of further magnonic excitations beside the fundamental ones. This fact makes more difficult the calculation of the twist field form factors compared to the A_2 case considered here.

5.A Form factor bootstrap for Branch Point Twist Fields in the A_2 massless flow

In this appendix, we provide more information on the technical derivation of the four-particle form factors for the standard and the composite BPTFs in the massless flow (5.3) from the tricritical to the critical Ising CFTs.

5.A.1 Form factors of the standard BPTF

We begin by recalling the most general ansatz (5.35) for FFs at any particle level, which reads

$$\begin{aligned} F^{\mathcal{T}}_{\underline{R},\underline{L}}(\underline{\theta},\underline{\theta}';n) = H^{\mathcal{T}}_{r,l}Q^{\mathcal{T}}_{r,l}(\underline{x},\underline{y};n) \prod_{1\leqslant i<j\leqslant r} \frac{f_{RR}(\theta_i-\theta_j;n)}{(x_i-\omega x_j)(x_j-\omega x_i)}\times \\ \times \prod_{i=1}^{r}\prod_{j=1}^{l} f_{RL}(\theta_i-\theta'_j;n) \prod_{1\leqslant i<j\leqslant l} \frac{f_{LL}(\theta'_i-\theta'_j;n)}{(y_i-\omega y_j)(y_j-\omega y_{ji})}\,. \end{aligned} \tag{5.154}$$

where we have r right-mover and l left-mover particles, $x_i = e^{\theta_i/n}$ and $y_i = e^{-\theta'_i/n}$. As discussed in the main text, the exchange (5.27) and the cyclic permutation axioms (5.28) are automatically satisfied by the above expression.

Our goal now is to identify the four-particle 'RRLL' form factors using the well-known two-particle quantities. For simplicity we place every particle on the first replica and specify Eq. (5.154) to the case of interest

$$\begin{aligned} &F^{\mathcal{T}}_{2,2}(\theta_1,\theta_2,\theta'_1,\theta'_2;n) = \\ &= H^{\mathcal{T}}_{2,2}Q^{\mathcal{T}}_{2,2}(x_1,x_2,y_1,y_2;n)\frac{f_{RR}(\theta_1-\theta_2;n)}{(x_1-\omega x_2)(x_2-\omega x_1)}\prod_{i=1}^{2}\prod_{j=1}^{2} f_{RL}(\theta_i-\theta'_j;n)\frac{f_{LL}(\theta'_1-\theta'_2;n)}{(y_1-\omega y_2)(y_2-\omega y_1)}\,. \end{aligned} \tag{5.155}$$

Applying now the residue axiom in Eq. (5.29) to the ansatz (5.155) we can derive recursive equations for the $H^{\mathcal{T}}_{2,2}$ normalisation factors and the $Q^{\mathcal{T}}_{2,2}$ functions. Let us first also recall that the minimal form factor f_{RL} satisfies the identity

$$\mathcal{N}_n f_{RL}(\theta+\mathrm{i}\pi;n)\mathcal{N}_n f_{RL}(\theta;n) = \left(1-e^{-\frac{\mathrm{i}\pi}{2n}}e^{-\frac{\theta}{n}}\right)^{-1}\,. \tag{5.156}$$

The residue of the denominator of the ansatz (5.155) takes the form

$$\begin{aligned} -\mathrm{i}\underset{\theta_1=\mathrm{i}\pi+\theta_2}{\mathrm{Res}}\frac{1}{(x_1-\omega x_2)(x_2-\omega x_1)}\frac{1}{(y_1-\omega y_2)(y_2-\omega y_1)} &= \\ &= -\mathrm{i}\frac{1}{(y_1-\omega y_2)(y_2-\omega y_1)}\frac{n\left(\omega x_0^2\right)^{-1}}{(e^{\frac{2\mathrm{i}\pi}{n}}-1)}\,, \end{aligned} \tag{5.157}$$

from which we can obtain the residue of the entire expression (5.155) as

$$\begin{aligned} &-\mathrm{i}\underset{\theta_1=i\pi+\theta_2}{\mathrm{Res}}F_{2,2}^{\mathcal{T}}(\theta_1,\theta_2,\theta_1',\theta_2';n)= \\ &=\mathrm{i}\,H_{2,2}^{\mathcal{T}}Q_{2,2}^{\mathcal{T}}(\omega x,x,y_1,y_2;n)f_{RR}(\mathrm{i}\pi;n)\frac{n\left(x^2\omega\right)^{-1}}{\omega^2-1}\times \\ &\qquad\times\prod_{j=1}^{2}f_{RL}(\theta+\mathrm{i}\pi-\theta_j';n)f_{RL}(\theta-\theta_j';n)\frac{f_{LL}(\theta_1'-\theta_2';n)}{(y_1-\omega y_2)(y_2-\omega y_1)} \\ &=\mathrm{i}\,H_{2,2}^{\mathcal{T}}Q_{2,2}^{\mathcal{T}}(\omega x,x,y_1,y_2;n)f_{RR}(\mathrm{i}\pi;n)\frac{n\left(x^2\omega\right)^{-1}}{\omega^2-1}\times \\ &\qquad\times\mathcal{N}_n^{-4}\frac{1}{1-\left(\omega^{1/2}xy_1\right)^{-1}}\frac{1}{1-\left(\omega^{1/2}xy_2\right)^{-1}}\frac{f_{LL}(\theta_1'-\theta_2';n)}{(y_1-\omega y_2)(y_2-\omega y_1)}\,, \end{aligned} \tag{5.158}$$

where we used Eqs. (5.156) and (5.157). Via algebraic manipulations we can simplify the above formula to

$$\begin{aligned} &-\mathrm{i}\underset{\theta_1=\mathrm{i}\pi+\theta_2}{\mathrm{Res}}F_{2,2}^{\mathcal{T}}(\theta_1,\theta_2,\theta_1',\theta_2';n)= \\ &=\mathrm{i}\,H_{2,2}^{\mathcal{T}}Q_{2,2}^{\mathcal{T}}(\omega x,x,y_1,y_2;n)\,\mathcal{N}_n^{-4}\frac{1}{(\omega^{1/2}xy_1-1)(\omega^{1/2}xy_2-1)}\left[\frac{4\omega}{n}\cos\frac{\pi}{2n}\right]^{-1}\times \\ &\qquad\times\frac{y_1y_2\,f_{LL}(\theta_1'-\theta_2';n)}{(y_1-\omega y_2)(y_2-\omega y_1)}\,. \end{aligned} \tag{5.159}$$

Following the residue axiom in Eq. (5.29), the residue of the kinematical pole in Eq. (5.159) has to reproduce the two-particle form factor in Eq. (5.48). We first recast it in the shape of our ansatz as

$$\begin{aligned} F_{0,2}^{\mathcal{T}}(\theta_1'-\theta_2';n) &= \frac{-\mathrm{i}\cos\left(\frac{\pi}{2n}\right)}{n\sinh\left(\frac{\mathrm{i}\pi+(\theta_1-\theta_2)}{2n}\right)\sinh\left(\frac{\mathrm{i}\pi-(\theta_1-\theta_2)}{2n}\right)}\sinh\left(\frac{\theta_1'-\theta_2'}{2n}\right) \\ &= H_{0,2}^{\mathcal{T}}Q_{0,2}^{\mathcal{T}}(y_1,y_2)\,\frac{f_{LL}(\theta_1'-\theta_2';n)}{(y_1-\omega y_2)(y_2-\omega y_1)}\,, \end{aligned} \tag{5.160}$$

where we have defined

$$H^{\mathcal{T}}_{0,2} = -\mathrm{i}\frac{4\,\omega}{n}\cos\frac{\pi}{2n}\,, \tag{5.161}$$

$$Q^{\mathcal{T}}_{0,2}(y_1,y_2) = \sigma_2(y_1,y_2) = y_1y_2\,. \tag{5.162}$$

Comparing the residue in Eq. (5.159) with the two-particle form factor in Eq. (5.160) leads to the recursion equations for $H^{\mathcal{T}}_{2,2}$ and for the polynomial $Q^{\mathcal{T}}_{2,2}$

$$H^{\mathcal{T}}_{2,2}Q^{\mathcal{T}}_{2,2}(\omega x,x,y_1,y_2;n) = -\mathcal{N}_n^4\left[\frac{4\,\omega}{n}\cos\frac{\pi}{2n}\right]^2(\omega^{1/2}xy_1-1)(\omega^{1/2}xy_2-1)\,, \tag{5.163}$$

which we separate as

$$H^{\mathcal{T}}_{2,2} = -\mathcal{N}_n^4\left[\frac{4\,\omega}{n}\cos\frac{\pi}{2n}\right]^2, \tag{5.164}$$

$$Q^{\mathcal{T}}_{2,2}(\omega x,x,y_1,y_2;n) = (\omega^{1/2}xy_1-1)(\omega^{1/2}xy_2-1) = 1-\omega^{1/2}x\,(y_1+y_2)+\omega x^2y_1y_2\,. \tag{5.165}$$

We postulate a solution to Eq. (5.165) completely symmetrical in x_1,x_2,y_1,y_2 and hence writing

$$\begin{aligned}Q^{\mathcal{T}}_{2,2}(x_1,x_2,y_1,y_2;n) &= 1+A\sigma_1(x_1,x_2)\sigma_1(y_1,y_2)+\sigma_2(x_1,x_2)\sigma_2(y_1,y_2) = \\ &= 1+A\,(x_1+x_2)\,(y_1+y_2)+x_1x_2y_1y_2\,,\end{aligned} \tag{5.166}$$

which is the most general expression compatible with the fact that the form factor has zero Lorentz spin, and that sending each rapidity to ±∞ the entire FF converges to zero. Posing $x_1=\omega x$, $x_2=x$, we get a unique solution for the unknown constant A, namely

$$A = -\frac{\omega^{1/2}}{1+\omega} = -\frac{1}{\omega^{1/2}+\omega^{-1/2}} = -\frac{1}{2\cos\frac{\pi}{2n}}\,. \tag{5.167}$$

This means that the entire solution can be written as

$$\begin{aligned}F^{\mathcal{T}}_{2,2}(\theta_1,\theta_2,\theta'_1,\theta'_2;n) = -\mathcal{N}_n^4\left[\frac{4\,\omega}{n}\cos\frac{\pi}{2n}\right]^2&\left[1-\frac{1}{2\cos\frac{\pi}{2n}}\,(x_1+x_2)\,(y_1+y_2)+x_1x_2y_1y_2\right]\times\\ \times\,\frac{f_{RR}(\theta_1-\theta_2;n)}{(x_1-\omega x_2)(x_2-\omega x_1)}&\prod_{i=1}^{2}\prod_{j=1}^{2}f_{RL}(\theta_i-\theta'_j;n)\frac{f_{LL}(\theta'_1-\theta'_2;n)}{(y_1-\omega y_2)(y_2-\omega y_1)},\end{aligned} \tag{5.168}$$

which we can also rewrite as

$$\begin{aligned}
&F^{\mathcal{T}}_{2,2}(\theta_1,\theta_2,\theta'_1,\theta'_2;n) = \\
&= -2\mathcal{N}_n^4 e^{-\frac{\theta_1+\theta_2-\theta'_1-\theta'_2}{2n}} \left[\cosh\!\left(\frac{\theta_1+\theta_2-\theta'_1-\theta'_2}{2n}\right) - \frac{\cosh\!\left(\frac{\theta_1+\theta_2}{2n}\right)\cosh\!\left(\frac{\theta'_1+\theta'_2}{2n}\right)}{\cos\!\left(\frac{\pi}{2n}\right)}\right] \times \\
&\qquad \times F^{\mathcal{T}}_{2,0}(\theta_1,\theta_2;n)\prod_{i=1}^{2}\prod_{j=1}^{2} f_{RL}(\theta_i-\theta'_j;n) F^{\mathcal{T}}_{0,2}(\theta_1,\theta_2;n)\,.
\end{aligned} \tag{5.169}$$

5.A.2 Form factors of the $\mathbb{Z}_2$-composite BPTF

Once again, we start our derivation by recalling and repeating the ansatz for $\mathbb{Z}_2$-composite BPTF

$$\begin{aligned}
F^{\mathcal{T}^\mu}_{\underline{R},\underline{L}}(\underline{\theta},\underline{\theta}';n) = H^{\mathcal{T}^\mu}_{r,l} Q^{\mathcal{T}^\mu}_{r,l}(\underline{x},,\underline{y};n) \prod_{1\leqslant i<j\leqslant r} \frac{f^\mu_{RR}(\theta_i-\theta_j;n)}{(x_i-\omega x_j)(x_j-\omega x_i)} \times \\
\times \prod_{i=1}^{r}\prod_{j=1}^{l} f^\mu_{RL}(\theta_i-\theta'_j;n) \prod_{1\leqslant i<j\leqslant l} \frac{f^\mu_{LL}(\theta'_i-\theta'_j;n)}{(y_i-\omega y_j)(y_j-\omega y_i)}\,,
\end{aligned} \tag{5.170}$$

where we have r right-mover and l left-mover particles and again $x_i = e^{\theta_i/n}$ and $y_i = e^{-\theta'_i/n}$. The cyclic permutation and the exchange axioms are already satisfied since

$$f^\mu_{\gamma\gamma}(2\pi i n-\theta;n) = -f^\mu_{\gamma\gamma}(\theta;n) = f^\mu_{\gamma\gamma}(-\theta;n)\,, \tag{5.171}$$

is fulfilled via

$$f^\mu_{\gamma\gamma}(\theta;n) = 2\cosh(\theta/(2n)) f_{\gamma\gamma}(\theta;n) = \sinh(\theta/n)\,. \tag{5.172}$$

Defining $f^\mu_{RL}(\theta;n)$ as

$$f^\mu_{RL}(\theta;n) = e^{\theta/(2n)} f_{RL}(\theta;n)\,, \tag{5.173}$$

for γ' different from γ, we similarly satisfy

$$f^\mu_{\gamma\gamma'}(2\pi i n-\theta;n) = -f^\mu_{\gamma'\gamma}(\theta;n) = -S_{\gamma'\gamma}(\theta) f^\mu_{\gamma'\gamma}(-\theta;n)\,. \tag{5.174}$$

In full analogy to what we have done in the previous section for the standard twist field, we apply the residue axiom Eq. (5.64) to the ansatz (5.170) in order to derive recursive equations for the normalisation factors $H^{\mathcal{T}^\mu}_{r,l}$ and the $Q^{\mathcal{T}^\mu}_{r,l}$ functions. Since the denominator of the ansatz (5.170) is the same as the one for the standard twist fields in Eq. (5.154), we can reuse the same residue we have computed in Eq. (5.157). Using again the property (5.156) of the minimal form factor, the residue of the ansatz with 4 particles yields

$$\begin{aligned}
&-\mathrm{i}\underset{\theta_1=\mathrm{i}\pi+\theta_0}{\mathrm{Res}} F_{2,2}^{\mathcal{T}^\mu}(\theta_1,\theta_2,\theta_1',\theta_2';n)=\\
&=\mathrm{i}\,H_{2,2}^{\mathcal{T}^\mu}Q_{2,2}^{\mathcal{T}^\mu}(\omega x,x,y_1,y_2;n)f_{RR}^{\mu}(\mathrm{i}\pi;n)\frac{n\left(x^2\omega\right)^{-1}}{\omega^2-1}\times\\
&\qquad\times\prod_{j=1} 2f_{RL}^{\mu}(\theta+i\pi-\theta_j';n)f_{RL}^{\mu}(\theta-\theta_j';n)\frac{f_{LL}^{\mu}(\theta_1'-\theta_2';n)}{(y_1-\omega y_2)(y_2-\omega y_1)} \qquad (5.175)\\
&=\mathrm{i}\,\frac{n\omega}{\omega(\omega-\omega^{-1})}H_{2,2}^{\mathcal{T}^\mu}\mathcal{N}_n^{-4}\frac{x^2(y_1y_2)^2Q_{2,2}^{\mathcal{T}^\mu}(\omega x,x,y_1,y_2;n)}{(\sqrt{\omega}xy_1-1)(\sqrt{\omega}xy_2-1)}\sinh(\mathrm{i}\pi/n)\times\\
&\qquad\times\frac{f_{LL}^{\mu}(\theta_1'-\theta_2';n)}{(y_1-\omega y_2)(y_2-\omega y_1)}\,.
\end{aligned}$$

Again, from the residue axiom (5.64), this expression must be compared with the two-particle FF, which we can rewrite as

$$\begin{aligned}
F_{2,0}^{\mathcal{T}^\mu}\left(\theta_1'-\theta_2';n\right)&=\frac{\langle\mathcal{T}_n^\mu\rangle\sin\frac{\pi}{n}}{2n\sinh\frac{\mathrm{i}\pi+\theta_1'-\theta_2'}{2n}\sinh\frac{\mathrm{i}\pi-(\theta_1'-\theta_2')}{2n}}\frac{\sinh((\theta_1'-\theta_2')/n)}{\sinh(\mathrm{i}\pi/n)}\\
&=\langle\mathcal{T}_n\rangle\frac{\mathrm{i}\omega}{n}\frac{\left(y_1^2-y_2^2\right)}{2y_1y_2}\frac{2y_1y_2}{(y_1-\omega y_2)(y_2-\omega y_1)}\,,
\end{aligned} \qquad (5.176)$$

where $\left(y_2^2-y_1^2\right)/(2y_1y_2)=\sinh((\theta_1'-\theta_2')/n)$. We then end up with the equation for $Q_{2,2}^{\mathcal{T}^\mu}$ as well as the normalisation

$$H_{2,2}^{\mathcal{T}^\mu}\mathcal{N}_n^{-4}Q_{2,2}^{\mathcal{T}^\mu}(\omega x,x,y_1,y_2;n)=-\langle\mathcal{T}_n^\mu\rangle 4\frac{\omega^2}{n^2\omega x^2y_1y_2}\left(\sqrt{\omega}xy_1-1\right)\left(\sqrt{\omega}xy_2-1\right), \qquad (5.177)$$

which we can separate as

$$H_{2,2}^{\mathcal{T}^\mu}=-4\langle\mathcal{T}_n^\mu\rangle\mathcal{N}_n^4\,, \qquad (5.178)$$

$$Q_{2,2}^{\mathcal{T}^\mu}(\omega x,x,y_1,y_2;n)=\frac{\omega^2}{n^2\omega x^2y_1y_2}(\sqrt{\omega}xy_1-1)(\sqrt{\omega}xy_2-1)\,. \qquad (5.179)$$

Notice that, differently from what happened in Eq. (5.165) for the standard twist field, now the function $Q_{2,2}^{\mathcal{T}^\mu}$ is not a polynomial but a rational function.

We write the solution to Eq. (5.179) as

$$Q_{2,2}^{\mathcal{T}^\mu}(x_1,x_2,y_1,y_2;n)=\frac{\omega^2}{n^2x_1x_2y_1y_2}\left(1+x_1x_2y_1y_2+A(x_1+x_2)(y_1+y_2)\right), \qquad (5.180)$$

which is the most general expression compatible with (i) the form factor has zero Lorentz spin, and (ii) sending each rapidity to $\pm\infty$ the entire FF converges to a constant. When setting $x_1 = \omega x$ and $x_2 = x$ we can obtain the same solution for A as for the case of the standard BPTF, namely $A = -\frac{1}{2\cos\frac{\pi}{2n}}$ and hence

$$Q_{2,2}^{\mathcal{T}^\mu}(x_1, x_2, y_1, y_2; n)^{(0)} = \frac{\omega^2}{n^2 x_1 x_2 y_1 y_2}\left(1 - \frac{(x_1+x_2)(y_1+y_2)}{2\cos\frac{\pi}{2n}} + x_1 x_2 y_1 y_2\right). \tag{5.181}$$

The ansatz with the above fraction of polynomial $Q_{2,2}^{\mathcal{T}^\mu}(\omega x_1, x_2, y_1, y_2; n)^{(0)}$ satisfies all the FF axioms. Notice that while the $n \to 1$ limit of the standard BPTF is not well defined, the FFs of the composite twist field reduce to those of the disorder field

$$F_{2,2}^{\mu} = H_{2,2}^{\mu}\frac{1 + x_1 x_2 y_1 y_2}{x_1 x_2 y_1 y_2}\frac{\sinh(\theta_1 - \theta_2)}{(x_1+x_2)^2}\frac{\sinh(\theta_1' - \theta_2')}{(y_1+y_2)^2}\prod_{i=1}^{2}\prod_{j=1}^{2} f_{RL}^{\mu}(\theta_i - \theta_j'; 1). \tag{5.182}$$

As pointed out in the main text, the solution of the bootstrap equation is in general not unique, since we can often add to our polynomial Q also a (non-trivial) kernel solution, that is, another polynomial (or fraction of polynomials) $Q^{(k)}$ which satisfies the homogeneous equation

$$Q_{2,2}^{\mathcal{T}^\mu}(\omega x, x, y_1, y_2; n)^{(k)} = 0. \tag{5.183}$$

Polynomial kernel solutions at the two- and four-particle level have been identified in [193]. In particular, the two-particle kernel solution reads as

$$Q_{2,0}(x_1, x_2; n)^{(k)} = x_1 x_2 - \left(\frac{x_1 + x_2}{2\cos\frac{\pi}{2n}}\right)^2 \tag{5.184}$$

from which the required four-particle kernel solution for the flow can be constructed by squaring the expression due to the anticipated symmetry between the variables of the RR and LL particles. Based on the above consideration, we can write the eventual kernel as

$$\begin{aligned} Q_{2,2}^{\mathcal{T}^\mu}(x_1, x_2, y_1, y_2; n)^{(k)} = & \frac{\omega^2}{n^2}\frac{8\cos^3\left(\frac{\pi}{2n}\right)\left(x_1x_2 - \frac{1}{4}\sec^2\left(\frac{\pi}{2n}\right)(x_1+x_2)^2\right)}{(x_1x_2)(x_1+x_2)(y_1+y_2)} \times \\ & \times \frac{\left(y_1y_2 - \frac{1}{4}\sec^2\left(\frac{\pi}{2n}\right)(y_1+y_2)^2\right)}{y_1y_2(y_1+y_2)} \end{aligned} \tag{5.185}$$

that is, taking the product of (5.184) and additionally, by also renormalising the expression with $(x_1x_2y_1y_2)(x_1+x_2)(y_1+y_2)$ which does not spoil the kernel property. We chose the pre-factor in a way that the entire expression for the polynomial

$$\begin{aligned} & Q_{2,2}^{\mathcal{T}^\mu}(x_1, x_2, y_1, y_2; n) = Q_{2,2}^{\mathcal{T}^\mu}(x_1, x_2, y_1, y_2; n)^{(0)} + Q_{2,2}^{\mathcal{T}^\mu}(x_1, x_2, y_1, y_2; n)^{(k)} \\ & = \frac{\omega^2}{n^2}\frac{1 + x_1x_2y_1y_2}{x_1x_2y_1y_2} + \\ & \qquad - \frac{2\omega^2\cos\frac{\pi}{2n}}{n^2}\frac{\left(x_1x_2(y_1+y_2)^2 + y_1y_2(x_1+x_2)^2 - 2x_1x_2y_1y_2(\cos\left(\frac{\pi}{n}\right)+1)\right)}{(x_1x_2y_1y_2)(x_1+x_2)(y_1+y_2)}, \end{aligned} \tag{5.186}$$

gives $(1+x_1x_2y_1y_2)/(x_1x_2y_1y_2)$ in the $n \to 1$ limit, which reproduces $Q^{\mu}_{2,2}$. The normalisation factors match as well, since $H^{\mu}_{2,2} = -4\mathcal{N}_1^4 = 2\,e^{-4G/\pi}$.

5.B Form factor bootstrap for branch point twist fields in the sinh-Gordon model

In this appendix, we first report the known results for the four-particle form factor of the standard twist field in the sinh-Gordon model and we then derive the previously unknown form factor of the composite one.

5.B.1 Form factors of the standard BPTF

In the sinh-Gordon model, the four-particle form factor of the standard branch point twist field has been computed in [193] using the bootstrap program. In Sec. 5.5 of the main text, this known result has been the starting point for the roaming limit. For completeness, in this appendix we report its explicit expression.

The solution is written in the usual form, reported in Eq. (5.93)

$$F_4^{\mathcal{T}}(\theta_1,\theta_2,\theta_3,\theta_4;n) = \, H_4^{\mathcal{T}}\, Q_4^{\mathcal{T}}(x_1,x_2,x_3,x_4;n) \prod_{1\leqslant i<j\leqslant 4} \frac{f_{\mathrm{ShG}}(\theta_i-\theta_j,B;n)}{(x_i-\omega x_j)(x_j-\omega x_i)}\,. \tag{5.187}$$

where f_{ShG} is the minimal form factor in the sinh-Gordon model, shown in the main text in Eq. (5.94). The normalisation $H_4^{\mathcal{T}}$ was found in [193] to be

$$H_4^{\mathcal{T}} = \left(\frac{2\,\sin\frac{\pi}{n}\,\omega^2}{n\,f_{\mathrm{ShG}}(\mathrm{i}\pi)}\right)^2 \omega^2 \langle \mathcal{T}_n \rangle, \tag{5.188}$$

while the polynomial $Q_4^{\mathcal{T}}$ takes the form [193]

$$\begin{aligned} Q_4^{\mathcal{T}}(x_1,x_2,x_3,x_4;n) = \frac{\sigma_4}{\beta^2\,\omega^4\,(\omega+1)} \Big[& \sigma_1\sigma_3\left[A_2\sigma_1\sigma_3 + A_6\sigma_4 + A_7\sigma_2^2\right] + \sigma_2^2\left[A_1\sigma_2^2 + A_5\sigma_4\right] + \\ & + A_3\left(\sigma_1^2\sigma_4 + \sigma_3^2\right)\sigma_2 + A_4\sigma_4^2 \Big]\,, \end{aligned} \tag{5.189}$$

with coefficients

$$\begin{aligned} A_1 &= \beta^2\omega^4\,(\omega+1)\,,\\ A_2 &= \beta\,\omega^3\,(\omega+1)\,(\beta+\omega+1)\,(\beta\omega+\beta+\omega)\,,\\ A_3 &= -\beta\,\omega^2\left(\omega^2+\omega+1\right)(\beta\omega-1)\left(\beta-\omega^2\right),\\ A_4 &= (\omega+1)\left(\omega^2+1\right)^2\left(\beta^2+\beta\omega+\beta+\omega^2+\omega+1\right)\left(\left(\beta^2+\beta+1\right)\omega^2+\beta^2+(\beta+1)\beta\omega\right), \end{aligned}$$

$$\begin{aligned}
A_5 &= \omega^2\left(\omega+1\right)\Big(\beta^4\omega+\beta^3\left(\omega+1\right)^3-\beta^2\left(\omega^2-4\,\omega+1\right)\left(\omega^2+\omega+1\right)+\beta\omega\left(\omega+1\right)^3+\omega^3\Big)\,,\\
A_6 &= -\left(\left(\omega+1\right)\omega^2\left(\beta^2+\beta\omega+\beta+\omega^2+\omega+1\right)\left(\left(\beta^2+\beta+1\right)\omega^2+\beta^2+\left(\beta+1\right)\beta\omega\right)\right)+\\
&\qquad-\beta\left(\omega+1\right)\left(\omega^2+1\right)^2\omega\left(\beta+\omega+1\right)\left(\beta\omega+\beta+\omega\right),\\
A_7 &= -\beta\,\omega^3\left(\beta^2\omega+\beta\left(\omega+1\right)\left(\omega^2+3\,\omega+1\right)+\omega^2\right),
\end{aligned} \tag{5.190}$$

where $\beta=e^{\frac{\mathrm{i}\pi B}{2n}}$ and B is defined in terms of the sinh-Gordon coupling as in Eq. (5.91).

5.B.2 Form factors of the $\mathbb{Z}_2$-composite BPTF

As we mentioned in the main text, differently from the four-particle form factor of the standard twist field $\mathcal{T}_n$, in the sinh-Gordon model the one of the composite field $\mathcal{T}_n^{\mu}$ was not previously known in the literature. In this appendix we compute this form factor by constructing and solving the bootstrap equations, in full analogy to what we have done in Sec. 5.4 and in Sec. 5.A.2 in the case of the massless flow.

The minimal form factors f^{μ}_{ShG} of the composite twist field have been obtained in the main text in Eq. (5.95) by multiplying the standard minimal form factor (5.94) by the monodromy changing factor $2\cosh(\theta/2n)$. Using this result, we parameterise the form factor in the usual way, as reported in Eq. (5.93)

$$F_k^{\mathcal{T}^{\mu}|1\ldots1}(\theta_1,\ldots,\theta_k)=H_k^{\mathcal{T}^{\mu}}\,Q_k^{\mathcal{T}^{\mu}}(x_1,\ldots,x_k)\prod_{1\leqslant i<j\leqslant k}\frac{f^{\mu}_{\mathrm{ShG}}(\theta_i-\theta_j;n)}{\left(x_i-\omega x_j\right)\left(x_j-\omega x_i\right)}. \tag{5.191}$$

Recall however that, as we discussed below Eq. (5.75), for the composite twist field the function $Q_k^{\mathcal{T}^{\mu}}$ appearing in the ansatz (5.191) is not guaranteed to be a polynomial but is in general a rational function. In the following, we will find it convenient to explicitly extract the denominator of the function $Q_k^{\mathcal{T}^{\mu}}$ by defining

$$\widetilde{Q}_k^{\mathcal{T}^{\mu}}(x_1,\ldots,x_k)=\frac{Q_k^{\mathcal{T}^{\mu}}(x_1,\ldots,x_k)}{\prod_{1\leqslant i<j\leqslant k}\left(x_i+x_j\right)}\,. \tag{5.192}$$

As we will see, extracting this factor is sufficient to guarantee that $\widetilde{Q}_k^{\mathcal{T}^{\mu}}$ is indeed a polynomial. We stress that the denominator (x_i+x_j) does not introduce additional poles, as its zeroes exactly cancel out with those of the monodromy changing factor in f^{μ}_{ShG}. Plugging the polynomial (5.192) in the ansatz (5.191), the form factor is alternatively parameterised as

$$F_k^{\mathcal{T}^{\mu}|1\ldots1}(\theta_1,\ldots,\theta_k)=H_k^{\mathcal{T}^{\mu}}\,\widetilde{Q}_k^{\mathcal{T}^{\mu}}(x_1,\ldots,x_k)\prod_{1\leqslant i<j\leqslant k}\frac{f^{\mu}_{\mathrm{ShG}}(\theta_i-\theta_j;n)}{\left(x_i+x_j\right)\left(x_i-\omega x_j\right)\left(x_j-\omega x_i\right)}\,. \tag{5.193}$$

Before moving to the actual computation, we present a useful identity of the minimal form factor. It is known that the standard minimal form factor f_{ShG} in the sinh-Gordon theory satisfies the identity [188]

$$f_{\rm ShG}(\theta_0+{\rm i}\pi-\theta_i;n)\,f_{\rm ShG}(\theta_0-\theta_i;n)=\frac{(x_0-x_i)\,(\omega x_0-x_i)}{(\beta x_0-x_i)\,(\omega\beta^{-1}x_0-x_i)}\,, \tag{5.194}$$

where $\beta=e^{\frac{{\rm i}\pi B}{2n}}$ and B is related to the sinh-Gordon coupling through Eq. (5.91). In order to extend this relation to the composite minimal form factor, notice that for the monodromy changing factor we have

$$2\cosh\!\left(\frac{\theta_0+{\rm i}\pi-\theta_i}{2n}\right)2\cosh\!\left(\frac{\theta_0-\theta_i}{2n}\right)=\frac{\omega x_0+x_i}{(\omega x_0x_i)^{1/2}}\frac{x_0+x_i}{(x_0x_i)^{1/2}}=\frac{(x_0+x_i)\,(\omega x_0+x_i)}{\omega^{1/2}x_0x_i}\,, \tag{5.195}$$

which from the definition of $f^{\mu}_{\rm ShG}$ in Eq. (5.72) directly implies

$$f^{\mu}_{\rm ShG}(\theta_0+{\rm i}\pi-\theta_i;n)\,f^{\mu}_{\rm ShG}(\theta_0-\theta_i;n)=\frac{\left(x_0^2-x_i^2\right)\left(\omega^2x_0^2-x_i^2\right)}{\omega^{1/2}x_0x_i\,(\beta x_0-x_i)\,(\omega\beta^{-1}x_0-x_i)}\,. \tag{5.196}$$

We now have everything we need to write the bootstrap equation. For simplicity we consider all particles on the first replica and we apply the kinematic residue axiom of Eq. (5.64) to the modified ansatz (5.193). Setting the first rapidity equal to $\theta_{-1}={\rm i}\pi+\theta_0$, the residue of the denominator (including the additional factor (x_i+x_j)) becomes

$$\begin{aligned}
&-{\rm i}\underset{\theta_{-1}=i\pi+\theta_0}{\rm Res}\prod_{-1\leqslant i<j\leqslant k}\frac{1}{(x_i-\omega x_j)\,(x_j-\omega x_i)\,(x_i+x_j)}\\
&=-{\rm i}\prod_{1\leqslant i<j\leqslant k}\frac{1}{(x_i-\omega x_j)\,(x_j-\omega x_i)\,(x_i+x_j)}\times\\
&\quad\times\left(-\frac{n\,x_0^{-3}}{\omega(\omega^2-1)(\omega+1)}\right)\left[\omega^k\prod_{i=1}^{k}(x_0-\omega x_i)\left(x_i^2-\omega^2x_0^2\right)\left(x_0^2-x_i^2\right)\left(x_i-\omega^2x_0\right)\right]^{-1}\\
&=\prod_{1\leqslant i<j\leqslant k}\frac{1}{(x_i-\omega x_j)\,(x_j-\omega x_i)\,(x_i+x_j)}\times\\
&\quad\times\frac{n\,x_0^{-3}\,\omega^{-(k+2)}}{2\,(\omega+1)\sin\frac{\pi}{n}}\left[\prod_{i=1}^{k}(x_0-\omega x_i)\left(x_i^2-\omega^2x_0^2\right)\left(x_0^2-x_i^2\right)\left(x_i-\omega^2x_0\right)\right]^{-1}.
\end{aligned} \tag{5.197}$$

Using this residue, the ansatz (5.193) for the $(k+2)$-particle form factor reduces to

$$\begin{aligned}
&-{\rm i}\underset{\theta_{-1}={\rm i}\pi+\theta_0}{\rm Res}F_{k+2}^{\mathcal{T}^{\mu}|1\ldots}(\theta_{-1},\theta_0,\theta_1,\ldots)=\\
&=H_{k+2}^{\mathcal{T}^{\mu}}\widetilde{Q}_{k+2}^{\mathcal{T}^{\mu}}(\omega x_0,x_0,x_1,\ldots)\prod_{1\leqslant i<j\leqslant k}\frac{f^{\mu}_{\rm ShG}(\theta_i-\theta_j;n)}{(x_i-\omega x_j)\,(x_j-\omega x_i)\,(x_i+x_j)}\times\\
&\quad\times\frac{n\,x_0^{-3}\,f^{\mu}_{\rm ShG}({\rm i}\pi;n)}{2\,\omega^{k+2}\,(\omega+1)\sin\frac{\pi}{n}}\left[\prod_{i=1}^{k}\frac{f^{\mu}_{\rm ShG}(\theta_0+{\rm i}\pi-\theta_i;n)\,f^{\mu}_{\rm ShG}(\theta_0-\theta_i;n)}{(x_0-\omega x_i)\left(x_i^2-\omega^2x_0^2\right)\left(x_0^2-x_i^2\right)\left(x_i-\omega^2x_0\right)}\right]
\end{aligned}$$

$$
\begin{aligned}
&= H_{k+2}^{\mathcal{T}^\mu}\widetilde{Q}_{k+2}^{\mathcal{T}^\mu}(\omega x_0, x_0, x_1,\ldots)\prod_{1\leqslant i<j\leqslant k}\frac{f^\mu_{\mathrm{ShG}}(\theta_i-\theta_j;n)}{(x_i-\omega x_j)\,(x_j-\omega x_i)\,(x_i+x_j)}\times\\
&\quad\times\frac{n\,f^\mu_{\mathrm{ShG}}(\mathrm{i}\pi;n)}{2\,\omega^{k+2}\,(\omega+1)\sin\frac{\pi}{n}}\left[x_0^{k+3}\omega^{k/2}\prod_{i=1}^{k}x_i\left(x_i-\omega^2x_0\right)(x_0-\omega x_i)\left(x_i-\omega\beta^{-1}x_0\right)(\beta x_0-x_i)\right]^{-1}.
\end{aligned}
\tag{5.198}
$$

where we have applied the identity in Eq. (5.196). Following the residue axiom in Eq. (5.64), we compare the residue in Eq. (5.198) with the ansatz (5.193) for k-particles, extracting immediately the recursion relation for the normalisation

$$
H_{k+2}^{\mathcal{T}^\mu}=\frac{2\,\omega^{k+2}\,(\omega+1)\sin\frac{\pi}{n}}{n\,f^\mu_{\mathrm{ShG}}(\mathrm{i}\pi;n)}\,H_k^{\mathcal{T}^\mu}\,,
\tag{5.199}
$$

which, using $H_0^{\mathcal{T}^\mu}=\langle\mathcal{T}_n^\mu\rangle$, is solved as

$$
H_k^{\mathcal{T}^\mu}=\left(\frac{2\,(\omega+1)\sin\frac{\pi}{n}}{n\,f^\mu_{\mathrm{ShG}}(\mathrm{i}\pi;n)}\right)^{\frac{k}{2}}\omega^{\frac{k}{2}\left(\frac{k}{2}+1\right)}\,\langle\mathcal{T}_n^\mu\rangle\,.
\tag{5.200}
$$

The recursion relation for the polynomial $\widetilde{Q}_k^{\mathcal{T}^\mu}$ instead takes the form

$$
\widetilde{Q}_{k+2}^{\mathcal{T}^\mu}(\omega x_0,x_0,x_1,\ldots,x_k)=\widetilde{P}_k(x_0,x_1,\ldots,x_k)\,\widetilde{Q}_k^{\mathcal{T}^\mu}(x_1,\ldots,x_k)\,,
\tag{5.201}
$$

with the polynomial

$$
\begin{aligned}
\widetilde{P}_k(x_0,x_1,\ldots,x_k)&=x_0^{k+3}\omega^{k/2}\prod_{a,b,c,d,i=1}^{k}x_i\left(x_a-\omega^2x_0\right)(x_0-\omega x_b)\left(x_c-\omega\beta^{-1}x_0\right)(\beta x_0-x_d)\\
&=x_0^{k+3}\omega^{\frac{3}{2}k}\,\sigma_k\sum_{a,b,c,d=1}^{k}\left(-\omega^2x_0\right)^{k-a}\left(-\omega^{-1}x_0\right)^{k-b}\left(-\omega\beta^{-1}x_0\right)^{k-c}\left(-\beta x_0\right)^{k-d}\sigma_a\,\sigma_b\,\sigma_c\,\sigma_d\,,
\end{aligned}
\tag{5.202}
$$

where σ_j are the fully symmetric polynomials of degree j in k variables and again we have $\beta=e^{\frac{\mathrm{i}\pi B}{2n}}$.

In order to solve the recursion equation in Eq. (5.201) for the four-particle form factor, we need to first rewrite the known two-particle form factor in Eq. (5.99) in the form of our ansatz (5.191), (5.193)

$$
\begin{aligned}
F_2^{\mathcal{T}^\mu|11}(\theta_i-\theta_j)&=\frac{\langle\mathcal{T}^\mu\rangle\sin\frac{\pi}{n}}{2n\sinh\!\left(\frac{\mathrm{i}\pi+\theta_i-\theta_j}{2n}\right)\sinh\!\left(\frac{\mathrm{i}\pi-\theta_i+\theta_j}{2n}\right)}\frac{f^\mu_{\mathrm{ShG}}(\theta_i-\theta_j;n)}{f^\mu_{\mathrm{ShG}}(\mathrm{i}\pi;n)}\\
&=\langle\mathcal{T}_n^\mu\rangle\frac{2\,\omega^2\,(\omega+1)\sin\frac{\pi}{n}}{nf^\mu_{\mathrm{ShG}}(\mathrm{i}\pi;n)}\,\frac{x_ix_j}{\omega\,(\omega+1)}\,\frac{f^\mu_{\mathrm{ShG}}(\theta_i-\theta_j;n)}{(x_i-\omega x_j)(x_j-\omega x_i)}\,,
\end{aligned}
\tag{5.203}
$$

which in agreement with Eq. (5.200) has to be divided as

$$H_2^{\mathcal{T}^\mu} = \frac{2\,\omega^2\,(\omega+1)\sin\frac{\pi}{n}}{n f^{\mu}_{\mathrm{ShG}}(\mathrm{i}\pi;n)}\langle\mathcal{T}^\mu_n\rangle, \tag{5.204}$$

$$Q_2^{\mathcal{T}^\mu}(x_1,x_2) = \frac{x_i x_j}{\omega\,(\omega+1)} = \frac{\sigma_2}{\omega\,(\omega+1)}\,, \quad \widetilde{Q}_2^{\mathcal{T}^\mu}(x_1,x_2) = (x_i+x_j)\,Q_2^{\mathcal{T}^\mu}(x_1,x_2) = \frac{\sigma_1\sigma_2}{\omega\,(\omega+1)}\,, \tag{5.205}$$

where σ_1, σ_2 are the fully symmetric polynomials in two variables. Notice that the polynomial $\widetilde{Q}_2^{\mathcal{T}^\mu}$ has total degree 3 and partial degree 2 in each variable. Since the polynomial $\widetilde{P}_k$ in the recursion equation Eq. (5.201) has partial degree 5 for any number of particles, this implies that $\widetilde{Q}_k^{\mathcal{T}^\mu}$ at the k-particle order has partial degree $\frac{5}{2}k-3$.

Assuming that the solution of Eq. (5.201) is completely symmetrical in the variables x_i, it is in general not unique since one can always add a kernel solution, i.e., a solution of the homogeneous equation

$$\widetilde{Q}_{k+2}^{\mathcal{T}^\mu}(\omega x_0, x_0, x_1, \ldots, x_k) = 0. \tag{5.206}$$

However, imposing that the polynomial has maximum partial degree $\frac{5}{2}k-3$ in each variable, for $k=2$ the kernel equation (5.206) has no solutions and the solution to the recursion equation Eq. (5.201) is actually unique. We finally find the result

$$\begin{aligned}\widetilde{Q}_4^{\mathcal{T}^\mu}(x_1,x_2,x_3,x_4) = \frac{\sigma_4^2}{\beta^2\omega^4(\omega+1)^2}\Big[&\sigma_1\sigma_3\left[B_1\sigma_2^3 + B_2\sigma_1\sigma_2\sigma_3 + B_5\left(\sigma_1^2\sigma_4+\sigma_3^2\right) + B_8\sigma_2\sigma_4\right] + \\ &+ \sigma_2^2\left[B_3\sigma_2\sigma_4 + B_4\left(\sigma_1^2\sigma_4+\sigma_3^2\right)\right] + \sigma_4\left[B_6\sigma_2\sigma_4 + B_7\left(\sigma_1^2\sigma_4+\sigma_3^2\right)\right]\Big],\end{aligned} \tag{5.207}$$

$$Q_4^{\mathcal{T}^\mu}(x_1,x_2,x_3,x_4) = \frac{\widetilde{Q}_4^{\mathcal{T}^\mu}(x_1,x_2,x_3,x_4)}{\prod_{1\leqslant i<j\leqslant 4}(x_i+x_j)}\,, \tag{5.208}$$

where the coefficients are

$$\begin{aligned}
B_1 &= \beta^2\omega^4, \\
B_2 &= -\beta^2\omega^3\left(\omega^2+\omega+1\right), \\
B_3 &= \beta\omega^2\,(\beta+1)\,(\omega+1)^3\,(\beta+\omega)\,, \\
B_4 &= -\beta\omega^3\,(\beta+\omega+1)\,(\beta\omega+\beta+\omega)\,, \\
B_5 &= \beta\omega^2\left(\omega^2+\omega+1\right)(\beta+\omega+1)\,(\beta\omega+\beta+\omega)\,, \\
B_6 &= (\beta+1)\,(\omega+1)^3\left(\omega^2+1\right)(\beta+\omega)\left(\beta^2+(\beta+1)^2\omega+\omega^2\right), \\
B_7 &= -\omega\left(\omega^2+\omega+1\right)\left(\beta^2+\beta\omega+\beta+\omega^2+\omega+1\right)\times \\
&\qquad\times\left(\left(\beta^2+\beta+1\right)\omega^2+\beta^2+(\beta+1)\beta\omega\right),
\end{aligned} \tag{5.209}$$

$$
\begin{aligned}
B_8 = -\omega \Big(& \beta^3 + \beta\omega^6 + \beta\omega^5\left(\beta^2+5\beta+5\right) + \omega^4\left(5\beta^3+9\beta^2+6\beta-1\right) + \\
& + 2\,\beta\omega^3\left(3\beta^2+5\beta+3\right) + \beta\omega^2\left(9\beta-\beta^3+6\beta^2+5\right) + \beta\omega\left(5\beta^2+5\beta+1\right) \Big) .
\end{aligned}
$$

Plugging the function $Q_4^{\mathcal{T}^\mu}$ in Eqs. (5.207)-(5.209) and the normalisation $H_4^{\mathcal{T}^\mu}$ from Eq. (5.200) in the ansatz (5.191) we finally obtain the four-particle form factor for the composite twist field that we used in Sec. 5.5.2.

5.C Cumulant expansion of the entanglement entropy in the massive Ising theory

In this appendix, we review the known results for the form factor expansion of the entanglement entropy in the massive Ising model, obtained in Refs. [192]. In particular, we find a direct relation between UV limit of the cumulant expansion of the entropy in the massive Ising and the non-interacting part of the expansion in the massless flow, studied in Sec. 5.6.2.

In the massive Ising theory, if we denote by m the mass gap, the ground state Rényi entanglement entropy admits the following cumulant expansion [192],

$$
S_n^{\text{Ising}}(m\ell) \approx \frac{1}{1-n} \sum_{k \text{ even}} c^{\mathcal{T}}_{k,\text{ Ising}}(m\ell;n) + \text{const}, \tag{5.210}
$$

where

$$
c^{\mathcal{T}}_{k,\text{ Ising}}(m\ell;n) = \sum_{j_1,\dots,j_k=1}^{n} \int_{-\infty}^{+\infty} \frac{\prod_{i=1}^{k} \mathrm{d}\theta_i}{k!\,(2\pi)^k}\, f^{\mathcal{T}|j_1\dots j_k}_{k,\text{ Ising}}(\theta_1,\dots,\theta_k;n)\, e^{-m\ell\sum_i \cosh\theta_i}. \tag{5.211}
$$

These cumulants can be reexpressed as in Eq. (5.129) and, therefore, the k-particle cumulant $c^{\mathcal{T}}_{k,\text{ Ising}}$ is similar to the k-right- or k-left-mover non-interacting cumulants $c^{\mathcal{T}}_{k,0}$, $c^{\mathcal{T}}_{0,k}$ in the massless flow (5.125), differing only in the energy E in the exponential factor. In the massive Ising theory, the energy of k particles is

$$
E(\theta_1,\dots,\theta_k) = \sum_{i=1}^{k} m\cosh(\theta_i)\,. \tag{5.212}
$$

If we move to the center-of-mass coordinates, $A = \frac{1}{k}\sum_i \theta_i$ and $\theta_{ij} = \theta_i - \theta_j$, then the energy (5.212) takes the form

$$
\begin{aligned}
E(\theta_1,\dots,\theta_k) &= m\sum_{j=1}^{k}\cosh\theta_j = m\sum_{j=1}^{k}\cosh(\theta_j + A - A) = \\
&= m\left[\cosh A\left(\sum_{j=1}^{k}\cosh\xi_j(\theta_{12},\dots,\theta_{k-1,k})\right) + \sinh A\left(\sum_{j=1}^{k}\sinh\xi_j(\theta_{12},\dots,\theta_{k-1,k})\right)\right].
\end{aligned} \tag{5.213}
$$

Let us first analyse the two-particle cumulant $c^{\mathcal{T}}_{2,\,\mathrm{Ising}}$. In a massive theory, the exponential $e^{-\ell E}$ is responsible for a double exponential suppression in both the $\theta \to \infty$ and $\theta \to -\infty$ regimes, ensuring the convergence of the integrals. For two particles, in particular, after changing coordinates to the relative $\theta_{12} = \theta_1 - \theta_2$ and center-of-mass rapidities $A = (\theta_1 + \theta_2)/2$, we can integrate out the center-of-mass rapidity obtaining [188, 190, 192, 193]

$$\begin{aligned} c^{\mathcal{T}}_{2,\,\mathrm{Ising}}(m\ell; n) &= \frac{n}{2\,(2\pi)^2} \sum_{j_2} \int_{-\infty}^{+\infty} \mathrm{d}\theta_{12}\, f_2^{\mathcal{T}|1j_2}(\theta_{12}; n) \int_{-\infty}^{+\infty} \mathrm{d}A\, e^{-2m\ell \cosh A \cosh \frac{\theta_{12}}{2}} \\ &= \frac{n}{2\,(2\pi)^2} \sum_{j_2} \int_{-\infty}^{+\infty} \mathrm{d}\theta_{12}\, f_2^{\mathcal{T}|1j_2}(\theta_{12}; n)\, 2K_0(2m\ell \cosh(\theta_{12}/2))\,. \end{aligned} \tag{5.214}$$

As shown in Ref. [188], in the UV limit $m\ell \ll 1$, the expansion of the Bessel function K_0

$$K_0(x) \underset{x \ll 1}{\approx} -\log\frac{x}{2} - \gamma + \mathcal{O}\big(x^2\big)\,, \tag{5.215}$$

reproduces the expected UV logarithmic behaviour of the entanglement entropy up to an additive constant [188]

$$c^{\mathcal{T}}_{2,\,\mathrm{Ising}}(m\ell; n) \underset{m\ell \ll 1}{\approx} -z_2(n) \log m\ell + \mathrm{const}, \tag{5.216}$$

where the function $z_2(n)$ was introduced in Eq. (5.135).

We can now investigate the higher-particle cumulants $c^{\mathcal{T}}_{k,\,\mathrm{Ising}}$. If we write them in terms of the center-of-mass coordinates, we can apply the integral identity

$$\int_{-\infty}^{+\infty} \mathrm{d}t\, \exp\big\{ - C\cosh t - S \sinh t \big\} = 2K_0\Big(\sqrt{C^2 - S^2}\Big)\,, \tag{5.217}$$

and the fact that the form factors only depend on the relative rapidities to integrate out the center-of-mass rapidity A. We then obtain

$$\begin{aligned} c^{\mathcal{T}}_{k,\,\mathrm{Ising}}(m\ell; n) &= \frac{n}{k!\,(2\pi)^k} \sum_{j} \int_{-\infty}^{+\infty} \prod_{j=1}^{k-1} \mathrm{d}\theta_{j,j+1}\, f_k^{\mathcal{T}}(\theta_{12}, \ldots; n) \int_{-\infty}^{+\infty} \mathrm{d}A\, e^{-m\ell\,(C\cosh A + S \sinh A)} \\ &= \frac{2n}{k!\,(2\pi)^k} \sum_{j} \int_{-\infty}^{+\infty} \prod_{j=1}^{k-1} \mathrm{d}\theta_{j,j+1}\, f_k^{\mathcal{T}}(\theta_{12}, \ldots; n)\; K_0\Big(m\ell\sqrt{C^2 - S^2}\Big)\,, \end{aligned} \tag{5.218}$$

where

$$C(\theta_{12}, \ldots) = \sum_{j=1}^{k} \cosh(\xi_j(\theta_{12}, \ldots))\,, \quad S(\theta_{12}, \ldots) = \sum_{j=1}^{k} \sinh(\xi_j(\theta_{12}, \ldots))\,, \tag{5.219}$$

and ξ_j are defined in Eq. (5.136). In the UV limit $m\ell \ll 1$, by expanding the Bessel function using Eq. (5.215), we get at leading order the logarithmic behaviour of the entropy expected in the Ising CFT up to an additive constant

$$c^{\mathcal{T}}_{k,\,\text{Ising}}(m\ell; n) \underset{m\ell \ll 1}{\approx} -z_k(n)\,\log(m\ell) + \text{const}, \tag{5.220}$$

where the coefficient z_k is the same as in Eq. (5.140). Comparing Eq. (5.220) with the analogous formula in Eq. (5.139), we can immediately see that the UV limit of the k-particle massive Ising cumulants is twice the k-right-mover cumulants of our massless flow. Notice that the factor 2 comes from the expansion of the Bessel function and ultimately its origin is the difference in the energy of the two models.

Before concluding this appendix, let us make a remark on the computation of the coefficients $z_k(n)$. The expression in Eq. (5.140) contains $k-1$ integrals and, therefore, it is not practical for numerical calculations. In Ref. [192], the analytic continuation of Eq. (5.140) was carried out for $n \geqslant 1$ replicas, writing $z_k(n)$ as a single integral for any k (see also [198, 268])

$$z_k(n) = \frac{2n}{k\,(4\pi)^k} \int_0^\infty \mathrm{d}x\, \mathcal{J}_k(x)^2\, \mathcal{W}_k(x;n)\,, \tag{5.221}$$

where, for $k = 2p$,

$$\mathcal{J}_{2p}(x) = \frac{(2\pi)^{p-1}}{(p-1)!} \begin{cases} \frac{x}{\pi}\frac{1}{\sinh\left(\frac{x}{2}\right)} \prod_{j=1}^{\frac{p}{2}-1} \left(\frac{x^2}{\pi^2} + (2j)^2\right), & \text{for } p \text{ even}, \\ \frac{1}{\cosh\left(\frac{x}{2}\right)} \prod_{j=1}^{\frac{p-1}{2}} \left(\frac{x^2}{\pi^2} + (2j-1)^2\right), & \text{for } p \text{ odd}, \end{cases} \tag{5.222}$$

$$\mathcal{W}_{2p}(x;n) = (-1)^p\,\mathrm{i}\,\sinh(x) \sum_{j=1}^{p} \binom{2p-1}{p-j} \left[w(2x + (2j-1)\,\mathrm{i}\,\pi; n) + w(2x - (2j-1)\,\mathrm{i}\,\pi; n)\right], \tag{5.223}$$

and $w(\theta; n)$ is given in Eq. (5.130). Eq. (5.221) is efficient for numerical calculations. We employed it to compute the first 30 non-interacting cumulants in the truncated expansion of the entropies of the massless flow plotted in Fig. 5.3.

Part III

Entanglement dynamics in out-of-equilibrium quantum systems

Chapter 6

Entanglement Hamiltonian during a domain wall melting in the free Fermi chain

The topic of this last part of the thesis will be the out-of-equilibrium properties of quantum integrable models in one spatial dimension [270, 271]. This field has seen a tremendous progress in the last decade, thanks in large part to the idea of reducing complicated many-body quantum models on the lattice to an effective field theory having the same properties in the low energy regime, thus unveiling some universal aspects of the quantum fluids [272–275]. In this way, it has been possible to characterise the large-distance behaviour of correlation functions [274–277] and the entanglement [18, 22] of a large class of equilibrium homogeneous quantum systems. The extension to non-homogeneous one has been made possible by the recent observation that their low energy regime is described by an effective field theory in curved space-time [85, 278–284]. Roughly in parallel, the dynamical problem was also studied with the goal of completing such asymptotic approach with a quantum hydrodynamic theory. Thanks to the re-quantisation of the semi-classical evolution established by the generalised hydrodynamics [285, 286], it has been possible to obtain promising results for the large-scale dynamics of the entanglement entropy [287–291] and to reproduce the numerical data obtained for the microscopic models with an impressive precision.

The present Chapter, based on Ref. [141], fits in this context with the goal of extending the hydrodynamic approach to the calculation of the entanglement Hamiltonian (1.11). We present an analysis of the entanglement Hamiltonian K_A for the prototypical setting of a free Fermi lattice gas initially prepared in a domain wall configuration $|\Psi_0\rangle \sim |\bullet \cdots \bullet \circ \cdots \circ\rangle$ and subsequently let to freely expand. This problem has been thoroughly studied in the literature, both with lattice techniques e.g. [292–299] and in the field theory regime e.g. [85, 278, 289, 290, 300–302]. In particular, it was one of the first models for which a semi-classical hydrodynamics has been formulated in the modern language [292, 298], the first non-equilibrium setting for which the entanglement dynamics has been computed via quantum hydrodynamics [85], and one of the extremely rare cases for which a non-equilibrium CFT description of quantum fluctuations has been formulated [278].

6.1 The model and the quench protocol

We consider a chain of free fermions particles with nearest-neighbour interactions loaded on an infinite one-dimensional lattice $i \in \mathbb{Z}$ and coupled to an external potential V_i, described by the Hamiltonian

$$H = -\frac{1}{2} \sum_{i \in \mathbb{Z}} \left[\left(c_i^\dagger c_{i+1} + c_{i+1}^\dagger c_i \right) + V_i \; c_i^\dagger c_i \right]. \tag{6.1}$$

Here, $c_i^\dagger$ (resp. c_i) denotes the creation (resp. annihilation) operator of lattice spinless fermions satisfying canonical anticommutation relations $\{c_i, c_j^\dagger\} = \delta_{i,j}$. The system is initially prepared in the ground state of the Hamiltonian (6.1) with potential

$$V_i(t \leqslant 0) = \lim_{\Lambda \to \infty} \begin{cases} -\Lambda, & \text{if } i \leqslant 0; \\ \Lambda, & \text{otherwise,} \end{cases} \tag{6.2}$$

which gives rise to the initial configuration

$$|\Psi_0\rangle = \bigotimes_{i \leqslant 0} |1\rangle_i \bigotimes_{i > 0} |0\rangle_i \,, \tag{6.3}$$

where $|\alpha = 0, 1\rangle_i$ are the eigenstates of the number operator $c_i^\dagger c_i$ with eigenvalues $\alpha = 0, 1$. For times $t > 0$, we set $V_i = 0$ and we let the system to evolve unitarily with the hopping Hamiltonian (6.1)

$$|\Psi(t)\rangle = e^{-\mathrm{i}tH} \, |\Psi_0\rangle \,. \tag{6.4}$$

In other words, we investigate a fully-filled gas of hard-core particles initially confined on the left side of an infinite lattice and let to freely expand towards the right vacuum. The product state (6.3) is usually referred to as a *domain wall* and the quench dynamics (6.4) as *domain wall melting*, in reference to the equivalent formulation in terms of the XX spin chain.

Although the non-interacting nature of the underlying problem typically allows for exact lattice calculations, we rather consider its Euler hydrodynamic description where space-time scales $i, t \to \infty$ at fixed ratio i/t. Indeed, employing such a hydrodynamic description not only gives access to asymptotically exact results for conserved quantities [292–299] but it further allows to investigate several non-trivial properties of the model, including correlation functions [279–282] and Rényi entropies [283, 287–290], which are currently not accessible by standard lattice techniques even for the free Fermi gas in such non-homogeneous and non-equilibrium settings. Hence, following this program, the macrostate at $t = 0$ is given by the fermionic occupation function [303, 304]

$$n_0(x,k) = \begin{cases} 1, & \text{if } x \leqslant 0 \text{ and } -\pi \leqslant k \leqslant \pi; \\ 0, & \text{otherwise,} \end{cases} \tag{6.5}$$

as it reproduces, in the hydrodynamic limit, the initial domain wall state of Eq. (6.3) with left part of the system entirely filled with modes $-\pi \leqslant k \leqslant \pi$ and right side left empty. Notice that the lattice site i is now replaced by a continuous variable $x \equiv ia \in \mathbb{R}$, where a is the lattice spacing. At times $t > 0$, the evolution of $n_0(x,k)$ can be deduced from the trajectory of each mode k that propagates independently with constant velocity $v(k) = \sin k$ from its initial position. This hydrodynamic picture leads to the macrostate

$$n_t(x,k) \equiv n_0(x - t\sin k, k) = \begin{cases} 1, & \text{if } k_F^-(x,t) \leqslant k \leqslant k_F^+(x,t); \\ 0, & \text{otherwise,} \end{cases} \tag{6.6}$$

with local Fermi points $k_F^{\pm}(x,t)$ given as solution of the zero-entropy hydrodynamic equation [305]

$$\left(\partial_t + \sin k_F^{\pm} \partial_x\right) k_F^{\pm} = 0. \tag{6.7}$$

More precisely, for a given time $t > 0$ and position $0 \leqslant x \leqslant t$, one finds the Fermi sea

$$\Gamma_t(x) \equiv \left[k_F^-(x,t); k_F^+(x,t)\right] = \left[\arcsin\frac{x}{t}; \pi - \arcsin\frac{x}{t}\right] \tag{6.8}$$

and an analogous treatment applies for $-t \leqslant x < 0$ exploiting the particle-hole symmetry of the problem. The fastest excitations of this setting are the modes $k = \pm\pi/2$ with velocity $v(k = \pm\pi/2) = \pm 1$. These define the *light-cone region* $|x| \leqslant t$ inside which correlations and entanglement spread during the quench dynamics and the particle density shows a non-homogeneous profile [292, 298]

$$\rho(|x| \leqslant t) = \int_{\Gamma_t(x)} \frac{dk}{2\pi} = \frac{1}{\pi}\arccos\frac{x}{t}. \tag{6.9}$$

Outside the light cone, i.e., for $x > t$ (resp. $x < -t$), the system keeps its initial configuration with fermionic density $\rho = 0$ (resp. $\rho = 1$). In Fig. 6.1, we show an illustration of the domain wall state and of the melting dynamics considered in this Chapter.

6.2 Quantum hydrodynamic description

The hydrodynamic theory outlined so far describes the semi-classical evolution in phase space of the free fermions but it does not account for the quantum fluctuations of the expanding gas. As such, it allows us to compute the semi-classical profiles of conserved quantities, but it is not sufficient for the study of entanglement. Since a microscopic derivation of the missing quantum effects is quite demanding, we look for an effective field theory description that is able to capture the relevant quantum processes in the low-energy regime.

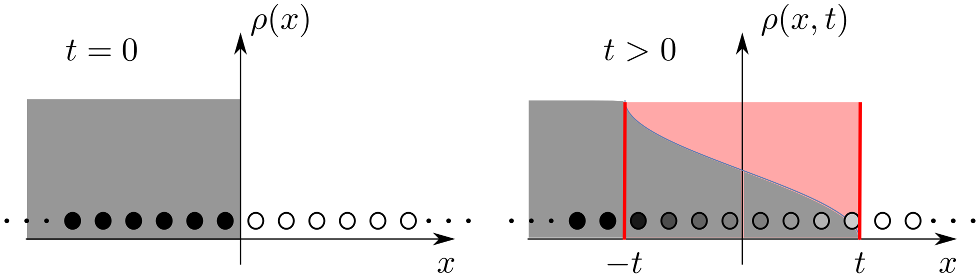

Figure 6.1: Illustration of the domain wall setting. At $t=0$ the system is entirely filled on the l.h.s. and left empty on r.h.s.; the fermionic density is $\rho(x)=\Theta(-x)$. At $t>0$ the domain wall melts inside the light cone region $|x|\leqslant t$ (*light red region*) and the system develops a non-homogeneous density profile given by Eq. (6.9).

6.2.1 Equilibrium description of quantum fluctuations

We first revisit the homogeneous gas at equilibrium, i.e. the ground state of the Hamiltonian (6.1) with $V=0$. In this simple case, the correlation functions at large distances are effectively reproduced by expanding the lattice fermionic operators as [275, 306] (see also Sec. 2.4 in Chapter 2)

$$\frac{c_i}{\sqrt{a}} \sim e^{-\mathrm{i}k_F x}\psi_R(x) + e^{\mathrm{i}k_F x}\psi_L(x), \tag{6.10}$$

where ψ_L (ψ_R) is the left- (right-) moving chiral component of a massless Dirac fermion, whose action in imaginary time τ reads ($z\equiv x+\mathrm{i}\tau$)

$$S=\frac{1}{2\pi}\int\left[\psi_R^\dagger\,\partial_{\bar z}\,\psi_R+\psi_L^\dagger\,\partial_z\,\psi_L\right]\mathrm{d}^2z. \tag{6.11}$$

In the inhomogeneous case $V\neq 0$, the trapped gas is characterised by a spatially-dependent Fermi velocity $v_F(x)=\sin k_F(x)$. As a consequence, the effective field theory description in terms of a massless Dirac fermion requires a non-flat metric with line element [85, 278]

$$\mathrm{d}s^2=\mathrm{d}x^2+v_F^2(x)\mathrm{d}\tau^2. \tag{6.12}$$

It is then useful to find a set of *isothermal coordinates* $z,\bar z$ in terms of which the metric is flat up to a Weyl factor, $\mathrm{d}s^2=e^{2\sigma(z,\bar z)}\mathrm{d}z\mathrm{d}\bar z$ [85]. For the metric in Eq. (6.12), a simple choice is given by

$$z(x,\tau)=\int^x\frac{\mathrm{d}u}{v_F(u)}+\mathrm{i}\tau=\tilde x+\mathrm{i}\tau\,, \tag{6.13}$$

and the Weyl factor is equal to the Fermi velocity $e^{\sigma(x)}=v_F(x)$. Indeed, using isothermal coordinates, the action of the Dirac fermion in curved space takes the simple form

$$S=\frac{1}{2\pi}\int e^{\sigma(z,\bar z)}\left[\psi_R^\dagger\,\partial_{\bar z}\,\psi_R+\psi_L^\dagger\,\partial_z\,\psi_L\right]\mathrm{d}^2z. \tag{6.14}$$

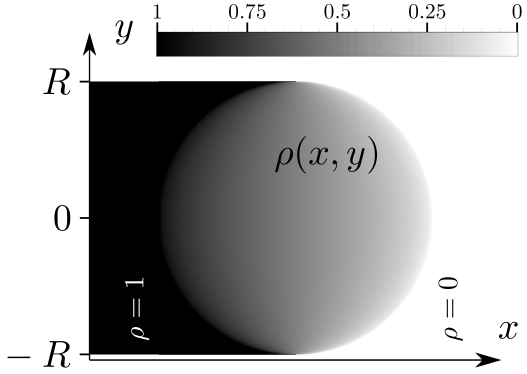

Figure 6.2: Illustration of the fermionic density of Eq. (6.18) in the euclidean strip $\mathscr{S}$: $\rho(x, y)$ takes non-trivial values only inside the disk $x^2 + y^2 \leqslant R^2$, outside which it matches the boundary conditions imposed by the initial domain wall configuration.

Notice that under a Weyl transformation $e^{2\sigma(z,\bar{z})}\mathrm{d}z\mathrm{d}\bar{z} \to \mathrm{d}z\mathrm{d}\bar{z}$ to flat space, a primary field ϕ of scaling dimension Δ transforms as

$$\phi(z, \bar{z}) \to e^{-\Delta\sigma(z,\bar{z})}\phi(z, \bar{z}). \tag{6.15}$$

It is then possible to obtain the asymptotic behaviour of the correlations of primary fields in curved space from the knowledge of those computed in a flat geometry, see e.g. Refs. [279–282]. Another important consequence of the position-dependent Fermi momentum is the phase appearing in the expansion of the lattice fermions in terms of $\psi_{L,R}$ (cf. Eq. (6.10))

$$\frac{c_i}{\sqrt{a}} \sim e^{-\mathrm{i}\varphi^+(x)}\psi_R(x) + e^{-\mathrm{i}\varphi^-(x)}\psi_L(x)\,, \tag{6.16}$$

where $\varphi^{\pm}(x)$ is defined through the position-dependent differential phase

$$\mathrm{d}\varphi^{\pm}(x) = \pm k_F(x)\,\mathrm{d}x\,. \tag{6.17}$$

6.2.2 Effective field theory in the arctic circle

We are now looking for an effective field theory which captures the quantum fluctuations of the domain wall quench problem discussed in Sec. 6.1. Following Refs. [85, 86, 278, 307], we study the non-equilibrium dynamics in imaginary time $y \equiv \mathrm{i}t \in [-R, R]$, introducing a finite width R in the imaginary time direction. Doing so, the original quench problem is mapped in the euclidean strip $\mathscr{S} = \mathbb{R} \times [-R, R] \subset \mathbb{R}^2$, with boundary conditions set to reproduce the initial domain wall configuration. In this geometry, one can show that the fermionic density has a non-trivial profile only inside the disk $x^2 + y^2 \leqslant R^2$, typically referred to as *arctic circle* [278]

$$\rho(x,y) = \begin{cases} 1, & x < -\sqrt{R^2-y^2}; \\ \frac{1}{\pi}\arccos\left(\frac{x}{\sqrt{R^2-y^2}}\right), & |x| \leqslant \sqrt{R^2-y^2}; \\ 0, & x > \sqrt{R^2-y^2}, \end{cases} \tag{6.18}$$

and outside which it matches the boundary conditions imposed by the initial domain wall, see Fig. 6.2 for an illustration. The real time evolution is recovered by first performing an analytic continuation to real time $y \to it$ and then by taking the limit $R \to 0$ [86,307]. With this prescription, Eq. (6.18) reduces to the fermionic density in Eq. (6.9). Inside the strip $\mathscr{S}$, the Fermi points (6.8) become [278]

$$\begin{aligned} k_F^+(x,y) &= z(x,y); \\ k_F^-(x,y) &= -\bar{z}(x,y), \end{aligned} \tag{6.19}$$

where we introduced the coordinate

$$z(x,y) = \arccos\left(\frac{x}{\sqrt{R^2-y^2}}\right) - \mathrm{i}\ \operatorname{arcth}\frac{y}{R}. \tag{6.20}$$

Indeed, performing the continuation to real time $-\mathrm{i}\ \operatorname{arcth}\frac{y}{R} = \arctan\frac{t}{R} \to \frac{\pi}{2}$, thus recovering the real time Fermi points of Eq. (6.8).

We are now ready to investigate the quantum fluctuations around the Fermi points (6.19). Quantum fluctuations take place only inside the arctic circle, which is nothing but the light-cone region $|x| \leqslant t$ in imaginary time. Analogously to the case at equilibrium, the effective field theory for the quench problem is the one of a massless Dirac fermion in curved spacetime, with action given in Eq. (6.14). For this problem, both the metric and the isothermal coordinates were found in Ref. [278]. In particular, the line element is

$$\mathrm{d}s^2 = \mathrm{d}x^2 + \frac{2xy}{R^2-y^2}\mathrm{d}x\ \mathrm{d}y + \frac{R^2-x^2}{R^2-y^2}\ \mathrm{d}y^2, \tag{6.21}$$

for which the isothermal coordinates are given by $(x,y) \to (z,\bar{z})$, with $z(x,y)$ defined in Eq. (6.20). In real time, this set of coordinates corresponds to the parametrisation of the right and left movers with their Fermi points. One can verify that, in terms of these coordinates, the metric (6.21) becomes proportional to the flat one

$$\mathrm{d}s^2 = e^{2\sigma(x,y)}\mathrm{d}z\ \mathrm{d}\bar{z} \tag{6.22}$$

with Weyl factor

$$e^{\sigma(x,y)} = \sqrt{R^2-y^2-x^2}. \tag{6.23}$$

For later purposes, we mention that the time evolved fermionic operator $c_i(t)$ picks up a space-time dependent semi-classical phase $\varphi_\pm(x,t)$ (similarly to Eq. (6.16)), defined through the differential [85, 282]

$$\mathrm{d}\varphi_\pm(x,t) = k_F^\pm(x,t)\ \mathrm{d}x - \varepsilon(k_F^\pm(x,t),x)\ \mathrm{d}t. \tag{6.24}$$

We remark that the knowledge of such non-equilibrium effective field theory in a curved space-time and, particularly, its reduction to a conformally flat one is a highly non-trivial result. To our best knowledge, the domain wall melting and the dynamics of the Tonks-Girardeau gas in a time-dependent harmonic trap (see Ref. [282, 308–313]) are the only two out-of-equilibrium inhomogeneous cases for which an isothermal set of coordinates has been found [278,282]. In more general situations, one can construct an effective field theory for the initial non-homogeneous state following the procedure outlined in Sec. 6.2.1 and determine the dynamics of the quantum fluctuations using quantum generalised hydrodynamics, see e.g. [287–290].

We also mention that this description has been used in Ref. [85] to calculate the entanglement entropy with the twist field approach [18, 22, 188], which we reviewed in Chapter 5. In the following, we will consider instead the annulus method [34, 140] that will allow us to derive exact asymptotic results for the entanglement Hamiltonian, alongside recovering the known results for the entanglement entropies.

6.3 Calculation of the entanglement Hamiltonian

We now move to the analysis of the entanglement spreading during the melting dynamics. As anticipated, although this problem has been already fully characterised in Ref. [85], we shall present in the following an alternative derivation that also allows us to derive an asymptotically exact prediction for the entanglement Hamiltonian.

6.3.1 The annulus method

In Refs. [34,35], it has been shown that it is possible to study the entanglement of $2d$ boundary conformal field theories by mapping the original geometry into an *annulus*. Furthermore, with the help of the Weyl transformation discussed in Sec. 6.2, this method has been applied also to non-homogeneous systems [140]. In the following, we wish to extend this procedure to non-equilibrium inhomogeneous settings, building on some preliminary considerations put forward in Refs. [34, 140]. We shall briefly review the annulus method before considering the specific case of a domain wall melting.

Let us consider a $2d$ boundary conformal field theory defined on a geometry $(x,y) \in \mathscr{G} \subset \mathbb{R}^2$. We further consider a cutting point (x_0, y_0) and we investigate the entanglement in the subsystem A between the position x_0 and the boundary of $\mathscr{G}$. Following Ref. [20, 21, 34, 35], we introduce a UV regularization of the theory by removing a small circle of radius 2ϵ around

(x_0, y_0) and we map the resulting geometry (which has the topology of a finite cylinder) into an annulus with a conformal transformation $z(x,y) \to w(z)$. The latter may be viewed as a rectangle of width $\mathcal{W}_A$ in the real direction and length 2π in the imaginary one with the identification $\mathrm{Im}\, w + 2\pi \equiv \mathrm{Im}\, w$. Once the mapping from the original geometry $\mathscr{G}$ to the annulus is performed, the entanglement Hamiltonian is obtained as the generator of translations in the imaginary direction [34, 140]

$$K_A \equiv \int_{v=\mathrm{cst}} T_{vv}\ \mathrm{d}u = \int_{w(A)} T_R(w)\ \mathrm{d}w + \int_{\bar{w}(A)} T_L(\bar{w})\ \mathrm{d}\bar{w}, \tag{6.25}$$

where $w = u + \mathrm{i}v$ are the coordinates of the annulus, T_L (T_R) are the chiral components of T and $w(A)$ is the image of the subsystem A. In other words, it is sufficient to find an inverse map from the annulus back to $\mathscr{G}$ (for us, the arctic circle) to obtain the entanglement Hamiltonian using Eq. (6.25). Since the Rényi entropy (1.7) in terms of K_A is

$$S^{(n)} = \frac{1}{1-n} \log \mathrm{Tr}\, e^{-2\pi n K_A}, \tag{6.26}$$

it is just related to the width $\mathcal{W}_A$ as [34, 35, 140]

$$S^{(n)} = \frac{c}{12}\frac{n+1}{n}\mathcal{W}_A, \tag{6.27}$$

where c is the central charge of the conformal field theory, $c = 1$ for the free Fermi gas. Notice that the aforementioned UV regularisation enters in $S^{(n)}$ only through $\mathcal{W}_A$. The exact expression of the UV cut-off appearing in Eq. (6.27) cannot be found within the field theory framework but requires exact lattice calculations, e.g. based on the Fisher-Hartwig conjecture, see [314, 315] and Sec. 6.3.2 below. In particular, in homogeneous systems such non-universal term would simply amount to an additive constant while, in non-homogeneous cases, it carries a non-trivial spatial dependence [85].

We now apply the annulus method to the domain wall melting problem. We set the imaginary time to a value y_0 such that $-R \leqslant y_0 \leqslant R$ and we study the entanglement of a bipartition with cut at position x_0. As seen in Sec. 6.2.2, quantum fluctuations are present only inside the arctic circle. Therefore, the subsystem A of interest is given by the intersection of the (regularised) right subchain $(x_0 + 2\epsilon, +\infty)$ with the arctic circle, i.e.,

$$A = \left\{ (x,y)\ : x \in \left(x_0 + 2\epsilon, \sqrt{R^2 - y_0^2} \right], y = y_0 \right\}. \tag{6.28}$$

The conformal transformation to the annulus is shown in Fig. 6.3. The first step consists in a Weyl transformation to isothermal coordinates $(x,y) \to (z,\bar{z})$, with $z(x,y) \equiv \tilde{x} + \mathrm{i}\tilde{y}$ given in Eq. (6.20), which maps the arctic circle into the flat strip $(\tilde{x},\tilde{y}) \in [0,\pi] \times \mathbb{R}$. In particular, the entangling point (x_0,y_0) is mapped to $z_0 = z(x_0,y_0) = \tilde{x}_0 + \mathrm{i}\tilde{y}_0$, while the boundary point $(\sqrt{R^2 - y_0^2}, y_0)$ on the arctic circle maps to

$$z\left(x \equiv \sqrt{R^2 - y_0^2}, y \equiv y_0 \right) = \mathrm{i}\tilde{y}_0. \tag{6.29}$$

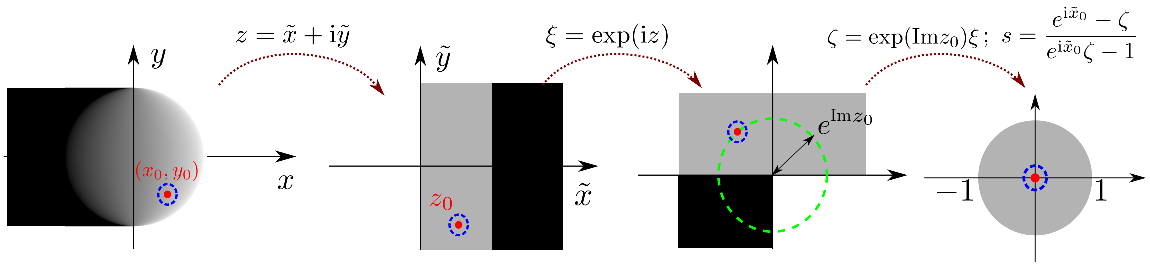

Figure 6.3: Illustration of the conformal mapping from the arctic circle to the annulus.

Under the Weyl transformation, the UV regularization changes as

$$\tilde{x}(x + 2\epsilon, y) \approx \tilde{x}_0 - \frac{2\epsilon}{\sqrt{R^2 - y_0^2 - x_0^2}} \equiv \tilde{x}_0 - 2\tilde{\epsilon} \tag{6.30}$$

where

$$\tilde{\epsilon} = \frac{\epsilon}{\sqrt{R^2 - y_0^2 - x_0^2}} = e^{-\sigma(x_0, y_0)}\epsilon. \tag{6.31}$$

We now use an exponential transformation $\xi(z) \equiv \exp(\mathrm{i}z)$ to map the flat strip into the upper half plane (UHP) and a further dilatation $\zeta(\xi) \equiv \exp(\mathrm{Im}\, z_0)\xi$ such that the image of $\tilde{y}_0$ lies on the unitary circumference. At this point, we map the UHP into the unitary disc with a Möbius transformation

$$s = \frac{e^{\mathrm{i}\tilde{x}_0} - \zeta}{e^{\mathrm{i}\tilde{x}_0}\zeta - 1}, \tag{6.32}$$

under which the entangling point x_0 goes to 0 and the image of A is the interval $(0, 1]$ on the real line. Finally, we end up in the annulus geometry by taking the logarithm

$$w \equiv \log s = \log\left[\frac{\sin\left(\frac{z_0 - z}{2}\right)}{\sin\left(\frac{\bar{z}_0 + z}{2}\right)}\right]. \tag{6.33}$$

Under this transformation, the boundary point of A on the arctic circle $(\sqrt{R^2 - y_0^2}, y_0)$ is mapped to

$$w(z \equiv \mathrm{i}\tilde{y}_0) = \log\left[\frac{\sin\left(\frac{\mathrm{Re}\, z_0}{2}\right)}{\sin\left(\frac{\mathrm{Re}\, z_0}{2}\right)}\right] = 0, \tag{6.34}$$

while the boundary point on the cut-off circle $(x_0 + 2\epsilon, y_0)$ becomes

$$w(z \equiv z_0 - 2\tilde{\epsilon}) = \log\left[\frac{\sin\tilde{\epsilon}}{\sin\left(\mathrm{Re}\, z_0 - \tilde{\epsilon}\right)}\right] \approx -\log\frac{\sin\tilde{x}_0}{\tilde{\epsilon}}. \tag{6.35}$$

Remarkably, the image $w(A)$ of the subsystem A in (6.28) lies on the real line, i.e., $\mathrm{Im}\, w(A) = 0$. Although this is a general result at equilibrium, the same is not true for out-of-equilibrium situations, for which $w(A)$ can be a generic curve on the annulus [34]. Thanks to this simplification, the width of the annulus is simply given by

$$\widetilde{\mathcal{W}}_A = \log \frac{\sin \tilde{x}_0}{\tilde{\epsilon}}. \tag{6.36}$$

To obtain the entanglement Hamiltonian, we also need the derivative of the transformation $z \to w(z)$ to the annulus. Therefore, for future convenience, we report

$$w'(z) = \frac{\sin \operatorname{Re} z_0}{\cos \operatorname{Re} z_0 - \cos(z - \mathrm{i}\ \operatorname{Im} z_0)} = \frac{\sin \tilde{x}_0}{\cos \tilde{x}_0 - \cos(z - \mathrm{i}\tilde{y}_0)}. \tag{6.37}$$

6.3.2 Entanglement entropy

Plugging Eqs. (6.31) and (6.36) into Eq. (6.27), we get after simple algebra the Rényi entropy for a cutting position x_0 and euclidean time y_0 as

$$\begin{aligned} S^{(n)} &= \frac{n+1}{12n}\widetilde{\mathcal{W}}_A = \frac{n+1}{12n} \log\left[\frac{e^{\sigma(x_0,y_0)}}{\epsilon(x_0,y_0)} \sin \operatorname{Re} z(x_0,y_0)\right] \\ &= \frac{n+1}{12n} \log\left[\frac{R^2 - y_0^2 - x_0^2}{\epsilon(x_0,y_0)\sqrt{R^2-y_0^2}}\right]. \end{aligned} \tag{6.38}$$

The UV cut-off ϵ appearing in (6.38) is set by the inverse local fermionic density $\rho^{-1}(x_0,y_0)$ in Eq. (6.18), because the latter is the only microscopic scale entering in the problem. In particular, for a connected Fermi sea one finds [85]

$$\epsilon(x,y) = \frac{C_n}{\sin(\pi\rho(x,y))} = C_n\sqrt{\frac{R^2-y^2}{R^2-y^2-x^2}}, \tag{6.39}$$

with C_n a known dimensionless non-universal constant [314, 315]. A more general result for split Fermi seas can be found in Refs. [287, 290, 291]. Plugging this expression in Eq. (6.38), we obtain

$$S^{(n)}(x_0,y_0) = \frac{n+1}{12n} \log\left[\frac{(R^2-y_0^2-x_0^2)^{3/2}}{R^2-y_0^2}\right] + \kappa_n, \tag{6.40}$$

$\kappa_n \equiv -\frac{n+1}{12n}\log C_n$, and performing the analytic continuation $R \to 0$, $y_0 \to \mathrm{i}t$

$$S^{(n)}(x_0,t) = \frac{n+1}{12n} \log\left[t\left(1+\frac{x_0^2}{t^2}\right)^{3/2}\right] + \kappa_n. \tag{6.41}$$

Finally, in the replica limit $n \to 1$, one finds the entanglement entropy

$$S(x_0,t) = \frac{1}{6} \log\left[t\left(1+\frac{x_0^2}{t^2}\right)^{3/2}\right] + \kappa_1, \tag{6.42}$$

with $c_1 \simeq 0.4785$ [314], in agreement with the result of Ref. [85] obtained with the twist field method.

6.3.3 Entanglement Hamiltonian

We now study the entanglement Hamiltonian, starting from the result in Eq. (6.25) for the annulus and mapping it back to the arctic circle with conformal transformations. In particular, recalling that under conformal transformations the stress-energy tensor changes as (neglecting the Schwarzian derivative that only contributes to K_A with an additive constant)

$$T(z) = |w'(z)|^2 \, T(w(z)), \tag{6.43}$$

we find that Eq. (6.25) becomes

$$\begin{aligned} K_A &= \int_{\mathrm{i}\tilde{y}_0}^{\tilde{x}_0 - 2\tilde{\epsilon} + \mathrm{i}\tilde{y}_0} \frac{T_R(z)}{|w'(z)|} \mathrm{d}z + \int_{-\mathrm{i}\tilde{y}_0}^{\tilde{x}_0 - 2\tilde{\epsilon} - \mathrm{i}\tilde{y}_0} \frac{T_L(\bar{z})}{|\bar{w}'(\bar{z})|} \mathrm{d}\bar{z} \\ &= \int_0^{\tilde{x}_0 - 2\tilde{\epsilon}} \left| \frac{\cos\tilde{x}_0 - \cos\tilde{x}}{\sin\tilde{x}_0} \right| \left[T_R(\tilde{x} + \mathrm{i}\tilde{y}_0) + T_L(\tilde{x} - \mathrm{i}\tilde{y}_0) \right] \mathrm{d}\tilde{x}. \end{aligned} \tag{6.44}$$

At this point, we consider the inverse Weyl transformation $(z, \bar{z}) \to (x, y)$ back to the arctic circle:

$$T(x, y) = e^{-2\sigma(x,y)} \, T(z, \bar{z}) \tag{6.45}$$

with Jacobian $\mathrm{d}\tilde{x} = e^{-\sigma(x,y)} \mathrm{d}x$ and we obtain

$$\begin{aligned} K_A &= \int_{x_0 + 2\epsilon}^{\sqrt{R^2 - y_0^2}} \left[\frac{T_R(x, \mathrm{i}y_0))}{|w'(z(x, y_0))| e^{-\sigma(x, y_0)}} + \frac{T_L(x, -\mathrm{i}y_0)}{|\bar{w}'(\bar{z}(x, y_0))| e^{-\sigma(x, y_0)}} \right] \mathrm{d}x \\ &= \int_{x_0 + 2\epsilon}^{\sqrt{R^2 - y_0^2}} \left[(x - x_0) \sqrt{\frac{R^2 - x^2 - y_0^2}{R^2 - x_0^2 - y_0^2}} \right] \left[T_R(x, \mathrm{i}y_0) + T_L(x, -\mathrm{i}y_0) \right] \mathrm{d}x. \end{aligned} \tag{6.46}$$

Finally, rotating back to real time $y_0 \to \mathrm{i}t$ and taking the limit $R \to 0$, we find

$$K_A = \int_{x_0 + 2\epsilon}^{t} \beta^{\mathrm{loc}}(x, t) \left[T_R(x, -t) + T_L(x, t) \right] \mathrm{d}x \tag{6.47}$$

with entanglement temperature

$$\beta^{\mathrm{loc}}(x, t) = (x - x_0) \sqrt{\frac{t^2 - x^2}{t^2 - x_0^2}}. \tag{6.48}$$

By Taylor-expanding the entanglement temperature (6.48) around the entangling point x_0, we recover at the leading order the general prediction by Bisognano-Wichmann theorem (1.12)

$$\beta^{\mathrm{loc}}(x, t) \approx (x - x_0) \left[1 - \frac{x_0}{t^2 - x_0^2} (x - x_0) + \dots \right]. \tag{6.49}$$

Eq. (6.48) is the major field theoretical result of this Chapter and fully characterise, in the scaling limit, the entanglement Hamiltonian for the domain wall melting problem.

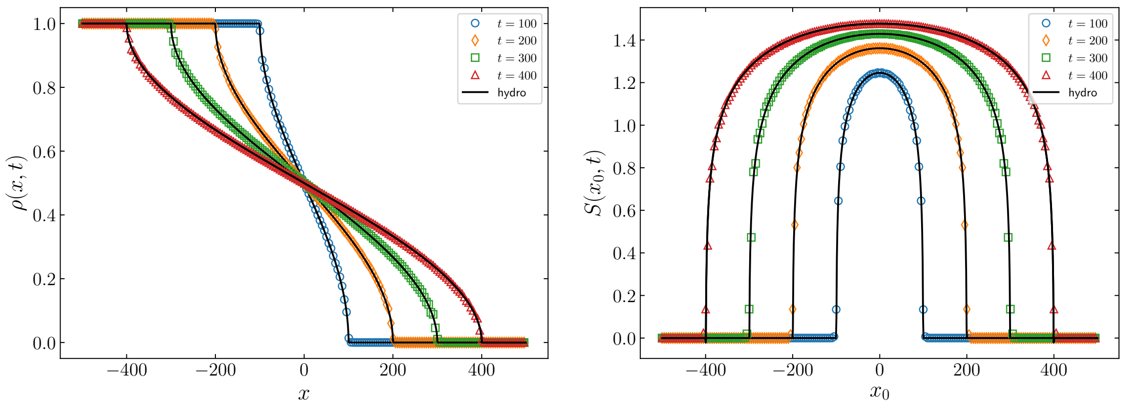

Figure 6.4: Snapshots of (left) the fermionic density profile and of (right) the Von Neumann entropy after a quench from the domain wall initial state at different times. The exact asymptotic predictions of Eqs. (6.9) and (6.42) (*black full line*) are compared with the numerical data (*symbols*) obtained for a system of size $L = 1000$. We observe an extremely good agreement even at short times.

6.4 Exact lattice results for the entanglement Hamiltonian

In this section, we investigate numerically the lattice entanglement Hamiltonian for a domain wall melting and we discuss how to correctly recover the field theory prediction (6.48). Since for a free Fermi gas the reduced density matrix is Gaussian, we can derive the entanglement properties from the two-point correlation function, similarly to what we have done in Secs. 2.4 and 3.3 for the equilibrium case. Recall that the relationship between the kernel h of the lattice entanglement Hamiltonian and the correlation matrix $(C_A)_{ij} = \langle c_i^\dagger c_j \rangle_{i,j\in A}$ is given by Eq. (1.15) (see discussion in the Introduction). Moreover, as a consequence of Eq. (1.15), the n-Rényi and the von Neumann entanglement entropies (1.7) can be obtained from the eigenvalues σ_i of the restricted correlation matrix using Eq. (1.16). Recall also from Sec. 2.4 that the computation of the entanglement Hamiltonian is sensitive to the eigenvalues σ_i of C_A which are very close to the edges 0 and 1 and must be performed at high precision [52, 135–137]. In our numerical analysis, we used the open-source Python library mpmath [139] and we kept up to 500 digits. In contrast, the entanglement entropies (1.16) are only sensitive to those eigenvalues of C_A which are far from either 0 or 1 and eventual numerical instabilities in their calculation can be simply handled introducing a cut-off on the eigenvalues.

As a warm up, in Fig. 6.4, we show the numerical results for the fermionic density $\rho(i,t) = \delta_{i,j}C_{i,j}(t)$ and for the entanglement entropy in the subsystem $A = [x_0, \infty]$, together with the hydrodynamic predictions given in Eqs. (6.9) and (6.42) respectively. The numerics

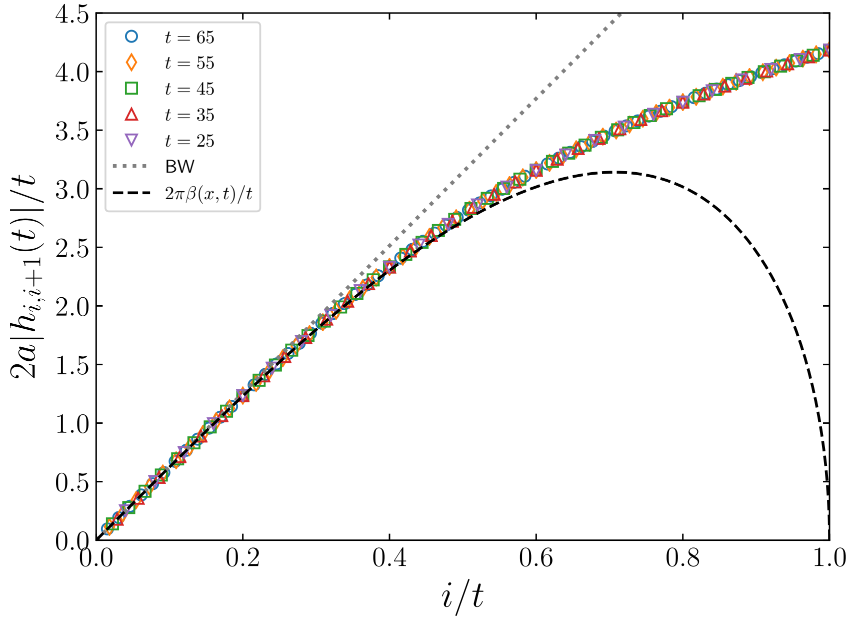

Figure 6.5: Nearest-neighbour entanglement Hamiltonian after the domain wall quench for the subsystem $A = [0, L/2]$, with $L = 200$ and $a = 1$. We report the (rescaled) value of $|h_{i,i+1}|$ for different times t after the quench as a function of i/t, showing an excellent data collapse. For $i \lesssim 0.3t$, they match rather well the linear behaviour expected naively from the discretisation of the Bisognano-Wichmann modular Hamiltonian.

are for $L = 1000$ sites with $-L/2 < i \leqslant L/2$ and the subsystem is $A = [x_0, L/2]$. The agreement of the hydrodynamic curves with the numerical data is extremely good.

6.4.1 The lattice entanglement Hamiltonian

In Sec. 2.4 we have discussed in detail the comparison between the lattice EH with the field-theoretical prediction. It turns out that in general, even when the QFT entanglement Hamiltonian is completely local (see e.g. Eq. (1.13)), the corresponding lattice expression contains non-vanishings couplings between fermions at arbitrary distances [135, 136, 316, 317]. In the domain wall melting protocol, for the subsystem $A = [0, \infty]$ one would naively expect that in the hydrodynamic limit $i, t \to \infty$ with i/t fixed, only the nearest neighbour term $h_{i,i+1}$ would scale like t (cf. Eq. (6.47)) while all the other hoppings would be subdominant. To show the incorrectness of this expectation, we report the hopping elements $|h_{i,i+1}|$ in Fig. 6.5. It is evident that for all i/t the data collapse, but they are well reproduced by Eq. (6.47) only for $i \lesssim 0.3t$ (where it is actually linear and the correct behaviour could be inferred from the Bisognano-Wichmann theorem without performing any calculation). It is instructive to compare this behaviour with what we described in Chapters 2 to 4 for homogeneous systems. While also in the homogeneous case the next-neighbour coupling $h_{i,i+1}$ presented a discrepancy with respect to the field theoretical entanglement temperature β^{loc}, the two expression had the same qualitative behaviour, differently from the plots in Fig. 6.5. In the homogeneous case, the solution to the discrepancy consisted in properly taking the continuum limit of the lattice result by retaining all long-range hoppings [132,133], as we reviewed in detail in Sec. 2.4. In the next section we will show how the continuum limit can be adapted to the inhomogeneous case by properly taking into account the position dependent fermion density, which will cure the different qualitative behaviour in Fig. 6.5.

6.4.2 Continuum limit of the entanglement Hamiltonian

As we showed in Sec. 2.4, the starting point of the continuum limit of Refs. [133, 134] is the same expansion (6.10) of the lattice fermion in terms of left- and right-moving fermions that forms the basis of the hydrodynamics description of Sec. 6.2. We start by writing the lattice EH K_A as

$$2\pi K_A = \sum_i \left[h_{ii} c_i^\dagger c_i + \sum_{r=1}^{\infty} \left(h_{i,i+r} c_i^\dagger c_{i+r} + \text{h.c.} \right) \right], \tag{6.50}$$

analogously to Eq. (2.102). From the derivation in Eqs. (2.111) and (2.112) we see that the limit is performed by substituting the expansion of the lattice fermion c_i in the EH (6.50), keeping only the lowest order in the lattice spacing s. In the expansion in Eq. (2.111), the product of two left- or two right-moving continuum fermions appears weighted by the differential phase $e^{\pm \mathrm{i} k_F r s}$ between the fermion computed at position x and the one at position $x + rs$. On the other hand, the products of one left- and one right-mover vanish in the $s \to 0$ limit because they acquire an highly oscillating phase (see Eq. (2.111) and discussion below).

Considering now the domain wall melting problem, the differential phase $\mathrm{d}\varphi^\pm$ appearing in the expansion becomes position and time dependent. This phase can be read directly from the expression of the Fermi points $k_F^\pm$ in Eq. (6.19)

$$\mathrm{d}\varphi^\pm \approx k_F^\pm(x,y) rs = r \left[\pm \arccos\left(\frac{x}{\sqrt{R^2 - y^2}} \right) - \mathrm{i} \,\mathrm{arcth}\, \frac{y}{R} \right] \overset{y \to \mathrm{i}t;\, R \to 0}{\longrightarrow} \frac{r\pi}{2} \pm rs\pi\rho(x,t). \tag{6.51}$$

In the last expression, we have a term proportional to the fermionic density $\rho(x,t)$, which is analogous to the case at equilibrium, but we do have an additional $r\pi/2$ phase. Using Eq. (6.51) and neglecting the highly oscillating terms, one finds that the derivation in

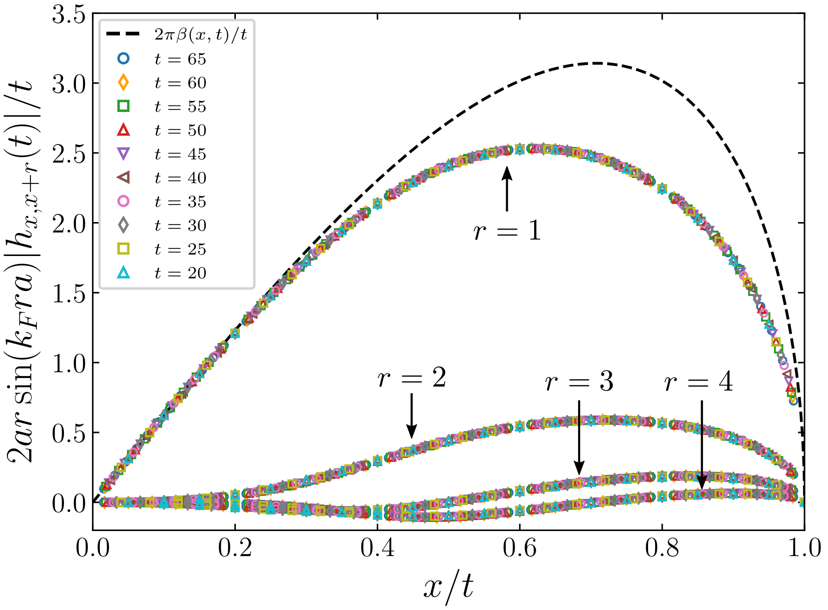

Figure 6.6: The elements of the sum at fixed distance r entering in the final entanglement Hamiltonian (6.54). We consider the subsystem $A = [0, L/2]$ with $L = 200$ and $a = 1$.

Eqs. (2.111) and (2.112) is modified as

$$\begin{aligned}
& h_{i,i+r}(y)\left[c_i^\dagger c_{i+r} + c_{i+r}^\dagger c_i\right] \\
&\approx s\, h_{x,x+rs}(y)\left[e^{-\mathrm{i}\,\mathrm{d}\varphi^+}\psi_R^\dagger(z)\psi_R(z+rs) + e^{-\mathrm{i}\,\mathrm{d}\varphi^-}\psi_L^\dagger(\bar z)\psi_L(\bar z + rs) + \text{h.c.}\right] \\
&\approx s\, e^{-\mathrm{i}\,r\left(-\mathrm{i}\,\mathrm{arcth}\left(\frac{y}{R}\right)\right)} h_{x,x+rs}(y)\Big[2\cos(\pi\rho(x,y)rs)\left(\psi_R^\dagger\psi_R + \psi_L^\dagger\psi_L\right) + \\
&\qquad - \mathrm{i}\sin(\pi\rho(x,y)rs)\; rs\left(\psi_R^\dagger\partial_z\psi_R - \partial_z\psi_R^\dagger\psi_R - \psi_L^\dagger\partial_{\bar z}\psi_L + \partial_{\bar z}\psi_L^\dagger\psi_L\right)\Big] + \\
&\qquad\qquad + \text{higher orders} \\
&\xrightarrow{y\to\mathrm{i}t;\ R\to 0} 2rs\, e^{-\mathrm{i}\,r\frac{\pi}{2}} h_{x,x+ra}(t)\cos(\pi\rho(x,t)rs)\left[N_L(x,t) + N_R(x,-t)\right] \\
&\qquad\qquad - 2rs^2 e^{-\mathrm{i}\,r\frac{\pi}{2}} h_{x,x+ra}(t)\sin(\pi\rho(x,t)rs)\left[T_L(x,t) + T_R(x,-t)\right],
\end{aligned} \tag{6.52}$$

where the operators N_L and N_R are respectively the left- and right-moving part of the fermion number operator (2.113). In Sec. 2.4 we argued that the terms proportional to the number operator should vanish, since they do not appear in the field theoretical expression (6.47). In the domain wall melting we have indeed verified numerically that the expression multiplying N_L, N_R in Eq. (6.52) goes to zero in the hydrodynamic limit $x, t \to \infty$. We moreover numerically observe that the additional phase $-e^{-\mathrm{i}r\pi/2}$ exactly cancels the phase of $h_{i,i+r}(t)$, leading to the real quantity $|h_{i,i+r}| \equiv -e^{-\mathrm{i}r\pi/2}h_{i,i+r}$.

Finally, summing up to a maximum distance $r_{\max}$, from Eq. (6.52) we can write the continuum limit of the lattice entanglement Hamiltonian (6.50) for the domain wall quench problem as

$$K_A \approx \frac{1}{2\pi}\int \mathrm{d}x\, \mathcal{S}^{\mathrm{loc}}(x,t)\,[T_L + T_R]\,, \tag{6.53}$$

where the expression

$$\mathcal{S}^{\mathrm{loc}}(x,t) = 2a\sum_{r=1}^{r_{\max}} r\sin(\pi\rho(x,t)ra)|h_{x,x+r}(t)|. \tag{6.54}$$

is the out-of-equilibrium analogue of Eq. (2.115) and is expected to reproduce the entanglement temperature (6.48).

If we compare Eq. (6.54) with the expression in Eq. (2.115) for the continuum limit in the homogeneous case, we find two differences. First, the sum in Eq. (6.54) is performed along the rows of the matrix, differently from the one in Eq. (2.115). This is just a matter of convenience and the two ways of summing agree up to higher orders in the lattice spacing [133]. A more significant difference is that the weight $\sin(\pi\rho(x,t)ra)$ which multiplies the coupling $|h_{x,x+r}|$ in the sum (6.54) is now position and time depend. In Fig. 6.6 we report a few elements entering into the sum (6.54) with $r \leqslant 4$. By comparing it with the naive expectation $|h_{x,x+1}|$ shown in Fig. 6.5, it is evident that the multiplication by the local Fermi momentum improves considerably the qualitative agreement of the data at $r = 1$ with the asymptotic result. Indeed, we now observe a non-monotonic behaviour which is forced by the fact that the density $\rho(x,t)$ vanishes at the light cone $x = t$.

Despite the differences, both the homogeneous and the inhomogeneous problems share the same main feature: the proper continuum limit in Eq. (6.54) requires to sum over couplings at all distances. In Fig. 6.7 we report the final result of our numerical analysis for the entanglement Hamiltonian of the subsystem $A = [0, L/2]$. The symbols are the limiting expression $\mathcal{S}^{\mathrm{loc}}$ in Eq. (6.54) with $r_{\max} = 8$, rescaled by the time t. We find an extremely good agreement with the field theoretical prediction in Eq. (6.48) (solid black line). In the inset of the same figure, we report the sum truncated at different $r_{\max}$ for $t = 65$ showing that all terms are necessary for a good match. For completeness, in Fig. 6.8 we report the same numerical analysis for $\mathcal{S}^{\mathrm{loc}}$ at different entangling point $x_0 = 0.25t$, $0.5t$ ($A = [x_0, L/2]$), for which we observe an excellent data collapse in x/t and a perfect agreement with the field theory prediction (6.48).

6.5 Final remarks

In this Chapter, we considered a one-dimensional lattice gas of free fermions initially prepared in a domain wall configuration $|\Psi_0\rangle = \bigotimes_{i\leqslant 0}|1\rangle_i \bigotimes_{i>0}|0\rangle_i$ and subsequently let to freely

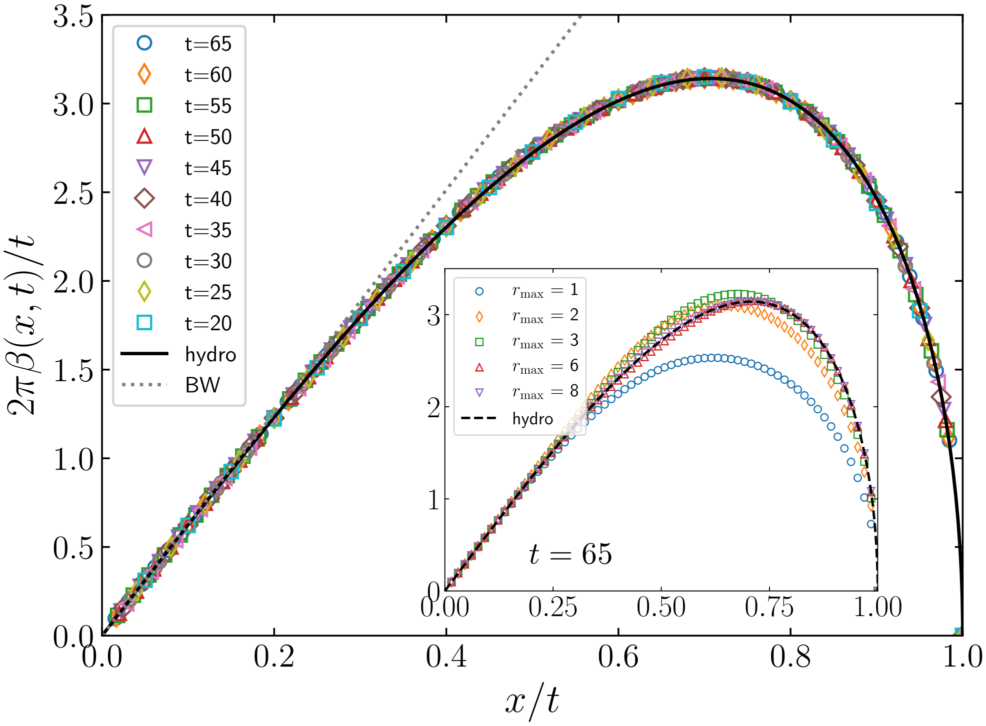

Figure 6.7: Spatial profile of the entanglement temperature $\beta^{\text{loc}}(x,t)$ (rescaled with t) for the domain wall melting problem as a function of the scaling variable x/t. The numerical data (symbols) are obtained from Eq. (6.54) and are compared with the asymptotic prediction (6.48) (solid line). The dotted line corresponds to the linear behaviour (slope 2π) from the Bisognano-Wichmann theorem. The data are for a system with $L = 200$ sites, for $A = [0, L/2]$, with a working precision of 500 digits and with $r_{\max} = 8$. Inset: The same with different $r_{\max} \leqslant 8$.

expand towards the right vacuum with Hamiltonian dynamics, $|\Psi(t)\rangle = e^{-\text{i}tH}|\Psi_0\rangle$. For this setting, we briefly discussed the semi-classical evolution, recalling some known results about the phase-space hydrodynamics and the semi-classical profiles of conserved quantities that follow. With the goal of studying the entanglement properties of the expanding gas, we re-built quantum correlations on top of the semi-classical hydrodynamic background by expressing the latter in terms of an effective field theory for a massless Dirac fermion in a curved space-time as in Ref. [278]. With this field theoretical description of the quench protocol at hand, we made use of the annulus method [34] to obtain asymptotic predictions for the Rényi entropies (see Eq. (6.41) and Ref. [85]) and for the entanglement Hamiltonian (see Eqs. (6.47) and (6.48)). Finally, we provided high-precision numerical lattice calculations and we carefully considered the limit of large space-time scales to test our hydrodynamic

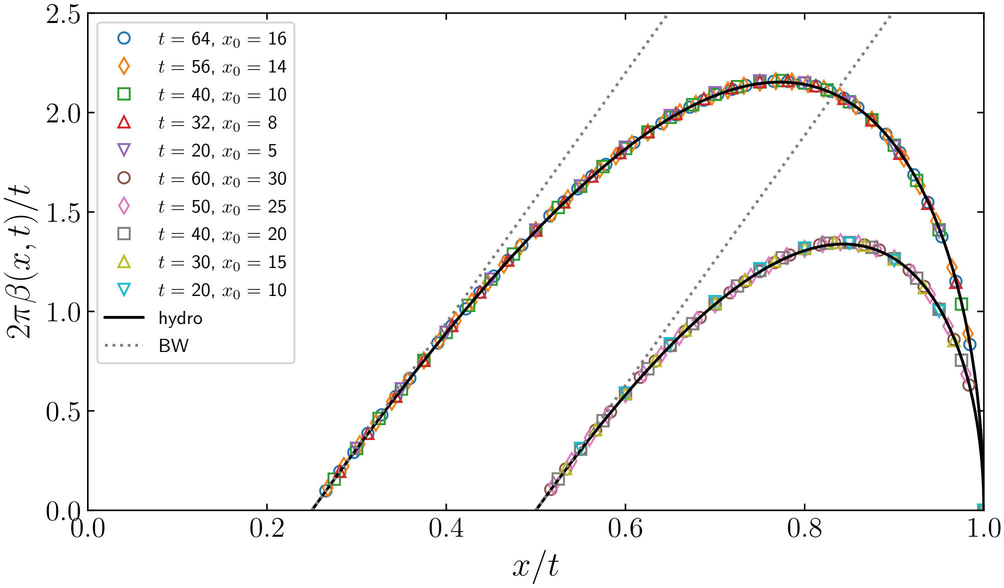

Figure 6.8: Spatial profile of the (rescaled) entanglement temperature for different entangling points x_0/t, as a function of the scaling variable x/t. The outer curve is for entangling point $x_0 = 0.25t$, while the inner has $x_0 = 0.5t$. As in Fig. 6.7, the numerical results (symbols) are compared with the asymptotic predictions (solid line), while the dotted line is the Bisognano-Wichmann linear behaviour. The data are for a system with $L = 200$ sites and $r_{\max} = 8$.

result. We observed an excellent agreement (cf Fig. 6.7), already at modest system sizes and for relatively short times.

The work in this Chapter, based on Ref. [141], served to prove the validity of the quantum fluctuating hydrodynamics framework for the calculation of the entanglement Hamiltonian in inhomogeneous quench problems and, therefore, it opens up a wide window for future applications. Clearly, the case of a domain wall melting is a particularly simple instance, for which previous results for the CFT description of quantum correlations in the Luttinger regime were known [278]. To our best knowledge, a similar result is only known for the dynamics of a driven Tonks-Girardeau gas in harmonic traps [282]. A natural extension of the proposed method for generic quench settings is to join it with quantum generalised hydrodynamics to trace backward in time the quantum correlations, similarly to what done for the entanglement entropies and spectrum [287–291]. A step in this direction has been taken in Ref. [318]. An interesting application of our result would be to discretise the field theoretical result (6.47) to engineer both numerically and experimentally the hydrodynamic entanglement Hamiltonian of the domain wall melting, on the lines of Refs. [36, 37, 39].

Chapter 7

Domain wall melting across a defect

This Chapter offers a natural continuation of the work in the previous one, by investigating how the domain wall melting protocol of Chapter 6 is modified by the introduction of a defect. The presence of a localised impurity is known to dramatically alter the global structure of a many-body quantum system, as well known from the textbook examples of Anderson orthogonality catastrophe [319] and the Kane-Fisher model [320,321]. In the latter, it has been shown that for repulsive interactions, the electrons are completely reflected by even the smallest scatterer, leading to a truly insulating weak link disconnecting the two halves. Conversely for attractive bulk interactions, the weak link is irrelevant, i.e., it is washed away at large scales. As a consequence free fermions represent the most interesting system in which the defect is marginal and there is a line of fixed points characterised by the the defect strength [94, 322].

In recent years, the physics of impurities in one-dimensional (1D) free-fermionic systems has been investigated a lot through the lens of entanglement. The marginality of the defect is reflected into a logarithmic scaling of the entanglement entropy with a prefactor that depends continuously on the defect strength [96, 127, 323–335]. Overall, thanks to all these studies nowadays we have a rather complete understanding of the physics of defects in *equilibrium* free fermionic systems. The same is definitively not true when the free fermionic chain is driven *out of equilibrium*; in fact, in spite of several works about the non-equilibrium behaviour across one defect (see, e.g., Refs. [123, 336–345]), a complete understanding is still far because of the many different ways of driving a system away from equilibrium.

In this regard, the melting of a domain wall configuration is a natural playground in which to investigate the effect of a defect on the time evolution. In the presence of a defect, the density, the currents, and other local quantities have been characterised in Ref. [346] where the emergence of a local non-equilibrium stationary state (NESS) has been rigorously established. However, little is known for the entanglement entropy, whose behaviour is affected, as any other non-local observable, by non-local correlations generated by the defect. Some lattice results were derived for the domain wall melting with defect in Ref. [336], and another important step forward has been done by Fraenkel and Goldstein [126, 347] in a slightly different context, but a general scheme to describe non-local correlations is still missing. In this Chapter, based on Ref. [348], we show that even the smallest defect has a remarkable effect on the entanglement entropy, whose evolution transitions from a logarithmic to a linear growth in time.

7.1 The model and the quench protocol

In the previous Chapter we considered a 1D chain of free spinless fermions with L sites and with nearest-neighbour hopping. In the same system we now introduce a defect of strength λ located at the centre of the chain. The Hamiltonian is

$$H = \sum_{i,j=-L/2+1}^{L/2} h_{i,j}\; c_i^{\dagger} c_j \tag{7.1}$$

with

$$h_{i,j} = -\frac{1}{2}(\delta_{i,j+1} + \delta_{i+1,j}), \quad \forall i, j \neq 0, 1 \tag{7.2}$$

and the defect takes the form

$$h_{0,1} = h_{1,0} = -\frac{\lambda}{2}, \qquad\qquad h_{0,0} = -h_{1,1} = \frac{1}{2}\sqrt{1-\lambda^2}. \tag{7.3}$$

Here $c_j^{\dagger}$, c_j are the creation and annihilation operators of spinless fermions at site j, satisfying $\{c_j^{\dagger}, c_i\} = \delta_{ij}$. We see that for $\lambda = 1$, Eq. (7.1) reduces to the standard hopping model considered in Sec. 6.1. At time $t = 0$, the system is initially prepared in the same domain wall state (6.3)

$$|\Psi_0\rangle = \bigotimes_{j=-L/2+1}^{0} |1\rangle_j \bigotimes_{j=1}^{L/2} |0\rangle_j\,, \tag{7.4}$$

used in the protocol in Chapter 6. For $t > 0$, the state (7.4) is unitarily evolved with Hamiltonian (7.1), $|\Psi_t\rangle = e^{-\mathrm{i}tH}\,|\Psi_0\rangle$.

The structure of the defect (7.3) does not spoil the exact solvability of the free fermionic model, for any value of $\lambda \in (0, 1]$ [325, 340]. Moreover, the eigenstates of H can be related to the eigenstates $\Psi_{q,L}(j) = \sin(k_q j)/\sqrt{L/2}$ of (7.1) in the absence of defect ($\lambda = 1$) as [340]

$$\Psi^{\mathrm{def}}_{q,L}(j) = \Theta(-j)\alpha_q^{+}(\lambda)\Psi_{q,L} + \Theta(j)\alpha_q^{-}(\lambda)\Psi_{q,L}, \tag{7.5}$$

with $\Theta(j)$ the Heaviside step function and coefficients $\alpha_q^{\pm}(\lambda) = [1 \pm (-1)^q\sqrt{1-\lambda^2}]^{1/2}$. For $L \to \infty$, this eigenproblem reduces to a scattering of plane waves across a localised defect, i.e.,

$$\Psi^{\mathrm{def}}_{k,\infty}(j) \propto \Theta(j)\lambda\; e^{\mathrm{i}kj} + \Theta(-j)\left(\sqrt{1-\lambda^2}\; e^{-\mathrm{i}kj} + e^{\mathrm{i}kj}\right), \tag{7.6}$$

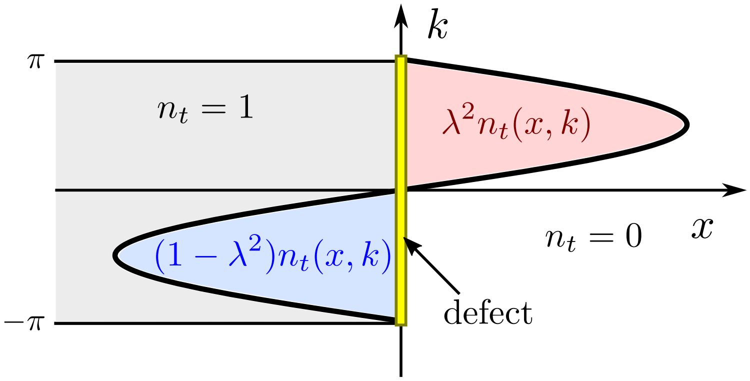

Figure 7.1: Illustration of the evolution of the Fermi occupation function $n_t^{(\lambda)}(x,k)$ in the presence of the defect. The light-grey area is the initial occupation (6.5), while the colored regions correspond to the time-evolved one.

with transmission probability $T(\lambda) \equiv \lambda^2$ and reflection probability $R(\lambda) \equiv 1 - \lambda^2$. These parameters do not depend on the momentum k of the scattered particle and so the defect (7.3) is also known as *conformal defect* [325, 326, 336].

7.1.1 Hydrodynamic limit

In Sec. 6.1 we showed how to recover the asymptotic results for the charges profiles in the hydrodynamic limit $L \to \infty$, $j \to \infty$, $t \to \infty$ at fixed j/t. The lattice index j and the quantised momenta k_q are replaced by continuous variables for the position $x = js \in \mathbb{R}$ (s is the lattice spacing) and for the momenta $-\pi \leqslant k \leqslant \pi$. In such scaling limit, the essential information on the state is retained by the local fermionic occupation. The occupation $n_0(x,k)$ in the initial state is given by Eq. (6.5),

$$n_0(x,k) = \begin{cases} 1, & \text{if } x \leqslant 0 \text{ and } -\pi \leqslant k \leqslant \pi; \\ 0, & \text{otherwise.} \end{cases} \tag{7.7}$$

In the absence of defect ($\lambda = 1$), the evolution of the occupation function was given by Euler equation (6.7), whose solution is simply $n_t(x,k) = n_0(x - t\sin k, k)$ in Eq. (6.6). Recall that, intuitively, this solution encodes the fact that each non-interacting particle moves along the ballistic trajectory with constant velocity $v(k) = \sin k$. If we now introduce a defect for $\lambda \neq 1$, a particle of momentum $k > 0$ travelling from $x < 0$ is scattered by the defect in such a way that it is reflected with probability $R(\lambda)$ and transmitted with probability $T(\lambda)$. Accordingly, the time-evolved occupation function in the presence of the defect takes the form [346]

$$n_t^{(\lambda)}(x,k) = \lambda^2 \Theta(x) n_t(x,k) + \Theta(-x)\left[(1-\lambda^2)n_t(-x,-k) + n_t(x,k)\right], \tag{7.8}$$

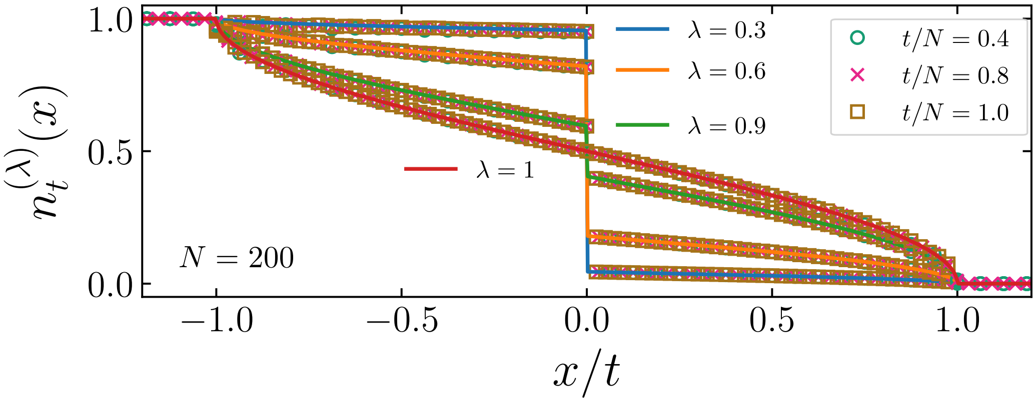

Figure 7.2: Fermionic density as function of x/t for different values of λ and t. Symbols show the numerical data obtained with exact lattice calculations with 400 sites while the full lines are given by Eq. (7.9).

as illustrated in Fig. 7.1. In our notations $n_t^{(\lambda\equiv 1)} = n_t$ in Eq. (6.6) is the occupation number in the absence of defects. As discussed in Sec. 6.1, the occupation function (7.8) gives us access to the asymptotic profiles of conserved charges as elementary integrals over the modes k, properly weighted with the single-particle eigenvalue of the associated charge [292, 298]. In the case without defect, this has been used to recover the particle density profile in Eq. (6.9). Including the defect, the density for $0 < x \leqslant t$ is modified as

$$n_t^{(\lambda)}(x) = \int_{-\pi}^{\pi} \frac{\mathrm{d}k \; n_t^{(\lambda)}(0 < x \leqslant t, k)}{2\pi} = \lambda^2 \frac{\arccos(x/t)}{\pi}. \tag{7.9}$$

For $-t \leqslant x < 0$, the profile is obtained via particle-hole symmetry and reads $n_t^{(\lambda)}(x) = 1 - \lambda^2 \arccos(|x|/t)/\pi$. Similarly to the purely transmissive case in Eq. (6.9), outside the light-cone region, i.e., for $|x| > t$, the systems keeps its initial configuration with constant density $n_t^{(\lambda)} = 1$ ($n_t^{(\lambda)} = 0$) on its left (right) part. On the other hand, for $\lambda > 1$ the density profile presents a jump at the defect location $x = 0$. In Fig. 7.2, we compare numerical results obtained from exact lattice calculations with the hydrodynamic result (7.9).

7.2 Entanglement dynamics

We now move to our main goal which is characterising the entanglement dynamics. Specifically, we focus on a bipartition of the system $A \cup B$ with a reduced density matrix $\hat{\rho}_t(A) = \mathrm{Tr}_B \left|\Psi_t\right\rangle \left\langle\Psi_t\right|$. An ab-initio description of the entanglement dynamics is very demanding even in the absence of defect, due to the non-equilibrium and non-homogeneous character of the quench problem under analysis. However, the asymptotic behaviour of

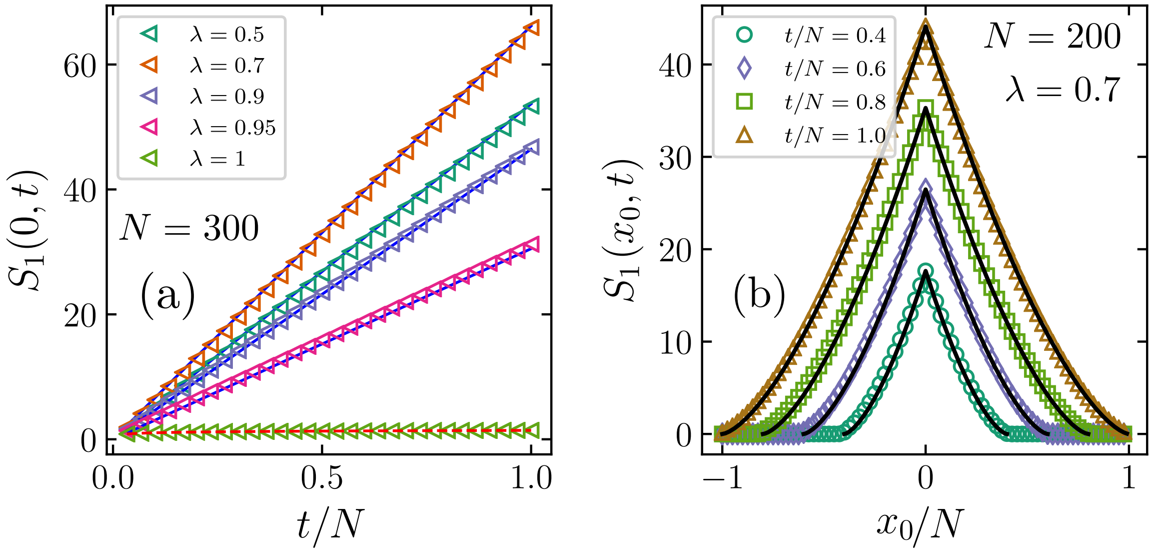

Figure 7.3: (a) – Half-system entanglement of $A = [-\infty, 0]$ for different values of λ as function of time. Symbols show the numerical data while the full lines (for $\lambda \neq 1$) are given by Eq. (7.13). At $\lambda = 1$, the half-system entanglement entropy is $S_1 = 1/6 \log(t) + \text{const}$ (dashed line) [85]. (b) – Entanglement profiles for $A = [-\infty, x_0]$ plotted as function of x_0 at different times and fixed $\lambda = 0.7$. Symbols show the numerical data while the full lines are given by Eq. (7.11).

entanglement can be determined with hydrodynamic arguments as follows. First of all, we recall the definition of the local Yang-Yang Rényi entropy [126, 349–351]

$$s_n(x,t) \equiv \frac{1}{1-n} \int_{-\pi}^{\pi} \frac{\mathrm{d}k}{2\pi} \log \left[n_t^{(\lambda)}(x,k)^n + (1 - n_t^{(\lambda)}(x,k))^n \right]. \tag{7.10}$$

The crucial observation is that the local occupation function (7.8) for $\lambda \neq 1$ assumes values which are different from 0 and 1. Consequently, the local entropy (7.10) is non vanishing, resulting in an extensive entanglement.

From an entanglement perspective, this entropy measures the correlations between the transmitted particles at position x with the reflected ones at $-x$ generated by the scattering at the defect, according to the quasiparticle picture [86, 352].

The total entanglement entropy of a region A which is entirely to the right or to the left of the defect (say $A = [-\infty, x_0]$) is then given by (see also [286, 341])

$$S_n(x_0,t) = \int_A \mathrm{d}x \, s_n(x,t) = \frac{\mathcal{N}_t(A)}{1-n} \log \left[\lambda^{2n} + (1-\lambda^2)^n \right], \tag{7.11}$$

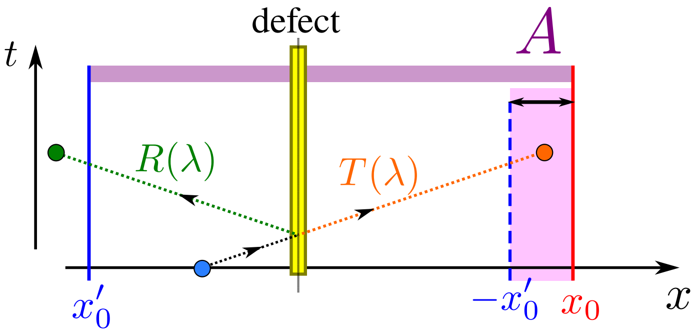

Figure 7.4: Illustration of the quasiparticle picture. The partial reflection $R(\lambda)$ and transmission $T(\lambda)$ at the defect causes entanglement between symmetric points. When computing the entanglement entropy of a sybsystem straddling the defect, the Yang-Yang entropy overcounts the quasiparticles: the correct counting is given by the shaded pink area in the figure.

with $\mathcal{N}_t(A)$ being the total number of entangled particles in the region A at time t. For example for $A = [-\infty, x_0]$ with $x_0 < 0$, we have

$$\mathcal{N}_t([-\infty, x_0]) = \frac{t}{\pi}\left(\sqrt{1-\frac{x_0^2}{t^2}} - \frac{x_0}{t}\arccos\frac{x_0}{t}\right). \tag{7.12}$$

By setting $x_0 = 0$, Eq. (7.11) predicts a linear growth of entanglement (see also Ref. [336])

$$S_n(0,t) = \frac{t}{\pi(1-n)}\log\left[\lambda^{2n} + (1-\lambda^2)^n\right]. \tag{7.13}$$

It is instructive to compare the entropy (7.11) with the results in the purely transmissive case $\lambda = 1$ in the previous Chapter. From Eq. (6.42) we see that in the absence of defect the half-system entanglement $S_n(0,t) \sim (n+1)/12n\log(t)$ grows logarithmically in time, arising from subleading contributions [85, 290, 353]. Indeed, for $\lambda = 1$ the local occupation function (6.6) is either 0 or 1 and the extensive Yang-Yang entropy (7.10) vanishes, as expected because of the absence of correlated quasiparticle pairs. Interestingly, the entanglement transition from logarithmic to linear law is observed even for values of λ very close to unit, see Fig. 7.3-(a) for a comparison with exact lattice calculations.

Eq. (7.11) fails to capture the behaviour of entanglement for a subsystem straddling the defect because it counts also for the pairs of entangled particles which are both in A, but on different sides of the defect. Such over-counting is however easily cured within the quasiparticle picture [86, 352]. First, for the case $A = [-\infty, x_0]$ with $x_0 > 0$, using particle-hole symmetry and $S_n(A,t) = S_n(\bar{A},t)$, we have $S_n(x_0,t) = S_n(-x_0,t)$ where the rhs is in Eq. (7.11). The validity of Eq. (7.11) is tested against exact lattice calculations in Fig. 7.3-(b).

For subsystems $A = [x_0', x_0]$ consisting of an interval straddling the defect (i.e., $x_0' < 0$ and $x_0 > 0$), we can simply correct the over-counting of Eq. (7.11) by subtracting the

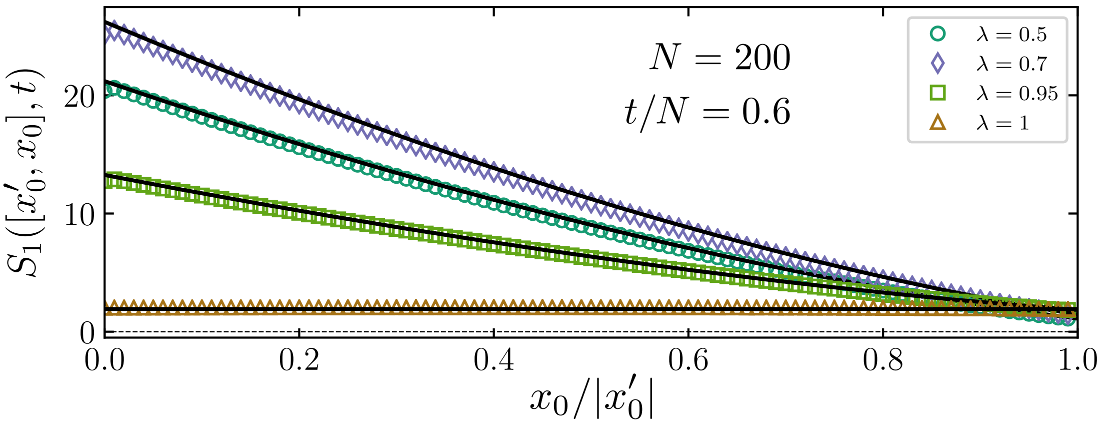

Figure 7.5: Entanglement entropy for $A = [x_0', x_0]$ at fixed time $t/N = 0.6$ and for different values of λ, plotted as function of the left endpoint x_0. Symbols show the numerical data while the full lines are given by Eq. (7.14), up to a fitted additive constant.

doubly-counted particles (see Fig. 7.4 for an illustration), resulting finally in

$$S_n([x_0', x_0], t) = \left|S_n(|x_0|, t) - S_n(|x_0'|, t)\right|. \tag{7.14}$$

In Fig. 7.5, numerical results for the lattice model are compared with the hydrodynamic prediction in Eq. (7.14), showing an excellent agreement.

Our results also show the appearance of long-range entanglement in the sense of Ref. [126]. Indeed, if we compute the mutual information $I_{A_1:A_2} \equiv S_{A_1} + S_{A_2} - S_{A_1 \cup A_2}$ between $A_1 = [-\infty, -x_0]$ and $A_2 = [x_0, \infty]$ we have

$$I_{A_1:A_2} = 2S_n([x_0, \infty], t) \tag{7.15}$$

because $S_{A_1 \cup A_2} = 0$, (up to subleading terms, see also the next section). The same remains true if A_1 and A_2 are two symmetric finite intervals. Such large (actually extensive for large t) mutual information is due to the constant presence of shared pairs between symmetric intervals, exactly as in Ref. [126].

7.2.1 Subleading behaviour

When the subsystem A is placed symmetrically across the defect, i.e., $A = [-x_0, x_0]$, the entanglement resulting from correlated pairs of particles in Eq. (7.14) vanishes. This is clearly due to the fact that entangled pairs have symmetric positions and so they are either both in A or in the complement. As a consequence, the behaviour of entanglement is entirely due to subleading contributions associated with quantum fluctuations, which

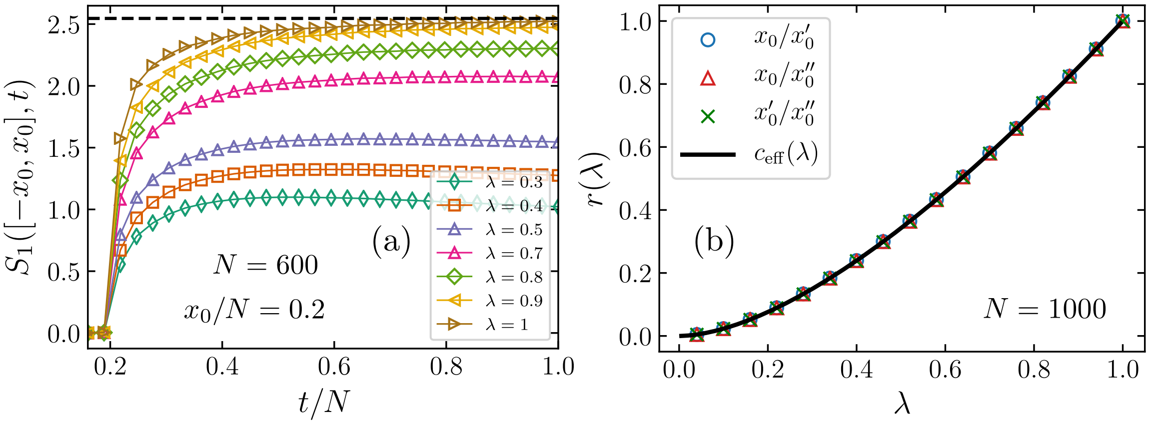

Figure 7.6: (a) – Numerical results for the entanglement of the symmetric interval $A = [-x_0, x_0]$ for different values of λ as function of time. The dashed horizontal line mark the plateau $S_1 = 1/3 \log(x_0) + 2\kappa_1$ for $\lambda = 1$. (b) – Plot of the ratios $r(\lambda)$ in Eq. (7.19) as function of λ and different values of the interval size $x_0 = 20$, $x_0' = 40$, $x_0'' = 60$. The full line shows the behaviour of $c_{\text{eff}}(\lambda)$, given by Eq. (7.20).

cannot be determined with a semiclassical approach. For the homogeneous Hamiltonian ($\lambda = 1$), the quantum fluctuations can be incorporated using the quantum hydrodynamic description [282, 287–291, 353, 354] that we have reviewed in Sec. 6.2. According to this theory, the relevant contribution to the entanglement in zero-entropic states is given by linear quantum fluctuations $\delta\hat{n}_t(x)$ at the edges of $n_t(x, k)$, which (in euclidean time) are described by the inhomogeneous field theory in the arctic circle of Sec. 6.2.2.

The time evolution of the entanglement entropy in the case without defect is a straightforward but tedious adaptation of the calculations reported, e.g., in Ref. [290] for a slightly different situation. We only report here the final result (which indeed coincides with the one in Refs. [290, 355])

$$S_n([-x_0, x_0], t) = \frac{n+1}{12n} \log\left[x_0^2(1 - x_0^2/t^2)^3\right] + 2\kappa_n, \tag{7.16}$$

where κ_n is the same non-universal amplitude that appeared in Eq. (6.42) for half-space, in particular $\kappa_1 \approx 0.4785$ [314, 315]. For $t \gg x_0$, Eq. (7.16) predicts a saturation of the half-system entanglement to the value $S_1([-x_0, x_0], t \gg x_0) \approx 1/3 \log(x_0) + 2\kappa_1$.

Numerical exact calculations for the lattice model reveal a similar behaviour for the half-system entanglement even in the presence of the defect $\lambda \in (0, 1)$, see Fig. 7.6-(a). We expect that the large-time plateaus in the figure scale like $\log(x_0)$ for large x_0, i.e., we expect

$$S_1([-x_0, x_0], \infty) \sim \frac{c_{\text{eff}}(\lambda)}{3} \log(x_0) + \gamma(\lambda). \tag{7.17}$$

To have an unbiased estimate of $c_{\text{eff}}(\lambda)$ we proceed as following. We first consider the difference of plateaus reached at fixed λ for different sizes of A, i.e.,

$$\Delta S_1^{(\lambda)}(x_0, x_0') \equiv S_1([-x_0, x_0], \infty) - S_1([-x_0', x_0'], \infty), \tag{7.18}$$

(where by "infinite time" we just means confidently within the plateau); then we take the ratio

$$r(\lambda) = \Delta S_1^{(\lambda)}(x_0, x_0') / \Delta S_1^{(1)}(x_0, x_0'), \tag{7.19}$$

that for large x_0, x_0' converges to $c_{\text{eff}}(\lambda)$ by construction. The perfect collapse in Fig. 7.6-(b) of the ratios $r(\lambda)$ for different pairs x_0, x_0' confirms the conjectured behaviour of Eq. (7.17). Moreover, the resulting factor $c_{\text{eff}}(\lambda)$ is numerically consistent with the effective central charge appearing in the ground-state entanglement of free fermions with defects [326] given by

$$\begin{aligned} c_{\text{eff}}(\lambda) = -\frac{6}{\pi^2}\Big\{ &(1+\lambda)\mathrm{Li}_2(-\lambda) + (1-\lambda)\mathrm{Li}_2(\lambda) \\ &+ \Big[(1+\lambda)\log(1+\lambda) + (1-\lambda)\log(1-\lambda)\Big]\log\lambda \Big\}, \end{aligned} \tag{7.20}$$

that satisfies $c_{\text{eff}}(0) = 0$ and $c_{\text{eff}}(1) = 1$. We believe that, being these logarithmic contributions related to zero-point fluctuations, it should be possible to map explicitly the equilibrium entanglement to the non-equilibrium one. However, this goes beyond the scope of this work.

7.3 Final remarks

We studied the time evolution of the entanglement entropy in a domain wall melting across a conformal defect. We showed that the pure-system logarithmic growth in time of the entanglement entropy is turned, by the smallest defect, into a linear one with an extensive stationary value corresponding to a non-vanishing thermodynamic Yang-Yang entropy. Furthermore we showed that there are extensive long-range correlations between sites which are mirror images of each other with respect to the defect. None of these effects has an equilibrium counterpart. We also characterised numerically the subleading logarithmic contributions, which are not captured by the quasiparticle picture.

A natural extension of this work could be the study of the dynamics in the presence of multiple defects. In that case, we expect a richer pattern of long-range correlations arising from multiple scattering across the defects, e.g. along the lines of Ref. [126]. However, we still do not know how to deal systematically with those effects and how to incorporate them in a quasiparticle picture for the entanglement.

Chapter 8

Entanglement Hamiltonians and the quasiparticle picture

We conclude the thesis with the present Chapter, based on Ref. [356], in which we study global quantum quenches in free fermionic models. We show that in general the entanglement Hamiltonian after such a quench can be reconstructed from the quasiparticle picture [86, 352, 357, 358]. Originally developed to describe entanglement entropy growth after a quantum quench in integrable systems, this picture posits that entanglement is carried by pairs of quasiparticles emitted from the initial state. As these quasiparticles propagate through the system, they spread entanglement in a manner that can be quantitatively tracked and predicted. It has since been shown to be applicable to the calculation of other quantities such as some correlation functions [359], negativity [122, 360], full counting statistics [361–363], symmetry resolved entanglement [363–365], operator entanglement [366, 367], and the entanglement asymmetry [368–370]. However, despite the fact that it contains information about most of these quantities, the application of the QPP to describe the EH has remained extremely elusive. In this Chapter, we fill this void and derive a very compact form for the EH after a generic integrable quench in a free-fermionic model.

8.1 Post-quench Entanglement Hamiltonian

We prepare our system in some pure initial state ρ and then allow it to undergo unitary time evolution according to the Hamiltonian of the form $H = \sum_k \varepsilon_k c_k^\dagger c_k$ where $c_k^\dagger, c_k$ are canonical fermions with energy ε_k such that $[H, \rho] \neq 0$. According to the QPP, each point in space acts as a source of quasiparticles that propagate through the system at velocity $v_k = \partial_k \varepsilon_k$ spreading correlations. Particle pairs entirely contained within a subsystem A (or its complement B) do not contribute to the entanglement between A and B, while shared pairs do. Hence, the post-quench RDM can be written as the tensor product of an entangling and of a pure part

$$\rho_A^{(t)} \approx \frac{e^{-K^{(t)}_{A,\,\mathrm{QP}}}}{Z_A} \otimes \rho^{(t)}_{\mathrm{pure}}\,. \tag{8.1}$$

Here the pure RDM comes from the pairs of quasiparticles that are both in A, while the entangling one, with EH $K^{(t)}_{A,\,\mathrm{QP}}$, describes the pairs shared between A and its complement B, which are entirely responsible for the entanglement. The main result of this paper is that $K^{(t)}_{A,\,\mathrm{QP}}$ takes the *two-body* form

$$K^{(t)}_{A,\,\mathrm{QP}} = \int_0^\ell \mathrm{d}x \int \mathrm{d}z\, [\mathcal{K}_R(x,z) + \mathcal{K}_L(x,z)]\, c^\dagger_x c_{x-z}\,, \tag{8.2}$$

where $\mathcal{K}_R$ and $\mathcal{K}_L$ are the kernels

$$\mathcal{K}_R(x,z) = \int_{k>0} \frac{\mathrm{d}k}{2\pi}\, \eta(k)\, \Theta(\min(2v_k t, \ell) - x)\, e^{\mathrm{i}kz}, \tag{8.3}$$

$$\mathcal{K}_L(x,z) = \int_{k<0} \frac{\mathrm{d}k}{2\pi}\, \eta(k)\, \Theta(\max(\ell + 2v_k t, 0) - x)\, e^{\mathrm{i}kz}, \tag{8.4}$$

$\Theta(x)$ is the Heaviside function, $c^\dagger_x, c_x$ are the real space fermion operators and $\ell = |A|$. Furthermore, we introduced

$$\eta(k) = \log\left[\frac{1-n(k)}{n(k)}\right], \tag{8.5}$$

where $n(k) = \mathrm{Tr}[\rho\, c^\dagger_k c_k]$. As a conserved quantity, $\eta(k)$ can be computed in the initial state without solving the dynamics. Therefore, this form of the EH clearly enables its reconstruction without needing to solve the dynamics. We stress that the main property of the form (8.2) is to be entirely determined by two-body terms with a kernel that depend on the distance z in a light-cone fashion, see also Fig. 8.1 for an explicit example.

The majority of the rest of this Chapter is devoted to deriving this result and presenting several checks, numerical and analytical, of its validity. Before this however, we make some brief comments on the structure of Eq. (8.2). Immediately after the quench, the RDM is entirely captured by $\rho^{(t)}_{\mathrm{pure}}$ since no quasiparticle are yet shared. As time grows, the quasiparticles pass through the entangling points moving between A and B. Accordingly, the pure part $\rho^{(t)}_{\mathrm{pure}}$ becomes progressively smaller, while the entangling one grows. The entangling part is governed by the kernels $\mathcal{K}_{L,R}(x,z)$ which can be interpreted as the contributions from the left (L) and right (R) moving quasiparticles which spread from the left and right edges of A respectively. From the structure of Eqs. (8.3) and (8.4), we see that for $t < \ell/(4v_{\max})$, where $v_{\max} = \max(v_k)$, the growth happens inside light-cones centred in 0 and ℓ, as expected from the quasiparticle picture. The real space structure of the EH is determined by the initial state through $\eta(k)$.

At sufficiently large times after the quench, the system relaxes locally to a stationary state which, generically for a free model is a generalised Gibbs ensemble (GGE) that incorporates all conserved charges. In the RDM (8.1), the pure part no longer contributes, and the EH (8.2) fully characterises the RDM. In this limit, the time dependence of $\mathcal{K}_{L,R}$ drops out and the asymptotic value of the EH (8.2) is

$$\begin{aligned} K^{(\infty)}_{A,\,\mathrm{QP}} &= \int_0^\ell \mathrm{d}x \int_0^\ell \mathrm{d}y \left[\int \frac{\mathrm{d}k}{2\pi}\,\eta(k)\,e^{\mathrm{i}k(x-y)}\right] c^\dagger_x c_y \\ &= \int \frac{\mathrm{d}k}{2\pi}\,\eta(k)\,c^\dagger_k c_k, \end{aligned} \tag{8.6}$$

which yields the expected GGE and allows $\eta(k)$ to be interpreted as the Lagrange multiplier of the conserved charges $c^\dagger_k c_k$ [371]. This shows that Eq. (8.2) correctly describes the generalised thermalisation of the subsystem after the quantum quench.

This light-cone behaviour and eventual relaxation is especially evident when the quenching Hamiltonian has a linear dispersion, $\varepsilon_k = vk$. In this case the quasiparticle velocity v is independent of k and the Heaviside functions can be taken outside of the mode integrals in (8.3), (8.4). Moreover, if $\eta(k) = \beta\varepsilon_k$, as happens after a quench in CFT [307], we find that

$$\begin{aligned} K^{(t)}_{A,\,\mathrm{QP}} = \beta &\int_0^{\min(2vt,\ell)} \mathrm{d}x \int \mathrm{d}z \int_{k>0} \frac{\mathrm{d}k}{2\pi}\,\varepsilon_k\,e^{\mathrm{i}kz}\,c^\dagger_x c_{x-z} \\ &\qquad + \beta \int_{\max(\ell-2vt,0)}^{\ell} \mathrm{d}x \int \mathrm{d}z \int_{k<0} \frac{\mathrm{d}k}{2\pi}\,\varepsilon_k\,e^{\mathrm{i}kz}\,c^\dagger_x c_{x-z} \\ = \beta &\left[\int_0^{\min(2vt,\ell)} \mathrm{d}x\,T(x) + \int_{\max(\ell-2vt,0)}^{\ell} \mathrm{d}x\,\overline{T}(x)\right], \end{aligned} \tag{8.7}$$

where T and $\overline{T}$ are the right and left moving stress-energy operators. Eq. (8.7) agrees with previous results for the post-quench entanglement Hamiltonian in a CFT [34, 372]. Note that in this case the system relaxes locally to a Gibbs state in which only the Hamiltonian appears [373] and accordingly the EH has only short ranged hopping terms. This however, is not generically the case and $K^{(t)}_{A,\,\mathrm{QP}}$ can have a more intricate structure depending on both the initial state as encoded in $\eta(k)$ and v_k.

In Fig. 8.1 we plot the values of the nearest neighbour and beyond nearest neighbour terms of $K^{(t)}_{A,\,\mathrm{QP}}$ for a particular case (see Sec. 8.1.2 for details). What is evident, is that each of the terms exhibits a light-cone like spreading emitting from the subsystem edges. Moreover we see that the quasiparticle structure has endowed the hopping terms with a parity effect such that at finite times hopping over an odd number of sites is even with respect to reflection about the subsystem centre while hopping over an even number of sites is odd with respect to this. As a result, in the long time limit only odd site hopping terms remain. From Fig. 8.2 we also see that the relative strength of these hopping terms decays with a power law behaviour as a function of hopping distance. Overall it is remarkable that the complicated shapes of the EH reported in the figures are captured perfectly by a simple quasiparticle form as Eq. (8.2).

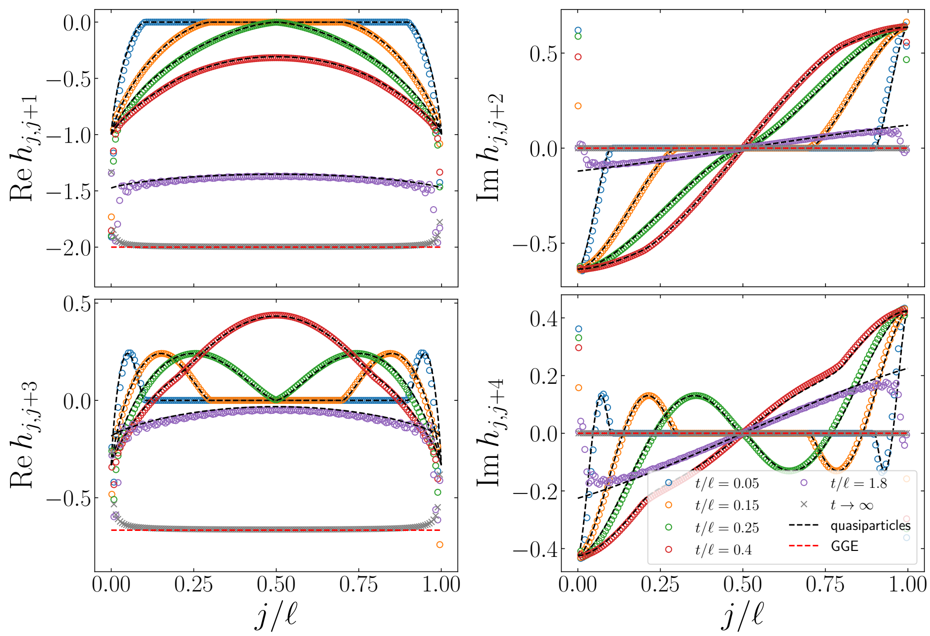

Figure 8.1: EH couplings $h_{j,j+z}$ between fermions at distances $z = 1, 2, 3, 4$ after a quench from the dimer state. We study an interval of length $\ell = 800$ at different times t after the quench. The symbols are obtained from Eq. (1.15) using the correlation matrix (8.23), while the dashed black line is the QPP prediction (8.2). The couplings are real for odd distances z, while they are imaginary for even z. For $t \to \infty$, (gray crosses), the data match the GGE, cf. Eq. (8.6) (red dashed line). We observe a perfect agreement, with minor deviations near the endpoints where the QPP is not expected to work. For times $t/\ell \leqslant 0.25$ (blue and orange symbols) the couplings are non zero only inside of two light-cones centered at the endpoints. For $t > 0.25\ell$, the two light-cones merge and the EH relaxes toward the GGE.

8.1.1 Derivation

As a starting point of our computation, we assume that at $t = 0$ the initial state is a squeezed state of the form

$$|\psi^{(0)}\rangle = \exp\left\{ \mathrm{i} \int_{k>0} \frac{\mathrm{d}k}{2\pi} \, \mathcal{M}(k) \, c_k^\dagger c_{-k}^\dagger \right\} |0\rangle \ , \tag{8.8}$$

where $|0\rangle$ is the vacuum state of the post-quench Hamiltonian and $\mathcal{M}(k)$ is some odd function whose particular form is unimportant. In states of the form (8.8), the population $n(k)$ of the fermionic modes is

$$n(k) = \frac{\mathcal{M}(k)^2}{1 + \mathcal{M}(k)^2} \, . \tag{8.9}$$

An important property of the state (8.8) is that it has a natural pair structure, in which only modes of opposite momenta are entangled. For this reason, it would seem that Eq. (8.8) is a very specific choice, however squeezed states appear ubiquitously in quantum quenches in integrable models, see, e.g., Ref. [374].

To show that the RDM follows a quasiparticle picture, in the spirit of Ref. [349] we employ an hydrodynamic description. We introduce hydrodynamic cells of length Δ much larger than the lattice spacing s (or any other short distance cutoff) but smaller than the typical length ℓ of our system $s \ll \Delta \ll \ell$, and we impose periodic boundary conditions at the edges of the cell. Quasiparticles are defined as wave-packets localised inside an hydrodynamic cell, obtained by performing a Fourier transform only inside the cell [349]

$$b^\dagger_{x,k} = \frac{1}{\Delta}\int_0^\Delta \mathrm{d}y\, e^{-\mathrm{i}ky}\, c^\dagger_{x+y}\,, \qquad c^\dagger_{x+y} = \sum_k e^{\mathrm{i}ky}\, b^\dagger_{x,k}\,, \tag{8.10}$$

where x labels the fluid cell and y the position inside the cell. We now make the fundamental assumption that the correlations in the initial state (8.8) decay fast enough with distance in real space. If this holds, by taking hydrodynamic cells larger than the correlation length $\Delta \gtrsim \xi$, we can neglect correlations between different cells and we can approximate the initial state as a tensor product over the cells

$$\rho^{(0)} = |\psi^{(0)}\rangle\langle\psi^{(0)}| \approx \bigotimes_{k>0}\bigotimes_{x_0} \rho^{(0)}_{k,x_0}\,, \tag{8.11}$$

where x_0 labels the hydrodynamic cell and $\rho^{(0)}_{k,x_0}$ is the density matrix of a single pair of quasiparticles [349]

$$\begin{aligned}\rho^{(0)}_{x_0,k} = n(k) b^\dagger_{x_0,k} b_{x_0,k} b^\dagger_{x_0,-k} b_{x_0,-k} + (1-n(k))(1 - b^\dagger_{x_0,k} b_{x_0,k} b^\dagger_{x_0,-k} b_{x_0,-k}) + \\ + \mathrm{i}\sqrt{n(k)(1-n(k))}(b^\dagger_{x_0,k} b^\dagger_{x_0,-k} - b_{x_0,-k} b_{x_0,k})\,.\end{aligned} \tag{8.12}$$

In this approximation, only pairs of quasiparticles with opposite momenta and occupying the same cell are entangled with each others [349].

At time $t > 0$, we evolve the state with the quenching Hamiltonian discussed above. If the hydrodynamic cells are large enough compared with the lattice spacing, the diffraction of the wave-packet is negligible and under unitary evolution the quasiparticles move ballistically with group velocity v_k

$$e^{\mathrm{i}Ht} b_{x_0,\pm k} e^{-\mathrm{i}Ht} = b_{x_0 \pm v_k t, k}\,. \tag{8.13}$$

The density matrix (8.12) of a single pair of quasiparticles which originated in x_0, at time t becomes [349]

$$\begin{aligned}\rho^{(t)}_{x_0,k} = {} & n(k)\, b^\dagger_{x_0+v_k t,k} b_{x_0+v_k t,k} b^\dagger_{x_0-v_k t,-k} b_{x_0-v_k t,-k} + \\ & + (1-n(k))(1 - b^\dagger_{x_0+v_k t,k} b_{x_0+v_k t,k} b^\dagger_{x_0-v_k t,-k} b_{x_0-v_k t,-k}) + \\ & + \mathrm{i}\sqrt{n(k)(1-n(k))}(b^\dagger_{x_0+v_k t,k} b^\dagger_{x_0-v_k t,-k} - b_{x_0-v_k t,-k} b_{x_0+v_k t,k})\,.\end{aligned} \tag{8.14}$$

We now compute the RDM of an interval $A = [0, \ell]$. Thanks to the structure of the density matrix as the product states of quasiparticle pairs, we only need to study the RDM of a single pair. To fix the ideas, consider a pair starting at position $x_0 \in A$. At the beginning of the evolution, both quasiparticles are contained in the interval. In this case, tracing out the degrees of freedom in the complement B has no effect on the RDM of the pair, which remains pure and equal to Eq. (8.14) and does not contribute to the entanglement entropy.

At a later time, the, e.g., left-moving quasiparticle escapes the interval $x_0 - v_k t < 0$, while the right-moving one is still inside $0 < x_0 + v_k t < \ell$. Tracing out over B we obtain the RDM of the right-moving fermion, which is mixed and equal to

$$\rho^{(t)}_{A,x_0,k} = n(k)\, b^\dagger_{x_0+v_k t,k} b_{x_0+v_k t,k} + (1 - n(k))(1 - b^\dagger_{x_0+v_k t,k} b_{x_0+v_k t,k})\,. \tag{8.15}$$

By following the trajectories of the quasiparticles, we see that at time t the quasiparticles that are shared between A and its complement are the right-movers that originated at $x_0 \in [-v_k t, \min(v_k t, \ell - v_k t)]$ and the left-movers that started at $x_0 \in [\ell - \min(|v_k|\, t, \ell - |v_k|\, t), \ell + |v_k|\, t]$. Expressing everything in terms of the current position of the quasiparticle $x = x_0 + v_k t$ for right-movers, $x = x_0 - |v_k|\, t$ for left movers, we have

$$\rho^{(t)}_A \approx \rho^{(t)}_{A,R\ \mathrm{QP}} \otimes \rho^{(t)}_{\mathrm{pure}} \otimes \rho^{(t)}_{A,L\ \mathrm{QP}}\,, \tag{8.16}$$

where

$$\rho^{(t)}_{A,R\ \mathrm{QP}} = \bigotimes_{k>0} \bigotimes_{x=0}^{\min(2v_k t,\ell)} \rho^{(t)}_{A,x,k}\,, \tag{8.17}$$

$$\rho^{(t)}_{A,L\ \mathrm{QP}} = \bigotimes_{k<0} \bigotimes_{\substack{x=\ell-\\ \min(2|v_k|t,\ell)}}^{\ell} \rho^{(t)}_{A,x,k}\,, \tag{8.18}$$

are the mixed parts of the RDM and $\rho^{(t)}_{\mathrm{pure}}$ is the pure part due to the non-shared pairs.

To find the entanglement Hamiltonian of the mixed part of Eq. (8.1), we rewrite Eq. (8.15) as an exponential, using the property $\left(b^\dagger b\right)^2 = b^\dagger b$. We obtain $\rho^{(t)}_A = e^{-K^{(t)}_{A,\ \mathrm{QP}}}/Z_A$, where Z_A is a normalisation and

$$K^{(t)}_{A,\ \mathrm{QP}} = \int_{k>0} \frac{\mathrm{d}k}{2\pi} \int_0^{\min(2v_k t,\ell)} \mathrm{d}x\, \eta(k)\, b^\dagger_{x,k} b_{x,k} + \int_{k<0} \frac{\mathrm{d}k}{2\pi} \int_{\max(\ell-2|v_k|t,0)}^{\ell} \mathrm{d}x\, \eta(k)\, b^\dagger_{x,k} b_{x,k}\,, \tag{8.19}$$

The final step is to express the EH (8.19) in terms of fermions in real space $c^\dagger_x$, c_x. This simply amounts to a change of basis, performed using the inverse Fourier transform in the cell (8.10). Performing this, we arrive to the main result of this work, Eq. (8.2). An analogous quasiparticle expression can also be determined for $\rho^{(t)}_{\mathrm{pure}}$ thereby completely fixing the full RDM.

As written in Eq. (8.19) it is straightforward to recover the quasiparticle picture prediction for the growth of the Rényi entanglement entropy $S_A^{(\alpha)} = \frac{1}{1-\alpha}\log \mathrm{Tr}_A\,(\rho_A)^\alpha$. To achieve this we note that the tensor product structure of the RDM means we can compute the contribution of each quasiparticle, $b^\dagger_{x,k}$ and that the entangling part for each of these takes the form of a generalised Gibbs state. Equating the Rényi entanglement entropy with the Fermi-Dirac Rényi entropy of this state and summing over all quasiparticle contributions we find

$$S_A^{(\alpha)}(t) = \int \frac{dk}{2\pi}\, \min(2|v_k|t,\ell)\, h_\alpha(n(k))\,, \tag{8.20}$$

where $h_\alpha(x) = \frac{1}{1-\alpha}\log(x^\alpha + (1-x)^\alpha)$. Along similar lines and by including also the form of the pure part one can reproduce all previous QPP predictions for correlation functions [359], full counting statistics [363] and symmetry resolved entanglement measures [363–365].

8.1.2 Numerical analysis

To verify the correctness of our entanglement Hamiltonian in Eq. (8.2), we study a quench from the dimer state

$$|D\rangle = \prod_{j=1}^{L/2} \frac{1}{\sqrt{2}}\left(c^\dagger_{2j} - c^\dagger_{2j-1}\right)|0\rangle\,. \tag{8.21}$$

to the hopping Hamiltonian

$$H = -\frac{1}{2}\sum_i c^\dagger_i c_{i+1} + \text{h.c.}\,. \tag{8.22}$$

This quench has been studied in Ref. [339], where it was found that the two-point correlation matrix at time t is given by [136, 339, 365]

$$C^{(t)}_{i,j} = C^{(\infty)}_{i,j} + \mathrm{i}\frac{i-j}{4t} e^{-\mathrm{i}\frac{\pi}{2}(i+j)} J_{i-j}(2t)\,, \tag{8.23}$$

where $J_\nu(z)$ is Bessel's function and we have introduced the asymptotic value of the correlation matrix [136, 339]

$$C^{(\infty)}_{i,j} = \frac{1}{2}\left[\delta_{i,j} + \frac{1}{2}\left(\delta_{i,j-1} + \delta_{i,j+1}\right)\right]. \tag{8.24}$$

As we have discussed in the Introduction, using Eq. (1.15) it is possible to directly compute the single particle entanglement Hamiltonian $h_{i,j}$ from the correlation matrix C_A restricted to the subsystem A, where $h_{i,j}$ is related to the full entanglement Hamiltonian through Eq. (1.14). In order to compare the result of Eq. (1.15) with our prediction in Eq. (8.2), however, we need to take into account that at finite time Eq. (8.2) only describes the low lying part of the entanglement spectrum. Since according to Eq. (1.15) the higher

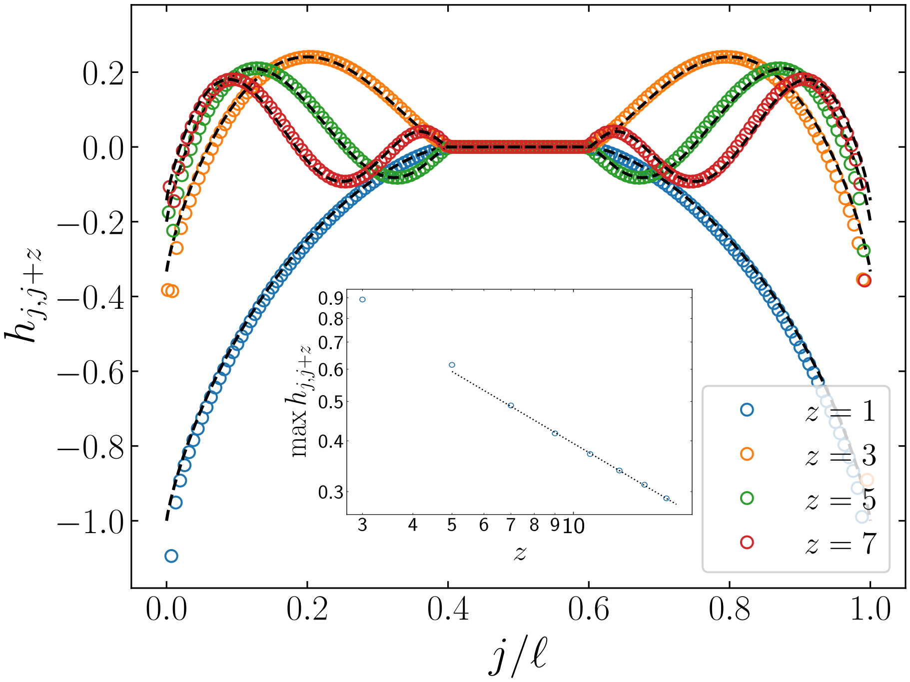

Figure 8.2: EH couplings $h_{j,j+z}$ after a quench from the dimer state. We consider an interval of length $\ell = 800$ at time $t/\ell = 0.2$. In the main plot we report the couplings (obtained using Eqs. (1.15) and (8.23)) for different (odd) distances z. The black dashed line is the prediction (8.2). The couplings present an oscillatory behaviour with a peak which is slowly decreasing as the distance z increases. The inset reports the peak value as a function of the separation z in logarithmic scales, for z odd from 3 to 17. The decay of the peak is compatible with a power law with power $\alpha = -0.6$ (black dotted line).

part of the entanglement spectrum is given by the eigenvalues of C_A that are close to either 0 or 1, we introduce a cut-off on the spectrum, projecting out all the eigenvalues of Eq. (8.23) which are smaller than 10^{-4} or larger than $1 - 10^{-4}$.

Applying Eq. (1.15) to the asymptotic value of the correlation matrix, we can also immediately compute the large time EH, which agrees with the expected GGE. In the $t \to \infty$ limit, the full entanglement spectrum is described by the GGE, therefore in this case we do not impose any cut-off on the spectrum. The time-dependent numerical results for the EH are reported in Figs. 8.1 and 8.2 showing a perfect match with the QPP prediction.

8.2 Final remarks

In this Chapter, we derived a quasiparticle prediction, Eq. (8.2), for the EH after a global quantum quench in any system of non-interacting fermions. Remarkably, this simple form effectively captures the complex structure of the EH.

Our result paves the way for many intriguing generalisations. One key advantage of the QPP is its adaptability for calculating the entanglement entropy of disjoint intervals [86,375], as well as more complex quantities like the negativity [122, 360]. Generalising these results to an operator level, such as calculating the entanglement Hamiltonian of disjoint intervals or the negativity Hamiltonian [81, 84, 131], would be extremely interesting. Additionally, the QPP applies also for certain dissipative systems [376–379], where also we could think of adapting our derivation. Furthermore, the QPP has been recently combined with dimensional reduction [380, 381] to describe the entanglement entropy [382] and asymmetry [383] in higher dimensional non-interacting models. The same could be done also for the EH. A significant challenge is generalising our result to interacting integrable models, where the QPP breaks down in the calculation of Rényi entanglement entropy [350] and charged moments [363].

From a speculative perspective, it is well known that the primary difficulty in numerically studying with tensor networks the time evolution after a quench lies in the rapid growth of entanglement entropy [384–386]. However, once the EH is known, its properties (e.g. the spectrum) may be extracted by means of equilibrium simulations (like quantum Monte Carlo) even when there is a volumetric scaling of the entropy. Furthermore, as recently proposed [36–38], the EHs may be engineered in cold-atom and trapped-ion setups to experimentally access the spectrum, even in the absence of a viable numerical algorithm.

Acknowledgments

It is perhaps a sort of cliché to claim that the present work would not have existed without the help of other people. It is, nevertheless, true. I am profoundly grateful to all my collaborators during these years, Stefano Scopa, Luca Capizzi, Sara Murciano, prof. Erik Tonni, Filiberto Ares, David Horváth, Michele Fossati, Colin Rylands and, of course, my supervisor, prof. Pasquale Calabrese. If any of these collaborations has been at times less than smooth, to use an euphemism, the fault lies squarely with my personality.

A special thank goes to prof. Olalla Castro-Alvaredo, Michele Mazzoni and Fabio Sailis, both for their collaboration and for making me feel at home.

Between all the people with which I have had the pleasure to interact, I wish to thank in particular one who dedicated several hours to discuss and explain to me, Michele. If my shallow understanding of physics has deepened a bit during the past four years, it is also thanks to the time spent together.

Even if arguing in favour of a certain kind of determinism in matters of life is somewhat incompatible with quantum mechanics (and thus with the present work), the reader shall excuse me if I claim that this thesis would not have existed without my mom and dad. All those evenings reading *Scientific American* with you are more responsible for my love of science than anything else life threw at me. I exited elementary school knowing that I would have become a (particle) physicist, and even if not everything played out as intended, I am closer to that goal that I had any right to hope for, and for this I am grateful.

Together with my parents I thank Lia and my grandparents. It was not easy to be away this past decade. Thank you for being a place I could call home.

Many things happen in four years. Without someone by your side to help carry its weight, life may overwhelm you. Thank you Chiara for carrying its weight with me. We are a team, always.

I finally thank Dr. M. Bucci, who greatly helped me navigating these four years.

Bibliography

[1] A. Einstein, B. Podolsky, and N. Rosen, *Can Quantum-Mechanical Description of Physical Reality Be Considered Complete?*, Phys. Rev. **47** (1935) 777.

[2] E. Schrödinger, *Discussion of Probability Relations between Separated Systems*, Mathematical Proceedings of the Cambridge Philosophical Society **31** (1935) 555.

[3] J. S. Bell, *On the Einstein Podolsky Rosen paradox*, Physics Physique Fizika **1** (1964) 195.

[4] J. S. Bell, *Speakable and Unspeakable in Quantum Mechanics*, Cambridge University Press, Cambridge (2004).

[5] J. F. Clauser, M. A. Horne, A. Shimony, and R. A. Holt, *Proposed Experiment to Test Local Hidden-Variable Theories*, Phys. Rev. Lett. **23** (1969) 880.

[6] S. J. Freedman and J. F. Clauser, *Experimental Test of Local Hidden-Variable Theories*, Phys. Rev. Lett. **28** (1972) 938.

[7] A. Aspect, P. Grangier, and G. Roger, *Experimental Tests of Realistic Local Theories via Bell's Theorem*, Phys. Rev. Lett. **47** (1981) 460.

[8] G. Aad *et al.* (ATLAS collaboration), *Observation of quantum entanglement in top-quark pairs using the ATLAS detector*, arXiv:2311.07288.

[9] M. A. Nielsen and I. L. Chuang, *Quantum computation and quantum information*, Cambridge University Press, Cambridge, UK, 10th anniversary ed. (2010).

[10] A. M. Dalzell *et al.*, *Quantum algorithms: A survey of applications and end-to-end complexities*, arXiv:2310.03011.

[11] L. Amico, R. Fazio, A. Osterloh, and V. Vedral, *Entanglement in many-body systems*, Rev. Mod. Phys. **80** (2008) 517.

[12] P. Calabrese, J. Cardy, and B. Doyon, *Entanglement entropy in extended quantum systems*, J. Phys. A **42** (2009) 500301.

[13] J. Eisert, M. Cramer, and M. B. Plenio, *Area laws for the entanglement entropy*, Rev. Mod. Phys. **82** (2010) 277.

[14] N. Laflorencie, *Quantum entanglement in condensed matter systems*, Phys. Rep. **646** (2016) 1.

[15] L. Bombelli, R. K. Koul, J. Lee, and R. D. Sorkin, *Quantum source of entropy for black holes*, Phys. Rev. D **34** (1986) 373.

[16] T. Nishioka, S. Ryu, and T. Takayanagi, *Holographic entanglement entropy: an overview*, J. Phys. A **42** (2009) 504008.

[17] M. Rangamani and T. Takayanagi, *Holographic Entanglement Entropy*, Lect. Notes Phys. **931** (2017).

[18] P. Calabrese and J. Cardy, *Entanglement entropy and conformal field theory*, J. Phys. A **42**, 504005 (2009).

[19] H. Casini and M. Huerta, *Lectures on entanglement in quantum field theory*, arXiv:2201.13310.

[20] C. G. Callan and F. Wilczek, *On Geometric Entropy*, Phys. Lett. B **333** (1994) 55.

[21] C. Holzhey, F. Larsen, and F. Wilczek, *Geometric and renormalized entropy in conformal field theory*, Nucl. Phys. B **424** (1994) 443.

[22] P. Calabrese and J. Cardy, *Entanglement entropy and quantum field theory*, J. Stat. Mech. (2004) P06002.

[23] R. Haag, *Local Quantum Physics: Fields, Particles, Algebras*, Springer, Berlin, Heidelberg, Germany (1996).

[24] E. Witten, *APS Medal for Exceptional Achievement in Research: Invited article on entanglement properties of quantum field theory*, Rev. Mod. Phys. **90**, 045003 (2018).

[25] M. Dalmonte, V. Eisler, M. Falconi, and B. Vermersch, *Entanglement Hamiltonians: from field theory, to lattice models and experiments*, Ann. Phys. (Berlin) **534** (2022) 2200064.

[26] J. J. Bisognano and E. H. Wichmann, *On the Duality Condition for a Hermitian Scalar Field*, J. Math. Phys. **16** (1975) 985.

[27] J. J. Bisognano and E. H. Wichmann, *On the Duality Condition for Quantum Fields*, J. Math. Phys. **17** (1976) 303.

[28] W. G. Unruh, *Notes on black-hole evaporation*, Phys. Rev. D **14** (1976) 870.

[29] S. A. Fulling, *Nonuniqueness of canonical field quantization in Riemannian space-time*, Phys. Rev. D **7** (1973) 2850.

[30] P. C. W. Davies, *Scalar particle production in Schwarzschild and Rindler metrics*, J. Phys. A **8** (1975) 609.

[31] P. Hislop and R. Longo, *Modular Structure of the Local Algebras Associated With the Free Massless Scalar Field Theory*, Commun. Math. Phys. **84** (1982) 71.

[32] H. Casini, M. Huerta, and R. Myers, *Towards a derivation of holographic entanglement entropy*, JHEP **05** (2011) 036.

[33] G. Wong, I. Klich, L. Pando Zayas, and D. Vaman, *Entanglement Temperature and Entanglement Entropy of Excited States*, JHEP **12** (2013) 020.

[34] J. Cardy and E. Tonni, *Entanglement hamiltonians in two-dimensional conformal field theory*, J. Stat. Mech. (2016) 123103.

[35] K. Ohmori and Y. Tachikawa, *Physics at the entangling surface*, J. Stat. Mech. (2015) P04010.

[36] M. Dalmonte, B. Vermersch, and P. Zoller, *Quantum Simulation and Spectroscopy of Entanglement Hamiltonians*, Nature Phys. **14** (2018) 827.

[37] C. Kokail, R. van Bijnen, A. Elben, B. Vermersch, and P. Zoller, *Entanglement Hamiltonian Tomography in Quantum Simulation*, Nature Phys. **17** (2021) 936.

[38] C. Kokail, B. Sundar, T. V. Zache, A. Elben, B. Vermersch, M. Dalmonte, R. van Bijnen, and P. Zoller, *Quantum Variational Learning of the Entanglement Hamiltonian*, Phys. Rev. Lett. **127** (2021) 170501.

[39] T. V. Zache, C. Kokail, B. Sundar, and P. Zoller, *Entanglement Spectroscopy and probing the Li-Haldane Conjecture in Topological Quantum Matter*, Quantum **6** (2022) 702.

[40] M. K. Joshi, C. Kokail, R. van Bijnen, F. Kranzl, T. V. Zache, R. Blatt, C. F. Roos, and P. Zoller, *Exploring large-scale entanglement in quantum simulation*, Nature **624** (2023) 539.

[41] I. Peschel, M. Kaulke, and O. Legeza, *Density-matrix spectra for integrable models*, Ann. Physik (Leipzig) **8** (1999) 153.

[42] I. Peschel and T. T. Truong, *Corner Transfer Matrices for the Gaussian Model*, Ann. Physik (Leipzig) **48** (1991) 185.

[43] I. Peschel and T. T. Truong, *Corner transfer matrices and conformal invariance*, Z. Phys. B **69** (1987) 385.

[44] B. Davies, *Corner transfer matrices for the Ising model*, Physica A **154** (1988) 1.

[45] T. T. Truong and I. Peschel, *Diagonalisation of finite-size corner transfer matrices and related spin chains*, Z. Phys. B **75** (1989) 119.

[46] B. Davies, *On the spectrum of six-vertex corner transfer matrices*, Physica A **159** (1989) 171.

[47] H. Frahm and H. B. Thacker, *Corner transfer matrix eigenstates for the six vertex model*, J. Phys. A **24** (1991) 5587.

[48] M. G. Tetel'man, *Lorentz group for two-dimensional integrable lattice systems*, Sov. Phys. JETP **55** (1982) 306.

[49] H. B. Thacker, *Corner Transfer Matrices and Lorentz Invariance on a Lattice*, Physica D **18** (1986) 348.

[50] E. Ercolessi, S. Evangelisti, and F. Ravanini, *Exact entanglement entropy of the XYZ model and its sine-Gordon limit*, Phys. Lett. A **374** (2010) 2101.

[51] I. Peschel and M.-C. Chung, *Density matrices for a chain of oscillators*, J. Phys. A **32** (1999) 8419.

[52] V. Eisler, G. Di Giulio, E. Tonni, and I. Peschel, *Entanglement hamiltonians for non-critical quantum chains*, J. Stat. Mech. (2020) 103102.

[53] G. Giudici, T. Mendes-Santos, P. Calabrese, and M. Dalmonte, *Entanglement hamiltonians of lattice models via the Bisognano-Wichmann theorem*, Phys. Rev. B **98** (2018) 134403.

[54] T. Mendes-Santos, G. Giudici, M. Dalmonte, and M. A. Rajabpour, *Entanglement Hamiltonian of quantum critical chains and conformal field theories*, Phys. Rev. B **100** (2019) 155122.

[55] J. Zhang, P. Calabrese, M. Dalmonte, and M. A. Rajabpour, *Lattice Bisognano-Wichmann modular Hamiltonian in critical quantum spin chains*, SciPost Phys. Core **2** (2020) 007.

[56] V. Eisler, *Entanglement Hamiltonian of a nonrelativistic Fermi gas*, Phys. Rev. B **109** (2024) L201113.

[57] R. J. Baxter, *Exactly solved models in statistical mechanics*. Academic Press, London, 1982.

[58] R. J. Baxter, *Corner transfer matrices of the eight-vertex model. 1. Low-temperature expansions and conjectured properties*, J. Stat. Phys. **15** (1976) 485.

[59] R. J. Baxter, *Corner transfer matrices of the eight-vertex model. 2. The Ising model case*, J. Stat. Phys. **17** (1977) 1.

[60] T. Nishino and K. Okunishi, *Corner transfer matrix algorithm for classical renormalization group*, J. Phys. Soc. Japan **66** (1997) 3040.

[61] H. Itoyama and H. B. Thacker, *Lattice Virasoro algebra and corner transfer matrices in the Baxter eight-vertex model*, Phys. Rev. Lett. **58** (1987) 1395.

[62] H. B. Thacker and H. Itoyama, *Integrability, Conformal Symmetry, and Noncritical Virasoro Algebras*, Nucl. Phys. B Proc. Suppl. **5** (1988) 9.

[63] H. Itoyama and H. B. Thacker, *Integrability and Virasoro Symmetry of the Noncritical Baxter-Ising Model*, Nucl. Phys. B **320** (1989) 541.

[64] H. Li and F. D. M. Haldane, *Entanglement spectrum as a generalization of entanglement entropy: Identification of topological order in non-abelian fractional quantum Hall effect states*, Phys. Rev. Lett. **101** (2008) 010504.

[65] X.-L. Qi, H. Katsura, and A. W. W. Ludwig, *General Relationship between the Entanglement Spectrum and the Edge State Spectrum of Topological Quantum States*, Phys. Rev. Lett. **108** (2012) 196402.

[66] B. Swingle and T. Senthil, *Geometric proof of the equality between entanglement and edge spectra*, Phys. Rev. B **86** (2012) 045117.

[67] M. Levin and X.-G. Wen, *Detecting Topological Order in a Ground State Wave Function*, Phys. Rev. Lett. **96** (2006) 110405.

[68] A. Kitaev and J. Preskill, *Topological Entanglement Entropy*, Phys. Rev. Lett. **96** (2006) 110404.

[69] L. Gurvits, *Classical complexity and quantum entanglement*, Journal of Computer and System Sciences **69** (2004) 448.

[70] Y. Huang, *Computing quantum discord is NP-complete*, New J. Phys. **16** (2014) 033027.

[71] L. Arceci, P. Silvi, and S. Montangero, *Entanglement of formation of mixed many-body quantum states via Tree Tensor Operators*, Phys. Rev. Lett. **128** (2022) 040501.

[72] A. Peres, *Separability Criterion for Density Matrices*, Phys. Rev. Lett. **77** (1996) 1413.

[73] R. Simon, *Peres-Horodecki Separability Criterion for Continuous Variable Systems*, Phys. Rev. Lett. **84** (2000) 2726.

[74] G. Vidal and R. F. Werner, *A computable measure of entanglement*, Phys. Rev. A **65** (2002) 032314.

[75] M. B. Plenio, *Logarithmic Negativity: A Full Entanglement Monotone That is not Convex*, Phys. Rev. Lett. **95** (2005) 090503.

[76] J. Eisert, *Entanglement in quantum information theory*, arXiv:quant-ph/0610253.

[77] P. Calabrese, J. Cardy, and E. Tonni, *Entanglement negativity in quantum field theory*, Phys. Rev. Lett. **109** (2012) 130502 .

[78] P. Calabrese, J. Cardy, and E. Tonni, *Entanglement negativity in extended systems: A field theoretical approach*, J. Stat. Mech. (2013) P02008.

[79] P. Calabrese, L. Tagliacozzo, and E. Tonni, *Entanglement negativity in the critical Ising chain*, J. Stat. Mech. (2013) P05002.

[80] P. Calabrese, J. Cardy, and E. Tonni, *Finite temperature entanglement negativity in conformal field theory*, J. Phys. A **48** (2015) 015006.

[81] S. Murciano, V. Vitale, M. Dalmonte, and P. Calabrese, *The Negativity Hamiltonian: An operator characterization of mixed-state entanglement*, Phys. Rev. Lett. **128** (2022) 140502.

[82] M. Goldstein and E. Sela, *Symmetry-Resolved Entanglement in Many-Body Systems*, Phys. Rev. Lett. **120** (2018) 200602.

[83] J. C. Xavier, F. C. Alcaraz, and G. Sierra, *Equipartition of the entanglement entropy*, Phys. Rev. B **98** (2018) 041106(R).

[84] F. Rottoli, S. Murciano, E. Tonni, and P. Calabrese, *Entanglement and negativity Hamiltonians for the massless Dirac field on the half line*, J. Stat. Mech. (2023) 013103.

[85] J. Dubail, J.-M. Stéphan, J. Viti, and P. Calabrese, *Conformal field theory for inhomogeneous one-dimensional quantum systems: the example of non-interacting Fermi gases*, SciPost Phys. **2** (2017) 002.

[86] P. Calabrese and J. Cardy, *Evolution of entanglement entropy in one-dimensional systems*, J. Stat. Mech. (2005) P04010.

[87] H. Casini and M. Huerta, *Reduced density matrix and internal dynamics for multicomponent regions*, Class. Quantum Grav. **26** (2009) 185005.

[88] R. E. Arias, H. Casini, M. Huerta, and D. Pontello, *Entropy and modular Hamiltonian for a free chiral scalar in two intervals*, Phys. Rev. D **98** (2018) 125008.

[89] M. Mintchev and E. Tonni, *Modular hamiltonians for the massless Dirac field in the presence of a boundary*, JHEP **03** (2021) 204.

[90] J. Cardy, *Conformal Invariance and Surface Critical Behavior*, Nucl. Phys. B **240** (1984) 514.

[91] J. Cardy, *Effect of Boundary Conditions on the Operator Content of Two-Dimensional Conformally Invariant Theories*, Nucl. Phys. B **275** (1986) 200.

[92] J. Cardy, *Boundary Conditions, Fusion Rules and the Verlinde Formula*, Nucl. Phys. **324** (1989) 581.

[93] A. Liguori and M. Mintchev, *Quantum field theory, bosonization and duality on the half-line*, Nucl. Phys. B **522** (1998) 345.

[94] B. Bellazzini and M. Mintchev, *Quantum Fields on Star Graphs*, J. Phys. A **39** (2006) 11101.

[95] M. Mintchev, *Non-equilibrium Steady States of Quantum Systems on Star Graphs*, J. Phys. A **44** (2011) 415201.

[96] M. Mintchev and E. Tonni, *Modular hamiltonians for the massless Dirac field in the presence of a defect*, JHEP **03** (2021) 205.

[97] S. Hollands, *On the Modular Operator of Mutli-component Regions in Chiral CFT*, Comm. Math. Phys. **384** (2021) 785.

[98] I. Klich, D. Vaman, and G. Wong, *Entanglement hamiltonians for chiral fermions with zero modes*, Phys. Rev. Lett. **119** (2017) 120401.

[99] N. I. Muskhelishvili, *Singular Integral Equations: Boundary problems of functions theory and their applications to mathematical physics*, Springer (1977).

[100] P. Di Francesco , P. Mathieu and D. Sénéchal, *Conformal Field Theory*, Graduate Texts in Contemporary Physics, Springer, New York (1996).

[101] G. Mussardo, *Statistical field theory: an introduction to exactly solved models in statistical physics*, second edition, Oxford University Press (2020).

[102] H. Casini, C. D. Fosco, and M. Huerta, *Entanglement and alpha entropies for a massive Dirac field in two dimensions*, J. Stat. Mech. (2005) P07007.

[103] M. Caraglio and F. Gliozzi, *Entanglement Entropy and Twist Fields*, JHEP **11** (2008) 076.

[104] S. Furukawa, V. Pasquier, and J. Shiraishi, *Mutual Information and Compactification Radius in a c=1 Critical Phase in One Dimension*, Phys. Rev. Lett. **102** (2009) 170602.

[105] P. Calabrese, J. Cardy, and E. Tonni, *Entanglement entropy of two disjoint intervals in conformal field theory*, J. Stat. Mech. (2009) P11001.

[106] P. Calabrese, J. Cardy, and E. Tonni, *Entanglement entropy of two disjoint intervals in conformal field theory II*, J. Stat. Mech. (2011) P01021.

[107] A. Coser, L. Tagliacozzo, and E. Tonni, *On Rényi entropies of disjoint intervals in conformal field theory*, J. Stat. Mech. (2014) P01008.

[108] I. Peschel and V. Eisler, *Reduced density matrices and entanglement entropy in free lattice models*, J. Phys. A **42** (2009) 504003.

[109] M. C. Chung and I. Peschel, *Density-matrix spectra of solvable fermionic systems*, Phys. Rev. B **64** (2001) 064412.

[110] I. Peschel, *Calculation of reduced density matrices from correlation functions*, J. Phys. A **36** (2003) L205.

[111] I. Peschel, *On the reduced density matrix for a chain of free electrons*, J. Stat. Mech. (2004) P06004.

[112] V. Eisler and Z. Zimborás, *On the partial transpose of fermionic gaussian states*, New J. Phys. **17** (2015) 053048.

[113] J. Eisert, V. Eisler, and Z. Zimborás, *Entanglement negativity bounds for fermionic Gaussian states*, Phys. Rev. B **97** (2018) 165123.

[114] A. Coser, E. Tonni, and P. Calabrese, *Partial transpose of two disjoint blocks in XY spin chains*, J. Stat. Mech. (2015) P08005.

[115] A. Coser, E. Tonni, and P. Calabrese, *Towards entanglement negativity of two disjoint intervals for a one dimensional free fermion*, J. Stat. Mech. (2016) 033116.

[116] A. Coser, E. Tonni, and P. Calabrese, *Spin structures and entanglement of two disjoint intervals in conformal field theories*, J. Stat. Mech. (2016) 053109.

[117] H. Shapourian, K. Shiozaki, and S. Ryu, *Partial time-reversal transformation and entanglement negativity in fermionic systems*, Phys. Rev. B **95** (2017) 165101.

[118] H. Shapourian, K. Shiozaki, and S. Ryu, *Many-Body Topological Invariants for Fermionic Symmetry-Protected Topological Phases*, Phys. Rev. Lett. **118** (2017) 216402.

[119] H. Shapourian and S. Ryu, *Entanglement negativity of fermions: monotonicity, separability criterion, and classification of few-mode states*, Phys. Rev. A **99** (2019) 022310.

[120] H. Shapourian, P. Ruggiero, S. Ryu, and P. Calabrese, *Twisted and untwisted negativity spectrum of free fermions*, SciPost Phys. **7** (2019) 037.

[121] H. Shapourian and S. Ryu, *Finite-temperature entanglement negativity of free fermions*, J. Stat. Mech. (2019) 043106.

[122] V. Alba and P. Calabrese, *Quantum information dynamics in multipartite integrable systems*, EPL **126** (2019) 60001.

[123] M. Gruber and V. Eisler, *Time evolution of entanglement negativity across a defect*, J. Phys. A **53** (2020) 205301.

[124] S. Murciano, R. Bonsignori, and P. Calabrese, *Symmetry decomposition of negativity of massless free fermions*, SciPost Phys. **10** (2021) 111.

[125] G. Parez, R. Bonsignori, and P. Calabrese, *Dynamics of charge-imbalance-resolved entanglement negativity after a quench in a free-fermion mode*, J. Stat. Mech. (2022) 053103.

[126] S. Fraenkel and M. Goldstein, *Extensive Long-Range Entanglement in a Nonequilibrium Steady State*, SciPost Phys. **15** (2023) 134.

[127] L. Capizzi, S. Murciano, and P. Calabrese, *Rényi entropy and negativity for massless Dirac fermions at conformal interfaces and junctions*, JHEP **08** (2022) 171.

[128] A. Foligno, S. Murciano, and P. Calabrese, *Entanglement resolution of free Dirac fermions on a torus*, JHEP **03** (2023) 96.

[129] A. Elben, R. Kueng, H.-Y. Huang, R. van Bijnen, C. Kokail, M. Dalmonte, P. Calabrese, B. Kraus, J. Preskill, P. Zoller, and B. Vermersch, *Mixed-state entanglement from local randomized measurements*, Phys. Rev. Lett. **125** (2020) 200501.

[130] A. Neven, J. Carrasco, V. Vitale, C. Kokail, A. Elben, M. Dalmonte, P. Calabrese, P. Zoller, B. Vermersch, R. Kueng and B. Kraus, *Symmetry-resolved entanglement detection using partial transpose moments*, npj Quantum Inf. **7** (2021) 152.

[131] F. Rottoli, S. Murciano, and P. Calabrese, *Finite temperature negativity Hamiltonians of the massless Dirac fermion*, JHEP **06** (2023) 139.

[132] R. Arias, D. Blanco, H. Casini, and M. Huerta, *Local temperatures and local terms in modular Hamiltonians*, Phys. Rev. D **95** (2017) 065005.

[133] V. Eisler, E. Tonni, and I. Peschel, *On the continuum limit of the entanglement hamiltonian*, J. Stat. Mech. (2019) 073101.

[134] V. Eisler, E. Tonni, and I. Peschel, *Local and non-local properties of the entanglement Hamiltonian for two disjoint intervals*, J. Stat. Mech. (2022) 083101.

[135] G. Di Giulio and E. Tonni, *On entanglement hamiltonians of an interval in massless harmonic chains*, J. Stat. Mech. (2020) 033102.

[136] G. Di Giulio, R. Arias, and E. Tonni, *Entanglement hamiltonians in 1d free lattice models after a global quantum quench*, J. Stat. Mech. (2019) 123103.

[137] N. Javerzat and E. Tonni, *On the continuum limit of the entanglement Hamiltonian of a sphere for the free massless scalar field*, JHEP **02** (2022) 086.

[138] M. Fagotti and P. Calabrese, *Universal parity effects in the entanglement entropy of XX chains with open boundary conditions*, J. Stat. Mech. (2011) P01017.

[139] F. Johansson et al, *mpmath: a Python library for arbitrary-precision floating-point arithmetic (v0.18)*, http://mpmath.org (2013).

[140] E. Tonni, Javier Rodríguez-Laguna, and G. Sierra, *Entanglement hamiltonian and entanglement contour in inhomogeneous 1D critical systems*, J. Stat. Mech. (2018) 043105.

[141] F. Rottoli, S. Scopa, and P. Calabrese, *Entanglement Hamiltonian during a domain wall melting in the free Fermi chain*, J. Stat. Mech. (2022) 063103.

[142] P. Fries and I. A. Reyes, *Entanglement spectrum of chiral fermions on the torus*, Phys. Rev. Lett. **123** (2019) 211603.

[143] D. Blanco and G. Pérez-Nadal, *Modular Hamiltonian of a chiral fermion on the torus*, Phys. Rev. D **100** (2019) 025003.

[144] D. Blanco, A. Garbarz, and G. Pérez-Nadal, *Entanglement of a chiral fermion on the torus*, JHEP **06** (2019) 76.

[145] J. I. Latorre, E. Rico, and G. Vidal, *Ground state entanglement in quantum spin chains*, Quant. Inf. Comput. **4** (2004) 48.

[146] R. Arias and J. Zhang, *Rényi entropy and subsystem distances in finite size and thermal states in critical XY chains*, J. Stat. Mech. (2020) 083112.

[147] I. Klich, D. Vaman, and G. Wong, *Entanglement Hamiltonians and entropy in (1+1)-dimensional chiral fermion systems*, Phys. Rev. B **98** (2018) 035134.

[148] I. Peschel, *Entanglement in solvable many-particle models*, Braz. J. Phys. **42** (2012) 267.

[149] P. Ruggiero, V. Alba, and P. Calabrese, *Negativity spectrum of one-dimensional conformal field theories*, Phys. Rev. B **94** (2016) 195121.

[150] V. Alba, P. Calabrese, and E. Tonni, *Entanglement spectrum degeneracy and Cardy formula in 1+1 dimensional conformal field theories*, J. Phys. A **51** (2018) 024001.

[151] J. Erdmenger, P. Fries, I. A. Reyes, and C. P. Simon, *Resolving modular flow: a toolkit for free fermions*, JHEP **12** (2020) 126.

[152] E. T. Whittaker and G. N. Watson, *A course of modern analysis*, 4 ed., Cambridge Mathematical Library, Cambridge University Press, 1996.

[153] N. Batir, *Monotonicity properties of q-digamma and q-trigamma functions*, J. Approximation Theory **192** (2015) 336.

[154] N. Moiseyev, *Non-Hermitian Quantum Mechanics*. Cambridge University Press, Cambridge, 2011.

[155] Y. Ashida, Z. Gong, and M. Ueda, *Non-Hermitian physics*, Adv. Phys. **69** (2021) 249.

[156] C. M. Bender and S. Boettcher, *Real spectra in nonHermitian Hamiltonians having PT symmetry*, Phys. Rev. Lett. **80** (1998) 5243.

[157] C. M. Bender, *PT-symmetric quantum theory*, J. Phys. Conf. Ser. **631** (2015) 012002.

[158] R. El-Ganainy, K. G. Makris, M. Khajavikhan, Z. H. Musslimani, S. Rotter, and D. N. Christodoulides, *Non-Hermitian physics and PT symmetry*, Nature Phys. **14** (2018) 11.

[159] R. Arouca, C. H. Lee, and C. Morais Smith, *Unconventional scaling at non-Hermitian critical points*, Phys. Rev. B **102** (2020) 245145.

[160] R. Arouca, E. C. Marino, and C. Morais Smith, *Non-Hermitian quantum gases: a platform for imaginary time crystals*, Quantum Frontiers **1** (2022) 2.

[161] L. Feng, R. El-Ganainy, and L. Ge, *Non-Hermitian photonics based on parity–time symmetry*, Nature Photon. **11** (2017) 752.

[162] M.-A. Miri and A. Alù, *Exceptional points in optics and photonics*, Science **363** (2019) 6422.

[163] E. M. Graefe, H. J. Korsch, and A. E. Niederle, *Mean-Field Dynamics of a Non-Hermitian Bose-Hubbard Dimer*, Phys. Rev. Lett. **101** (2008) 150408.

[164] I. Rotter, *A non-Hermitian Hamilton operator and the physics of open quantum systems*, J. Phys. A **42** (2009) 153001.

[165] M. Müller, S. Diehl, G. Pupillo, and P. Zoller, *Engineered Open Systems and Quantum Simulations with Atoms and Ions*, Advances in Atomic, Molecular and Optical Physics **61** (2012) 1.

[166] S. Gopalakrishnan and M. J. Gullans, *Entanglement and Purification Transitions in Non-Hermitian Quantum Mechanics*, Phys. Rev. Lett. **126** (2021) 170503.

[167] A. Biella and M. Schiró, *Many-Body Quantum Zeno Effect and Measurement-Induced Subradiance Transition*, Quantum **5** (2021) 528.

[168] X. Turkeshi, A. Biella, R. Fazio, M. Dalmonte, and M. Schiró, *Measurement-induced entanglement transitions in the quantum Ising chain: From infinite to zero clicks*, Phys. Rev. B **103** (2021) 224210.

[169] T. Müller, S. Diehl, and M. Buchhold, *Measurement-Induced Dark State Phase Transitions in Long-Ranged Fermion Systems*, Phys. Rev. Lett. **128** (2022) 010605.

[170] X. Turkeshi and M. Schiró, *Entanglement and correlation spreading in non-Hermitian spin chains*, Phys. Rev. B **107** (2023) L020403.

[171] P.-Y. Chang, J.-S. You, X. Wen, and S. Ryu, *Entanglement spectrum and entropy in topological non-Hermitian systems and nonunitary conformal field theory*, Phys. Rev. Res. **2** (2020) 033069.

[172] Y.-T. Tu, Y.-C. Tzeng, and P.-Y. Chang, *Rényi entropies and negative central charges in non-Hermitian quantum systems*, SciPost Phys. **12** (2022) 194.

[173] M. Fossati, F. Ares, and P. Calabrese, *Symmetry-resolved entanglement in critical non-Hermitian systems*, Phys. Rev. B **107** (2023) 205153.

[174] F. Rottoli, M. Fossati, and P. Calabrese, *Entanglement Hamiltonian in the non-Hermitian SSH model*, J. Stat. Mech. (2024) 063102.

[175] S. Lieu, *Topological phases in the non-Hermitian Su-Schrieffer-Heeger model*, Phys. Rev. B **97** (2018) 045106.

[176] D. Friedan, E. J. Martinec, and S. H. Shenker, *Conformal Invariance, Supersymmetry and String Theory*, Nucl. Phys. B **271** (1986) 93.

[177] S. Guruswamy and A. W. W. Ludwig, *Relating $c < 0$ and $c > 0$ conformal field theories*, Nucl. Phys. B **519** (1998) 661.

[178] H. G. Kausch, *Curiosities at $c = -2$*, arXiv:hep-th/9510149.

[179] H. G. Kausch, *Symplectic fermions*, Nucl. Phys. B **583** (2000) 513.

[180] D. C. Brody, *Biorthogonal quantum mechanics*, J. Phys. A **47** (2013) 035305.

[181] R. Couvreur, J. L. Jacobsen, and H. Saleur, *Entanglement in nonunitary quantum critical spin chains*, Phys. Rev. Lett. **119** (2017) 040601.

[182] T. Dupic, B. Estienne, and Y. Ikhlef, *Entanglement entropies of minimal models from null-vectors*, SciPost Phys. **4** (2018) 031.

[183] L. Herviou, N. Regnault, and J. H. Bardarson, *Entanglement spectrum and symmetries in non-Hermitian fermionic non-interacting models*, SciPost Phys. **7** (2019) 069.

[184] W. Tang, F. Verstraete, and J. Haegeman, *Matrix Product State Fixed Points of Non-Hermitian Transfer Matrices*, arXiv:2311.18733.

[185] V. Alba, M. Haque, and A. M. Läuchli, *Boundary-locality and perturbative structure of entanglement spectra in gapped systems*, Phys. Rev. Lett. **108** (2012) 227201.

[186] F. Smirnov, *Form factors in completely integrable models of quantum field theory*, Adv. Series in Math. Phys. 14, World Scientific, Singapore (1992).

[187] M. Karowski and P. Weisz, *Exact Form-Factors in (1+1)-Dimensional Field Theoretic Models With Soliton Behavior*, Nucl. Phys. B **139** (1978) 455.

[188] J. L. Cardy, O. A. Castro-Alvaredo, and B. Doyon, *Form factors of branch-point twist fields in quantum integrable models and entanglement entropy*, J. Stat. Phys. **130** (2008) 129.

[189] O. A. Castro-Alvaredo and B. Doyon, *Bi-partite entanglement entropy in integrable models with backscattering*, J. Phys. A **41** (2008) 275203.

[190] O. A. Castro-Alvaredo and B. Doyon, *Bi-partite entanglement entropy in massive (1+1)-dimensional quantum field theories*, J. Phys. A **42** (2009) 504006.

[191] B. Doyon, *Bipartite entanglement entropy in massive two-dimensional quantum field theory*, Phys. Rev. Lett. **102** (2009) 031602

[192] O. A. Castro-Alvaredo and B. Doyon, *Bi-partite entanglement entropy in massive QFT with a boundary: the Ising model*, J. Stat. Phys. **134** (2009) 105.

[193] O. A. Castro-Alvaredo and E. Levi, *Higher particle form factors of branch point twist fields in integrable quantum field theories*, J. Phys. A **44** (2011) 255401.

[194] O. A. Castro-Alvaredo, B. Doyon and E. Levi, *Arguments towards a c-theorem from branch-point twist fields*, J. Phys. A **44** (2011) 492003.

[195] E. Levi, *Composite branch-point twist fields in the Ising model and their expectation values*, J. Phys. A **45** (2012) 275401.

[196] E. Levi, O. A. Castro-Alvaredo, and B. Doyon, *Universal corrections to the entanglement entropy in gapped quantum spin chains: a numerical study*, Phys. Rev. B **88** (2013) 094439.

[197] O. Blondeau-Fournier, O. A. Castro-Alvaredo and B. Doyon, *Universal scaling of the logarithmic negativity in massive quantum field theory*, J. Phys. A **49** (2016) 125401.

[198] D. Bianchini and O. A. Castro-Alvaredo, *Branch Point Twist Field Correlators in the Massive Free Boson Theory*, Nucl. Phys. B **913** (2016) 879.

[199] O. A. Castro-Alvaredo, *Massive Corrections to Entanglement in Minimal E8 Toda Field Theory*, SciPost Phys. **2** (2017) 008.

[200] O. A. Castro-Alvaredo, C. De Fazio, B. Doyon and I. M. Szécsényi, *Entanglement Content of Quasi-Particle Excitations*, Phys. Rev. Lett. **121** (2018) 170602.

[201] O. A. Castro-Alvaredo, C. De Fazio, B. Doyon and I. M. Szécsényi, *Entanglement Content of Quantum Particle Excitations I. Free Field Theory*, JHEP **10** (2018) 039.

[202] O. A. Castro-Alvaredo, C. De Fazio, B. Doyon and I. M. Szécsényi, *Entanglement Content of Quantum Particle Excitations II. Disconnected Regions and Logarithmic Negativity*, JHEP **11** (2019) 058.

[203] O. A. Castro-Alvaredo, C. De Fazio, B. Doyon and I. M. Szécsényi, *Entanglement Content of Quantum Particle Excitations III. Graph Partition Functions*, J. Math. Phys. **60** (2019) 082301.

[204] O. A. Castro-Alvaredo, M. Lencsés, I. M. Szécsényi and J. Viti, *Entanglement Dynamics after a Quench in Ising Field Theory: A Branch Point Twist Field Approach*, JHEP **12** (2019) 079.

[205] O. A. Castro-Alvaredo, M. Lencsés, I. M. Szécsényi and J. Viti, *Entanglement Oscillations near a Quantum Critical Point*, Phys. Rev. Lett. **124** (2020) 230601.

[206] O. A. Castro-Alvaredo and D. X. Horváth, *Branch Point Twist Field Form Factors in the sine-Gordon Model I: Breather Fusion and Entanglement Dynamics*, SciPost Phys. **10** (2021) 132.

[207] A. B. Zamolodchikov, *Renormalization group and perturbation theory about fixed points in two-dimensional field theory*, Sov. J. Nucl. Phys. **46** (1987) 1090.

[208] A. W. W. Ludwig and J. L. Cardy, *Perturbative evaluation of the conformal anomaly at new critical points with applications to random systems*, Nucl. Phys. B **285** (1987) 687.

[209] Al. B. Zamolodchikov, *Thermodynamic Bethe ansatz for RSOS scattering theories*, Nucl. Phys. B **358** (1991) 497.

[210] Al. B. Zamolodchikov, *From tricritical Ising to critical Ising by thermodynamic Bethe ansatz*, Nucl. Phys. B **358** (1991) 524.

[211] Al. B. Zamolodchikov, *TBA equations for integrable perturbed* $SU(2)_k \times SU(2)_1$ $SU(2)_{k+1}$ *coset models*, Nucl. Phys. B **366** (1991) 122.

[212] A. B. Zamolodchikov, *Irreversibility of the Flux of the Renormalization Group in a 2D Field Theory*, JETP Lett. **43** (1986) 730 , Pisma Zh. Eksp. Teor. Fiz. **43** (1986) 565 .

[213] J. L. Cardy, *The Central Charge and Universal Combinations of Amplitudes in Two-dimensional Theories Away From Criticality*, Phys. Rev. Lett. **60** (1988) 2709.

[214] G. Delfino, P. Simonetti and J. L. Cardy, *Asymptotic factorisation of form factors in two-dimensional quantum field theory*, Phys. Lett. B **387** (1996) 327.

[215] H. Casini and M. Huerta, *A finite entanglement entropy and the c-theorem*, Phys. Lett. B **600** (2004) 142.

[216] G. Delfino, G. Mussardo and P. Simonetti, *Correlation functions along a massless flow*, Phys. Rev. D **51** (1995) R6620.

[217] Al. B. Zamolodchikov, *Resonance factorized scattering and roaming trajectories*, J. Phys. A **39** (2006) 12847.

[218] P. Dorey, G. Siviour and G. Takács, *Form factor relocalisation and interpolating renormalisation group flows from the staircase model*, JHEP **03** (2015) 054.

[219] D. X. Horváth, P.E. Dorey and G. Takács, *Roaming form factors for the tricritical to critical Ising flow*, JHEP **07** (2016) 051.

[220] M. Lassig, *Multiple crossover phenomena and scale hopping in two-dimensions*, Nucl. Phys. B **380** (1992) 601.

[221] M. J. Martins, *Renormalization group trajectories from resonance factorized* S*-matrices*, Phys. Rev. Lett. **69** (1992) 2461.

[222] P. E. Dorey and F. Ravanini, *Staircase models from affine Toda field theory*, Int. J. Mod. Phys. A **8** (1993) 873.

[223] M. J. Martins, *Analysis of asymptotic conditions in resonance functional hierarchies*, Phys. Lett. B **304** (1993) 111.

[224] P. Dorey and F. Ravanini, *Generalizing the staircase models*, Nucl. Phys. B **406** (1993) 708.

[225] C. Fernandez-Pousa, M. Gallas, T. Hollowood and J. Miramontes, *The symmetric space and homogeneous sine-Gordon theories*, Nucl. Phys. B **484** (1997) 609.

[226] O. A. Castro-Alvaredo, A. Fring, C. Korff and J. L. Miramontes, *Thermodynamic Bethe ansatz of the homogeneous sine-Gordon models*, Nucl. Phys. B **575** (2000) 535.

[227] O. A. Castro-Alvaredo and A. Fring, *Renormalization group flow with unstable particles*, Phys. Rev. D **63** (2001) 021701.

[228] D. Friedan, Z. Qiu and S. Shenker, *Superconformal invariance in two dimensions and the tricritical Ising model*, Phys. Lett. B **151** (1985) 37.

[229] Z. Qiu, *Supersymmetry, two-dimensional critical phenomena and the tricritical Ising model*, Nucl. Phys. B **270** (1986) 205.

[230] M. A. Bershadsky, V. G, Knizhnik and M. G. Teitelman, *Superconformal symmetry in two dimensions*, Phys. Lett. B **151** (1985) 31.

[231] D. A. Kastor, E. J. Martinec and S. H. Shenker, *RG flow in* $N = 1$ *discrete series*, Nucl. Phys. B **316** (1989) 590.

[232] A. B. Zamolodchikov, *Fractional Spin Integrals of Motion in Perturbed Conformal Field Theory in the Proceedings Conference Beijing 1989, "Fields, strings and quantum gravity", 349.*

[233] W. Donnelly and V. Shyam, *Entanglement Entropy and* $T\bar{T}$ *Deformation*, Phys. Rev. Lett. **121** (2018) 131602.

[234] A. Lewkowycz, J. Liu, E. Silverstein and G. Torroba, $T\bar{T}$ *and EE, with implications for (A)dS subregion encodings*, JHEP **04** (2020) 152.

[235] B. Chen, L. Chen and P.-X. Hao, *Entanglement entropy in* $T\bar{T}$*-deformed CFT*, Phys. Rev. D **98** (2018) 086025.

[236] A. Banerjee, A. Bhattacharyya and S. Chakraborty, *Entanglement Entropy for* $T\bar{T}$ *deformed CFT in general dimensions*, Nucl. Phys. B **948** (2019) 114775.

[237] H.S. Jeong, K.Y. Kim and M. Nishida, *Entanglement and Rényi Entropy of Multiple Intervals in* $T\bar{T}$*-Deformed CFT and Holography*, Phys. Rev. D **100** (2019) 106015.

[238] C. Murdia, Y. Nomura, P. Rath and N. Salzetta, *Comments on holographic entanglement entropy in $T\bar{T}$ deformed conformal field theories*, Phys. Rev. D **100** (2019) 026011.

[239] V. Gorbenko, E. Silverstein and G. Torroba, *dS/dS and $T\bar{T}$*, JHEP **03** (2019) 085.

[240] C. Park, *Holographic Entanglement Entropy in Cutoff AdS*, Int. J. Mod. Phys. A **33** (2019) 1850226.

[241] M. Asrat, *Entropic c-functions in $T\bar{T}$, $J\bar{T}$, $T\bar{J}$ deformations*, Nucl. Phys. B **960** (2020) 115186.

[242] S. He and H. Shu, *Correlation functions, entanglement and chaos in the $T\bar{T}/J\bar{T}$-deformed CFTs*, JHEP **02** (2020) 088.

[243] Y. Sun and J.R. Sun, *Note on the Rényi entropy of 2D perturbed fermions*, Phys. Rev. D **99** (2019) 106008.

[244] S. Grieninger, *Entanglement entropy and $T\bar{T}$ deformations beyond antipodal points from holography*, JHEP **11** (2019) 171.

[245] M. Asrat and J. Kudler-Flam, *$T\bar{T}$, the entanglement wedge cross section, and the breakdown of the split property*, Phys. Rev. D **102** (2020) 045009.

[246] O. A. Castro-Alvaredo, S. Negro and F. Sailis, *Entanglement Entropy from Form Factors in $T\bar{T}$-Deformed Integrable Quantum Field Theories*, JHEP **11** (2023) 129.

[247] D. X. Horváth, *Hydrodynamics of massless integrable RG flows and a non-equilibrium c-theorem*, JHEP **10** (2019) 020.

[248] J. Fröhlich, J. Fuchs, I. Runkel and C. Schweigert, *Kramers-Wannier Duality from Conformal Defects*, Phys. Rev. Lett. **93** (2004) 070601.

[249] D. Gaiotto, A. Kapustin, N. Seiberg and B. Willett, *Generalized global symmetries*, JHEP **02** (2015) 172.

[250] Y. Kusuki, S. Murciano, H. Ooguri, and S. Pal, *Symmetry-resolved Entanglement Entropy, Spectra & Boundary Conformal Field Theory*, JHEP **11** (2023) 216.

[251] D. X. Horváth, L. Capizzi, and P. Calabrese, *$U(1)$ symmetry resolved entanglement in free 1+1 dimensional field theories via form factor bootstrap*, JHEP **05** (2021) 197.

[252] D. X. Horváth, P. Calabrese, and O. A. Castro-Alvaredo, *Branch Point Twist Field Form Factors in the sine-Gordon Model II: Composite Twist Fields and Symmetry Resolved Entanglement*, SciPost Phys. **12** (2022) 088.

[253] D. X. Horváth and P. Calabrese, *Symmetry resolved entanglement in integrable field theories via form factor bootstrap*, JHEP **11** (2020) 131.

[254] S. Murciano, G. Di Giulio, and P. Calabrese, *Symmetry resolved entanglement in gapped integrable systems: a corner transfer matrix approach*, SciPost Phys. **8** (2020) 046.

[255] Al. B. Zamolodchikov, *Two-point correlation function in scaling Lee-Yang model*, Nucl. Phys. B **348** (1991) 619.

[256] F. A. Smirnov, *Reductions of the sine-Gordon model as a perturbation of minimal models of conformal field theory*, Nucl. Phys. B **337** (1990) 156.

[257] A. Koubek and G. Mussardo, *On the operator content of the sinh-Gordon model*, Phys. Lett. B **311** (1993) 193.

[258] O. A. Castro-Alvaredo and A. Fring, *Identifying the operator content, the homogeneous sine-Gordon models*, Nucl. Phys. B **604** (2001) 367.

[259] A. E. Arinshtein, V. A. Fateev and A. B. Zamolodchikov, *Quantum S-matrix of the (1+1)-Dimensional Todd Chain*, Phys. Lett. B **87** (1979) 389.

[260] A. Fring, G. Mussardo and P. Simonetti, *Form-factors for integrable Lagrangian field theories, the sinh-Gordon theory*, Nucl. Phys. B **393** (1993) 413.

[261] C. Ahn, G. Delfino and G. Mussardo, *Mapping between the sinh-Gordon and Ising models*, Phys. Lett. B **317** (1993) 573.

[262] S. Negro and F. Smirnov, *On one-point functions for sinh-Gordon model at finite temperature*, Nucl. Phys. B **875** (2013) 166.

[263] S. Negro, *On Sinh-Gordon Thermodynamic Bethe ansatz and fermionic basis*, Int. J. Mod. Phys. A **29** (2014) 1450111.

[264] D. X. Horváth, S. Sotiriadis and G. Takács, *Initial states in integrable quantum field theory quenches from an integral equation hierarchy*, Nucl. Phys. B **902** (2016) 508.

[265] R. Konik, M. Lájer and G. Mussardo, *Approaching the Self-Dual Point of the Sinh-Gordon model*, JHEP 01 (2021) 014.

[266] T. Hahn, *Cuba – a library for multidimensional numerical integration*, Comput. Phys. Commun. **168** (2005) 78.

[267] H. Babujian and M. Karowski, *Towards the Construction of Wightman Functions of Integrable Quantum Field Theories*, Int. J. Mod. Phys. A **19** (2004) 34.

[268] O. A. Castro-Alvaredo and M. Mazzoni, *Two-Point Functions of Composite Twist Fields in the Ising Field Theory*, J. Phys. A **56** (2023) 124001.

[269] F. Rottoli, F. Ares, P. Calabrese, and D. X. Horváth, *Entanglement entropy along a massless renormalisation flow: the tricritical to critical Ising crossover*, JHEP **02** (2024) 053.

[270] P. Calabrese, F. H. L. Essler, and G. Mussardo, *Introduction to "Quantum Integrability in Out of Equilibrium Systems"*, J. Stat. Mech. (2016) P064001.

[271] A. Bastianello, B. Bertini, B. Doyon, and R. Vasseur, *Introduction to the Special Issue on Emergent Hydrodynamics in Integrable Many-Body Systems*, J. Stat. Mech. (2022) 014001.

[272] F. D. M. Haldane, *Effective Harmonic-Fluid Approach to Low-Energy Properties of One-Dimensional Quantum Fluids*, Phys. Rev. Lett. **47** (1981) 1840

[273] F. D. M. Haldane, *'Luttinger liquid theory' of one-dimensional quantum fluids I. Properties of the Luttinger model and their extension to the general 1D interacting spinless Fermi gas*, J. Phys. C **14** (1981) 2585.

[274] F. D. M. Haldane, *Demonstration of the "Luttinger liquid" character of Bethe-ansatz-soluble models of 1-D quantum fluids*, Phys. Lett. A **81** (1981) 153.

[275] T. Giamarchi, *Quantum physics in one dimension*, Clarendon Press, Oxford (2003).

[276] V.E. Korepin, N.M. Bogoliubov, and A.G. Izergin, *Quantum inverse scattering method and correlation functions*, Cambridge University Press (1993).

[277] A. O. Gogolin, A. A. Nersesyan, and A. M. Tsvelik, *Bosonization and Strongly Correlated Systems*, Cambridge (1998).

[278] N. Allegra, J. Dubail, J.-M. Stéphan, and J. Viti, *Inhomogeneous field theory inside the arctic circle*, J. Stat. Mech. (2016) 053108.

[279] Y. Brun and J. Dubail, *One-particle density matrix of trapped one-dimensional impenetrable bosons from conformal invariance*, SciPost Phys. **2** (2017) 012.

[280] Y. Brun and J. Dubail, *The Inhomogeneous Gaussian Free Field, with application to ground state correlations of trapped 1d Bose gases*, SciPost Phys. **4** (2018) 037.

[281] S. Scopa, L. Piroli, and P. Calabrese, *One-particle density matrix of a trapped Lieb Liniger anyonic gas*, J. Stat. Mech. (2020) 093103.

[282] P. Ruggiero, Y. Brun, and J. Dubail, *Conformal field theory on top of a breathing one-dimensional gas of hard core bosons*, SciPost Phys. **6** (2019) 051.

[283] A. Bastianello, J. Dubail, and J.-M. Stéphan, *Entanglement entropies of inhomogeneous Luttinger liquids*, J. Phys. A **53** (2020) 23

[284] J. Dubail, J.-M. Stephan, and P. Calabrese, *Emergence of curved light-cones in a class of inhomogeneous Luttinger liquids*, SciPost Phys. **3** (2017) 019

[285] B. Bertini, M. Collura, J. De Nardis, and M. Fagotti, *Transport in out-of-equilibrium XXZ chains: Exact profiles of charges and currents*, Phys. Rev. Lett. **117** (2016) 207201.

[286] O. A. Castro-Alvaredo, B. Doyon, and T. Yoshimura, *Emergent hydrodynamics in integrable quantum systems out of equilibrium*, Phys. Rev. X **6** (2016) 041065.

[287] P. Ruggiero, P. Calabrese, B. Doyon, and J. Dubail, *Quantum Generalized Hydrodynamics*, Phys. Rev. Lett. **124** (2020) 140603.

[288] M. Collura, A. De Luca, P. Calabrese, and J. Dubail, *Domain wall melting in the spin-1/2 XXZ spin chain: Emergent Luttinger liquid with a fractal quasiparticle charge*, Phys. Rev. B **102** (2020) 180409.

[289] S. Scopa, A. Krajenbrink, P. Calabrese, and J. Dubail, *Exact entanglement growth of a one-dimensional hard core quantum gas during a free expansion*, J. Phys. A **54** (2021) 404002.

[290] S. Scopa, P. Calabrese, and J. Dubail, *Exact hydrodynamic solution of a double domain wall melting in the spin-1/2 XXZ model*, SciPost Phys. **12** (2022) 207.

[291] P. Ruggiero, P. Calabrese, B. Doyon, and J. Dubail, *Quantum generalized hydrodynamics of the Tonks-Girardeau gas: density fluctuations and entanglement entropy*, J. Phys. A **55** (2022) 024003.

[292] T. Antal, Z. Rácz, A. Rákos, and G. M. Schütz, *Transport in the XX chain at zero temperature: Emergence of flat magnetization profiles*, Phys. Rev. E **59** (1999) 4912.

[293] D. Karevski, *Scaling behaviour of the relaxation in quantum chains*, Eur. Phys. J. B **27** (2002) 147.

[294] M. Rigol and A. Muramatsu, *Emergence of Quasicondensates of Hard-Core Bosons at Finite Momentum*, Phys. Rev. Lett. **93** (2004) 230404.

[295] T. Platini and D. Karevski, *Scaling and front dynamics in Ising quantum chains*, Eur. Phys. J. B **48** (2005) 225.

[296] T. Platini and D. Karevski, *Relaxation in the XX quantum chain*, J. Phys. A **40** (2009) 1711.

[297] V. Hunyadi, Z. Rácz, and L. Sasvári, *Dynamic scaling of fronts in the quantum XX chain*, Phys. Rev. E **69** (2004) 066103.

[298] T. Antal, P. L. Krapivsky, and A. Rákos, *Logarithmic current fluctuations in nonequilibrium quantum spin chains*, Phys. Rev. E **78** (2008) 061115.

[299] L. Vidmar, J.P. Ronzheimer, M. Schreiber, S. Braun, S.S. Hodgman, S. Langer, F. Heidrich-Meisner, I. Bloch, and U. Schneider, *Dynamical Quasicondensation of Hard-Core Bosons at Finite Momenta*, Phys. Rev. Lett. **115** (2015) 175301.

[300] E. Vicari, *Quantum dynamics and entanglement in one-dimensional Fermi gases released from a trap*, Phys. Rev. A **85** (2012) 062324.

[301] V. Alba and F. Heidrich-Meisner, *Entanglement spreading after a geometric quench in quantum spin chains*, Phys. Rev. B **90** (2014) 075144.

[302] M. Gruber and V. Eisler, *Magnetization and entanglement after a geometric quench in the XXZ chain*, Phys. Rev. B **99** (2019) 174403.

[303] E. P. Wigner, *On the quantum correction for thermodynamic equilibrium*, Phys. Rev. **40** (1932) 749.

[304] M. Hinarejos, A. Pérez, and M. C. Banuls, *Wigner function for a particle in an infinite lattice*, New J. Phys. **14** (2012) 103009.

[305] B. Doyon, J. Dubail, R. Konik and T. Yoshimura, *Large-Scale Description of Interacting One-Dimensional Bose Gases: Generalized Hydrodynamics Supersedes Conventional Hydrodynamics*, Phys. Rev. Lett. **119** (2017) 195301.

[306] J. von Delft and H. Schoeller, *Bosonization for beginners – refermionization for experts*, Annalen der Physik **7** (1998) 225.

[307] P. Calabrese and J. Cardy, *Time-dependence of correlation functions following a quantum quench*, Phys. Rev. Lett. **96** (2006) 136801.

[308] H. R. Lewis and W. B. Riesenfeld, *An Exact Quantum Theory of the Time-Dependent Harmonic Oscillator and of a Charged Particle in a Time-Dependent Electromagnetic Field*, J. Math. Phys. **10** (1969) 1458.

[309] P. G. L. Leach and H. R. Lewis, *A direct approach to finding exact invariants for one-dimensional time-dependent classical Hamiltonians*, J. Math. Phys. **23** (1982) 2371.

[310] Y. Kagan, E. L. Surkov, and G. V. Shlyapnikov, *Evolution of a Bose-condensed gas under variations of the confining potential*, Phys. Rev. A **54** (1996) R1753.

[311] A. Minguzzi and D.M. Gangardt, *Exact coherent states of a harmonically confined Tonks-Girardeau gas*, Phys. Rev. Lett. **94** (2005) 240404.

[312] S. Scopa and D. Karevski, *One-dimensional Bose gas driven by a slow time-dependent harmonic trap*, J. Phys. A **50** (2017) 425301.

[313] S. Scopa, J. Unterberger, and D. Karevski, *Exact dynamics of a one dimensional Bose gas in a periodic time-dependent harmonic trap*, J. Phys. A **51** (2018) 185001.

[314] B. Q. Jin and V. E. Korepin, *Quantum spin chain, Toeplitz determinants and the Fisher-Hartwig conjecture*, J. Stat. Phys. **116** (2004) 79.

[315] P. Calabrese and F. H. L. Essler, *Universal corrections to scaling for block entanglement in spin-1/2 XX chains*, J. Stat. Mech. (2010) P08029.

[316] V. Eisler and I. Peschel, *Analytical results for the entanglement hamiltonian of a free-fermion chain*, J. Phys. A **50** (2017) 284003.

[317] V. Eisler and I. Peschel, *Properties of the entanglement hamiltonian for finite free-fermion chains*, J. Stat. Mech. (2018) 104001.

[318] A. Takács, S. Scopa, P. Calabrese, L. Vidmar, and J. Dubail, *Quasicondensation and off-diagonal long-range order of hard-core bosons during a free expansion*, arXiv:2401.16860.

[319] P. W. Anderson, *Infrared Catastrophe in Fermi Gases with Local Scattering Potentials*, Phys. Rev. Lett. **18** (1967) 1049.

[320] C. L. Kane and M. P. A. Fisher, *Transport in a one-channel Luttinger liquid*, Phys. Rev. Lett. **68** (1992) 1220.

[321] C. L. Kane and M. P. A. Fisher, *Transmission through barriers and resonant tunneling in an interacting one-dimensional electron gas*, Phys. Rev. B **46** (1992) 15233.

[322] C. Bachas, J. de Boer, R. Dijkgraaf, and H. Ooguri, *Permeable conformal walls and holography*, JHEP **06** (2002) 027.

[323] I. Peschel, *Entanglement entropy with interface defects*, J. Phys. A **38** (2005) 4327.

[324] K. Sakai and Y. Satoh, *Entanglement through conformal interfaces*, JHEP **12** (2008) 001.

[325] V. Eisler and I. Peschel, *Exact results for the entanglement across defects in critical chains*, J. Phys. A **45** (2012) 155301.

[326] V. Eisler and I. Peschel, *Solution of the fermionic entanglement problem with interface defects*, Ann. Phys. (Berlin) **522** (2010) 679.

[327] P. Calabrese, M. Mintchev, and E. Vicari, *Entanglement entropy of quantum wire junctions*, J. Phys. A **45** (2012) 105206.

[328] E. M. Brehm and I. Brunner, *Entanglement entropy through conformal interfaces in the 2D Ising model*, JHEP **09** (2015) 80.

[329] M. Gutperle and J. D. Miller, *Entanglement entropy at CFT junctions*, Phys. Rev. D **95** (2017) 106008.

[330] L. Capizzi, S. Murciano, and P. Calabrese, *Rényi entropy and negativity for massless complex boson at conformal interfaces and junctions*, JHEP **11** (2022) 105.

[331] D. Rogerson, F. Pollmann, and A. Roy, *Entanglement entropy and negativity in the Ising model with defects*, JHEP **06** (2022) 165.

[332] J. Kruthoff, R. Mahajan, and C. Murdia, *Free fermion entanglement with a semitransparent interface: the effect of graybody factors on entanglement islands*, SciPost Phys. **11** (2021) 063.

[333] A. Roy and H. Saleur, *Entanglement Entropy in the Ising Model with Topological Defects*, Phys. Rev. Lett. **128** (2022) 090603.

[334] P. Calabrese, M. Mintchev, and E. Vicari, *Exact relations between particle fluctuations and entanglement in Fermi gases*, EPL **98** (2012) 20003.

[335] I. Klich and L. Levitov, *Quantum Noise as an Entanglement Meter*, Phys. Rev. Lett. **102** (2009) 100502.

[336] V. Eisler and I. Peschel, *On entanglement evolution across defects in critical chains*, EPL **99** (2012) 20001.

[337] M. Collura and P. Calabrese, *Entanglement evolution across defects in critical anisotropic Heisenberg chains*, J. Phys. A **46** (2013) 175001.

[338] P. Ruggiero, P. Calabrese, T. Giamarchi, and L. Foini, *Electrostatic solution of massless quenches in Luttinger liquids*, SciPost Phys. **13** (2022) 111.

[339] V. Eisler and I. Peschel, *Evolution of entanglement after a local quench*, J. Stat. Mech. (2007) P06005.

[340] L. Capizzi and V. Eisler, *Entanglement evolution after a global quench across a conformal defect*, SciPost Phys. **14** (2023) 070.

[341] O. Gamayun, O. Lychkovskiy, and J.-S. Caux, *Fredholm determinants, full counting statistics and Loschmidt echo for domain wall profiles in one-dimensional free fermionic chains*, SciPost Phys. **8** (2020) 036.

[342] O. Gamayun, A. Slobodeniuk, J.-S. Caux, and O. Lychkovskiy, *Nonequilibrium phase transition in transport through a driven quantum point contact*, Phys. Rev. B **103** (2021) L041405.

[343] A. De Luca and A. Bastianello, *Entanglement front generated by an impurity traveling in an isolated many-body quantum system*, Phys. Rev. B **101** (2020) 085139.

[344] H. F. Song, C. Flindt, S. Rachel, I. Klich, and K. Le Hur, *Entanglement entropy from charge statistics: Exact relations for noninteracting many-body systems*, Phys. Rev. B **83** (2011) 161408(R).

[345] F. Iglói, Z. Szatmári, and Y. -C. Lin, *Entanglement entropy with localized and extended interface defects*, Phys. Rev. B **80** (2009) 024405.

[346] M. Ljubotina, S. Sotiriadis, and T. Prosen, *Non-equilibrium quantum transport in presence of a defect: the non-interacting case*, SciPost Phys. **6** (2019) 004.

[347] S. Fraenkel and M. Goldstein, *Entanglement Measures in a Nonequilibrium Steady State: Exact Results in One Dimension*, SciPost Phys. **11** (2021) 085.

[348] L. Capizzi, S. Scopa, F. Rottoli, and P. Calabrese, *Domain wall melting across a defect*, EPL **141** (2023) 31002.

[349] B. Bertini, M. Fagotti, L. Piroli, and P. Calabrese, *Entanglement evolution and generalised hydrodynamics: noninteracting systems*, J. Phys. A **51** (2018) 39LT01.

[350] B. Bertini, K. Klobas, V. Alba, G. Lagnese, and P. Calabrese, *Growth of Rényi Entropies in Interacting Integrable Models and the Breakdown of the Quasiparticle Picture*, Phys. Rev. X **12** (2022) 031016.

[351] V. Alba and P. Calabrese, *Quench action and Rényi entropies in integrable systems*, Phys. Rev. B **96** (2017) 115421.

[352] V. Alba and P. Calabrese, *Entanglement and thermodynamics after a quantum quench in integrable systems*, PNAS **114** (2017) 7947.

[353] F. Ares, S. Scopa and S. Wald, *Entanglement dynamics of a hard-core quantum gas during a Joule expansion*, J. Phys. A. **55** (2022) 375301.

[354] S. Scopa and D. X. Horváth, *Exact hydrodynamic description of symmetry-resolved Rényi entropies after a quantum quench*, J. Stat. Mech. (2022) 083104.

[355] V. Eisler, *Entanglement spreading after local and extended excitations in a free-fermion chain*, J. Phys. A **54** (2021) 424002.

[356] F. Rottoli, C. Rylands, and P. Calabrese, *Entanglement Hamiltonians and the quasiparticle picture*, arXiv:2407.01730.

[357] V. Alba and P. Calabrese, *Entanglement dynamics after quantum quenches in generic integrable systems*, SciPost Phys. **4** (2018) 017.

[358] P. Calabrese, *Entanglement and thermodynamics in non-equilibrium isolated quantum systems*, Physica A **504** (2018) 31.

[359] P. Calabrese, F. H. L. Essler, and M. Fagotti, *Quantum Quench in the Transverse Field Ising chain I: Time evolution of order parameter correlators* J. Stat. Mech. (2012) P07016.

[360] A. Coser, E. Tonni, and P. Calabrese, *Entanglement negativity after a global quantum quench*, J. Stat. Mech. P12017 (2014).

[361] S. Groha, F. H. L. Essler, and P. Calabrese, *Full Counting Statistics in the Transverse Field Ising Chain*, SciPost Phys. **4** (2018) 043.

[362] D. X. Horváth and C. Rylands, *Full counting statistics of charge in quenched quantum gases*, Phys. Rev. A **109** (2024) 043302.

[363] B. Bertini, P. Calabrese, M. Collura, K. Klobas, and C. Rylands, *Nonequilibrium Full Counting Statistics and Symmetry-Resolved Entanglement from Space-Time Duality*, Phys. Rev. Lett. **131** (2023) 140401.

[364] G. Parez, R. Bonsignori, and P. Calabrese, *Quasiparticle dynamics of symmetry resolved entanglement after a quench: the examples of conformal field theories and free fermions*, Phys. Rev. B **103** (2021) L041104

[365] G. Parez, R. Bonsignori, and P. Calabrese, *Exact quench dynamics of symmetry resolved entanglement in a free fermion chain*, J. Stat. Mech. (2021) 093102.

[366] J. Dubail, *Entanglement scaling of operators: a conformal field theory approach, with a glimpse of simulability of long-time dynamics in 1+1d*, J. Phys. A **50** (2017) 234001.

[367] A. Rath, V. Vitale, S. Murciano, M. Votto, J. Dubail, R. Kueng, C. Branciard, P. Calabrese, and B. Vermersch, *Entanglement barrier and its symmetry resolution: theory and experiment*, PRX Quantum **4** (2023) 010318.

[368] F. Ares, S. Murciano, and P. Calabrese, *Entanglement asymmetry as a probe of symmetry breaking*, Nature Commun. **14** (2023) 2036.

[369] S. Murciano, F. Ares, I. Klich, and P. Calabrese, *Entanglement asymmetry and quantum Mpemba effect in the XY spin chain*, J. Stat. Mech. (2024) 013103.

[370] B. Bertini, K. Klobas, M. Collura, P. Calabrese, and C. Rylands, *Dynamics of charge fluctuations from asymmetric initial states*, Phys. Rev. B **109** (2024) 184312.

[371] F. H. L. Essler and M. Fagotti, *Quench dynamics and relaxation in isolated integrable quantum spin chains* J. Stat. Mech. (2016) 064002.

[372] X. Wen, S. Ryu, and A. W. W. Ludwig, *Entanglement hamiltonian evolution during thermalization in conformal field theory*, J. Stat. Mech. (2018) 113103.

[373] J. Cardy, *Quantum Quenches to a Critical Point in One Dimension: some further results*, J. Stat. Mech. (2016) 023103.

[374] L. Piroli, B. Pozsgay, and E. Vernier, *What is an integrable quench?*, Nucl. Phys. B **925** (2017) 362.

[375] V. Alba and P. Calabrese, *Quantum information scrambling after a quantum quench*, Phys. Rev. B **100** (2019) 115150.

[376] V. Alba and F. Carollo, *Spreading of correlations in Markovian open quantum systems*, Phys. Rev. B **103** (2021) L020302.

[377] F. Carollo and V. Alba, *Emergent dissipative quasi-particle picture in noninteracting Markovian open quantum systems*, Phys. Rev. B **105** (2022) 144305.

[378] V. Alba and F. Carollo, *Hydrodynamics of quantum entropies in Ising chains with linear dissipation*, J. Phys. A **55** (2022) 074002.

[379] V. Alba and F. Caceffo, *Fate of entanglement in quadratic Markovian dissipative systems*, arXiv:2406.15328.

[380] M. C. Chung and I. Peschel, *Density-matrix spectra for two-dimensional quantum systems*, Phys. Rev. B **62** (2000) 4191.

[381] S. Murciano, P. Ruggiero, and P. Calabrese, *Symmetry resolved entanglement in two-dimensional systems via dimensional reduction*, J. Stat. Mech. (2020) 083102.

[382] S. Yamashika, F. Ares, and P. Calabrese, *Time evolution of entanglement entropy after quenches in two-dimensional free fermion systems: a dimensional reduction treatment*, Phys. Rev. B **109** (2024) 125122.

[383] S. Yamashika, F. Ares, and P. Calabrese, *Entanglement asymmetry and quantum Mpemba effect in two-dimensional free-fermion systems*, arXiv:2403.04486.

[384] J. I. Cirac and F. Verstraete, *Renormalization and tensor product states in spin chains and lattices*, J. Phys. A **42** (2009) 504004.

[385] U. Schollwöck, *The density-matrix renormalization group in the age of matrix product states*, Ann. Phys. **326** (2011) 96.

[386] R. Orus, *A practical introduction to tensor networks: Matrix product states and projected entangled pair states*, Ann. Phys. **349** (2014) 117.